

Polymer Nanocomposite Processing, Characterization, and Applications

Guest Editors: Gaurav Mago, Dilhan M. Kalyon,
Sadhan C. Jana, and Frank T. Fisher





Polymer Nanocomposite Processing, Characterization, and Applications

Journal of Nanomaterials

Polymer Nanocomposite Processing, Characterization, and Applications

Guest Editors: Gaurav Mago, Dilhan M. Kalyon,
Sadhan C. Jana, and Frank T. Fisher



Copyright © 2010 Hindawi Publishing Corporation. All rights reserved.

This is a special issue published in volume 2010 of “Journal of Nanomaterials.” All articles are open access articles distributed under the Creative Commons Attribution License, which permits unrestricted use, distribution, and reproduction in any medium, provided the original work is properly cited.

Editor-in-Chief

Michael Z. Hu, Oak Ridge National Laboratory, USA

Advisory Board

James H. Adair, USA
C. Jeffrey Brinker, USA
T. Hyeon, Republic of Korea
Nathan Lewis, USA

Ed Ma, USA
Alon V. McCormick, USA
Gary L. Messing, USA
Zhonglin Wang, USA

Enge Wang, China
Ching P. Wong, USA
N. Xu, China
Jackie Y. Ying, Singapore

Associate Editors

Xuedong Bai, China
Theodorian Borca-Tasciuc, USA
Christian Brosseau, France
Sang-Hee Cho, Republic of Korea
Cui ChunXiang, China
Ali Eftekhari, USA
Claude Estournes, France
Alan Fuchs, USA
Lian Gao, China
Hongchen Chen Gu, China
Michael Harris, USA
Justin D. Holmes, Ireland
David Hui, USA
Wanqin Jin, China

Rakesh K. Joshi, USA
Do K. Kim, Republic of Korea
Kin Tak Lau, Australia
Burtrand Lee, USA
Jun Li, Singapore
Shijun Liao, China
Gong Ru Lin, Taiwan
J. -Y. Liu, USA
Jun Liu, USA
Songwei Lu, USA
Daniel Lu, China
Gaurav Mago, USA
Sanjay R. Mathur, Germany
Nobuhiro Matsushita, Japan

Sherine Obare, USA
P. Panine, France
Edward Andrew Payzant, USA
Donglu Shi, USA
Bohua Sun, South Africa
Maryam Tabrizian, Canada
Theodore Tsotsis, USA
Xiaogong Wang, China
Yong Wang, China
Michael S. Wong, USA
Ping Xiao, UK
Zhi-Li Xiao, USA
Doron Yadlovker, Israel
Kui Yu, Canada

Contents

Polymer Nanocomposite Processing, Characterization, and Applications, Gaurav Mago, Dilhan M. Kalyon, Sadhan C. Jana, and Frank T. Fisher
Volume 2010, Article ID 325807, 2 pages

Frequency and Temperature Dependences of Dielectric Dispersion and Electrical Properties of Polyvinylidene Fluoride/Expanded Graphite Composites, Yu Chao Li, Robert Kwok Yiu Li, and Sie Chin Tjong
Volume 2010, Article ID 261748, 10 pages

Environmental Degradation and Durability of Epoxy-Clay Nanocomposites, Raman P. Singh, Mikhail Khait, Suraj C. Zunjarrao, Chad S. Korach, and Gajendra Pandey
Volume 2010, Article ID 352746, 13 pages

Design and Preparation of Cross-Linked Polystyrene Nanoparticles for Elastomer Reinforcement, Ming Lu, Jianjun Zhou, Liansheng Wang, Wei Zhao, Yonglai Lu, Liqun Zhang, and Yakang Liu
Volume 2010, Article ID 352914, 8 pages

Preparation and Characterization of Self-Assembled Nanoparticles of Hyaluronic Acid-Deoxycholic Acid Conjugates, Xuemeng Dong and Chenguang Liu
Volume 2010, Article ID 906936, 9 pages

Preparation and Characterization of Water-Soluble Chitosan Nanoparticles as Protein Delivery System, Hong-liang Zhang, Si-hui Wu, Yi Tao, Lin-quan Zang, and Zheng-quan Su
Volume 2010, Article ID 898910, 5 pages

The Effects of Coupling Agents on the Properties of Polyimide/Nano- Al_2O_3 Three-Layer Hybrid Films, Lizhu Liu, Ling Weng, Yuxia Song, Lin Gao, and Qingquan Lei
Volume 2010, Article ID 354364, 5 pages

Thermal and Mechanical Properties of Chitosan/ SiO_2 Hybrid Composites, F. Al-Sagheer and S. Muslim
Volume 2010, Article ID 490679, 7 pages

Multiscale Hybrid Micro-Nanocomposites Based on Carbon Nanotubes and Carbon Fibers, Fawad Inam, Doris W. Y. Wong, Manabu Kuwata, and Ton Peijs
Volume 2010, Article ID 453420, 12 pages

Foaming Behaviour, Structure, and Properties of Polypropylene Nanocomposites Foams, M. Antunes, V. Realinho, and J. I. Velasco
Volume 2010, Article ID 306384, 11 pages

Enhancing Fatigue Performance of Sandwich Composites with Nanophased Core, S. Zainuddin, H. Mahfuz, and S. Jeelani
Volume 2010, Article ID 712731, 8 pages

Mechanical and Fracture Behaviors of Elastomer-Rich Thermoplastic Polyolefin/ SiC_p Nanocomposites, Cheng Zhu Liao and Sie Chin Tjong
Volume 2010, Article ID 327973, 9 pages

Thermomechanical Assessment of Plastic Deformation in Model Amorphous Polyamide/Clay Nanocomposites, Kunal Tulsyan, Saurabh Toshniwal, Gowri Dorairaju, Daniel F. Schmidt, and Emmanuelle Reynaud
Volume 2010, Article ID 679786, 8 pages

Editorial

Polymer Nanocomposite Processing, Characterization, and Applications

Gaurav Mago,¹ Dilhan M. Kalyon,² Sadhan C. Jana,³ and Frank T. Fisher⁴

¹Lubrizol Advanced Materials, 550 Moore Road, Avon Lake, OH 44012, USA

²Highly Filled Materials Institute and Department of Chemical Engineering and Materials Science, Stevens Institute of Technology, Hoboken, NJ 07030, USA

³Department of Polymer Engineering, The University of Akron, 250 South Forge Street, Akron, OH 44325, USA

⁴Department of Mechanical Engineering, Stevens Institute of Technology, Hoboken, NJ 07030, USA

Correspondence should be addressed to Frank T. Fisher, frank.fisher@stevens.edu

Received 25 August 2010; Accepted 25 August 2010

Copyright © 2010 Gaurav Mago et al. This is an open access article distributed under the Creative Commons Attribution License, which permits unrestricted use, distribution, and reproduction in any medium, provided the original work is properly cited.

Nanoparticles, such as carbon nanotubes, carbon nanofibers, nanoclay, and exfoliated graphite, are of great interest due to their nanoscale dimensions and remarkable prospect for improvement of mechanical, thermal, electrical, and chemical properties when introduced in small quantities in polymer matrix composites. This prospect has spurred considerable research effort in the polymer community in seeking ways to leverage the properties of these nanoscale inclusions in the development of next generation polymeric materials, as either stand-alone inclusions or as components in hybrid, multiscale composite architectures, often with enhanced multifunctional properties, where simultaneous enhancements in two or more properties are sought. The relevance of these next-generation nanocomposite materials in numerous applications spanning, but not limited to, the biomedical, sensor, aerospace, and defense sectors, continues to motivate further research and development work.

While a number of advances have been made in the development of polymer nanocomposites, it is clear that significant research and development still need to be done. For example, the role of processing of these nanocomposite materials cannot be underestimated, as often a slight change in base polymer material, nanoparticle type, and/or processing conditions can drastically alter the dispersion, orientation, and/or microstructure of the nanocomposite, with corresponding changes in the resulting nanocomposite properties. There is also a need for enhanced, and more quantitative, techniques to characterize the distributions and

orientations of nanoparticles, as well as to experimentally assess the properties of the interface between the polymer and the nanoparticles. The continued development of better, more rigorous multiscale computational models is also necessary to accurately predict the mechanical and other functional properties of the polymer nanocomposite as a function of critical factors such as nanoparticle geometry, nanoparticle orientation, type of functional groups or coupling agents, molecular weight of the polymer chain, and the interfacial properties. These and other advances in the realm of polymer nanocomposites will be necessary before the full potential of polymer nanocomposites can actually be realized.

The objective of this special issue is to bring together some selected examples of current research efforts related to the processing, characterization, and applications of polymer nanocomposites. In this regard, this issue includes samples of topical basic and applied materials research efforts focusing on nanocomposite preparation techniques, characterization, nanoparticle dispersion, morphology and functional properties of polymer nanocomposites for sensors, actuators, and other applications. The twelve research papers comprising this special issue cover topics in the realm of melt processing of polymer nanocomposites with exfoliated graphite to improve dielectric properties and electrical conductivity, the environmental degradation of nanocomposites containing nanoclays, the application of polymer nanoparticles as mechanical reinforcement for

elastomers and of water-soluble chitosan nanoparticles for protein delivery, the effects of coupling agents on the preparation of nanoscale thin films, the generation of hybrid nanocomposites using combinations of nanoparticles with different sizes and surface chemistries and foaming behavior, microstructure, and properties of nanocomposite foams. Additional papers report on the mechanical properties of different nanocomposite systems prepared via conventional processing methods such as extrusion and injection molding. We hope that the collection of articles comprising this special issue will be of interest to a wide range of the readers who are working in this exciting, challenging, and rapidly evolving field.

*Gaurav Mago
Dilhan M. Kalyon
Sadhan C. Jana
Frank T. Fisher*

Acknowledgments

The editors would like to acknowledge and thank the authors, reviewers, and staff members of Hindawi Publishing Corporation for their contributions to this special issue.

Research Article

Frequency and Temperature Dependences of Dielectric Dispersion and Electrical Properties of Polyvinylidene Fluoride/Expanded Graphite Composites

Yu Chao Li, Robert Kwok Yiu Li, and Sie Chin Tjong

Department of Physics and Materials Science, City University of Hong Kong, Kowloon Town, Hong Kong

Correspondence should be addressed to Sie Chin Tjong, aptjong@cityu.edu.hk

Received 19 June 2009; Accepted 21 October 2009

Academic Editor: Gaurav Mago

Copyright © 2010 Yu Chao Li et al. This is an open access article distributed under the Creative Commons Attribution License, which permits unrestricted use, distribution, and reproduction in any medium, provided the original work is properly cited.

A conductive nanofiller, expanded graphite (EG), was introduced into polyvinylidene fluoride (PVDF) by direct melt blending process. The electrical conductivity and dielectric properties of resulting PVDF/EG composites were investigated in a wide range of frequencies from 10^2 to 10^8 Hz. The dielectric dispersion and conductivity of the composite system exhibited a strong frequency dependence particularly in the vicinity of percolation threshold ($\Phi_c = 6$ vol%). Moreover, the dielectric permittivity tended to decrease with increasing frequency while the conductivity displayed a reverse trend. A large permittivity was found in the composite having EG content near Φ_c . Accordingly, percolation concept and biased random walk approach can be used to describe the carrier transport of percolating PVDF/EG system. The conductivity and permittivity of percolating PVDF/EG composites were observed to be temperature dependent.

1. Introduction

Conductive polymer composites reinforced with carbon black (CB) microparticles have been used extensively in industrial sectors as materials for antistatic and electromagnetic shielding. Such polymer microcomposites generally require a large filler concentration to achieve desired electrical properties. The additions of large filler content to polymers lead to poor processability and inferior mechanical properties. In contrast, polymer nanocomposites reinforced with expanded graphite (EG) platelets have shown substantial improvements in electrical conductivity and mechanical property over microcomposites reinforced with CB [1].

Graphite is a carbonaceous material available commercially at relatively low cost. Its structure consists of carbon layers in an alternating stacked sequence. These layers are bonded by weak van der Waals forces. Consequently, oxidizing agent such as sulfuric acid can be easily intercalated into graphite interlayers, forming the so-called graphite intercalation compound (GIC). Expanded graphite (EG) with a high aspect ratio and excellent electrical conductivity can be produced by exfoliating GIC through rapid heating

in a furnace or microwave environment. EG nanoplatelets have been successfully incorporated into polyamide-6, poly(methylmethacrylate), polystyrene and polyolefins to improve their thermal stability, electrical and mechanical performances [2–4].

Polyvinylidene fluoride (PVDF) is a semi-crystalline thermoplastic having remarkable high piezoelectric coefficient [5, 6], excellent thermal stability and chemical resistance compared with other polymers. Consequently, PVDF and its copolymers find widespread industrial applications in transducers, transistor and capacitors. Moreover, PVDF is an attractive polymer matrix for micro- and nanocomposites with superior mechanical and electrical properties [7–11]. Very recently, Almasri et al. [11] investigated the microstructure, electrical and thermomechanical behaviors of solution cast PVDF composites reinforced with carbon nanotubes (CNTs). Their results show that the double-walled CNTs act as nucleation sites for PVDF polymer chains during solution processing. Electrical measurement revealed that the PVDF/CNT nanocomposites exhibit a low percolation threshold. The low percolation filler concentration for electrical conductivity is resulted from very high aspect ratio

TABLE 1: Physical properties of PVDF (Kynar 740).

Physical properties	Value
Density	1.78 g/cm ³
Melting flow rate	1.1 g/10 min (230°C/5 kg load)
Melting point	168°C
Electrical resistivity	2 × 10 ¹⁴ ohm.cm
Dielectric constant	7.70 under 10 ⁶ Hz 10.8 under 100 Hz

(above 1000) of CNTs [12, 13]. However, the high cost of CNTs precludes their extensive application as nanofillers for polymers. In contrast, graphite is naturally abundant and available at a relatively low cost. Graphite nanoplatelets also exhibit good electrical conductivity ($\sim 10^4$ S/cm), thus are ideal nanofillers for conducting polymer nanocomposites. The aspect ratio of graphite nanoplatelets (~ 250) is smaller than that of CNTs, but conducting filler network can also be established in the polymer/EG nanocomposites. This implies that the polymer/EG nanocomposites only require low EG loadings to achieve high electrical conductivity [14]. In terms of economic consideration, it is more cost effective to use EG nanoplatelets to prepare PVDF/EG nanocomposites. However, little is known on the PVDF/EG nanocomposites as far as we know. Accordingly, we prepared PVDF/EG nanocomposites via melt blending and investigated their electrical behavior at various frequencies and temperatures in details. The results are discussed and compared with existing models. The fabrication, microstructure and thermal properties of PVDF/EG nanocomposites have been reported elsewhere [15].

2. Experimental

2.1. Materials. Commercial grade of PVDF (Kynar 740) was supplied by Atofina Chemicals Inc., USA. The physical properties of the matrix material are shown in Table 1. Expandable graphite flake (GIC, 220-50N) was purchased from GrafTech Ltd., USA. EG was obtained via simple thermal-shock treatment of the as-received GIC in an oven at 700°C for 10 seconds. The obtained EG maintains excellent electric conductivity ($\sim 10^4$ S · cm⁻¹) similar to natural graphite. Figures 1(a)–1(d) show SEM images of expandable graphite (Figures 1(a) and 1(b)) and resulting expanded graphite (Figures 1(c) and 1(d)), respectively. The expandable graphite commonly known as the graphite intercalation compound (GIC) comprises of stacked graphene layers intercalated with acid reagents. The incorporation of intercalants at graphite galleries leads to an expansion of the graphite lattice (Figure 2) [16]. From Figure 1(c), EG appears as a loose, porous or worm-like morphology having numerous entangled nanosheets. The thickness of individual graphite sheet determined from the SEM micrograph at higher magnification is ~ 50 nm (Figure 1d).

2.2. Fabrication of Nanocomposites. The fabrication procedure could be seen in our previous study [16]. Briefly,

PVDF/EG nanocomposites were compounded in an internal mixer (Haake, Rheomix 600) at 220°C under 80 rpm for 15 minutes. The EG contents of nanocomposites were fixed at 2, 4, 6, 8, 10, 12, 14 wt%, corresponding to volume concentration of 1.56, 3.14, 4.73, 6.33, 7.95, 9.59 and 11.2%, respectively. The volume content (Φ_{vol}) of EG can be determined from the following equation [15]:

$$\phi_{vol} = \frac{\phi_{wt}/\rho_{EG}}{\phi_{wt}/\rho_{EG} + (1 - \phi_{wt})/\rho_{PVDF}} \times 100\%, \quad (1)$$

where Φ_{wt} represents the EG weight concentration, ρ_{EG} and ρ_{PVDF} are the density of EG (2.29 g/cm³) and PVDF (1.78 g/cm³), respectively. Although EG exhibits a loose, porous structure, its density is assumed closer to that of natural graphite (2.25 \sim 2.30 g/cm³). The resulting composites were compression-molded at 230°C under 20 MPa for 10 minutes. Disk samples with diameter of 12 mm were punched from these molded plates.

2.3. Electrical Measurements. The disk specimens were polished and then coated with silver paste at both sides as two electrodes. AC electrical conductance and capacitance were measured using an impedance analyzer (Agilent model 4294) from frequency 10² to 10⁸ Hz at room temperature. The impedance analyzer was equipped with a small furnace for high temperature measurements. The heating rate of the furnace was maintained at 5°C/min.

3. Results and Discussion

3.1. AC Electrical Properties. Figures 3(a)–3(c) display the frequency dependence of electrical properties. The variation of σ (AC conductivity) with frequency for different EG content of composites is shown in Figure 3(a) at room temperature. At low EG contents (≤ 6 wt%), the electrical conductivity of the nanocomposites increases with increasing frequency. These specimens show a typical insulating behavior with a frequency-dependent conductivity. When the EG content reaches 8 wt%, there is a transition from an insulator to semiconductor. The transition filler concentration of the composite from insulating to conducting is defined as percolation threshold (Φ_c) associated with the formation of conducting network. The insulator-conductor transition is also confirmed by the large dissipation factor ($\tan \delta$) for PVDF/8 wt% EG composite (Figure 3(b)). Above Φ_c , the AC conductivity remains nearly unchanged in the lower frequency region, but becomes frequency dependent approaching the onset frequency (f_c). In this case, the composites display a conducting characteristic over entire range of frequency studied. The frequency independent conductivity is commonly regarded as DC conductivity.

The variations of ϵ' (the real part of the complex dielectric permittivity: $\epsilon^* = \epsilon' - j\epsilon''$) PVDF/EG nanocomposites as a function of frequencies at room temperature is shown in Figure 3(c). As expected, the variation tendency of dielectric constant with frequency is the reverse of electrical conductivity. The ϵ' attains high value at low frequency and decreases exponentially with increase in frequency. The decrease of

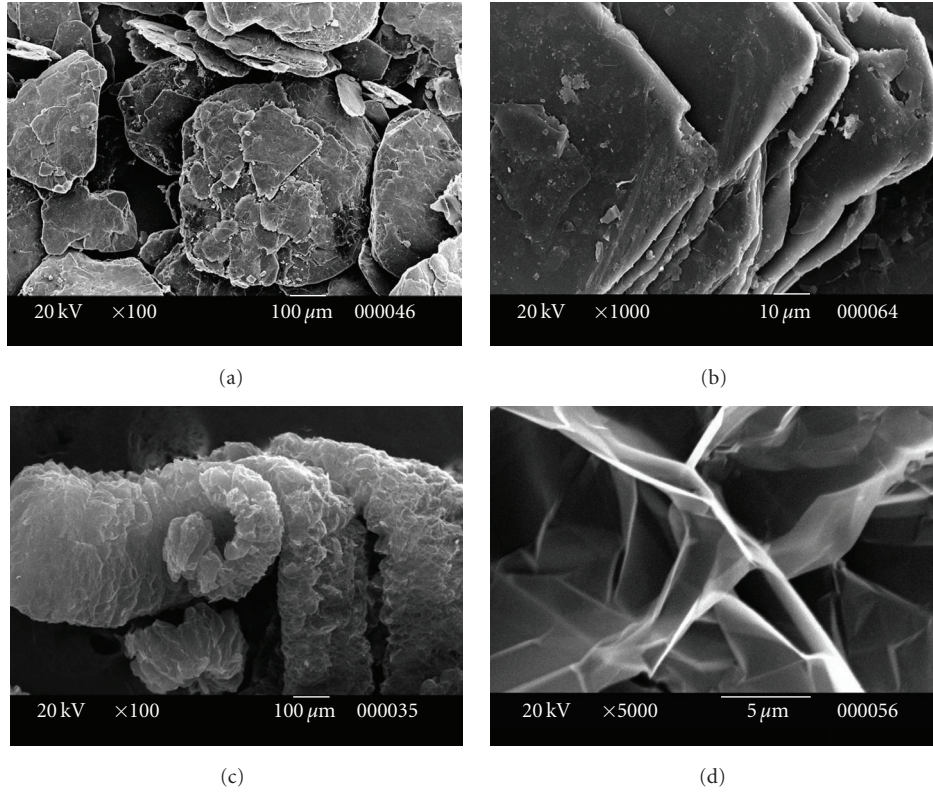


FIGURE 1: SEM images of expandable graphite (a), (b) and expanded graphite (c), (d).

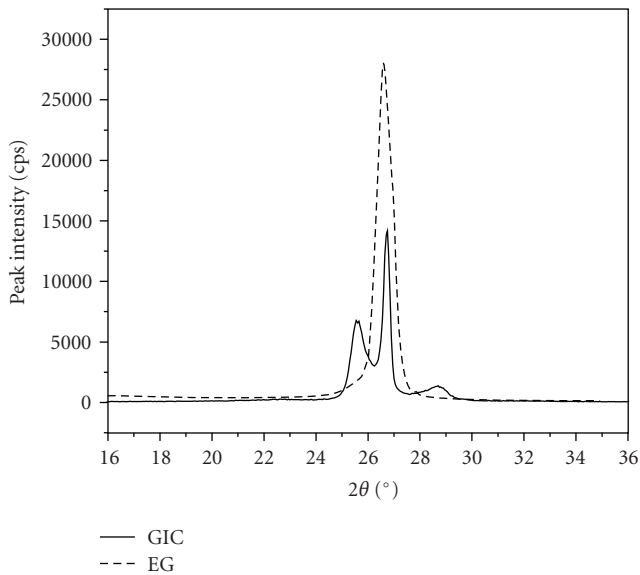


FIGURE 2: XRD patterns of expandable graphite (GIC, Solid line) and expanded graphite (EG, dashed line).

dielectric constant is mainly attributed to the mis-match of interfacial polarization of composites to external electric field at elevated frequencies [17]. The permittivity increases dramatically near the percolation threshold. It is usually believed that the percolation threshold is an important

point at which electrical property varies a lot. Therefore, study conducting composites in the vicinity of percolation threshold is an effective way to know the electrical transport behavior of composites.

According to the percolation theory [18], the variations of $\sigma(f)$ and $\epsilon'(f)$ with frequency follows a power law as the EG content approaches percolation threshold:

$$\sigma(f, \phi_c) \propto \omega^u \quad (2)$$

$$\epsilon'(f, \phi_c) \propto \omega^{-v}, \quad (3)$$

where $\omega = 2\pi f$ is the angular frequency, u , v are critical exponents and theoretically in $u + v = 1$. In practice, the AC conductivity response for various materials can be determined by two parts mathematically as expressed in the following equation [19–21]:

$$\sigma(f) = \sigma_{DC} + A\omega^u, \quad (4)$$

where σ_{DC} is DC conductivity of composites, A is a temperature dependant constant. Equation (4) is often called “AC universal dynamic response” [21] or “AC universality law” [22] because various materials display such behavior. Therefore, AC conductivity can be recognized as the combined effect of DC conductivity ($f = 0$ Hz) caused by migrating charge carriers and frequency induced dielectric dispersion. In this case, a large DC conductivity caused by formation of conducting path-way significantly dominates the transport behavior in a broad frequency range as seen the plateau

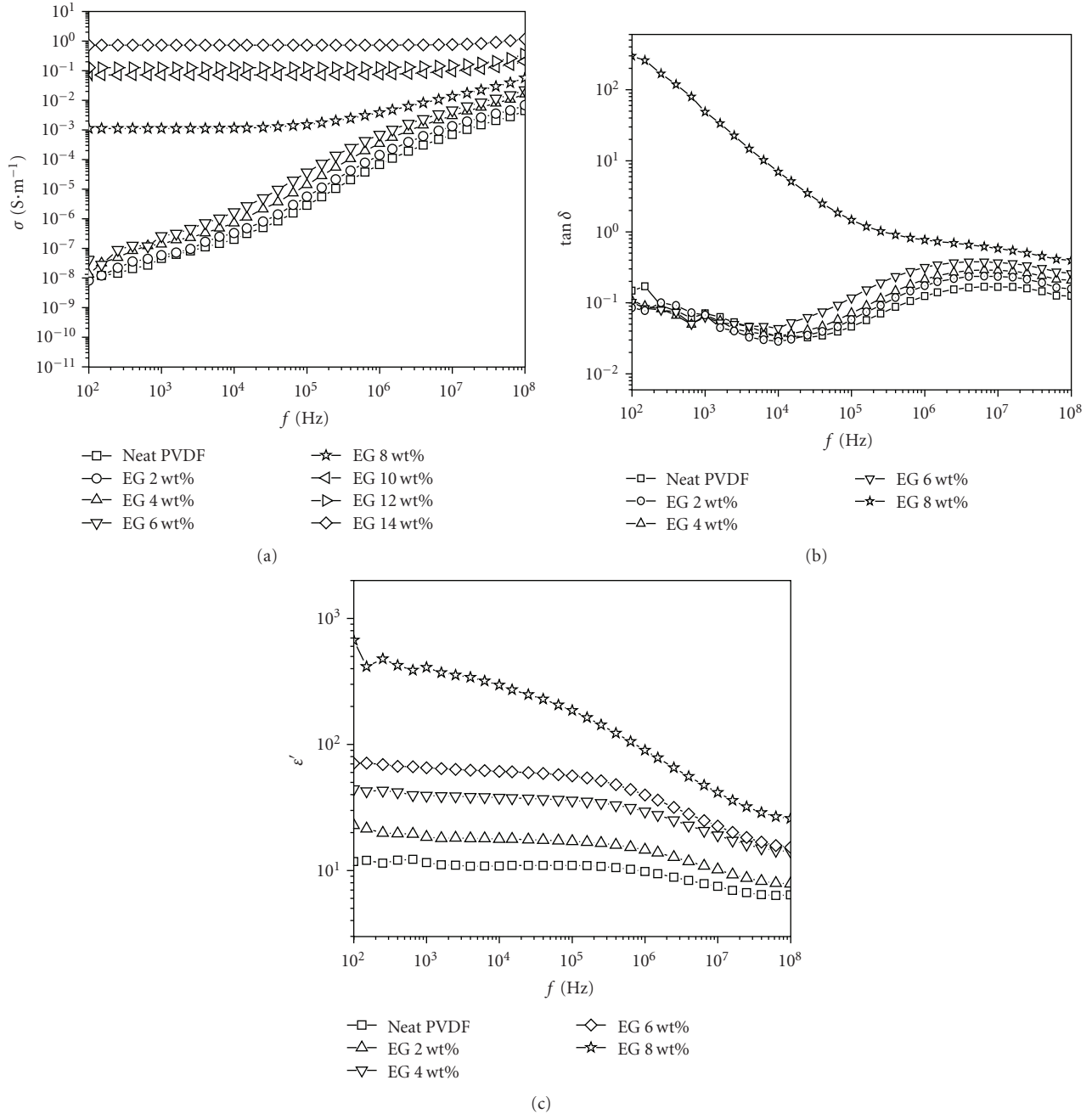
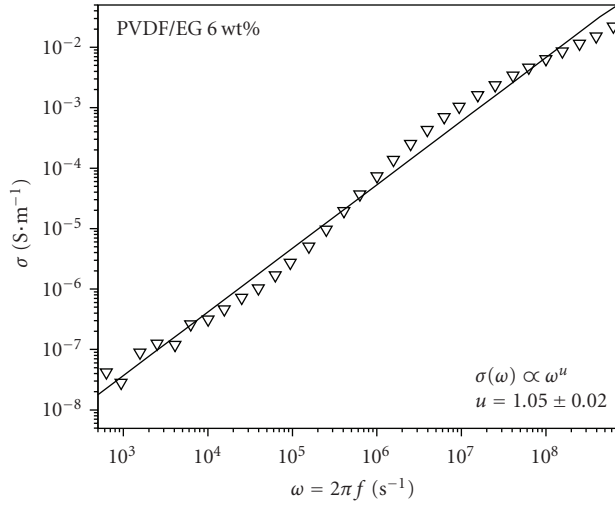


FIGURE 3: (a) Electrical conductivity, (b) loss tangent, and (c) dielectric constant of PVDF/EG composites as a function of frequency.

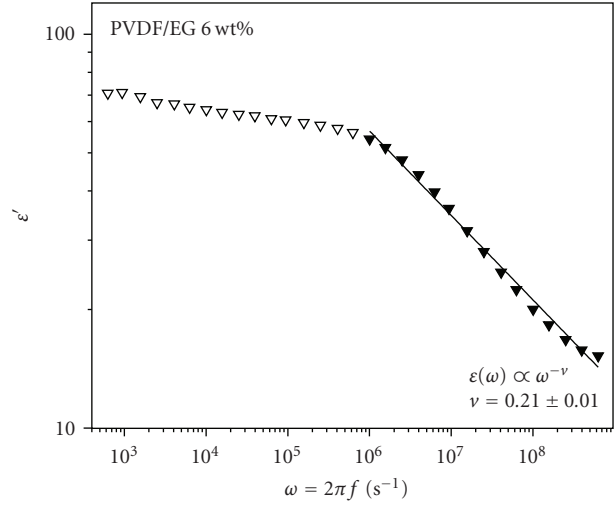
region in Figure 3(a). The effect of frequency highlights only in the high frequency range. Below percolation threshold, σ_{DC} is very small and can be neglect. Equation (4) equals to (2) and frequency prevails in the whole frequency region.

Figures 4(a) and 4(b) show the best fit of frequency dependent conductivity from (2) and (4) for representative PVDF/EG nanocomposites filled with EG contents of 6 and 8 wt% (the vicinity of Φ_c). Accordingly, the variation in dielectric constant with frequency for these nanocomposites is fitted via (3) as shown in Figures 5(a) and 5(b), respectively. For the PVDF/6 wt% EG nanocomposite, the electrical

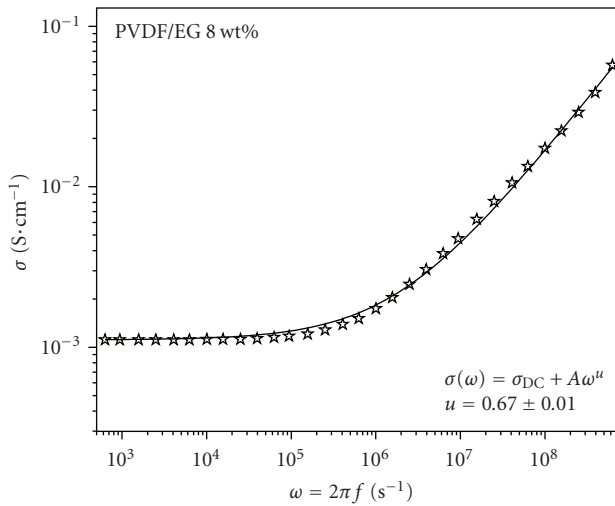
conductivity in the tested frequency region can be well described via (2) deriving a critical exponent (u) of 1.05 ± 0.02 as seen in Figure 4(a). Correspondingly, the dielectric constant of this composite is fitted via (3), but only high frequency region was used (Figure 5(a)), yielding a critical exponent (v) of 0.21 ± 0.01 . It is because, as mentioned above, the influence of frequency prevails or the dipolar polarizations of composites lose the response to electric fields in the high frequency region and the analyzed value in this region according to (3) is therefore much more precise to predict the frequency dependence of dielectric constant. For



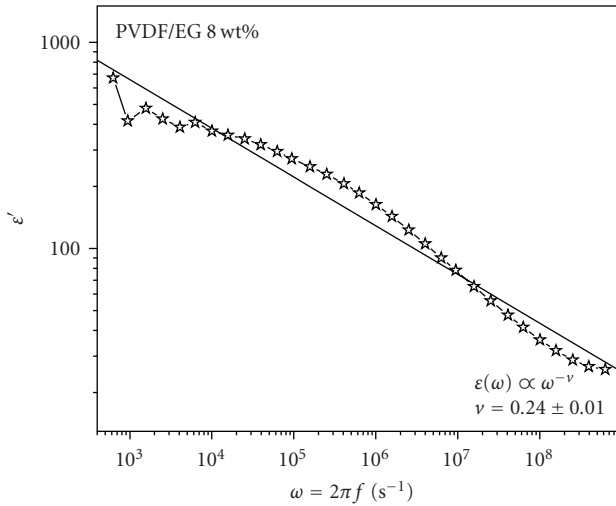
(a)



(a)



(b)



(b)

FIGURE 4: Best fit of frequency dependent conductivity for (a) PVDF/6 wt% EG, and (b) PVDF/8 wt% EG composites.

FIGURE 5: Best fit of frequency dependent dielectric constant for (a) PVDF/6 wt% EG and (b) PVDF/8 wt% EG composites according to (3).

the PVDF/8 wt% EG nanocomposite, the combined effect of σ_{DC} and f is clearly seen (Figure 4(b)). Above f_c which is determined at which the AC conductivity reaches 110% of σ_{DC} , that is, $\sigma_f = 1.1 \sigma_{DC}$ [23], the influence of frequency on conductivity became significant. The critical value u derived from (4) is 0.67. A sharp decrease of u from 1.05 to 0.67 can be attributed to the large DC conductivity which results in the plateau region of the curve in the tested frequency ranges. Accordingly, the change in dielectric constant for PVDF/8 wt% EG composite shows much more dependant in the tested frequency region and the derived critical value $\nu = 0.24$ which a little larger than that of PVDF/6 wt% EG composite.

For composites below Φ_c , the σ_{DC} , ϵ_{DC} , can be determined from the σ_{AC} versus f and ϵ' versus f responses by simply extrapolating to $f = 0$ Hz, respectively. Correspondingly, the temperature dependant parameter A can

be obtained by applying the AC universal law conversely (equation (4)). The σ_{DC} , ϵ_{DC} , u , ν , A and f_c of nanocomposites investigated are listed in Table 2. The value of $u + \nu$ for PVDF/6, 8wt% EG composites are 1.26 and 0.91, respectively. The deviance from theoretical value ($u + \nu = 1$) at Φ_c as presented above indicates the discrepancy of the use of percolation theory to interpret the real composites system with filler content far away from the percolation threshold.

3.2. DC Electrical Performance. To further discuss the charge transport of composites, we herein present their DC electrical performances. The plots of σ_{DC} and ϵ_{DC} (Table 2) versus EG volume content are depicted in Figures 6 and 7. A sharp increase in electrical conductivity ($\sim 10^{-1} \text{ S} \cdot \text{m}^{-1}$) can be readily seen in Figure 6 when the EG content reaches 6.33 vol% (8 wt%). This is over eight orders of magnitude higher than that of pure PVDF ($3.26 \times 10^{-11} \text{ S} \cdot \text{m}^{-1}$). The

TABLE 2: Parameters depicting the frequency dependence of electrical properties of PVDF/EG composites.

Φ (wt%/vol%)	σ_{DC} ($S \cdot m^{-1}$)	f_c (Hz)	u	A	ϵ_{DC}	ν
0/0	$3.26E - 11$	—	1.03 ± 0.02	$4.06E - 12$	12.7	—
2/1.56	$3.63E - 11$	—	1.06 ± 0.02	$3.55E - 12$	24.3	—
4/3.14	$8.38E - 11$	—	1.06 ± 0.02	$8.40E - 12$	48.8	—
6/4.73	$1.78E - 10$	—	1.05 ± 0.02	$1.41E - 11$	82.3	0.21 ± 0.01
8/6.33	$1.07E - 3$	$4.0E + 4$	0.67 ± 0.01	$6.88E - 8$	680	0.24 ± 0.01
10/7.95	0.072	$2.5E + 6$	—	$1.18E - 8$	—	—
12/9.59	0.127	$6.5E + 6$	—	$6.12E - 11$	—	—
14/11.24	0.729	$1.6E + 7$	—	$3.37E - 10$	—	—

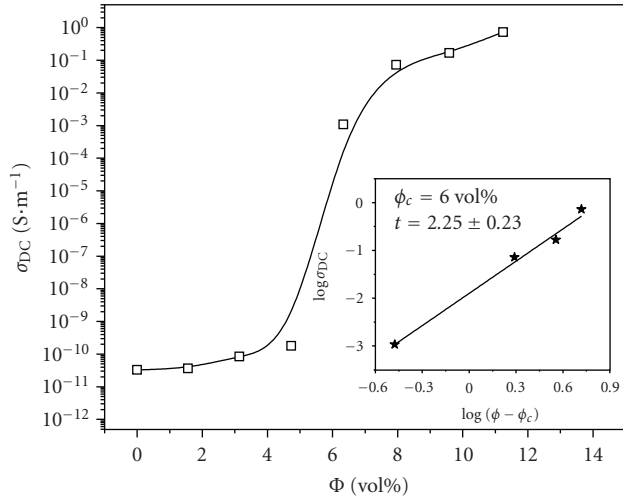


FIGURE 6: DC conductivity as a function of EG concentration.

conductivity levels off above 7.95 vol% (10 wt%) due to the formation of entire conducting network in polymer matrix.

The conductivity generally follows the universal scaling law near the percolation concentration:

$$\sigma_m = \sigma_f (\phi - \phi_c)^t \quad \text{for } \Phi > \Phi_c, \quad (5)$$

where σ_m is the conductivity of composite, σ_f is the conductivity of filler, Φ is the volume fraction of filler, Φ_c the percolation threshold and t the critical exponent. It can be seen from the inset of Figure 6 that the plot of $\log \sigma$ versus $\log(\Phi - \Phi_c)$ yields the best-fit line with a percolation threshold of 6 vol% (~ 7.6 wt%) and a critical exponent of $t = 2.25$. For comparison, the percolation threshold of melt blended PVDF/MWCNT system is found to be 2–2.5 wt% [24, 25]. The low percolation threshold of the PVDF/MWCNT system can be attributed to the large aspect-ratio of CNTs. Since EG with worm-like morphology exhibits lower aspect ratio than CNTs, thus the percolation threshold of PVDF/EG system is much higher than that of the PVDF/MWCNT system. It is noted that the processing route for fabricating PVDF/EG nanocomposites also can affect their percolation threshold. In general, solution blending method tends to yield lower percolation threshold than the

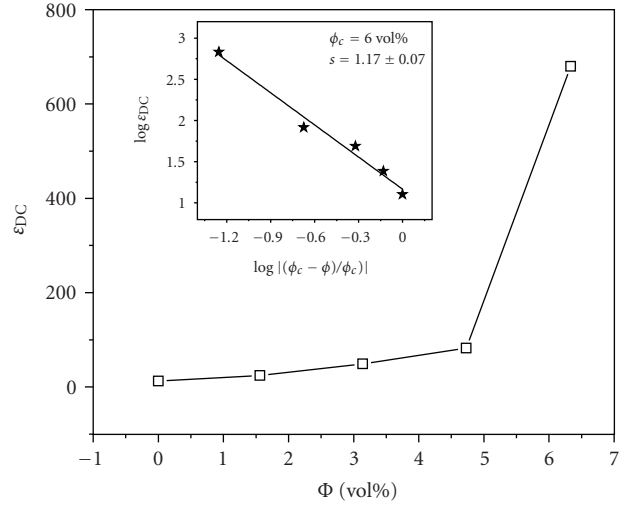


FIGURE 7: DC dielectric constant as a function of EG concentration.

melt blending process. Furthermore, the structure of EG can be further exfoliated to independent graphite nanoplatelets by subjecting to sonication. In this respect, the percolation threshold of PVDF/exfoliated graphite nanocomposites reduces considerably to 1 vol% [14].

In the present study, the value of critical exponent is slightly higher than universal values ($1.6 \sim 2$) reported for three dimensional randomly dispersed system [26]. It is recognized that tunneling conduction in real composites yields nonuniversal critical exponent values [27–30]. Recognizing the fact that the EG nanoplatelets are coated with thin PVDF film, thus tunneling conduction between nanoplatelets prevails above percolation concentration.

Similarly, the variation of dielectric constant in the neighborhood of Φ_c also follows the scaling law:

$$\epsilon_m = \epsilon_p \left| \frac{\phi_c - \phi}{\phi_c} \right|^{-s} \quad \text{for } \Phi < \Phi_c, \quad (6)$$

where ϵ_p is the dielectric constant of PVDF, ϵ_m is the dielectric constant of composites, and s is the critical exponent. Figure 7 shows the variation of dielectric constant with EG content for the PVDF/EG nanocomposites. A sharp increase in dielectric constant ($\epsilon = 680$) is found when

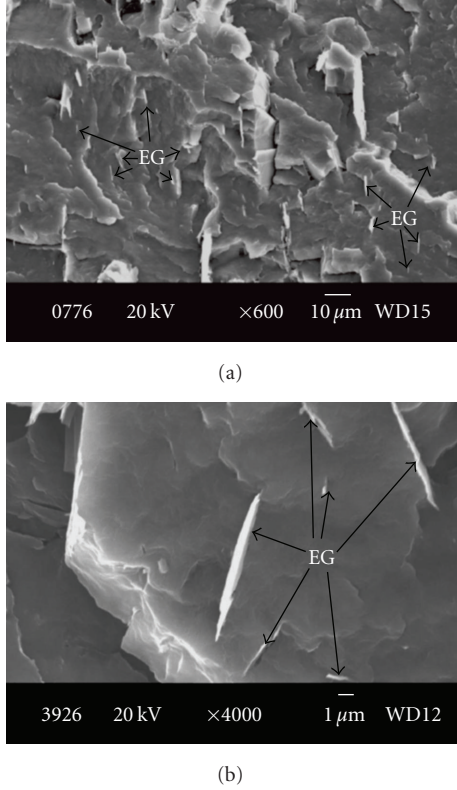


FIGURE 8: (a) Low and (b) large magnification SEM images of PVDF/6 wt% EG composites.

EG content reaches 6.33 vol% (8 wt%). It is nearly 70 times higher than that of neat PVDF matrix. Linear regression fit of experimental data using (6) yields a critical exponent of $s = 1.17$ and Φ_c of 6 vol% (inset of Figure (7)). Such high dielectric constant at percolation concentration can be attributed to the minicapacitor effect. The minicapacitors consist of various graphite nanoplatelets separated by a thin insulating polymer matrix. This high dielectric behavior can be utilized to create high charge-storage devices [31].

The electrical properties of composites generally depend on the particle size, dispersion state and geometry of conducting fillers as well as the property of host polymer. Figures 8(a) and 8(b) are SEM images of the resulting PVDF/6 wt% EG composite. Most EG nanoplatelets of large aspect-ratios can be seen to disperse homogeneously in PVDF matrix. From the literature, conducting nanofillers with large surface areas generally enhance the electrical transport in polymer composites [32]. Figure 9 shows the XRD patterns of representative composites. The peaks located at 18.5° and 19.9° can be assigned to the (020) and (110) reflections of α -PVDF (inset). The graphite characteristic (002) peak can be readily seen at $2\theta = 26.6^\circ$ and its intensity increases with increasing EG loading.

3.3. Biased Random Walk Approximation. The transport properties of the percolating system are formulated in terms of diffusion (random walk) within the filler clusters [27].

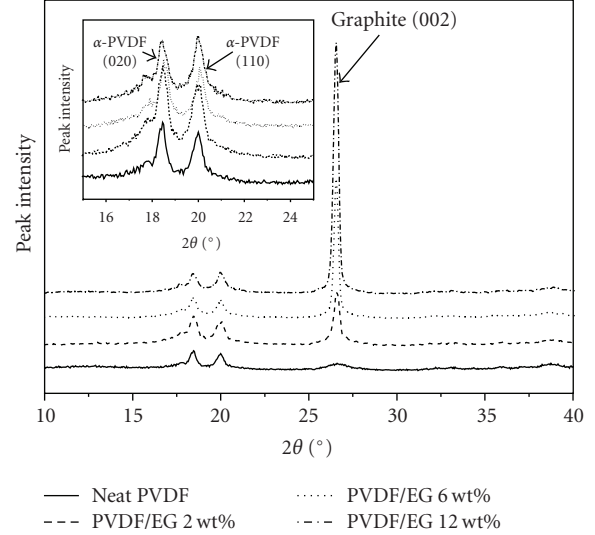


FIGURE 9: XRD curves for PVDF and representative PVDF/EG nanocomposites.

Accordingly, the correlation length ξ , defined as mean distance between the connectivity in the network can be used to describe the characteristic length scale of the system. At Φ_c , the correlation length can be expressed as

$$\xi \propto (\phi - \phi_c)^{-\gamma}, \quad (7)$$

where the γ has the value of $4/3$ in two dimensions [23, 27] and 0.88 in three dimensions [21]. Recently, Kilbride et al. studied the AC and DC conducting behavior of polymer-carbon nanotube thin films [23]. They assumed that charge carriers undergo a biased random walk (BRW) along the conducting network with the relevant distance L being traveled through the network. And then the frequency required for the carrier to travel a distance L in one half period is given by $\omega \sim L^{-1/a}$ with a in the range of $0.5 \sim 1$.

Assuming that $\omega_c = \omega_\xi$, where ω_ξ is the frequency at which a carrier scans a distance equivalent to the correlation length ξ . Then, ω_ξ can be expressed as follows:

$$\omega_\xi \propto \xi^{-1/a}. \quad (8)$$

Combining (6) and (7) and $\omega = 2\pi f$, the critical frequency can be expressed as

$$f_c \propto (\phi - \phi_c)^{\gamma/a}. \quad (9)$$

The critical frequency f_c for composites containing 8–14 wt% of EG listed in Table 2 is plotted against $(\Phi - \Phi_c)$ on a log-log scale as shown in Figure 10. It is clear that f_c versus $\Phi - \Phi_c$ of PVDF/EG composites follow the power law relation quite well. From the slope of linear fit straight line, the exponent γ/a is found to be 2.17. It has also been reported that f_c has the relationship with σ_{DC} above Φ_c by a scaling power law [21, 29]:

$$f_c \propto \sigma_{DC}^b. \quad (10)$$

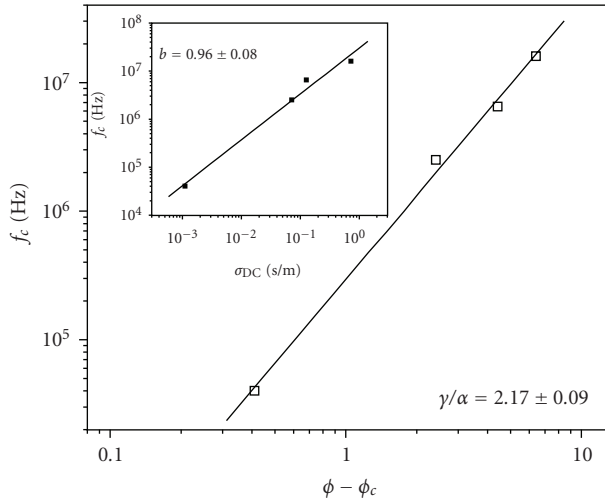


FIGURE 10: Log-log plot of critical frequency f_c versus $(\Phi - \Phi_c)$ for PVDF/EG nanocomposites. The inset displays the relationship between f_c and σ_{DC} .

As can be seen from the inset of Figure 10, the experimental data well obeys this equation with an exponent $b = 0.96$.

From (9) and (10), the relation $\sigma_{DC} \propto (\Phi - \Phi_c)^{\gamma/\alpha b}$ can be deduced, and this corresponds to the percolation conductivity as given in (5). Accordingly, $t = \gamma/\alpha b = 2.17/0.96 = 2.26$. This value is very close to 2.25 directly obtained from the classical percolating equation as mentioned above. In this regard, the biased random walk approach and the assumption of $\omega_c \equiv \omega_\xi$ well describes the conductivity of percolating PVDF/EG system.

3.4. Effect of Temperature. Figure 11 illustrates the variation of resistivity (reciprocal of conductivity) of these nanocomposites, normalized to that at 30°C, with increasing of temperature. The normalized resistivity of composite specimens increases slowly with increasing temperature up to the onset melting point (T_m) of PVDF, follows by a sharp increase near peak melting temperature ($T_m \approx 160^\circ\text{C}$). The increase in resistivity for the PVDF/EG 8 wt% composite near the melting point is more than three orders of magnitude. This behavior is known as the positive temperature coefficient (PTC) effect commonly found in conducting filler/semicrystalline polymer composites [33–37]. Above T_m , the normalized resistivity decreases markedly, referring to as the negative temperature coefficient (NTC) effect. Very recently, Ansari and Giannelis also reported the occurrence of NTC effect in the PVDF/EG system [38]. The exact mechanisms of PTC effect are complicated. Most researchers believe that the volume expansion of the matrix contribute to the abrupt increase of resistivity [33, 35].

The effect of temperature on dielectric constant for representative PVDF/8 wt% EG composite at several frequencies is shown in Figure 12. The dielectric constant increases with decreasing frequency, showing consistent frequency dependence of dielectric constant (Figure 3(c)). In addition, the dielectric constant shows a plateau in low temperature

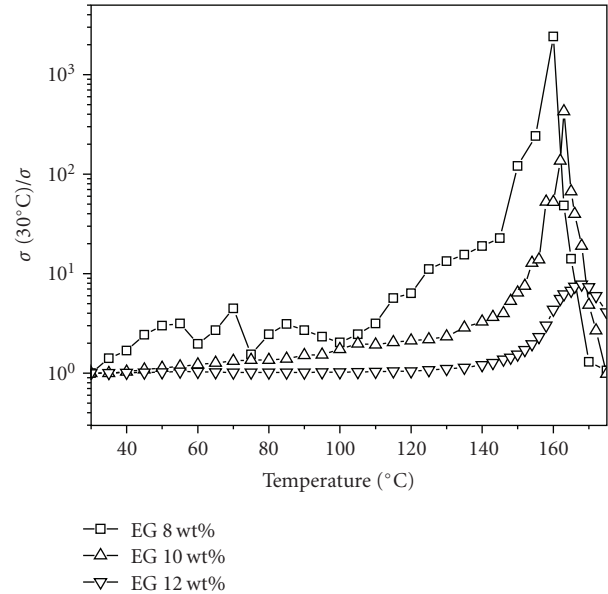


FIGURE 11: Variation of normalized resistivity with temperature.

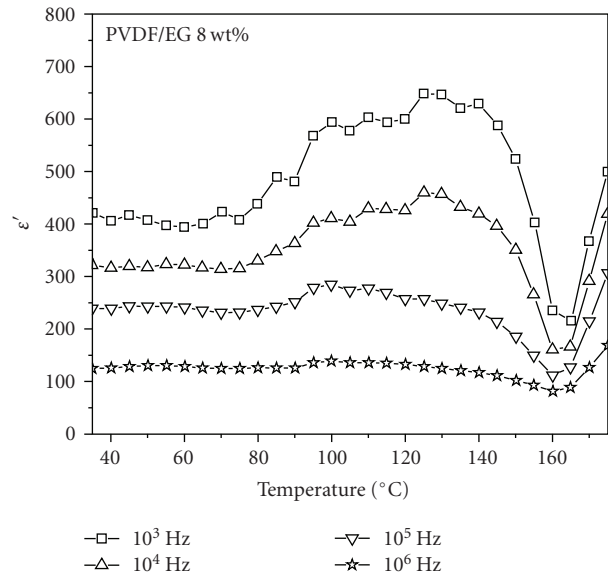


FIGURE 12: Dielectric constant as a function of frequency at various temperatures for PVDF/8 wt% EG nanocomposite.

region ($T < 80^\circ\text{C}$), while a broad peak emerges in temperature range of 80–140°C. This behavior is particularly apparent for the composite tested at 10³ and 10⁴ Hz, and associated with the α -relaxation process of crystalline PVDF [39]. Above 140°C, the dielectric constant decreases and exhibits an apparent minimum near the melting point of composites.

4. Conclusions

PVDF/EG composites were fabricated via direct melt compounding process. The electrical conductivity and dielectric

properties of PVDF/EG composites were measured in a wide range of frequencies from 10^2 to 10^8 Hz at various temperatures. The results showed that the AC conductivity (σ) and dielectric constant (ϵ') of the PVDF/EG composites near the percolation threshold were frequency dependent and obeyed the power law relations ($\sigma \propto \omega^u$ and $\epsilon' \propto \omega^{-v}$). The value of critical exponents $u + v$ for PVDF/6 wt% EG and PVDF/8 wt% EG composites were determined to be 1.26 and 0.91, respectively. The DC conductivity and dielectric constant extrapolated from AC results followed with the percolation scaling law, yielding a percolation threshold $\Phi_c = 6$ vol% and critical exponents $t = 2.25$ and $s = 1.17$, respectively. The introduction of biased random walk approach well described the conductivity of percolating PVDF/EG system. Finally, percolating PVDF/EG composites displayed positive temperature coefficient effect near the melting point of composites. The dielectric constant showed a broad peak in temperature range of 80–140°C which denoted as the α -relaxation process of crystalline PVDF.

References

- [1] K. Kalaitzidou, H. Fukushima, and L. T. Drzal, "Mechanical properties and morphological characterization of exfoliated graphite-polypropylene nanocomposites," *Composites Part A*, vol. 38, no. 7, pp. 1675–1682, 2007.
- [2] F. M. Uhl, Q. Yao, H. Nakajima, E. Manias, and C. A. Wilkie, "Expandable graphite/polyamide-6 nanocomposites," *Polymer Degradation and Stability*, vol. 89, no. 1, pp. 70–84, 2005.
- [3] W. Zheng and S.-C. Wong, "Electrical conductivity and dielectric properties of PMMA/expanded graphite composites," *Composites Science and Technology*, vol. 63, no. 2, pp. 225–235, 2003.
- [4] G. Chen, W. Weng, D. Wu, and C. Wu, "PMMA/graphite nanosheets composite and its conducting properties," *European Polymer Journal*, vol. 39, no. 12, pp. 2329–2335, 2003.
- [5] P. Pötschke, S. M. Dudkin, and I. Alig, "Dielectric spectroscopy on melt processed polycarbonate—multiwalled carbon nanotube composites," *Polymer*, vol. 44, no. 17, pp. 5023–5030, 2003.
- [6] Z. Ounaies, C. Park, K. E. Wise, E. J. Siochi, and J. S. Harrison, "Electrical properties of single wall carbon nanotube reinforced polyimide composites," *Composites Science and Technology*, vol. 63, no. 11, pp. 1637–1646, 2003.
- [7] A. Boudenne, L. Ibos, M. Fois, J. C. Majesté, and E. Géhin, "Electrical and thermal behavior of polypropylene filled with copper particles," *Composites Part A*, vol. 36, no. 11, pp. 1545–1554, 2005.
- [8] J.-W. Kim, W.-J. Cho, and C.-S. Ha, "Morphology, crystalline structure, and properties of poly(vinylidene fluoride)/silica hybrid composites," *Journal of Polymer Science, Part B*, vol. 40, no. 1, pp. 19–30, 2002.
- [9] M. Wang, J.-H. Shi, K. P. Pramoda, and S. H. Goh, "Microstructure, crystallization and dynamic mechanical behaviour of poly(vinylidene fluoride) composites containing poly(methyl methacrylate)-grafted multiwalled carbon nanotubes," *Nanotechnology*, vol. 18, no. 23, Article ID 235701, 7 pages, 2007.
- [10] D. Shah, P. Maiti, E. Gunn, et al., "Dramatic enhancements in toughness of polyvinylidene fluoride nanocomposites via nanoclay-directed crystal structure and morphology," *Advanced Materials*, vol. 16, no. 14, pp. 1173–1177, 2004.
- [11] A. Almasri, Z. Ounaies, Y. S. Kim, and J. Grunlan, "Characterization of solution-processed double-walled carbon nanotube/poly(vinylidene fluoride) nanocomposites," *Macromolecular Materials and Engineering*, vol. 293, no. 2, pp. 123–131, 2008.
- [12] S. C. Tjong, G. D. Liang, and S. P. Bao, "Electrical behavior of polypropylene/multiwalled carbon nanotube nanocomposites with low percolation threshold," *Scripta Materialia*, vol. 57, no. 6, pp. 461–464, 2007.
- [13] G. D. Liang and S. C. Tjong, "Electrical properties of percolative polystyrene/carbon nanofiber composites," *IEEE Transactions on Dielectrics and Electrical Insulation*, vol. 15, no. 1, pp. 214–220, 2008.
- [14] F. He, S. Lau, H. L. Chan, and J. Fan, "High dielectric permittivity and low percolation threshold in nanocomposites based on poly(vinylidene fluoride) and exfoliated graphite nanoplates," *Advanced Materials*, vol. 21, no. 6, pp. 710–715, 2009.
- [15] Y. Li, R. K. Y. Li, and S. C. Tjong, "Fabrication and properties of PVDF/expanded graphite nanocomposites," *E-Polymers*, no. 19, pp. 1–13, 2009.
- [16] H. Quan, B.-Q. Zhang, Q. Zhao, R. K. K. Yuen, and R. K. Y. Li, "Facile preparation and thermal degradation studies of graphite nanoplatelets (GNPs) filled thermoplastic polyurethane (TPU) nanocomposites," *Composites Part A*, vol. 40, no. 9, pp. 1506–1513, 2009.
- [17] J. Meyer, "Glass transition temperature as a guide to selection of polymers suitable for PTC materials," *Polymer Engineering and Science*, vol. 13, no. 6, pp. 462–468, 1973.
- [18] C.-W. Nan, "Physics of inhomogeneous inorganic materials," *Progress in Materials Science*, vol. 37, no. 1, pp. 1–116, 1993.
- [19] G. C. Psarras, E. Manolakaki, and G. M. Tsangaris, "Dielectric dispersion and ac conductivity in—Iron particles loaded—polymer composites," *Composites Part A*, vol. 34, no. 12, pp. 1187–1198, 2003.
- [20] H. Böttger and V. V. Bryksin, *Hopping Conduction in Solids*, Akademie, Berlin, Germany, 1985.
- [21] S. Barrau, P. Demont, A. Peigney, C. Laurent, and C. Lacabanne, "DC and AC conductivity of carbon nanotubes-polyepoxy composites," *Macromolecules*, vol. 36, no. 14, pp. 5187–5194, 2003.
- [22] G. C. Psarras, "Hopping conductivity in polymer matrix-metal particles composites," *Composites Part A*, vol. 37, no. 10, pp. 1545–1553, 2006.
- [23] B. E. Kilbride, J. N. Coleman, J. Fraysse, et al., "Experimental observation of scaling laws for alternating current and direct current conductivity in polymer-carbon nanotube composite thin films," *Journal of Applied Physics*, vol. 92, no. 7, pp. 4024–4030, 2002.
- [24] Y. W. Nam, W. N. Kim, Y. H. Cho, et al., "Morphology and physical properties of binary blend based on PVDF and multiwalled carbon nanotube," *Macromolecular Symposia*, vol. 249–250, pp. 478–484, 2007.
- [25] S. M. Hong and S. S. Hwang, "Physical properties of thin PVDF/MWNT (multi-walled carbon nanotube) composite films by melt blending," *Journal of Nanoscience and Nanotechnology*, vol. 8, no. 9, pp. 4860–4863, 2008.
- [26] S. Kirkpatrick, "Percolation and conduction," *Reviews of Modern Physics*, vol. 45, no. 4, pp. 574–588, 1973.
- [27] D. Stauffer and A. Aharony, *Introduction to Percolation Theory*, Taylor & Francis, London, UK, 1994.
- [28] I. Balberg, "Tunneling and nonuniversal conductivity in composite materials," *Physical Review Letters*, vol. 59, no. 12, pp. 1305–1308, 1987.

- [29] J. C. Dyre and T. B. Schröder, "Universality of AC conduction in disordered solids," *Reviews of Modern Physics*, vol. 72, no. 3, pp. 873–892, 2000.
- [30] J. R. Macdonald, "Impedance spectroscopy," *Annals of Biomedical Engineering*, vol. 20, no. 3, pp. 289–305, 1992.
- [31] L. Wang and Z.-M. Dang, "Carbon nanotube composites with high dielectric constant at low percolation threshold," *Applied Physics Letters*, vol. 87, no. 4, Article ID 042903, 3 pages, 2005.
- [32] J. K. Nelson and J. C. Fothergill, "Internal charge behaviour of nanocomposites," *Nanotechnology*, vol. 15, no. 5, pp. 586–595, 2004.
- [33] Y. Song, Y. Pan, Q. Zheng, and X.-S. Yi, "Electric self-heating behavior of graphite-filled high-density polyethylene composites," *Journal of Polymer Science, Part B*, vol. 38, no. 13, pp. 1756–1763, 2000.
- [34] H. Xie, P. Deng, L. Dong, and J. Sun, "LDPE/carbon black conductive composites: influence of radiation crosslinking on PTC and NTC properties," *Journal of Applied Polymer Science*, vol. 85, no. 13, pp. 2742–2749, 2002.
- [35] J. Fournier, G. Boiteux, G. Seytre, and G. Marichy, "Positive temperature coefficient effect in carbon black/epoxy polymer composites," *Journal of Materials Science Letters*, vol. 16, no. 20, pp. 1677–1679, 1997.
- [36] X. He, L. Wang, and X. Chen, "PTC effect in carbon black-filled ethylene-propylene-diene terpolymer systems," *Journal of Applied Polymer Science*, vol. 80, no. 9, pp. 1571–1574, 2001.
- [37] X. J. He, J. H. Du, Z. Ying, H. M. Cheng, and X. J. He, "Positive temperature coefficient effect in multiwalled carbon nanotube/high-density polyethylene composites," *Applied Physics Letters*, vol. 86, no. 6, Article ID 062112, 3 pages, 2005.
- [38] S. Ansari and E. P. Giannelis, "Functionalized graphene sheet-poly(vinylidene fluoride) conductive nanocomposites," *Journal of Polymer Science, Part B*, vol. 47, no. 9, pp. 888–897, 2009.
- [39] Z.-M. Dang, W.-T. Yan, and H.-P. Xu, "Novel high-dielectric-permittivity poly(vinylidene fluoride)/polypropylene blend composites: the influence of the poly(vinylidene fluoride) concentration and compatibilizer," *Journal of Applied Polymer Science*, vol. 105, no. 6, pp. 3649–3655, 2007.

Research Article

Environmental Degradation and Durability of Epoxy-Clay Nanocomposites

Raman P. Singh,¹ Mikhail Khait,² Suraj C. Zunjarrao,¹ Chad S. Korach,² and Gajendra Pandey¹

¹*Mechanics of Advanced Materials Laboratory, School of Mechanical and Aerospace Engineering, Oklahoma State University, 218 Helmerich Research Center, 700 N. Greenwood Avenue, Tulsa, OK 74106-0700, USA*

²*Laboratory for Nanotribology and Wear Mechanics, Department of Mechanical Engineering, State University of New York, 131 Light Engineering, Stony Brook, NY 11794-2300, USA*

Correspondence should be addressed to Raman P. Singh, raman.singh@okstate.edu

Received 17 December 2009; Accepted 2 June 2010

Academic Editor: Gaurav Mago

Copyright © 2010 Raman P. Singh et al. This is an open access article distributed under the Creative Commons Attribution License, which permits unrestricted use, distribution, and reproduction in any medium, provided the original work is properly cited.

This experimental investigation reports on the durability of epoxy-clay nanocomposites upon exposure to multiple environments. Nanocomposites are fabricated by mixing the clay particles using various combinations of mechanical mixing, high-shear dispersion, and ultrasonication. Clay morphology is characterized using X-ray diffraction and transmission electron microscopy. Specimens of both neat epoxy and the epoxy-clay nanocomposite are subjected to two environmental conditions: combined UV radiation and condensation on 3-hour repeat cycle and constant temperature-humidity, for a total exposure duration of 4770 hours. The presence of nanoscale clay inhibits moisture uptake, as demonstrated by exposure to constant temperature-humidity. Nonetheless, both materials lose mass under exposure to combined UV radiation and condensation due to the erosion of epoxy by a synergistic process. Surprisingly, the epoxy-clay specimens exhibit greater mass loss, as compared to neat epoxy. Mechanical testing shows that either environment does not significantly affect the flexure modulus of either material. On the other hand, both materials undergo degradation in flexural strength when exposed to either environment. However, the epoxy-clay nanocomposite retains 37% more flexure strength than the neat epoxy after 4072 hours of exposure.

1. Introduction

Epoxy-based thermosetting polymer resins have received great attention for aerospace and automotive applications due to their superior thermal and mechanical properties such as high modulus, high creep resistance, high glass transition temperature, low shrinkage at elevated temperature, and good resistance to chemicals. These properties have motivated the use of these resins as the matrix in fiber-reinforced composites that are currently being used extensively in aerospace and automotive industries. Such composites have also found applications in infrastructure applications such as bridges, buildings, transport pipelines, and off-shore drilling platforms due to their superior and directional dependent properties. Despite their inherent advantages, however, such composites are susceptible to

environmental conditions, primarily due to the degradation of the epoxy matrix. Hence, there are concerns regarding their overall long-term durability, especially as related to the capacity for sustained performance under harsh and changing environmental conditions.

The fiber reinforced composites used in infrastructure applications undergo mechanical and thermal loading while being exposed to adverse environments including ultraviolet (UV) radiation, moisture (relative humidity), water vapor condensation, and alkaline/salt environment [1]. The properties of the composites degrade when subjected to these harsh environments. Compared to other environments, UV radiation and water vapor are considered to be predominantly responsible for degradation during outdoor service [2]. Since most polymers have bond dissociation energy in the range of the wavelength of UV radiation (290–400 nm),

they get affected greatly by exposure to the solar spectrum. Ultraviolet photons absorbed by polymers result in photo-oxidative reactions that alter the chemical structure by molecular chain scission or chain crosslinking that results in material deterioration [3]. Chain scission lowers the molecular weight of the polymer, giving rise to reduced strength and heat resistance; chain crosslinking leads to excessive brittleness and can result in microcracking. For prolonged exposure to UV radiation, the matrix dominated properties, such as interlaminar shear strength, flexural strength, and flexural stiffness can suffer severe deterioration [2, 4–7]. Moisture diffusion into the epoxy matrix on the other hand leads to plasticization and hydrolysis, which can cause both reversible and irreversible changes in thermophysical, mechanical, and chemical characteristics [1, 7–9]. Both these processes lower the modulus, glass transition temperature and other matrix-dominated properties such as compressive strength, interlaminar shear strength; fatigue and impact tolerance can also deteriorate [1, 9–14]. Plasticization is usually reversible upon desorption of moisture, while hydrolysis of chemical bonds results in permanent irreversible damage. At the same time, moisture wicking along the fiber-matrix interface can degrade the fiber-matrix bond, resulting in loss of microstructural integrity. Furthermore, degradation phenomena due to UV radiation and moisture when acting together can significantly accelerate the degradation process of the matrix. Kumar et al. [6] studied the combined effect of UV and water vapor condensation and found that cyclic exposure leads to a synergistic degradation mechanism causing extensive matrix erosion and resulting loss of mechanical properties.

The reinforcement of polymers with nanoscale fillers offers the potential for significantly enhanced mechanical [15], thermal, and barrier properties [16]. In these nanocomposites, the enhancement in properties is directly related to the surface area of the reinforcement [17]. For a given volume fraction, the surface area of these nanoscale fillers is much higher as compared to that of micron-sized fillers. As a result, significant enhancement in various properties can be observed using very low volume fractions of nanoscale fillers. Among the various nano-sized reinforcements, high-aspect ratio layered silicates (nano-clay) are especially attractive for enhancing the barrier properties and hence the resistance to environmental degradation. Furthermore, nano-clays are readily available, are cheaper than other nanoscale fillers, and have well understood intercalation chemistry [17–19]. Polymer-clay nanocomposites can exhibit markedly improved mechanical, thermal, and physicochemical properties, as first demonstrated by Toyota researchers in the early 1990s [20]. Motivated by these studies, many researchers have synthesized and studied the properties of various clay-filled thermoplastic resins such as polyamides, polyimides, polyethylene, poly(methyl methacrylate), and ethylene vinyl acetate copolymers. Alexandre and Dubois [21] provide a summary of different polymers and fabrication routes available in the literature. The focus on polymer-clay nanocomposites based on thermosetting resins, especially epoxy, is more recent [18, 22–24].

In comparison to spherical or fiber-like reinforcement the addition of nanoscale clay reinforcement more effectively enhances the barrier properties such as resistance to helium permeability [25] and resistance to moisture transport [26–29]. Kim et al. [29] found that the appropriate choice of organically modified clay can reduce the moisture permeability by as much as 80% for clay loading of only 4 wt.%. Furthermore, Kim et al. observe much higher glass transition temperature for the nanocomposites than the neat epoxy under both dry and wet conditions. These results indicate that reduced moisture permeability could then lead to enhanced environmental resistance and that hypothesis motivates this investigation.

The focus of this paper is on the characterization of the environmental degradation of epoxy-clay nanocomposite under cyclic exposure to both ultraviolet radiation and water vapor condensation. In the past, our studies have shown that these two environments operate in a synergistic manner that leads to extensive degradation by the erosion of the epoxy matrix [6]. It is expected that the addition of clay could mitigate this mechanism by offering a barrier to moisture transport. Furthermore, for the mixing of clay particles in epoxy, prolonged mechanical mixing in association with high-shear dispersion or ultrasonication was investigated following another previous study [24]. The effect of these mixing techniques on the clay morphology and in turn on mechanical properties of epoxy-clay nanocomposites is also investigated.

2. Experimental Methods

2.1. Material Fabrication. A commercially available octadecyl ammonium ion modified montmorillonite (MMT) layered silicate (Nanomer I.30E, Nanocor Inc., Arlington Heights, Illinois, USA) was used as the reinforcing agent. The epoxy resin used was Epon 862 (Shell Chemicals, USA) which is a diglycidyl ether of bisphenol F, and the curing agent used was Epikure 3274 (Shell Chemicals, USA) which is a moderately reactive, low viscosity aliphatic amine curing agent. A mechanical mixer (Model 350 Lab Stirrer, Arrow Engineering, Hillside, New Jersey, USA), a high speed shear dispenser (SV 25 KV—25 F dispersing element, IKA Works Inc., Wilmington, North Carolina, USA), and an ultrasonic agitator (Model TSX750, Tekmar Dohrmann, Mason, Ohio, USA) were used to mix the clay in epoxy resin in five different ways.

Two different set of samples were fabricated in order to first establish the mixing process by enhancing the mechanical properties, then characterizing the environmental durability of the epoxy-clay nanocomposite. In the first set of samples 2% clay by volume fraction was used, and the mechanical properties of the different nanocomposite fabricated by using different mixing techniques were compared. To maximize the barrier properties due to addition of clay, it is desired to maximize the volume fraction of the same in the epoxy resin. Previous work by Zunjarrao et al. has shown that no agglomeration-induced deterioration of mechanical properties occurs as the volume fraction of clay

is increased up to 4% [24]. Therefore, 4 vol.% clay was used to fabricate epoxy-clay nanocomposite by using the effecting mixing technique that was established before to evaluate the environmental durability of the nanocomposite. Note that, mechanical property enhancement, especially fracture toughness, is directly correlated to exfoliation and dispersion of clay in the epoxy matrix. The greater the exfoliation, the more the enhancement in barrier properties, and thus, greater resistance to environmental degradation.

The first set of epoxy-clay nanocomposite fabrication started with the addition of 2% clay by volume fraction to liquid epoxy resin preheated to a temperature of 60°C. The clay was then dispersed in epoxy by five different ways generating five nanocomposites with same constituents but formed by different processing techniques. In the first and second cases clay was dispersed by simply ultrasonication or high-shear dispersion, respectively, both for a period of 30 minutes. Both these processes led to heat generation due to viscous mixing. Since high temperatures can have a deleterious affect on the epoxy resin used, the temperature of the mixture was maintained at 60–65°C by using an ice bath. In the third case, clay was dispersed by stirring the mixture using a mechanical stirrer for a period of 14 hours. While in the fourth and fifth cases, the epoxy-clay mixture was first mixed for 14 hours using a mechanical stirrer and then further mixed using ultrasonication and high-shear dispersion, respectively, both again for 30 minutes. All the five mixtures were further processed and subjected to in situ polymerization using the same procedure. Mixture of clay and epoxy was degassed in a vacuum chamber for 12 hours to completely remove trapped air. A stoichiometric amount of the curing agent was added and hand mixed gently to avoid introduction of any air bubbles due to mixing action. The final slurry, free of air bubbles, was poured into an aluminium mold and allowed to cure under room temperature for 24 hours followed by postcuring at 121°C for 6 hours. Specimens for fracture toughness and flexural modulus tests were then cut out of the final cured sheet.

Two types of materials were prepared for environmental durability testing, Neat epoxy samples were prepared as before using Epon 862 and Epikure 3274 mixed with mechanical agitation. The mixed resin was degassed under vacuum for one hour before being poured into a teflon-coated aluminum mold. Curing occurred at 25°C for 48 hours followed by postcuring at 121°C for 8 hours. The epoxy-clay nanocomposite was fabricated using the previously established procedure that results in optimal dispersion of the nanoclay. First, a desired amount of clay, to result in a final volume fraction of 4%, was added to liquid epoxy resin preheated to 60°C. This mixture was mixed using a mechanical stirrer for 14 hours while maintaining the temperature at 60°C using a hot plate. Subsequently, the mixture was processed for 30 minutes in a high-speed shear dispenser operating at 15,000 rpm. The high-shear process produces heat due to frictional dissipation in the polymer, and the temperature of the mixture was maintained at 60–65°C using an ice bath. The mixture was then degassed in a vacuum chamber for 2 hours to completely remove any trapped air. A stoichiometric amount of the curing agent was

then added and hand mixed gently to avoid introduction of any air bubbles due to mixing action. The final slurry, free of air bubbles, was poured into a teflon-coated aluminum mold and allowed to cure at 25°C for 48 hours followed by postcuring at 121°C for 8 hours.

In this manner, three sheets each of neat epoxy and epoxy-clay were fabricated with nominal dimensions of 110 × 110 × 3.2 mm. Specimens were then machined out of the fabricated sheets with nominal dimensions of 63.5 × 12.7 × 3.2 mm using a water-cooled, high-speed diamond saw. This specimen size was required for the flexure tests to be conducted after environmental exposure. Each sheet yielded fourteen specimens, which lead to a sufficiently large number of samples for generating statistically relevant data. The cured sheets and machined specimens were stored in a dessicator prior to environmental exposure and conditioning.

2.2. Mechanical Properties. Mechanical properties of epoxy-clay composites to establish the mixing procedure were characterised in terms of the flexural modulus and critical stress intensity factor.

The flexural moduli of neat epoxy and the epoxy-clay nanocomposites were determined as per ASTM standard D6272-10 [30]. Specimens with a nominal size of 63.5 × 12.7 × 6.35 mm (2.5 × 0.5 × 0.25 in) were quasistatically loaded under four-point bending on a bench-top testing frame (Tira Test 2500, TIRA GmbH, Schalkau, Germany) at a crosshead speed of 1.5 mm/minute, support span width of 49.6 mm, and a loading span width of 24.8 mm. The load was measured using a 2000 N load cell, and the load-point specimen displacement was measured using a linear variable displacement transducer (Schaevitz Sensors, Hampton, Virginia, USA). At least four samples were tested for each volume fraction and each material processing technique used.

Fracture tests were carried out on neat epoxy and epoxy-clay nanocomposites using single edge notched specimens having a nominal size of 55.8 × 12.7 × 6.35 mm (2.2 × 0.5 × 0.25 in). Specimens were quasistatically loaded under three-point bending on the bench-top testing frame. In order to generate a starter crack, first a 4.8 mm deep notch was machined into the specimen using a high-speed diamond saw (MK-370, MK Diamond Products Inc., Torrance, CA). Subsequently, a razor blade was inserted into this machined notch and tapped with a small load using a jig designed in-house to generate a small, yet well-controlled starter precrack. The peak load, as obtained from the load-displacement curve, was used as the maximum applied force, P , to determine the fracture toughness.

Precise measurement of the actual crack length, a , was done after the fracture experiments using an optical microscope equipped with a micrometer stage. All specimens considered valid for fracture tests had a nominal crack length to specimen width ratio, a/W , of 0.45–0.5, as per ASTM standard 5045 [31]. The fracture toughness was calculated using $K_{Ic} = P/(B\sqrt{W})f(a/W)$, where P is the maximum applied force, B is the thickness of specimen, W is width of

the specimen, and the function $f(a/W)$ is a geometry factor [32].

2.3. Clay Dispersion Morphology. In order to investigate the structure of clay formed in the final composites fabricated for establishing the mixing procedure, wide angle X-ray diffraction (WAXD) measurements were carried out on the epoxy-clay composites using Scintag PAD-X automated diffractometer with a $\text{CuK}\alpha$ radiation ($\lambda = 0.1540 \text{ nm}$) and a scanning rate of 0.5°C per min. The generator was operated at 45 kV and 25 mA. WAXD measurements were also performed on cured samples of neat epoxy (EPON 862) and pure clay powder (Nanocor I.30E).

The morphology of clay particles was also studied under a transmission electron microscope (TEM). Specimens were cut from nanocomposite blocks using an ultramicrotome. The structure of clay particles in the nanocomposites was observed using a Phillips CM12 TEM at an accelerated voltage of 80 kV. Several specimens were cut from each material to investigate the extent of clay exfoliation and the presence of agglomerated particles.

2.4. Environmental Exposure. Neat epoxy and epoxy-clay nanocomposite specimens were subjected to two environmental conditions for characterizing their environmental durability.

2.4.1. Combined UV Radiation and Condensation. The samples were exposed to alternating 3-hour cycles of UV radiation and water vapor condensation at a temperature of 50°C . The combined environment was simulated on a QUV/se Accelerated Weathering Tester, (Q-Panel Lab Products, Cleveland, Ohio, USA).

2.4.2. Relative Humidity. The samples were exposed to a constant 80% relative humidity environment at 50°C in a temperature-humidity chamber (Benchmaster BTRS, Tenney Environmental, Williamsport, Pennsylvania, USA). From each batch five samples were used for each environmental condition, and four samples were held as control. Various exposure details were employed, and Table 1 lists details of the two environmental exposure conditions.

Throughout the exposure process, samples were removed on a regular basis for mass loss measurements. For the first two weeks the samples were weighed every 24 hours. Afterwards, the samples were weighed every 48 hours and finally every 72 hours. The samples in the QUV chamber were turned over after every weight measurement to ensure even exposure to the UV and condensation on both sides of the specimen. The time required to reach thermal equilibrium for the QUV environmental chamber is $\sim 15\text{--}20$ minutes. Therefore, in order to ensure the most accurate weight reading, the samples in the QUV chamber were removed ten minutes prior to the end of the UV cycle. This ensured that the samples were dry and that the temperature within the chamber remained close to 50°C .

2.5. Post-Degradation Testing. At the end of the environmental exposure, the specimens were tested to determine the flexural modulus and strength as per ASTM standard D6272-10 [30]. Specimens with a nominal size of $63.5 \times 12.7 \times 3.2 \text{ mm}$ were quasistatically loaded under four-point bending on a bench-top testing frame (Model 5567, Instron, Canton, Massachusetts, USA) at a crosshead speed of 13.13 mm/min , with a support span of 49.6 mm and a loading span of 24.8 mm . The load was measured using a 30 kN load cell, and the load-point specimen displacement was measured using the crosshead motion. Flexure modulus and strength were studied as an environmental exposure duration for both neat epoxy and the epoxy-clay nanocomposite. At least four specimens were tested for each material, environmental exposure, and exposure duration.

2.6. Postdegradation Surface Degradation. The surface of both neat epoxy and epoxy-clay composite samples was imaged using a high resolution digital microscope (Keyence Digital Microscope VHX 500, Osaka, Japan), as a function of environmental exposure. This camera records multiple images for each location at various focussing depths to create a 3-dimensional reconstruction of the surface. This process produces images that are in sharp focus and also allows for quantitative surface analysis. The imaging was conducted at a magnification power of $500\times$, which yielded a $610 \mu\text{m} \times 457 \mu\text{m}$ (0.279 mm^2) viewing area. The camera is capable of an 18 mega pixel resolution. For this study, however, a resolution of 3.2 mega pixels was found to be adequate for both qualitative observations and quantitative image analysis. Up to ten images were taken for each sample, at different locations, to obtain an accurate representation of the surface. Finally, due to the amount of time required to take photographs of each sample, the imaging was done only at the end of each degradation cycle.

3. Results and Discussion

3.1. Mechanical Properties. The comparison of flexural modulus values for epoxy-clay nanocomposites prepared in five different ways is shown in Table 2. For comparison purposes the flexural modulus of neat epoxy resin was also determined and is listed in the table. In general, all the nanocomposites showed improved modulus as compared to neat epoxy. Nanocomposites processed using either ultrasonication or high-shear dispersion exhibited higher modulus than processing by just mechanical mixing. Furthermore, nanocomposites processed by combination of mechanical mixing and ultrasonication or high-shear dispersion showed higher modulus than nanocomposites processed by only mechanical mixing and by either ultrasonication or high-shear dispersion alone. It can be seen that high-shear dispersion led to higher modulus vis-à-vis ultrasonic mixing. Of all the nanocomposites prepared by the five different mixing methods, the nanocomposites processed by prolonged mechanical mixing followed by high-shear dispersion lead to the greatest improvement in flexural modulus.

TABLE 1: Details of the environmental exposure conditions.

Environment	Exposure condition	Duration
Combined UV radiation and condensation	3-hour repeated cycle	1320, 2712, and 4098 hours
	UV: 0.68 W/m ² irradiance at 340 nm	
	Condensation: 100% relative humidity Temperature: 50°C	
Moisture	Continuous exposure 80% relative humidity Temperature: 50°C	1320, 2712, and 4098 hours

TABLE 2: Initial mass gain and final mass loss for exposure to UV radiation and condensation.

Material	Processing	Flexure modulus (GPa)	Fracture toughness (MPa√m)
Neat epoxy	None	2.70 ± 0.05	0.94 ± 0.05
	Hand mix + ultrasonication	3.59 ± 0.11	1.23 ± 0.07
Epoxy-clay	Hand mix + high-shear dispersion	3.69 ± 0.04	1.31 ± 0.04
Nanocomposite	14 hour mechanical mixing	3.50 ± 0.06	1.29 ± 0.02
	14 hours mechanical + ultrasonication	3.75 ± 0.10	1.17 ± 0.03
	14 hours mechanical + high-shear dispersion	3.94 ± 0.20	1.34 ± 0.05

Table 2 also lists the fracture toughness values for epoxy-clay nanocomposites prepared in five different ways. Fracture toughness was also determined for plain epoxy samples and is listed for comparison. Unlike flexural modulus, fracture toughness was higher for nanocomposite processed with just prolonged mechanical mixing as compared to that processed by 1 hour mechanical and 30 minutes high-shear dispersion. Nanocomposite processed by just high-shear dispersion exhibited higher fracture toughness than that processed by just mechanical mixing, and nanocomposite processed by combination of 14 hours mechanical and 30 minutes high-shear dispersion exhibited the highest values for fracture toughness of all the nanocomposites studied. However, nanocomposites processed by ultrasonic mixing and combination of mechanical and ultrasonic mixing exhibited lower values for fracture toughness.

The incorporation of extended mechanical mixing contributes significantly to the exfoliation of clay, and the best properties are obtained for extended mechanical mixing followed by high-shear dispersion. In fact the values of modulus and fracture toughness obtained in this study are both higher than properties obtained in an earlier investigation that employed only 1 hour of mechanical mixing. The improved properties of epoxy-clay nanocomposites processed by just high-shear dispersion and combination of prolonged mechanical and high-shear dispersion as compared to just ultrasonication can be attributed to the better dispersion of clay and the greater exfoliation of clay particles, which is indicated by XRD measurements discussed in the following section.

3.2. Morphology. X-ray diffraction studies (XRD) were performed on the epoxy-clay specimens to study the morphology of clay particles in the cured composites. Figure 1 shows the diffractograms obtained for a cured specimen of plain

epoxy (a), clay powder (g), and all the epoxy-clay specimens (b)–(f). It can be seen that neat epoxy did not show any peaks in the diffraction pattern, as is expected owing to its amorphous nature. A distinct 2.2 nm peak can be seen in the diffractogram obtained for composites fabricated by just ultrasonication (b). Also, slight peaks can also be observed for materials processed using just high-shear dispersion (c). These peaks are suggestive of intercalated clay morphology where in the clay platelet separation is not very large. On the other hand, epoxy clay nanocomposites fabricated by 14 hours of just mechanical mixing (d), those fabricated by mechanical mixing followed by ultrasonication (e) and those fabricated by mechanical followed by high-shear dispersion (f), show no peaks, indicating that complete exfoliation of clay is achieved in these composites. Figure 1 also shows diffractogram obtained for pure I.30E clay powder (g) in which characteristic peaks corresponding to (001) and (002) planes can be seen at 2.2 nm and 1.1 nm, respectively.

Clay morphology was further characterised using transmission electron microscopy (TEM). Figure 2 shows four TEM images obtained from a sample fabricated using 14 hours of mechanical mixing followed by high-shear dispersion. As can be seen from Figures 2(a)–2(c), several regions of the material show the presence of exfoliated clay platelets. Nonetheless, even with this processing technique there were regions that exhibited clay particles that were neither exfoliated nor intercalated, as shown in Figure 2(d).

3.2.1. Mass Loss or Gain upon Environmental Exposure.

When exposed to constant relative humidity conditions in the temperature-humidity chamber, both neat epoxy and epoxy-clay composite samples gained mass due to moisture uptake, as can be seen in Figures 3 and 4. These figures show data from multiple samples, to demonstrate scatter, and also plots the averaged variation. A comparison of

TABLE 3: Flexure modulus values in GPa for neat epoxy and epoxy-clay nanocomposites, as a function of exposure duration, subjected to environmental exposure by either temperature-humidity or by combined UV radiation and condensation.

Exposure duration	Temperature-humidity		UV and condensation	
	Neat epoxy	Epoxy-clay	Neat epoxy	Epoxy-clay
0	4.4 ± 0.3	4.6 ± 0.2	4.4 ± 0.3	4.6 ± 0.2
1320	4.9 ± 0.1	4.8 ± 0.3	4.2 ± 0.2	5.1 ± 0.4
2712	4.8 ± 0.3	4.9 ± 0.3	3.7 ± 0.4	4.5 ± 0.3
4098	5.1 ± 0.2	4.8 ± 0.2	3.9 ± 0.2	4.3 ± 0.2

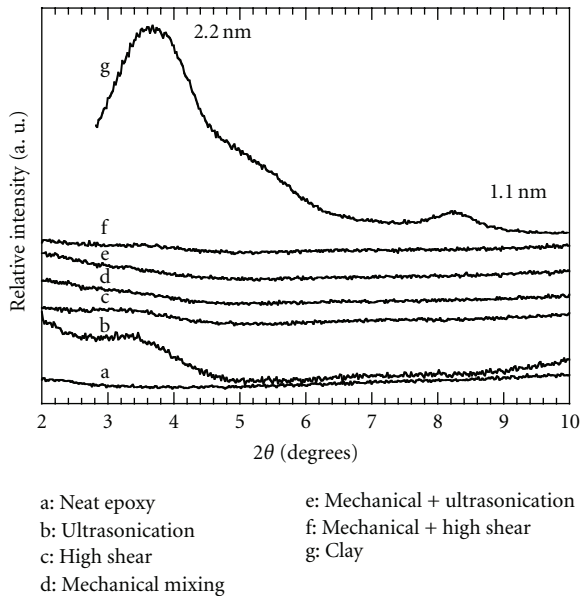


FIGURE 1: Wide angle X-ray diffraction (WAXD) patterns for epoxy-clay nanocomposites prepared using various processing techniques, along with the reference patterns for neat epoxy and clay powder.

the moisture absorption for neat epoxy and the epoxy-clay nanocomposites is shown in Figure 5 after taking an average reading from all the samples.

Both materials started gaining mass at a similar high rate for the first 250–325 hours and exhibited an increase of $\sim 1.6\%$. Shortly thereafter, the rate of moisture absorption for the epoxy-clay nanocomposite was minimal. Meanwhile, the neat epoxy specimens continued to increase in mass, and were not approaching saturation even after 4770 hours of exposure. The final mass gain by the epoxy-clay samples was 2.0% and for neat epoxy was 3.4%.

The variations in specimen mass for neat epoxy and epoxy-clay nanocomposite specimens exposed to combined UV radiation and condensation are shown in Figures 6 and 7. A comparison of averaged mass loss data for neat epoxy and epoxy-clay nanocomposites exposed to combined UV radiation and condensation is shown in Figure 8. In both cases, the samples gained in mass, for the first 100–500 hours, due to moisture uptake by the epoxy. Subsequently, the specimens started to lose mass by an epoxy erosion process. This process was first demonstrated

by Kumar et al. [6], albeit for a different epoxy matrix, and is related to the synergistic physicochemical degradation of epoxy upon exposure to combined UV radiation and condensation.

At the end of the exposure duration, at 4770 hours, the neat epoxy samples had lost ~ 1.8 wt.% while the epoxy-clay nanocomposite specimens had lost 2.87 wt.%. It was surprising to note that the epoxy-clay specimens exhibited greater mass loss, as compared to neat epoxy. This could indicate a greater degradation for the latter material due to synergistic erosion of the epoxy matrix. Nevertheless, this is not readily apparent given the moisture uptake results obtained for exposure to a constant relative humidity environment. During the exposure to combined UV radiation and condensation, there are two competing mechanisms that govern the variation of specimen mass: decrease in mass due to loss of epoxy matrix and increase in mass due to moisture absorption. Therefore, the increased mass loss for epoxy-clay nanocomposites could indicate *either* increased erosion of the epoxy matrix *or* a decreased uptake of moisture. Just based on mass loss or gain measurements it is not possible to identify which mechanism leads to the observed increase in mass loss.

3.2.2. Effect of Environmental Exposure on Residual Properties.

Table 3 lists the measured values of flexure modulus, as a function of exposure duration, for neat epoxy and epoxy-clay nanocomposites exposed to the two environmental conditions. As shown, exposure to relative humidity does not lead to a significant change in modulus for either material. In fact it appears that the modulus marginally increases due to moisture absorption, however, data scatter (in $\pm 1\sigma$) precludes a concrete observation. For exposure to UV radiation and condensation, the flexure modulus marginally decreases for both materials with increasing exposure duration. This modulus decrease is due to epoxy erosion from synergistic material degradation. The decrease in modulus is slightly greater for the neat epoxy specimens as compared to the epoxy-clay nanocomposite, which indicates that the presence of clay leads to increased environmental durability.

The measured values of flexure strength, as a function of exposure duration, are listed in Table 4. Both materials undergo degradation in strength when exposed to either environment. The decrease in flexural strength is severe especially for the case of exposure to combined UV radiation and condensation. Nevertheless, the decrease is lower for the

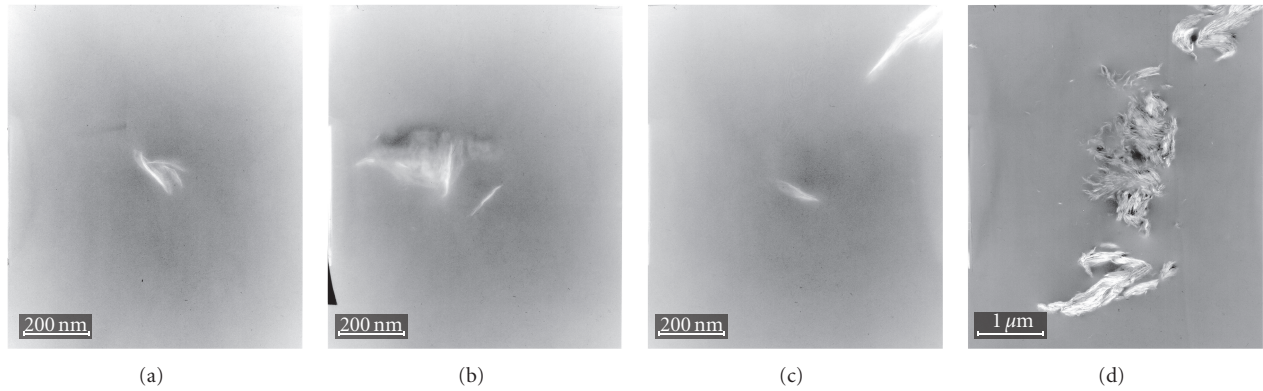
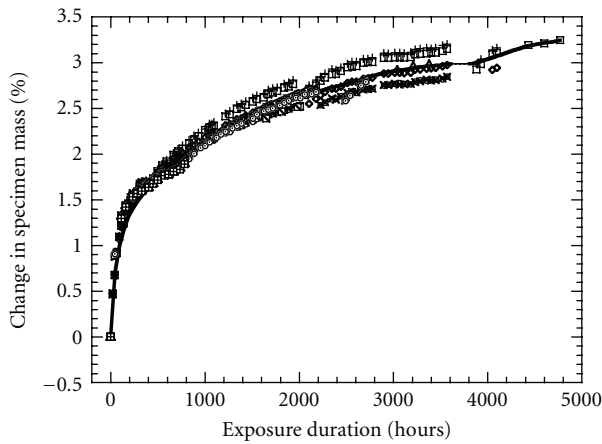
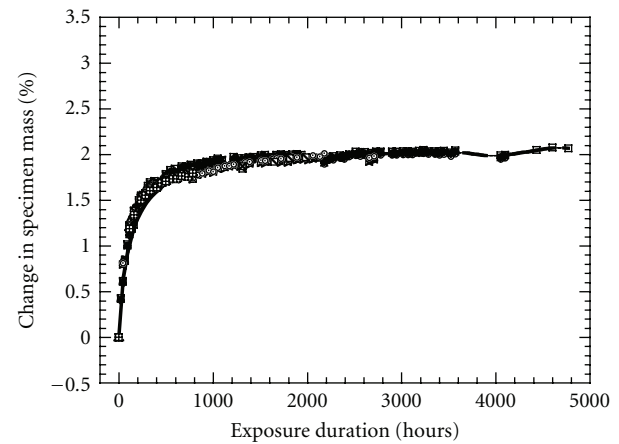


FIGURE 2: TEM images obtained from different regions of an epoxy-clay nanocomposite sample processed using 14 hours of mechanical mixing followed by high-shear dispersion.



○ PE10N	◁ PE25N	▣ PE40N
□ PE11N	▷ PE26N	▵ PE41N
◇ PE12N	● PE27N	▩ PE42N
× PE13N	○ PE28N	— Average
+ PE14N	▨ PE38N	
△ PE24N	▮ PE39N	

FIGURE 3: Moisture uptake for neat epoxy samples upon exposure to at moisture 80% relative humidity and 50°C.



○ EC10N	◁ EC25N	▣ EC40N
□ EC11N	▷ EC26N	▵ EC41N
◇ EC12N	● EC27N	▩ EC42N
× EC13N	○ EC28N	— Average
+ EC14N	▨ EC38N	
△ EC24N	▮ EC39N	

FIGURE 4: Moisture uptake for epoxy-clay composite samples upon exposure to at moisture 80% relative humidity and 50°C.

epoxy-clay nanocomposite, again leading to the conclusion that the addition of clay particles leads to enhancement in the resistance to environmental degradation.

Since the as fabricated epoxy-clay nanocomposite specimens have a higher modulus and strength than neat epoxy, the results of flexure strength degradation have been normalized and are listed in Table 5. The flexure strengths for both neat epoxy and epoxy-clay nanocomposite have been normalized by their respective undegraded values. The relative strength listed is for epoxy-clay as compared to neat epoxy for a given exposure duration and environment. As illustrated in this table, the incorporation of nanoscale clay particles leads to enhancement of resistance to environmental degradation for combined UV radiation and condensation, but not for moisture.

3.3. Environmentally Induced Surface Degradation. Exposure of epoxy resins to UV radiation leads to the formation of microcracks, which can then serve as localized sites for further material degradation, especially when synergistic degradation mechanisms are operative. In this investigation, the surfaces of both neat epoxy and epoxy-clay composite samples were monitored as a function of exposure duration.

Specimens exposed to UV radiation and condensation started exhibiting surface degradation, that was even visible by eye, after approximately two weeks (336 hours) of exposure. With increasing exposure, further degradation of the surface was observed. Initially, small cracks developed close to the surface. As exposure progressed, the cracks became larger in size and increased in quantity. After about 3500 hours of exposure, hemispherical dome-shape dimples

TABLE 4: Flexure strength values in MPa for neat epoxy and epoxy-clay nanocomposites, as a function of exposure duration, subjected to environmental exposure by either temperature-humidity or by combined UV radiation and condensation.

Exposure duration	Temperature-humidity		UV and condensation	
	Neat epoxy	Epoxy-clay	Neat epoxy	Epoxy-clay
0	99 ± 8	107 ± 10	99 ± 8	107 ± 10
1320	76 ± 33	52 ± 14	24 ± 2	33 ± 4
2712	61 ± 16	51 ± 16	16 ± 3	27 ± 3
4098	51 ± 18	50 ± 14	19 ± 2	29 ± 4

TABLE 5: Normalized flexure strength for specimens, as a function of exposure duration.

Environment	Exposure duration	Normalized Flexure Strength		Relative strength
		Neat epoxy	Epoxy-clay	
Moisture	0	1.00	1.00	0.0%
	1320	0.61	0.49	-19.4%
	2712	0.62	0.49	-21.3%
	4098	0.53	0.47	-12.2%
UV radiation and condensation	0	1.00	1.00	0.0%
	1320	0.24	0.31	29.6%
	2712	0.17	0.25	47.9%
	4098	0.19	0.26	37.3%

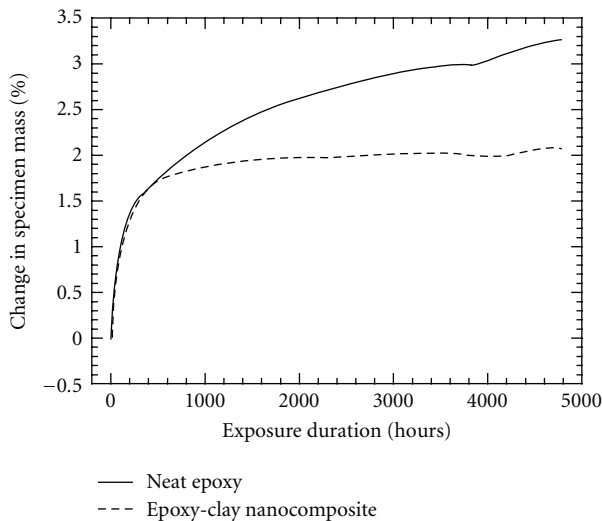


FIGURE 5: Comparison of average moisture uptake for neat epoxy and epoxy-clay nanocomposite specimens.

were observed on some areas of the surface. The dimples varied in size and were visible to the naked eye. The surface degradation, however, was not uniform throughout the sample. Microcracking was mostly observed near the center of samples, while the dimples developed closer to the edges near the sample holders. Therefore, it is conceivable that microcracking dominated surface changes were due to inherent material degradation, while the dimples were results of physicochemical interaction with the sample holders. Therefore, only the microcracked regions were imaged using

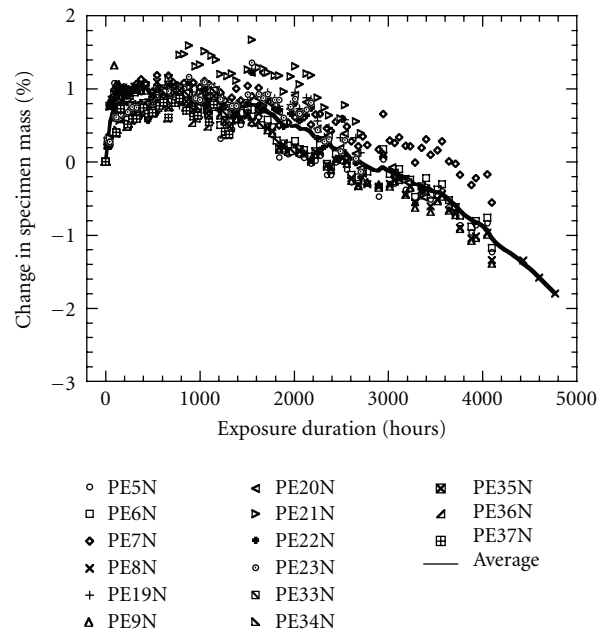


FIGURE 6: Mass variation for neat epoxy specimens upon exposure to combined UV radiation and water vapor condensation.

high-resolution microscopy for further quantitative and qualitative analysis.

Figure 9 shows images for neat epoxy samples taken after 1320, 2712, and 4098 hours of exposure to UV radiation and condensation. These are typical images taken from different specimens at the end of each selected degradation cycle. From these images, it is apparent that the microcracks

formed by exposure to UV radiation become focus sites for subsequent degradation and erosion upon exposure to cyclic UV radiation and condensation. Previously, Kumar et al. discussed this synergistic degradation mechanism in multi-environment exposure of epoxy. In this case, condensation droplets could get trapped in the microtrenches, leading to more and more erosion in the trench. As a result, degradation proceeds by the microcracks eroding to form trenches (or channels), and then the trenches get bigger and bigger with continued material removal.

A similar set of images obtained for epoxy-clay composite samples is shown in Figure 10. In this case, as for the neat epoxy, material degradation proceeded by erosion of channels initially formed due to UV radiation-induced microcracking. Also, in addition to the increase in size and depth of the trenches (channels), the density of trenches increased as well. This is simply due to the formation of additional microcracks during the UV radiation segments of the cyclic exposure protocol.

From a direct visual comparison of Figures 9 and 10 it is apparent that less material erosion takes place for the epoxy-clay nanocomposites. This indicates that the presence of clay platelets helps in ameliorating material loss due to synergistic material degradation. Figures 11 and 12 show the evolution of trench cross-section profiles, as a function of exposure duration, for the neat epoxy and the epoxy-clay composite samples, respectively. Data for both materials has been plotted at the same scale to facilitate comparison. From the figures it is apparent that trench formation in the case of neat epoxy was much more aggressive than for the case of epoxy-clay composites. This again indicates that the presence of clay is significant in slowing down material erosion due to synergistic degradation. It is important to note that Figures 11 and 12 are not representative of the entire surface and are localized areas of degradation; other locations on the same sample would yield different crack depths and widths. Nonetheless, these figures illustrate the quantitative difference in trench formation for the two materials.

The 3-dimensional imaging data was also used to determine the changes in volume and surface area for the two materials. The microscope cannot directly provide the actual change in volume due to material degradation. Instead, it provides a measurement of the current volume of the remaining material. This data was used to calculate the relative change in material volume, as a function of exposure duration. The change in material volume, normalized with respect to the viewing area of the Keyence microscope, is plotted in Figure 13. The average rate of volume change for the neat epoxy materials was $\sim 6.4 \times 10^{-3} \mu\text{m}^3/\mu\text{m}^2$ per unit area per hour, while that for the epoxy-clay nanocomposite was nearly half at $\sim 3.4 \times 10^{-3} \mu\text{m}^3/\mu\text{m}^2$ per unit area per hour. Also, for the durations considered, the change in material volume continues to increase. This implies that material erosion will continue to occur because of synergistic degradation.

The imaging data can also be used to determine the change in material surface area. Figure 14 plots the change in material surface area, normalized with respect to the viewing

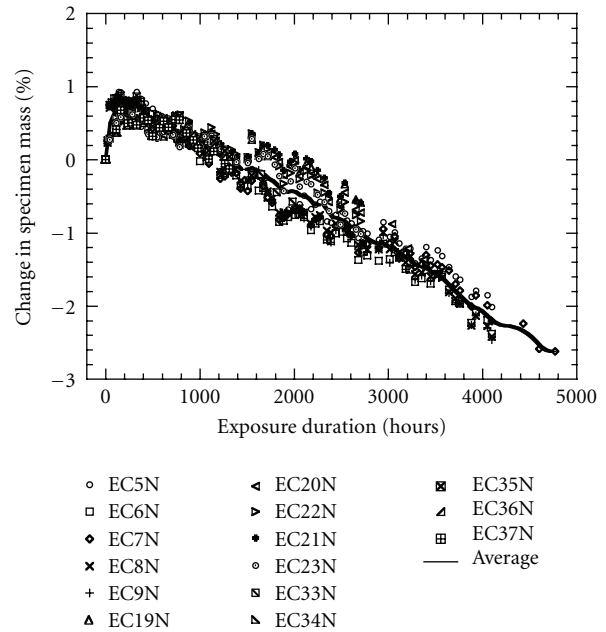


FIGURE 7: Mass variation for epoxy-clay nanocomposite specimens upon exposure to combined UV radiation and water vapor condensation.

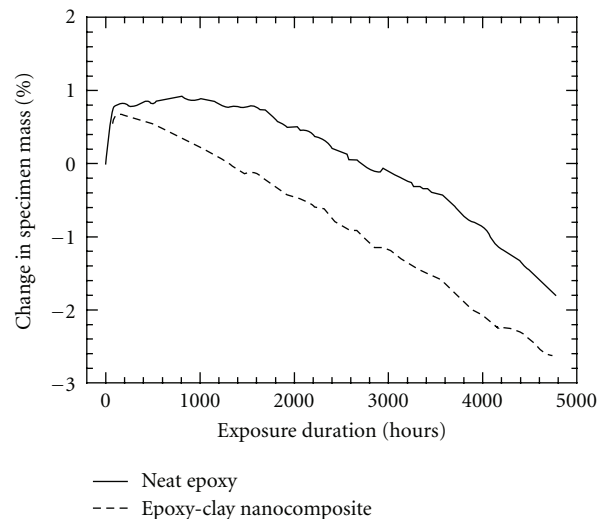


FIGURE 8: Comparison of mass variation for neat epoxy and epoxy-clay nanocomposite specimens upon exposure to combined UV radiation and water vapor condensation.

area, for neat epoxy and epoxy-clay composites, as a function of exposure duration. The average rate of surface change for the neat epoxy materials was $\sim 3.8 \times 10^{-5} \mu\text{m}^2/\mu\text{m}^2$ per unit area per hour, while that for the epoxy-clay nanocomposite was nearly half at $\sim 1.5 \times 10^{-5} \mu\text{m}^2/\mu\text{m}^2$ per unit area per hour. As for the material volume change, the surface change continues to increase for the durations considered.

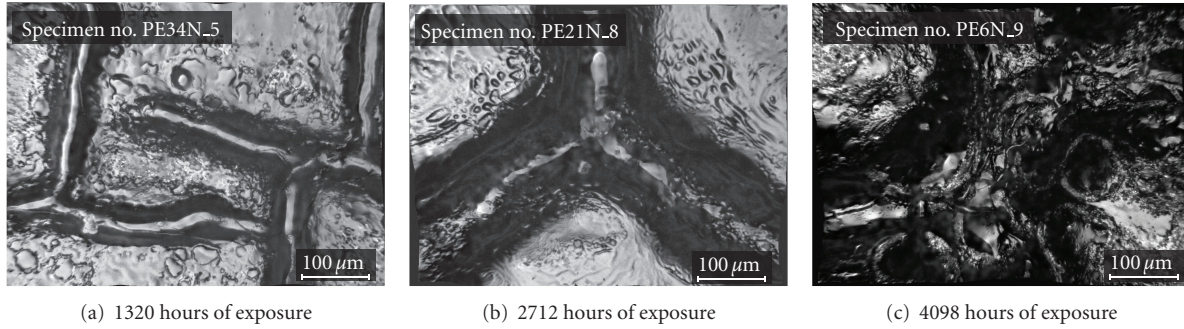


FIGURE 9: Images of neat epoxy specimens after exposure to UV radiation and condensation showing progressive erosion of microcracks.

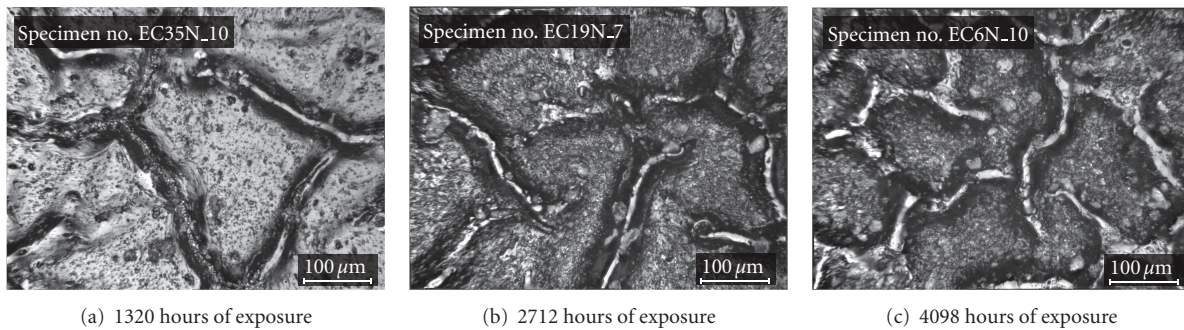


FIGURE 10: Images of epoxy-clay composites after exposure to UV radiation and condensation showing progressive erosion of microcracks.

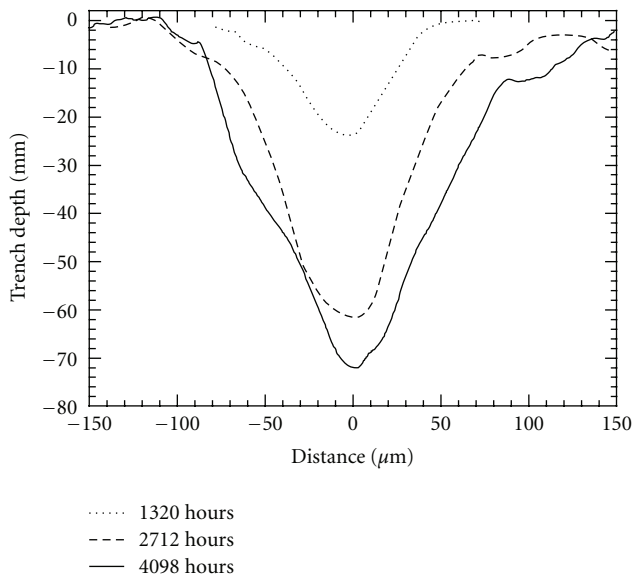


FIGURE 11: Selected trench profiles for neat epoxy samples at various stages of environmental degradation.

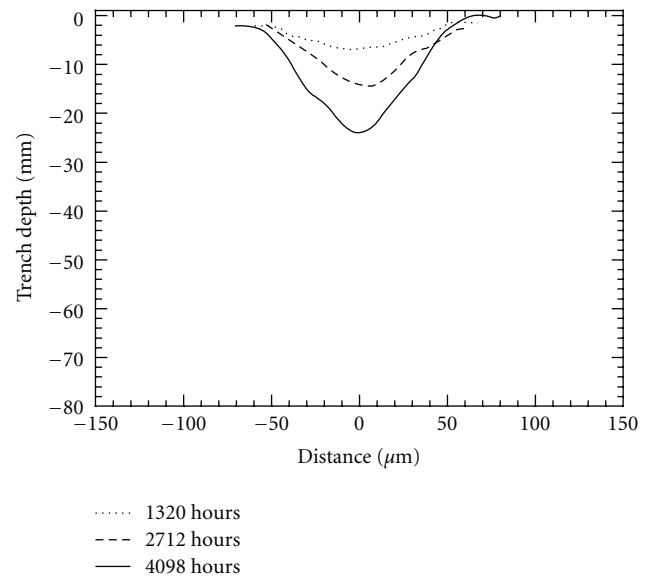


FIGURE 12: Selected trench profiles for epoxy-clay nanocomposite samples at various stages of environmental degradation.

4. Conclusion

The influence of nanoscale clay reinforcement of epoxy on the resistance to environmental degradation was studied. An epoxy-clay nanocomposite was fabricated using Epon 862, a bisphenol F-based epoxy resin, cured using Epikure

3274, a moderately reactive aliphatic amine, and reinforced with 4 vol.% of Nanomer I.30E, an organically modified clay. The clay particles were mixed and exfoliated with extensive mechanical mixing for 14 hours followed by high-shear dispersion for 30 minutes. Various mixing techniques were evaluated, and the selected process resulted in the greatest

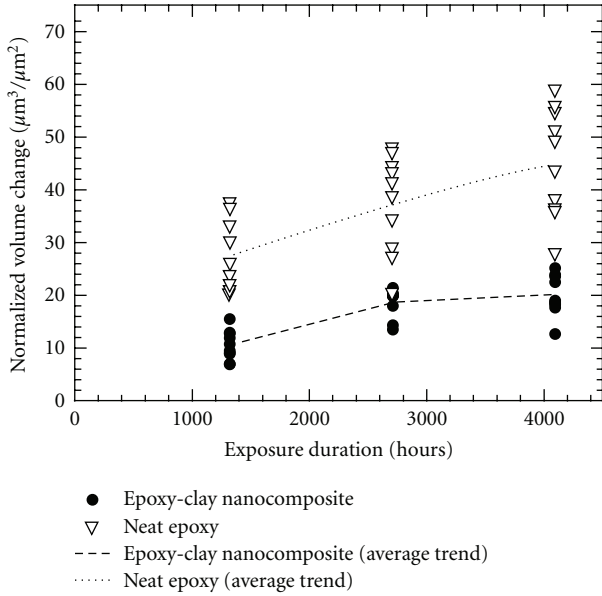


FIGURE 13: Change in material volume, normalized with respect to the viewing area, as a function of exposure duration for neat epoxy and epoxy-clay samples exposed to combined UV radiation and condensation.

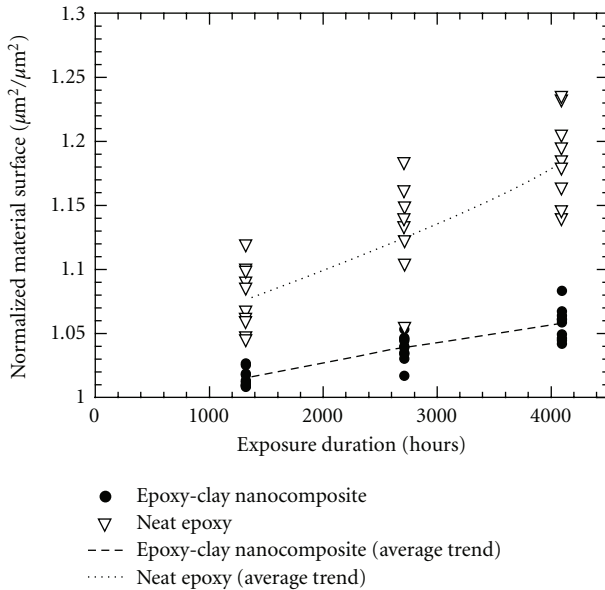


FIGURE 14: Change in material surface, normalized with respect to the viewing area, as a function of exposure duration for neat epoxy and epoxy-clay samples exposed to combined UV radiation and condensation.

improvement in mechanical properties indicating complete, or near complete, exfoliation of the clay platelets.

The nanocomposites were subjected to two environmental conditions, namely, combined UV radiation and condensation on a three-hour repeat cycle and constant relative humidity. Both types of exposures were conducted for 4770 hours and at fixed temperatures of 50°C.

The variation of mass loss or gain was recorded to serve as an indicator of material degradation or moisture uptake. Batches of samples were removed after 1320, 2712 and 4098 hours to test for flexure modulus and strength using four-point bend testing.

Under the exposure of constant relative humidity it was found that both neat epoxy and the epoxy-clay nanocomposite gained mass. However, the presence of nanoscale reinforcements in the epoxy matrix acted as a barrier and significantly hindered the moisture absorption. As the result, the final moisture uptake value and the rate of the moisture uptake were both measurably reduced, as expected, in comparison to neat epoxy also reduced in epoxy-clay nanocomposites.

The combined exposure of UV radiation and condensation resulted in the loss of mass of both materials due to the erosion of epoxy by a synergistic physicochemical process that was previously identified and characterized by Kumar et al. [6]. They suggested the formation of photo-oxidative byproducts that underwent dissolution by water vapor condensation and run-off results in the removal of surface layers degraded by UV radiation. Therefore, cyclic exposure to both UV radiation and water vapor condensation results in a continual material degradation and erosion process. Recently, Woo et al. also suggested that the presence of moisture can enhance the mobility of free radicals and ions and, thereby, enhance the photo-oxidative effects of UV radiation [33, 34].

In the present study the epoxy-clay specimens exhibited greater mass loss as compared to neat epoxy, which was surprising. The variation of the mass was governed by two competing mechanisms, namely, decrease in mass due to loss of epoxy and increase in mass due to moisture absorption. It was hypothesized, and later confirmed, that the increased mass loss for epoxy-clay nanocomposites is due to decreased uptake of moisture and not increased erosion of the epoxy matrix. This was in accordance with the measurements of flexure modulus and strength after exposure to the two environments as a function of exposure duration. Exposure to relative humidity did not result in a measurable decrease in modulus for either neat epoxy or the epoxy-clay nanocomposite. For exposure to UV radiation and condensation the flexure modulus decreased for both materials with increasing exposure duration. This modulus decrease was due to epoxy erosion resulting from synergistic material degradation. Nonetheless, the decrease in modulus was greater for the neat epoxy specimens as compared to the epoxy-clay nanocomposite, which demonstrated that the addition of nanoscale clay is effective in enhancing resistance to moisture degradation.

The investigation into the flexure strength revealed that both materials underwent degradation in strength when exposed to either environment. The decrease in flexural strength was especially severe for exposure to combined UV radiation and condensation. This decrease in the flexure strength is primary due to surface erosion and formation of channels on the material surface. The channels originate as microcracks from UV exposure and then grow and deepen

upon material erosion due to synergistic degradation. Nevertheless, the decrease in flexural strength was lower for the epoxy-clay nanocomposite, again leading to the conclusion that the addition of clay particles leads to enhancement in the resistance to environmental degradation. A comparison of the normalized flexure strength showed that the epoxy-clay nanocomposite had retained ~37% more strength than the neat epoxy after 4072 hours of exposure to combined UV radiation and condensation. Under exposure to constant relative humidity, however, the neat epoxy specimens retained greater strength.

High resolution imaging was used to quantify material volume and surface change due to environmental degradation. The change in material volume due to synergistic erosion was representative of overall material loss. On the other hand, the change in material surface was indicative of surface roughening due to the growth of trenches (or channels) on the specimen surface. The presence of clay reduced the formation and growth of channels from UV radiation-induced microcracking and subsequent erosion during combined exposure to UV radiation and condensation. These surface channels acted as defects and lowered the flexural strength. Therefore, a reduction in channel formation and growth, due to the presence of clay, led to greater strength retention. The formation and growth of these channels were identified as being more deleterious than overall material volume loss. This is also why the exposure to UV radiation and condensation led to a greater loss of flexural strength rather than modulus.

This investigation demonstrated that the nanoscale clay reinforcements in an epoxy matrix act as barriers to environmental degradation. The clay particles provide resistance to moisture transport. Nevertheless, the moisture absorption process in polymer clay nanocomposites is governed by numerous factors, including the cross linking density around the clay layers, degree of net cure, and the total exposed surface area of the clay platelets [28, 29]. In addition, the interaction between UV exposure, moisture, and epoxy-clay chemistry is driven by complex physicochemical mechanisms. Therefore, further investigation is warranted to analyze the chemical and microstructural characteristics of the degradation process and establish the process kinetics in polymer nanocomposites subjected to varied environments.

Acknowledgement

The authors gratefully acknowledge the support of the National Science Foundation via Grant no. CMS 0219250.

References

- [1] G. Pritchard, *Reinforced Plastics Durability*, Woodhead Publishing, Cambridge, UK, 1998.
- [2] J. W. Chin, T. Nguyen, and K. Aouadi, "Effects of environmental exposure on Fiber-Reinforced Plastic (FRP) materials used in construction," *Journal of Composites Technology and Research*, vol. 19, no. 4, pp. 205–213, 1997.
- [3] B. Ranby and J. Rabek, *Photodegradation, Photo-Oxidation and Photostabilization of Polymers*, John Wiley & Sons, London, UK, 1975.
- [4] W. B. Liao and F. P. Tseng, "The effect of long-term ultraviolet light irradiation on polymer matrix composites," *Polymer Composites*, vol. 19, no. 4, pp. 440–445, 1998.
- [5] K.-B. Shin, C.-G. Kim, C.-S. Hong, and H.-H. Lee, "Prediction of failure thermal cycles in graphite/epoxy composite materials under simulated low earth orbit environments," *Composites Part B*, vol. 31, no. 3, pp. 223–235, 2000.
- [6] B. G. Kumar, R. P. Singh, and T. Nakamura, "Degradation of carbon fiber-reinforced epoxy composites by ultraviolet radiation and condensation," *Journal of Composite Materials*, vol. 36, no. 24, pp. 2713–2733, 2002.
- [7] A. W. Signor, M. R. VanLandingham, and J. W. Chin, "Effects of ultraviolet radiation exposure on vinyl ester resins: characterization of chemical, physical and mechanical damage," *Polymer Degradation and Stability*, vol. 79, no. 2, pp. 359–368, 2003.
- [8] C. Shen and G. S. Springer, "Moisture absorption and desorption of composite materials," *Journal of Composite Materials*, vol. 10, no. 1, pp. 2–20, 1976.
- [9] Y. Weitsman, *Fatigue of Composite Materials*, Elsevier, New York, NY, USA, 1991.
- [10] Q. Zheng and R. J. Morgan, "Synergistic thermal-moisture damage mechanisms of epoxies and their carbon fiber composites," *Journal of Composite Materials*, vol. 27, no. 15, pp. 1465–1478, 1993.
- [11] R. D. Adams and M. M. Singh, "The dynamic properties of fibre-reinforced polymers exposed to hot, wet conditions," *Composites Science and Technology*, vol. 56, no. 8, pp. 977–997, 1996.
- [12] H. S. Choi, K. J. Ahn, J.-D. Nam, and H. J. Chun, "Hygroscopic aspects of epoxy/carbon fiber composite laminates in aircraft environments," *Composites Part A*, vol. 32, no. 5, pp. 709–720, 2001.
- [13] C. Soutis and D. Turkmen, "Moisture and temperature effects of the compressive failure of CFRP unidirectional laminates," *Journal of Composite Materials*, vol. 31, no. 8, pp. 832–849, 1997.
- [14] G. Sala, "Composite degradation due to fluid absorption," *Composites Part B*, vol. 31, no. 5, pp. 357–373, 2000.
- [15] G. Mago, F. T. Fisher, and D. M. Kalyon, "Effects of multi-walled carbon nanotubes on the shear-induced crystallization behavior of poly(butylene terephthalate)," *Macromolecules*, vol. 41, no. 21, pp. 8103–8113, 2008.
- [16] E. T. Thostenson, C. Li, and T.-W. Chou, "Nanocomposites in context," *Composites Science and Technology*, vol. 65, no. 3–4, pp. 491–516, 2005.
- [17] R. A. Vaia and E. P. Giannelis, "Polymer nanocomposites: status and opportunities," *MRS Bulletin*, vol. 26, no. 5, pp. 394–401, 2001.
- [18] T. Pinnavaia, T. Lan, Z. Wang, H. Shi, and P. D. Kaviratna, *Nanotechnology*, vol. 622 of *ACS Symposium Series*, American Chemical Society, Washington, DC, USA, 1996.
- [19] R. Krishnamoorti and R. A. Vaia, "Polymer nanocomposites: synthesis, characterization, and modeling," in *Proceedings of the 219th National Meeting of the American Chemical Society*, San Francisco, Calif, USA, 2000.
- [20] A. Usuki, Y. Kojima, M. Kawasumi, A. Okada, T. Kurauchi, and O. Kamigaito, "Characterization and properties of nylon 6. Clay hybrid," in *Proceedings of the ACS Division of Polymer Chemistry Meeting*, pp. 651–652, Washington, DC, USA, August 1990.

- [21] M. Alexandre and P. Dubois, "Polymer-layered silicate nanocomposites: preparation, properties and uses of a new class of materials," *Materials Science and Engineering R*, vol. 28, no. 1, pp. 1–63, 2000.
- [22] O. Becker, R. Varley, and G. Simon, "Morphology, thermal relaxations and mechanical properties of layered silicate nanocomposites based upon high-functionality epoxy resins," *Polymer*, vol. 43, no. 16, pp. 4365–4373, 2002.
- [23] D. Ratna, N. R. Manoj, R. Varley, R. K. Singh Raman, and G. P. Simon, "Clay-reinforced epoxy nanocomposites," *Polymer International*, vol. 52, no. 9, pp. 1403–1407, 2003.
- [24] S. C. Zunjarrao, R. Sriraman, and R. P. Singh, "Effect of processing parameters and clay volume fraction on the mechanical properties of epoxy-clay nanocomposites," *Journal of Materials Science*, vol. 41, no. 8, pp. 2219–2228, 2006.
- [25] T. Ogasawara, Y. Ishida, and T. Ishikawa, "Helium gas permeability of montmorillonite dispersed nanocomposites," in *Proceedings of the 11th US-Japan Conference on Composite Materials*, Yamagata, Japan, 2004.
- [26] Y. Kojima, A. Usuki, M. Kawasumi, A. Okada, T. Kurauchi, and O. Kamigaito, "Sorption of water in nylon 6-clay hybrid," *Journal of Applied Polymer Science*, vol. 49, no. 7, pp. 1259–1264, 1993.
- [27] T. Lan and T. J. Pinnavaia, "Clay-reinforced epoxy nanocomposites," *Chemistry of Materials*, vol. 6, no. 12, pp. 2216–2219, 1994.
- [28] T. Hwang, L. Pu, S. W. Kim, Y.-S. Oh, and J.-D. Nam, "Synthesis and barrier properties of poly(vinylidene chloride-co-acrylonitrile)/SiO₂ hybrid composites by sol-gel process," *Journal of Membrane Science*, vol. 345, no. 1-2, pp. 90–96, 2009.
- [29] J.-K. Kim, C. Hu, R. S. C. Woo, and M.-L. Sham, "Moisture barrier characteristics of organoclay-epoxy nanocomposites," *Composites Science and Technology*, vol. 65, no. 5, pp. 805–813, 2005.
- [30] "Standard test method for flexural properties of unreinforced and reinforced plastics and electrical insulating materials by four-point bending," ASTM D6272–10, American Society for Testing and Materials, 2010.
- [31] "Standard test methods for plane-strain fracture toughness and strain energy release rate of plastic materials," ASTM D5045, American Society for Testing and Materials, 1999.
- [32] T. L. Anderson, "Fracture mechanics: fundamentals and applications," CRC Press 2004.
- [33] R. S. C. Woo, Y. Chen, H. Zhu, J. Li, J.-K. Kim, and C. K. Y. Leung, "Environmental degradation of epoxy-organoclay nanocomposites due to UV exposure. Part I: photo-degradation," *Composites Science and Technology*, vol. 67, no. 15-16, pp. 3448–3456, 2007.
- [34] R. S. C. Woo, H. Zhu, C. K. Y. Leung, and J.-K. Kim, "Environmental degradation of epoxy-organoclay nanocomposites due to UV exposure. Part II: residual mechanical properties," *Composites Science and Technology*, vol. 68, no. 9, pp. 2149–2155, 2008.

Research Article

Design and Preparation of Cross-Linked Polystyrene Nanoparticles for Elastomer Reinforcement

Ming Lu,¹ Jianjun Zhou,¹ Liansheng Wang,¹ Wei Zhao,¹ Yonglai Lu,¹ Liqun Zhang,^{1,2} and Yakang Liu³

¹The Key Laboratory for Nanomaterials of Ministry of Education, Beijing University of Chemical Technology, Beijing 100029, China

²The Key Laboratory of Beijing City for Preparation and Processing of Novel Polymer Materials, Beijing University of Chemical Technology, Beijing 100029, China

³Department of Polymer Science, Beijing University of Chemical Technology, Beijing 100029, China

Correspondence should be addressed to Liqun Zhang, zhanglq@mail.buct.edu.cn

Received 31 October 2009; Revised 1 February 2010; Accepted 31 March 2010

Academic Editor: Gaurav Mago

Copyright © 2010 Ming Lu et al. This is an open access article distributed under the Creative Commons Attribution License, which permits unrestricted use, distribution, and reproduction in any medium, provided the original work is properly cited.

Cross-linked polystyrene (PS) particles in a latex form were synthesized by free radical emulsion polymerization. The nano-PS-filled elastomer composites were prepared by the energy-saving latex compounding method. Results showed that the PS particles took a spherical shape in the size of 40–60 nm with a narrow size distribution, and the glass-transition temperature of the PS nanoparticles increased with the cross-linking density. The outcomes from the mechanical properties demonstrated that when filled into styrene-butadiene rubber (SBR), nitrile-butadiene rubber (NBR), and natural rubber (NR), the cross-linked PS nanoparticles exhibited excellent reinforcing capabilities in all the three matrices, and the best in the SBR matrix. In comparison with that of the carbon black filled composites, another distinguished advantage of the cross-linked PS particles filled elastomer composites was found to be light weight in density, which could help to save tremendous amount of energy when put into end products.

1. Introduction

Most widely applied elastomer materials, due to the weaknesses in modulus and strength, usually require some kind of reinforcement before putting into use. As this case stands, great parts of the rubber products are actually composites made of the elastomeric matrix and some kind of fillers as well as some other curatives. And the filler, especially the reinforcing filler, plays an important role in determining the performance of the filled rubber compounds [1–9].

In the rubber industry, many types of reinforcing agents have already been developed; carbon black and silica are the ones that are commonly used. These conventional fillers are usually solid powders. Though being very effective in reinforcing, they also show up some drawbacks. As the result of the strong filler-filler interactions and weak filler-rubber interactions, it takes great energy and efforts to blend the powdered fillers with the high-viscous elastomer matrix in a mechanical blender. What's worse, because of the poor

compatibility with the rubber matrix, there is a tendency for the fillers to aggregate forming a strong filler network which may do harm to the dispersion of the fillers and the performance of the composites as well.

For further enhancing the performances of the filled elastomer composites, we had raised a concept of the *ideal fillers* for elastomer reinforcement [6, 10]. To be such an *ideal filler*, it should possess some distinguishing features: (1) size in the nanoscale, so as to provide excellent reinforcement to the elastomer matrix; (2) spherical shape, helping to reduce the processing-viscosity of the filled rubber; (3) easy access to a fine dispersion in the rubber matrix, holding back filler aggregation and weakening the filler network; (4) some chemical activity on the surface, providing certain chemical interaction between the filler and the matrix; (5) lower density, reducing the dynamically driving energy of the filled elastomer composites; (6) lower price. However, the conventional fillers, like carbon black and silica, do not possess all these features.

In our opinion, polymeric fillers may open a door for the development of some novel elastomer reinforcing agents. Different from the natural fillers which have taken certain structure and surface properties as born, the polymeric fillers can be designed and synthesized as the designer's intention. We can not only take the structure of the fillers in control, but also make some needed modification to the fillers for adjusting the filler-rubber interactions.

Few literatures reported some work in rubber academy using some polymeric filler, usually some rigid emulsion particles like polystyrene nano-particles, as the model fillers for the investigations on the mechanisms of elastomer reinforcement [11–14]. And rubber industry also started to show some interests in developing novel elastomer reinforcing agents from polymeric fillers. Zheng et al. [15] from *Goodyear Tire & Rubber Company* have synthesized some model hairy nano-particles of cross-linked polystyrene cores and polybutadiene brushes, and Wang et al. [16] from *Bridgestone Americas* have prepared various core-shell nano-particles with different shapes and sizes. They both thought the polymeric fillers capable as a novel elastomer reinforcing agents. But the end products of the polymeric fillers in their work were also in a powder state, and to the best of our knowledge, aggregates of the filler particles would inevitably come into being as the result of the flexible, rubber-like polybutadiene shell that they both had in their powdered products. When preparing the rubber compound mixture, they had to take great extra energy and efforts to disperse these polymeric fillers into the high-viscous rubber matrix again.

Our work was carried out in an attempt to provide a commercially viable method to prepare ideal fillers for elastomer reinforcement. Considering that most rubber types in use have their latex forms, we intended to prepare a kind of latex-formed polymeric fillers for the reinforcement of the elastomeric matrices. In this work, styrene was chosen as the monomer due to easy access and its compatibility with the commonly used elastomer matrices such as styrene-butadiene rubber (SBR) and nitrile-butadiene rubber (NBR). Divinyl benzene (DVB) was introduced into the polymerization system as the cross-linking agent for further enhancing the glass-transition temperature (T_g) and stiffness of the polymer particles in case of possible applications in hot environment. Emulsion radical polymerization was made as the synthesis technique to prepare such latex-formed polymeric fillers.

In our work, the cross-linked polystyrene (PS) filled elastomer composites were prepared by the energy-saving latex compounding method (LCM). As a water-mediating compounding method, LCM [17–19] greatly reduced the viscosity of both the filler system and the bulk matrix system, thus saving tremendous amount of energy and resulting in better dispersion of the fillers.

A soft shell (like polyisoprene) over the particles, composed of some polymer compatible with the elastomer matrix, helping to adjust the filler-rubber interactions, has also been designed. The work covering that part will be discussed in another paper. In this work, we focused on the PS particles themselves. The influence of cross-linking

density on the properties of the cross-linked polystyrene particles, and the reinforcement of the spherical PS nanoparticles to the elastomer matrices, were investigated respectively.

2. Experiment

2.1. Materials. Styrene (St) was purchased from Fuchen Chemical Agent Co., Ltd (Tianjin). Divinyl benzene (DVB) was supplied by Jinke Fine Chemical Agent (Tianjin) Co., Ltd. And sodium hydrogen carbonate (NaHCO_3) was supplied by Shanghai Linfeng Chemical Agent Co., Ltd., China. Ammonium persulfate (APS) was purchased from Beijing Chemical Agent Co., Ltd., China. Polyoxyethylene octylphenol ether (emulsifier OP-10) was supplied by Vason Chemical Agent Co., Ltd (Tianjin). Sodium dodecyl sulfonate (SDS) was a commercial product of Beijing Yili Fine Chemical Co., Ltd. Anhydrous calcium chloride (CaCl_2) was a product from Beijing Beihua Fine Chemicals Co., Ltd. Styrene-butadiene rubber (manufacture brand SBR-1502) and its latex were supplied by Jilin petrochemical Co. China. Nitrile-butadiene rubber latex (manufacture brand LHN-212), with acrylonitrile content of 26 wt%, was a product from Lanzhou petrochemical Co. China. Natural rubber latex was purchased from Beijing latex products factory (China). All other reagents for rubber compounds are commercial products.

2.2. Synthesis of the Cross-Linked Polystyrene. A four-necked flask equipped with a stirrer, a reflux condenser, a dropping funnel and a thermometer, was first charged with appropriate emulsifier SDS/OP-10 and deionized water. Start the stirrer at an appropriate speed for a while until an evenly blended mixture was obtained. The batch was then charged with certain amount of monomers of styrene and DVB at given ratio. Following another 30-min's emulsification, the batch was heated to 70°C. When temperature got stable, polymerization was initiated by adding APS water solution. NaHCO_3 water solution was added in order to adjust the pH value of the latex equal to 7. The batch temperature of 70°C was maintained during the entire polymerization process. Remaining monomers had been added by dripping since 30 minutes after the initiation. Several hours later, the emulsion polymerization reaction completed. And the cross-linked polystyrene latex was obtained.

2.3. Preparation of the Filled Composites. The PS-filled elastomer composites were prepared by LCM. The cross-linked polystyrene latex and rubber latex were mixed at given ratio by a mechanical stirrer for a period of time. After that, the even mixture was poured into the CaCl_2 water solution in stirring for coagulation. The master batch was washed several times before drying in an air oven at 50°C for 24 hours. All the ingredients of curatives (seen in Tables 1 and 2) were added in a two-roll miller. The master batch was then vulcanized at certain temperature (150°C for SBR, 160°C for NBR, and 145°C for NR) for a period of time of T_{90} under the pressure of 15 MPa.

TABLE 1: Recipe for SBR and NR composites.

Ingredients	Loading (phr ^a)
SBR or NR	100
PS	variation
ZnO	3.0
Stearic Acid (SA)	1.0
Accelerator D ^b	0.5
Accelerator DM ^c	0.5
Accelerator TT ^d	0.2
Antioxidant 4010NA ^e	1.0
Sulfur	2.0

^aparts per hundred rubber parts in weight; ^bDiphenyl guanidineine; ^c2,2'-dibenzothiazole disulfide; ^dTetramethylthiuram disulfide; ^eN-isopropyl-N'-phenyl-p-phenylenediamine.

TABLE 2: Recipe for NBR composites.

Ingredients	Loading (phr)
NBR	100
PS	30
ZnO	5.0
Stearic Acid (SA)	1.0
Accelerator DM	1.0
Antioxidant 4010NA	2.0
Sulfur	1.5

2.4. Characterization Techniques. The particle size and the particle size distribution was measured by Zetasizer Nano ZS particle analyzer (UK Malvern Instruments Ltd.) in the means of dynamic light scattering (DLS). The SEM and TEM images were obtained by S-4700 Scanning Electron Microscope (Japan Hitachi Co. Ltd.) and H-800 Transmission Electron Microscope (Japan Hitachi Co. Ltd.), respectively. DSC tests were carried out with DSC-2C differential scanning calorimeter (US Perkin-Elmer Co. Ltd.) in N₂ gas flow with a heating rate of 10°C/min. The tensile tests were conducted with dog-bone-shape samples on an Instron-type tensile testing machine at a speed of 500 mm/min according to ASTM D412. Measurement of dynamical mechanical rheology was performed with the rheometer RPA 2000 (Alpha Technologies, USA). Shore A hardness of the vulcanizates were measured according to ASTM D2240, using a XY-1 type A durometer (No. 4 Chemical Machinery Plant of Shanghai Chemical Equipment Co. Ltd., Shanghai, China), and three different spots of the sample (over 6 mm in thickness) were measured to give the average.

3. Results and Discussion

3.1. Size and Morphology. With semicontinuing feeding operation in starving state, the cross-linked polystyrene particles were prepared in an emulsion polymerization system. Products were analyzed with Zetasizer Nano ZS

particle analyzer and TEM. The results showed that the cross-linked polystyrene took a spherical shape in the size of 40–60 nm with a narrow distribution, as seen in Figure 1.

The nanosized particles are essential to the reinforcement of the elastomer matrix [20–23]. With high specific surface area, they provide sufficient interphase for the filler-rubber interactions, and make the orientation of the elastomer molecular chain segments possible in the stretching process [24]. The elastomer molecules stuck to the filler particles due to the filler-rubber interactions; when in tension, the elastomer molecules might slip along the surface of the filler particles; after that, the chains stuck back to the filler particles again. In further tension, the stick-slip process went round and round, resulting in the orientation of the elastomer molecular chain segments. Between the neighboring filler particles, the oriented segments at the same length became to bear the outer force simultaneously. And as a result, the inside details turned out to be higher modulus of the sample shown as strain hardening in the stress-strain curve.

3.2. Influence of the Cross-Linking Density. PS particles with different cross-linking densities were prepared by varying the consumption of DVB at 0 wt%, 10 wt%, 20 wt%, and 30 wt% of the styrene loading. With the increase of DVB consumption, the cross-linking density of the particles went higher. As results, the mobility of the polystyrene molecules decreased; the glass-transition temperature of the cross-linked polystyrene went up; and the particles achieved higher modulus. All the outcomes above could make the cross-linked PS particles more competent when in hot environment applications.

As seen in Figure 2, the glass-transition temperature of the PS particles increased with DVB consumption. Though theoretically, an access to higher T_g of the PS particles was possible with even higher consumption of DVB, 20 wt% would be a better choice, when we take the influence on the stability of the emulsion system into consideration.

In our experiments, when filtering the PS latex obtained after the emulsion polymerization, we found that the gel part in the PS latex increased with higher consumption of DVB. This could attribute to the cross-linking between the latex particles. As known, DVB has two functional groups of vinyl, which makes it a cross-linker in the polymerization. It linked not only the molecules in a latex particle when diffused into the latex particles but also the latex particles themselves when initiated outside by free radicals. At higher DVB consumption, the chances that the cross-linker was initiated outside the latex particles increased, and as a result, more latex particles were jointed together. Subsequently, the jointed latex particles turned out to be the loss in the stability of the emulsion polymerization system.

3.3. Reinforcement to Elastomer Matrices

3.3.1. With PS Fillers of Different Cross-Linking Densities. Composites filled with PS fillers of different cross-linking densities were prepared in order to investigate the influence of the cross-linking density on the reinforcing performances

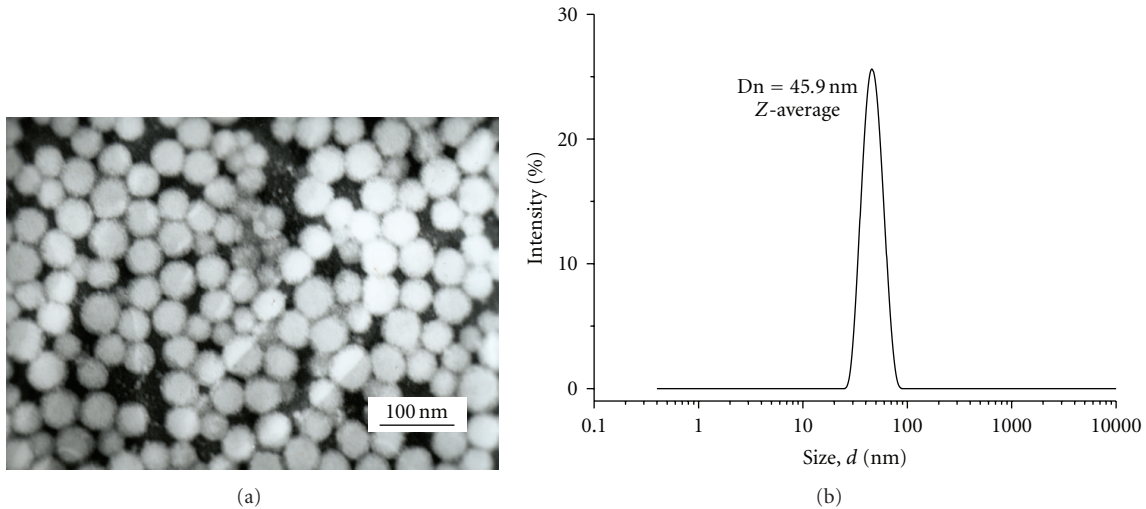


FIGURE 1: Morphology, size, and size distribution of cross-linked PS particles. (a) is the TEM image of cross-linked PS particles with DVB consumption of 20 wt% of styrene loading; (b) is the result of the same sample from the DLS test.

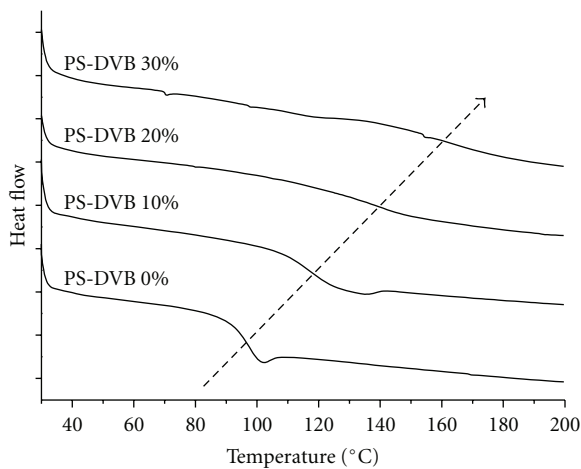


FIGURE 2: DSC curves of the PS particles with varied DVB consumption.

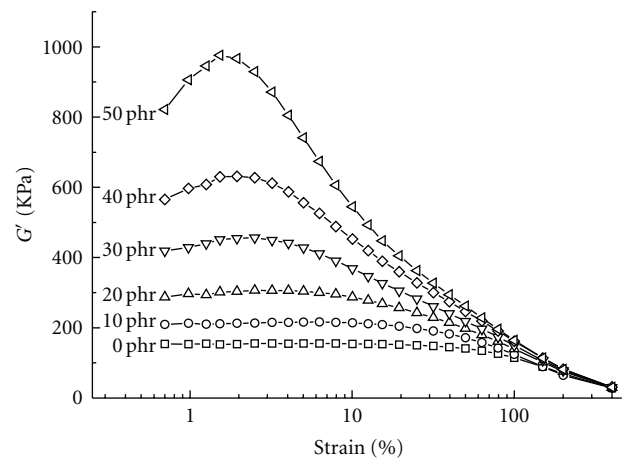


FIGURE 3: Strain amplitude dependence of storage modulus (G') of the PS-filled SBR composites.

of the PS particles. The composites of PS-filled SBR were vulcanized by a low-temperature curing system of benzyl peroxide (BPO) at 95°C , so as to prevent possible damage to the morphology of the PS particles when in high temperature like in the sulfur-curing system.

It was indicated in Table 3 that there were significant improvements in mechanical properties of PS-filled SBR nanocomposites, compared with those of the neat SBR. With higher DVB consumption, the tensile strength of the composites improved, while the hardness, permanent set, and tear strength of the composites varied a little. It is worth a special notice that stress at 300% elongation exhibited an extraordinary decrease when with higher DVB consumption. But the results from the sample of 30 wt% DVB consumption didn't keep the law as the other samples did. Unfortunately, we failed to find a suitable explanation for this.

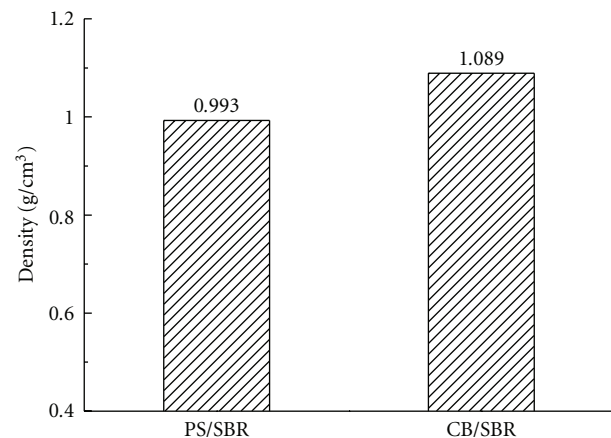


FIGURE 4: Comparison in density between PS-filled SBR and carbon black filled SBR.

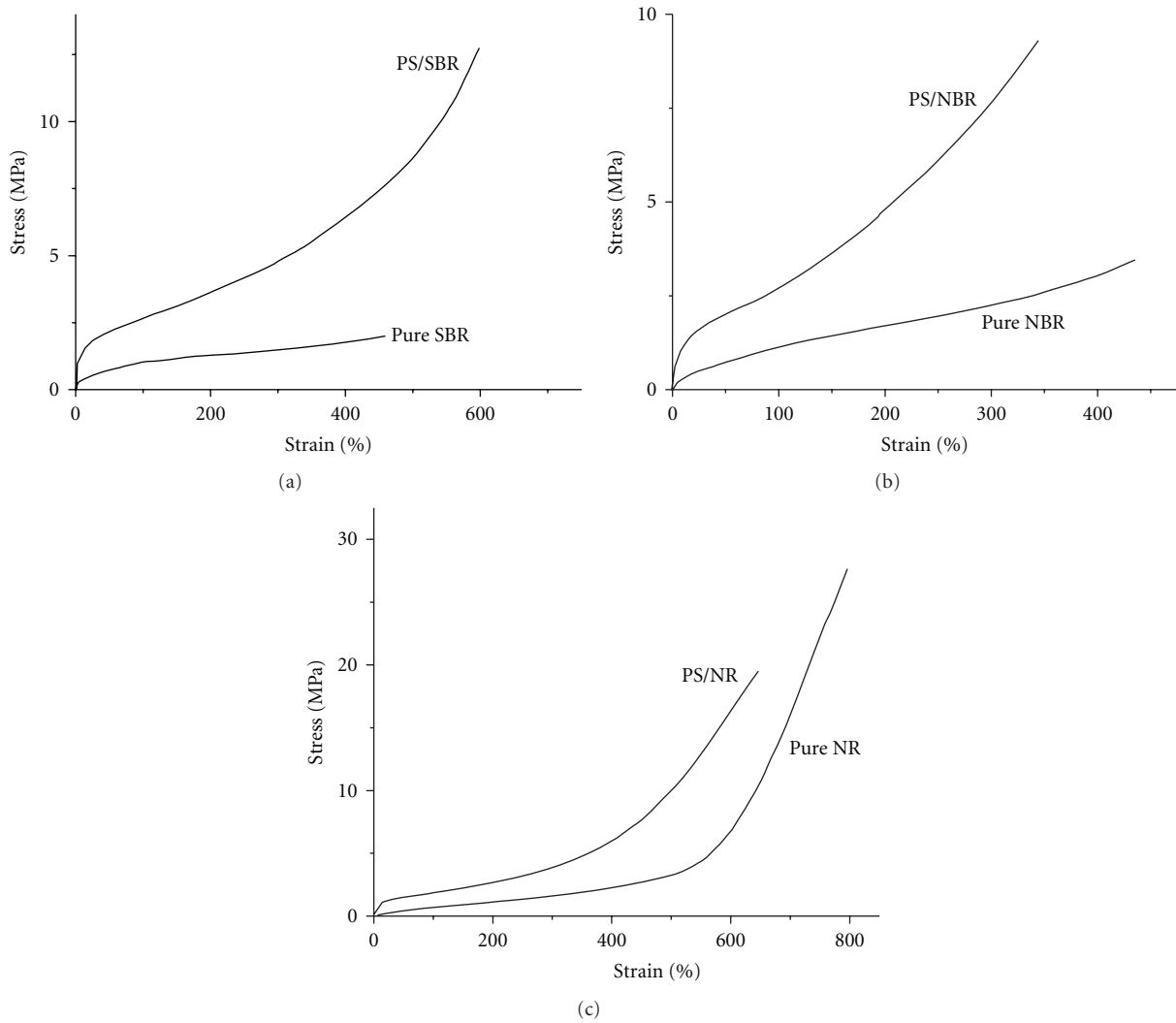


FIGURE 5: Reinforcing behavior of the cross-linked PS in different matrices with a loading of 30 phr. (a)–(c) represented the performances in SBR, NBR, and NR, respectively.

TABLE 3: Influence of DVB consumption on the mechanical properties of PS-filled SBR nanocomposites.

Samples	Stress at 300% Elongation/MPa	Tensile Strength/MPa	Elongation at Break/%	Permanent Set/%	Shore A Hardness/°	Tear Strength /KN/m	
Neat SBR	1.4	1.5	327	0	46	7	
PS/SBR	DVB 0%	3.3	9.3	535	20	70	20
	DVB 10%	2.3	12.5	607	16	70	21
	DVB 20%	2.2	15.9	630	14	66	18
	DVB 30%	2.5	13.6	593	10	65	20

Note that the loading of PS filler was 20 phr; the cross-linked PS filler were prepared with DVB consumption of 0 wt%, 10 wt%, 20 wt%, and 30 wt% of the styrene loading. The composites were cured with 4 phr benzyl peroxide (BPO) at 95°C for 120 minutes.

What brought about these changes was the increasing cross-linking density. With higher DVB consumption, the cross-linking density of the PS fillers increased, and thus the mobility of the molecules decreased, which made the diffusion more difficult at the interfaces between the fillers and the matrix. As a result, the interactions between the

SBR matrix and the PS fillers weakened; the stress at given elongation decreased.

This relatively weak filler-rubber interaction can also explain why at present, the stress at given elongation of the cross-linked polystyrene filled rubber composites didn't match those of the carbon black filled rubber at the same

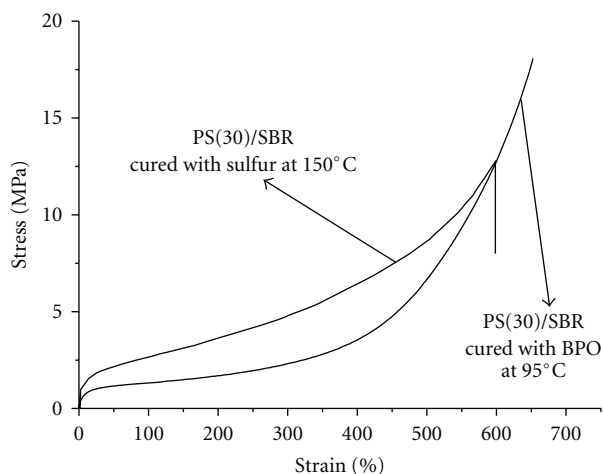


FIGURE 6: Comparison in mechanical performances of PS(30)/SBR composites with varied curing systems.

loading. Preparation of such a kind of polymeric filler with a core-shell structure was a solution for further enhancing the properties. A shell of some polymer of good compatibility with the elastomer matrix, like polyisoprene, would work to ameliorate the interaction between the rubber matrix and the polymeric fillers so as to improve the mechanical properties of the filled rubber composites. We will report the work covering this part in another paper.

3.3.2. With PS Fillers at Varied Loadings. The cross-linked polystyrene particles prepared with 20 wt% DVB consumption was chosen due to better performances in glass-transition temperature, emulsion polymerization process, and properties of the filled SBR composites. Mechanical properties of the cross-linked PS-filled SBR composites with filler loading of 0 phr, 10 phr, 20 phr, 30 phr, 40 phr, and 50 phr were tested, respectively.

As shown in Table 4, the stress at 300% elongation increased with filler loading, but it was still relatively low when compared with that of the carbon black filled samples at the same loading. The tensile strength improved remarkably with the increase of the filler loading at first and then stayed at a level with the loading of 30 phr and higher; the hardness, permanent set and tear strength increased with the filler loading. Higher loading of the PS fillers led to stronger filler network, as shown in Figure 3 that the Payne effect [25] became more enormous when filler loading increased. And because of stronger filler network at higher loading, hardness of the samples showed an increase by the numbers.

A distinguishing advantage of the polymeric fillers filled elastomer composites was the light weight, which could contribute to save tremendous amount of energy when made into products. Therefore, densities of the samples with varied filler loadings were tested. Results were listed in Table 5. A comparison in density between the PS-filled SBR and carbon black filled SBR was made with the same loading of 30 phr (seen in Figure 4), which again revealed the advantage of

the PS-filled SBR composites in weight. The density of PS-filled SBR composites with a loading of 50 phr was no more than 1.000 g/cm^3 , proving that the PS-filled SBR composites was superior in weight to the composites filled with those conventional fillers.

3.3.3. In Several Elastomer Matrices. Reinforcement of the cross-linked polystyrene particles to the elastomeric matrices of styrene-butadiene rubber (SBR), nitrile-butadiene rubber (NBR), and natural rubber (NR) was investigated with a filler loading of 30 phr. As long as the PS particles had been cross-linked, high-temperature vulcanization system of sulfur was employed to prepare the cured PS-filled elastomer composites with an attempt to promote molecule diffusion thus strengthening the filler-rubber interactions by heating.

As shown in Figure 5 and Table 6, remarkable improvements in mechanical properties were there. Tensile strength of the PS-filled NR composites was blighted. We speculated the reason could be that the strain-induced crystallization of NR was affected when the PS particles were introduced in. Except that, comparing with the three pure elastomer matrices, composites filled with the cross-linked PS particles exhibited great enhancement in stress at given elongation, tensile strength, and tear strength as well. Further more, the enhancement in the PS-filled SBR composite was very remarkable due to the good compatibility of the PS particles with the SBR matrix.

As we mentioned earlier, nano-particles provided much more interface for the stick-slip processes of the elastomer molecules, compared with the conventional microparticles. The oriented clusters of the elastomer molecules brought about by the stick-slip processes were the most important reason for the enhanced reinforcing performances of the elastomer composites. This could also explain why filled composites had higher percentage elongation than the pure matrix. In the cured neat elastomer, the cross-linking bonds randomly distributed in the molecules; the chain length between two cross-linking bonds varied from each other. Because of the chemical bonding, molecules were impossible to slip at the cross-linking bonds; thus no oriented clusters of elastomer molecules were there. In the filled composites, besides the chemical cross-links, the physical adhesion between the filler particles and the elastomer matrix functioned as supplemented physical cross-links. Elastomer molecules could easily debound and rebound to the filler surface, and this made the stick-slip process possible, resulting in improved strength and higher percentage elongation.

Compared with the results of the PS-filled SBR composites cured by BPO, the sulfur-cured PS-filled SBR composites exhibited stronger filler-rubber interactions, to be specific, higher stress at given elongation and hardness, as illustrated in Figure 6. But in the PS-filled SBR composites cured with BPO, tensile strength was higher, and strain-hardening was observed in the stress-strain curve at large deformation.

The different morphologies of the PS-filled SBR, NBR, and NR elastomeric matrices at the tensile fracture surface were shown in Figure 7. In SBR and NBR, a fine distribution

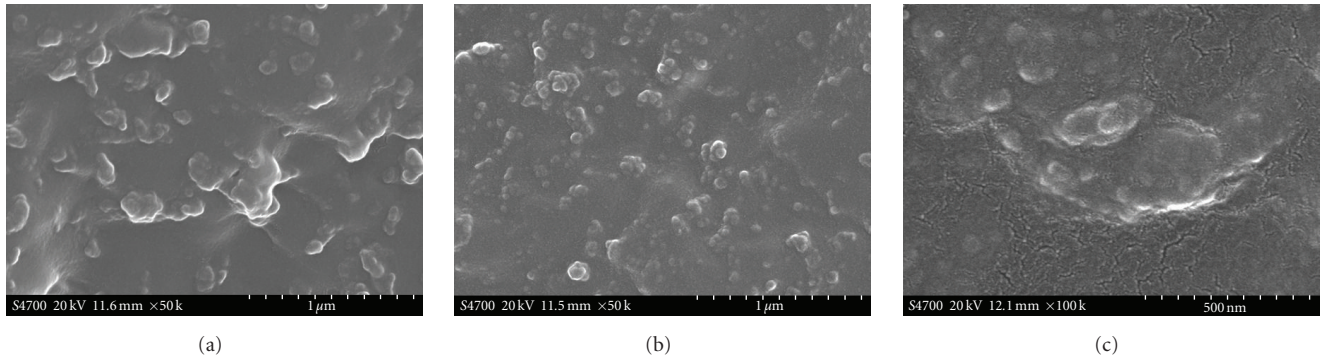


FIGURE 7: Morphology of the PS particles in different elastomeric matrices (tensile fracture surface). (a)–(c) represented the SEM images of the PS-filled SBR, NBR, and NR composites, respectively.

TABLE 4: Mechanical properties of the cross-linked PS-filled SBR composites with varied loadings.

Samples	Stress at 300% Elongation/MPa	Tensile Strength/MPa	Elongation at break/%	Permanent Set/%	Shore A Hardness/°	Tear Strength/KN/m
Neat SBR	1.4	1.5	327	0	46	7
PS(10)/SBR	1.9	10.7	581	10	58	16
PS(20)/SBR	2.2	14.5	623	16	65	22
PS(30)/SBR	2.3	17.6	652	18	72	28
PS(40)/SBR	2.4	18.0	649	24	77	31
PS(50)/SBR	2.6	17.7	644	26	82	36

Note that All samples were cured with 4 phr benzyl peroxide (BPO) at 95°C for 120 minutes.

TABLE 5: Density of the PS-filled SBR composites.

Samples	Density/(g/cm ³)
Neat SBR	0.958
PS(10)/SBR	0.978
PS(20)/SBR	0.985
PS(30)/SBR	0.993
PS(40)/SBR	0.996
PS(50)/SBR	0.998

of the PS particles in the matrices was observed, while in NR, there was a severe aggregation of the PS particles. In addition, over exposure to the high-energy electron beams during the longer-time exploring on the sample surface caused some cracking in the elastomer matrix, as observed in Figure 7(c).

It was the difference in the distribution of the PS particles that resulted in the diverse performances of the filled composites in the mechanical properties. Besides, PS particles in the SBR matrix possessed a rougher surface after break compared with those in the NBR matrix, as could be seen from Figures 7(a) and 7(b), which divulged the difference in filler-rubber interaction in these two composites that the PS particles had a better compatibility and stronger interaction with the SBR matrix.

4. Conclusion

Cross-linked polystyrene were prepared by free radical emulsion polymerization; the PS particles took a spherical shape in the size of 40–60 nm with a narrow distribution. The cross-linked PS particles exhibited excellent reinforcement to the polar and nonpolar elastomeric matrix such as SBR, NBR, and NR. But tensile strength of the PS-filled NR nanocomposites showed up deteriorated somehow. With the increase of filler loading, the mechanical properties of the composites gained remarkable enhancement. Particularly in the SBR matrix, the cross-linked polystyrene particles had good compatibility and strong interactions with the rubber matrix, therefore, resulting in a dramatic improvement in mechanical properties.

With the increase of the cross-linking density, the cross-linked PS spherical particles were provided with higher glass-transition temperature and thus the capability for hot environment applications, but less stability in the emulsion radical polymerization system. In compounds, the filler-rubber interactions of the PS-filled SBR composites weakened with the cross-linking density; however, in the high-temperature vulcanization system of sulfur, the filler-rubber interactions were improved after heated.

As a distinguishing advantage of the polymeric fillers, the cross-linked PS particles filled elastomer composites were superior to those filled with conventional fillers in weight and density.

TABLE 6: Mechanical properties of the cross-linked PS-filled SBR, NBR, and NR nanocomposites.

Samples	Shore A Hardness	Stress at 100% Elongation/MPa	Stress at 300% Elongation/MPa	Tensile Strength/MPa	Elongation at Break/%	Permanent Set/%	Tear Strength/KN/m
Pure SBR	48	1.1	1.5	2.0	461	4	11
PS (30)/SBR	81	2.7	4.8	12.9	601	36	39
Pure NBR	55	1.2	2.2	3.5	438	0	16
PS(30)/NBR	80	2.7	7.6	9.3	345	12	33
Pure NR	35	0.7	1.6	28.3	801	16	30
PS(30)/NR	75	1.9	3.9	19.7	650	56	76

Note that filler loading was 30 phr, all samples were cured with sulfur.

Acknowledgment

This work was supported by National Science Fund for Distinguished Young Scholars (50725310), China. We would like to express our appreciation to them.

References

- [1] J. E. Mark and D. W. Schaefer, "Polymer-based molecular composites," in *Proceedings of the Symposium on Materials Research Society*, vol. 171, p. 51, Pittsburgh, Pa, USA, 1190.
- [2] G. Kraus, "Reinforcement of elastomers by carbon black," *Rubber Chemistry and Technology*, vol. 51, no. 2, pp. 297–321, 1978.
- [3] G. Allen, "Two worlds of rubber technology—new products, new properties," *Plastics and Rubber*, vol. 1, p. 38, 1976.
- [4] A. R. Payne and R. E. Whittaker, "Reinforcement of rubber with carbon black," *Composites*, vol. 1, no. 4, pp. 203–214, 1970.
- [5] L. Bokobza, "The reinforcement of elastomeric networks by fillers," *Macromolecular Materials and Engineering*, vol. 289, no. 7, pp. 607–621, 2004.
- [6] L. Zhang and D. Jia, "The nano-reinforcing technique and science of rubber," in *Proceedings of the Symposium of International Rubber Conference*, p. 46, Beijing, China, 2004.
- [7] J. E. Mark, R. Abou-Hussein, T. Z. Sen, and A. Kloczkowski, "Some simulations on filler reinforcement in elastomers," *Polymer*, vol. 46, no. 21, pp. 8894–8904, 2005.
- [8] G. Heinrich, M. Kluppel, and T. A. Vilgis, "Reinforcement of elastomers," *Current Opinion in Solid State and Materials Science*, vol. 6, no. 3, pp. 195–203, 2002.
- [9] G. Kraus, "Reinforcement of elastomers by carbon black," *Fortschritte der Hochpolymeren-Forschung*, vol. 8, p. 155, 1971.
- [10] L. Zhang, "Ideal filler for reinforcement of elastomer," in *Proceedings of the 9th International Conference on Frontiers of Polymers and Advanced Materials (ICFPAM '07)*, Poznan, Poland, 2007.
- [11] G. Kraus, K. W. Rollmann, and J. T. Gruver, "Dynamic properties of a model reinforced elastomer. Styrene-butadiene reinforced with polystyrene," *Macromolecules*, vol. 3, no. 1, pp. 92–96, 1970.
- [12] M. Morton, "Mechanisms of reinforcement of elastomers by polymeric fillers," *Advances in Chemistry Series*, vol. 99, pp. 490–509, 1971.
- [13] J. J. Cai and R. Salovey, "Model filled rubber IV: dependence of stress-strain relationship on filler particle morphology," *Journal of Materials Science*, vol. 34, no. 19, pp. 4719–4726, 1999.
- [14] J. J. Cai and R. Salovey, "Model filled rubber—part V: mechanical properties of rubbery composites," *Journal of Materials Science*, vol. 36, no. 16, pp. 3947–3953, 2001.
- [15] L. Zheng, A. F. Xie, and J. T. Lean, "Polystyrene nanoparticles with anionically polymerized polybutadiene brushes," *Macromolecules*, vol. 37, no. 26, pp. 9954–9962, 2004.
- [16] X. Wang, J. E. Hall, S. Warren, et al., "Synthesis, characterization, and application of novel polymeric nanoparticles," *Macromolecules*, vol. 40, no. 3, pp. 499–508, 2007.
- [17] Y.-P. Wu, Y.-Q. Wang, H.-F. Zhang, et al., "Rubber-pristine clay nanocomposites prepared by co-coagulating rubber latex and clay aqueous suspension," *Composites Science and Technology*, vol. 65, no. 7–8, pp. 1195–1202, 2005.
- [18] Y.-Q. Wang, Y.-P. Wu, H.-F. Zhang, L.-Q. Zhang, B. Wang, and Z.-F. Wang, "Free volume of montmorillonite/styrene-butadiene rubber nanocomposites estimated by positron annihilation lifetime spectroscopy," *Macromolecular Rapid Communications*, vol. 25, no. 23, pp. 1973–1978, 2004.
- [19] J. Ma, P. Xiang, Y.-W. Mai, and L.-Q. Zhang, "A novel approach to high performance elastomer by using clay," *Macromolecular Rapid Communications*, vol. 25, no. 19, pp. 1692–1696, 2004.
- [20] L. Zhang, Y. Wu, Y. Wang, et al., "Nano-reinforcing and nano-compounding technique of rubber," *China Synthetic Rubber Industry*, vol. 23, no. 2, pp. 71–77, 2000.
- [21] L. Zhang, Z. Wang, Y. Wu, and S. Wu, "Percolation phenomena and mechanism in rubber reinforcement with different nano fillers," *China Synthetic Rubber Industry*, vol. 31, no. 4, p. 245, 2008.
- [22] G. R. Hamed, "Reinforcement of rubber," *Rubber Chemistry and Technology*, vol. 73, no. 3, pp. 524–533, 2000.
- [23] J. Liu, D. Cao, L. Zhang, and W. Wang, "Time-temperature and time-concentration superposition of nanofilled elastomers: a molecular dynamics study," *Macromolecules*, vol. 42, no. 7, pp. 2831–2842, 2009.
- [24] Z. H. Wang, J. Liu, S. Z. Wu, W. C. Wang, and L. Q. Zhang, "Novel percolation phenomena and mechanism of strengthening elastomers by nanofillers," *Physical Chemistry, Chemical Physics*, vol. 12, pp. 3014–3030, 2010.
- [25] A. R. Payne, "The dynamic properties of carbon black-loaded natural rubber vulcanizates," *Journal of Applied Polymer Science*, vol. 6, pp. 57–63, 1962.

Research Article

Preparation and Characterization of Self-Assembled Nanoparticles of Hyaluronic Acid-Deoxycholic Acid Conjugates

Xuemeng Dong and Chenguang Liu

College of Life Science, Ocean University of China, Yushan Road No. 5, Qingdao 266003, China

Correspondence should be addressed to Chenguang Liu, liucg@ouc.edu.cn

Received 14 October 2009; Accepted 31 March 2010

Academic Editor: Gaurav Mago

Copyright © 2010 X. Dong and C. Liu. This is an open access article distributed under the Creative Commons Attribution License, which permits unrestricted use, distribution, and reproduction in any medium, provided the original work is properly cited.

Novel amphiphilic biopolymers were synthesized using hyaluronic acid (HA) as a hydrophilic segment and deoxycholic acid (DOCA) as a hydrophobic segment by a 1-ethyl-3-(3-dimethylaminopropyl) carbodiimide mediated coupling reaction. The structural characteristics of the HA-DOCA conjugates were investigated using ^1H NMR. Self-assembled nanoparticles were prepared based on HA-DOCA conjugates, and its characteristics were investigated using dynamic laser light scattering, transmission electron microscopy (TEM), and fluorescence spectroscopy. The mean diameter was about 293.5 nm with unimodal size distribution in distilled water. The TEM images revealed that the shape of HA-DOCA self-aggregates was spherical. The critical aggregation concentration (CAC) was in the range of 0.025–0.056 mg/mL. The partition equilibrium constant (K_p) of pyrene in self-aggregates solution was from 1.45×10^4 to 3.64×10^4 . The aggregation number of DOCA groups per hydrophobic microdomain, estimated by the fluorescence quenching method using cetylpyridinium chloride, increased with increasing degree of substitution.

1. Introduction

Polymeric amphiphiles derived from hydrophobically modified soluble polymers have recently attracted much attention because of their potential application in drug delivery systems [1–3]. Such amphiphiles are able to spontaneously form micelles or nanoparticles via undergoing intra- and/or intermolecular association between hydrophobic moieties in aqueous environment. The hydrophobic parts form the core of the nanoparticles, which is a host system for various hydrophobic drugs, while the hydrophilic backbone forms corona or outer shells enwrapping the hydrophobic core. This shell prevents the inactivation of the encapsulated drug molecules by decreasing the contact with the inactivating species in the aqueous (blood) phase [4–6]. Furthermore, these polymeric nanoparticles exhibit unique characteristics, such as special rheological features, a rather narrow size distribution, considerable lower critical aggregation concentrations (CAC) than surfactant of low molecular weight, and thermodynamic stability [4, 7–9]. Recently, self-assembled nanoparticles based on natural polysaccharides have been of particular interest because of their good biocompatibility,

biodegradability, reduced toxic side effects, and improved therapeutic effects [10–12].

Hyaluronic acid (HA) is a natural mucopolysaccharide that consists of alternating residues D-glucuronic acid and N-acetyl-D-glucosamine. HA plays a key role in the structure and organization of the extracellular matrix, transport of nutrients, a regulation of cell adhesion, morphogenesis, and modulation of inflammation [13–16]. The immunoneutrality and nontoxicity of HA make it as an attractive building block for new biocompatible and biodegradable polymers [17]. HA has been applied in drug delivery systems, tissue engineering, and viscous supplementation [18]. Its major advantages as a drug carrier consist of its ability to bind CD44, a specific membrane receptor frequently overexpressed on the tumor cell surface [19, 20]. That is, targeting of anticancer agents to tumor cells and tumor metastases can be accomplished by receptor-mediated uptake of complexes of these agents and HA. Nevertheless, the poor biomechanical properties of HA prevent generation of new biomaterials, a fact that has given rise to a variety of chemical modifications of HA for providing mechanically and chemically stable materials [21]. The resulting HA derivatives have

better physicochemical properties than the native polymer, but retaining the biocompatibility and biodegradability of native HA. Previous studies have been performed on several different HA derivatives, for drug delivery, such as films, hydrogels, bioconjugates, and microspheres [22–25]. But few studies about nano-scaled HA derivatives have been reported [26, 27]. Nanoparticles as drug carriers have been considered to provide opportunities for the site-specific delivery of drugs by the enhanced permeation and retention (EPR) effect, and they have the ability to dissolve hydrophobic agents and protect the bioactive drug from host [28–30].

Herein the hydrophobically modified HA nanoparticles with favorable physicochemical properties are promising as drug delivery system for the pharmaceutical applications. In this study, chemical conjugates of HA and DOCA were synthesized by covalent attachment of DOCA to HA through amide formation. Physicochemical characteristics of the amphiphilic HA-DOCA conjugates in aqueous phase were revealed by dynamic light scattering, transmission electron microscopy and fluorescence probe techniques. Deoxycholic acid is known to form micelles in water as a result of its amphiphilicity [31]. Thus, it is expected that HA, hydrophobically modified with deoxycholic acid, will induce self-assembled aggregates.

2. Experimental

2.1. Materials. Hyaluronic acid (HA) (average $M_n = 16600$ Da) was purchased from Freda Biochemical company (Shandong, China). Deoxycholic acids (DOCA), 1-ethyl-3-(3-dimethylaminopropyl) carbodiimide (EDC), N-hydroxysuccinimide (NHS), N,N-dicyclohexyl carbodiimide (DCC), and cetylpyridinium chloride (CPC) were obtained from Sigma Chemical Co. (MO, USA). These reagents were all of analytical grade and used as received. Pyrene, as fluorescence probe was purchased from Sigma and purified by double recrystallization from absolute ethanol. Water was purified by distillation, deionization, and reverse osmosis (Milli-Q plus, Bedford, UK).

2.2. Synthesis of N-Deoxycholyethylene diamine (DOCA-NH₂). Firstly, the carboxylic group of deoxycholic acid was activated, as reported previously (11). In brief, DOCA (3.54 g) was mixed with DCC (2.40 g) and NHS (1.48 g) in 30 mL of THF. The feed mole ratio of DOCA, DCC and NHS were 1:1.2:1.2. The concentration of DCC and NHS was slightly higher than DOCA in order to activate DOCA completely. The mixture was allowed to react for 12 h at room temperature under a nitrogen atmosphere, and the precipitated dicyclohexylurea was removed by filtration. The filtered solution was poured into excessive hexane and the remaining NHS was dissolved in the hexane. The succinimido DOCA precipitate was filtered off and washed thoroughly with hexane, followed by vacuum-drying (DZF, Chemat, USA) at room temperature. The succinimido DOCA was stored at -20°C before use.

The N-deoxycholy-ethylene diamine (DOCA-NH₂) was synthesized by introducing ethylenediamine to the succinimido DOCA. The succinimido DOCA (5 g, 10 mmol) was

dissolved in DMF (20 mL) and the solution was slowly added dropwise into ethylenediamine solution (70 mL, 1 mol) in 250 mL beaker with separatory funnel (34731-00, Coleparmer, USA). The free mole ratio of succinimido DOCA and ethylenediamine was about 1:100. After reaction for 6 h, the mixture was precipitated in exceed distilled water. The filtered precipitation was carefully washed three times with distilled water and vacuum-drying at room temperature to obtain white powder DOCA-NH₂.

2.3. Preparation of HA-DOCA (HD) Conjugates. HA (0.1 g) was dissolved in formamide (5 mL) during gentle magnetic stirring, in a 20 mL beaker, at room temperature. Different amounts of EDC (the mole ratio to HA was 5:1, 10:1, 15:1, respectively) were thereafter added to the HA solution. Different amounts of DOCA-NH₂ (the mole ratio to HA was 10:1, 20:1, 40:1, respectively) were dissolved in DMF (5 mL) in a 20 mL beaker, by gentle heating (at 50°C) and added into the mixed solution of HA and EDC. The resulting solution was thereafter cooled at room temperature and then stirred under a nitrogen atmosphere for 24 h. The reaction mixture was extensively dialyzed against the excess amount of water/acetone (1v/3v-1v/1v) and distilled water for 3 days, followed by lyophilization.

Various HD conjugates were prepared by controlling the free mole ratios of DOCA-NH₂ to HA. The degree of substitution (DS), defined as the number of DOCA per one HA molecules, was determined by a titration method as previously reported (11). Briefly, HD conjugates (50 mg) were diffused in distilled water (20 mL) in a 50 mL beaker during magnetic stirring. After adding 0.05 mL of 0.1 N HCl, the solution was titrated with 0.01 N NaOH using microtitrator (PAX 100-3, Burkard, UK) while stirring and measuring the pH (Delta 320, Mettler Toledo, Switzerland).

The consumed amount of NaOH solution when the pH reached neutral value was recorded. By that, the DS of DOCA was calculated using the difference in the amounts of NaOH solution added to the solutions between standard HA solution and HD conjugate solutions.

2.4. Preparation of Self-Assembled Nanoparticles of HA-DOCA Conjugates. The HD conjugates were suspended in distilled water at 37°C for 24 h. The solution was then sonicated three times using a probe-type sonifier (Sonics Ultrasonic Processor, VC750) at 90 W for 2 min each, in which the pulse was turned off for 1 s with the interval of 5 s to prevent the increase in temperature. Solutions of different concentrations (0.0001–1 mg/mL) were obtained by diluting the stock solution with distilled water.

2.5. ¹H Nuclear Magnetic Resonance (NMR) Spectroscopy. The ¹H NMR spectra of the conjugates were obtained using a 500-MHz NMR (UNIYTINOVA-500 NMR, VARIAN) at 25°C . Samples of HA and HD conjugates were separately dissolved in solutions of D₂O or CDCl₃ (analytical reagent, Sigma), yielding a concentration of 10 mg/mL. The measurement conditions were as follows: a spectral window of 500 Hz, 32 k data points, a pulse angle of 30° , an acquisition

time of 2.03 s, and 32 scans with a delay of 1 s between scan [32].

2.6. Particle Size Distribution. To determine the average particle size and size distribution of self-aggregates, dynamic laser light scattering were performed using a helium ion laser system (Spectra Physics Laser Model 127-35). Three milliliters of self-aggregates suspension in distilled water (HD9: 1 mg/mL) was put into polystyrene latex cells and measured at a detector angle of 90°, a wavelength of 633 nm, and a temperature of 25°C.

2.7. Measurement of Fluorescence Spectroscopy. The fluorescence measurements were used to determine the critical aggregation concentration as previously described by Liu et al. [32]. Pyrene, used as a hydrophobic probe, was purified by repeated recrystallization from ethanol and vacuum-dried at 20°C. Purified pyrene was dissolved in pure ethanol (analytical reagent, Sigma) at the concentration of 0.04 mg/mL. About of 20 μ L of the result in solution was added into a 20 mL test tube and the ethanol was evacuated under purging of nitrogen gas. Four milliliters of HD nanoparticles solution was subsequently added to the test tube, resulting in a final pyrene concentration of 1.0×10^{-6} M. The concentration of nanoparticles in the solution ranged from 1×10^{-4} mg/mL to 1 mg/mL. The mixture was incubated for 3 h in a water bath at 65°C and shaken in a SHA-B shaking water bath GuoHua company, Hebei, China overnight at 20°C. Pyrene emission spectra were obtained using a Shimadzu RF-5301PC fluorescence spectrophotometer (Shimadzu Co., Kyoto, Japan). For measurements of intensity ratios for the third and the first peaks (I_3/I_1) in the emission spectra for pyrene, the slit openings for excitation and emission were set at 15 and 1.5 nm, respectively. The excitation (λ_{ex}) and emission (λ_{em}) wavelengths were 343 and 390 nm, respectively. The spectra were accumulated with an integration time of 3 s/nm.

The hydrophobicity of self-aggregates in this study was estimated by measuring the equilibrium constant (K_v), for partitioning of pyrene, between the water and nanoparticles phase as described by Wilhelm et al. [33],

$$\frac{F - F_{\min}}{F_{\max} - F} = \frac{K_v X_{\text{DOCA}}(c - cac)}{1000\rho_{\text{DOCA}}}, \quad (1)$$

Where F_{\max} and F_{\min} are the intensity ratios (I_3/I_1) at high and low concentration ranges of self-aggregates in Figure 6, and F is the intensity ratios (I_3/I_1) at the intermediate HD nanoparticle concentration region. X_{DOCA} is the weight fraction of DOCA in the conjugates, c is the concentration of the HD nanoparticles, and ρ_{DOCA} is the density of the inner core of self-aggregates, assumed to be equal to the density of DOCA (1.31 g/mL) [34].

The aggregation number of an associating DOCA hydrophobic domain was estimated by using the steady-state fluorescence quenching technique. CPC was used as quencher dissolving in distilled water to different concentrations (2.0×10^{-7} – 8.0×10^{-7} M). The CPC solution was added to the nanoparticle suspension with pyrene just before the measurement. Steady-state quenching data in

a microheterogeneous system such as an aqueous nanoparticle suspension fit in the quenching kinetics in [35]

$$\ln\left(\frac{I_0}{I}\right) = \frac{[Q]}{[M]}, \quad (2)$$

Where I and I_0 are the fluorescence intensities, in the presence or absence of a quencher, respectively, $[Q]$ is the concentration of the quencher, and $[M]$ is the concentration of hydrophobic domains in a polymer self-aggregates. Thus, $[M]$ can be obtained from the slope of $\ln(I_0/I) = f([Q])$ and the aggregation number per single hydrophobic microdomain (N_{DOCA}) is given by

$$N_{\text{DOCA}} = \frac{[\text{DOCA}]}{[M]}. \quad (3)$$

2.8. Transmission Electron Microscopy (TEM). To measure the morphology and size distribution of the nanoparticles, swatches were prepared by dropping the sample solution (1 mg/mL) onto a Formvar-coated copper grid. The grid was held horizontally for 2 min to allow the molecular aggregates to deposit. The surface water was then removed by tapping with a filter paper (9 cm, Xinhua company, China), followed by air-drying. One drop of 2% uranyl acetate solution (analytical reagent, Sigma) was added to the grid to give a negative stain for nanoparticles. The grid was then allowed to stand for 3 min at room temperature before the excess staining solution was removed by draining as above. The dried grid containing the nanoparticles was visualized using a Philips EM 400 transmission electron microscope (Koninklijke Philips Electronics N.V, the Netherlands) at an acceleration voltage of 80 KV.

3. Results and Discussion

3.1. Synthesis and Characterization of HA-DOCA Conjugates. Firstly, we activated DOCA with DCC and NHS then introduced a primary amino group to DOCA using ethylenediamine. For the synthesis of HD conjugates, we chemically coupled DOCA-NH₂ to HA with EDC as a cross-linker. EDC is a so-called “zero-length” cross-linker, which gives an amide linkage without leaving a spacer molecule. By this coupling reaction, various HD conjugates were prepared by controlling the free mole ratios of DOCA-NH₂ to HA. The schemes for the introduction amine group to the carboxylic acid of DOCA and subsequent coupling reaction of HA and N-deoxycholylethylenediamine (DOCA-NH₂) are shown in Figure 1.

The presence of DOCA in HA was verified by the characteristic peaks of DOCA appearing in the ¹H NMR spectra. Figure 2 shows the ¹H NMR spectrum of HA and HD conjugates in different solvent systems including both D₂O and CDCl₃. The proton assignment of HA (Figure 2(a)) is as follows: $\delta 2.0$ = (3H, NHCO-CH₃), $\delta 3.3$ – 3.9 = (1H, H-2, 3, 4, 5, and 6) [36]. The proton assignment of HD (Figure 2(b)) is as follows: $\delta 0.67$ = (3H, 18-CH₃), $\delta 0.85$ = (3H, 19-CH₃), $\delta 0.99$ = (3H, 21-CH₃), $\delta 1.06$ – 2.32 = (25H, steroidal H), $\delta 2.22$ = (3H, -NH-CO-CH₃) [37]. The presence of DOCA in HA was evaluated by the characteristic

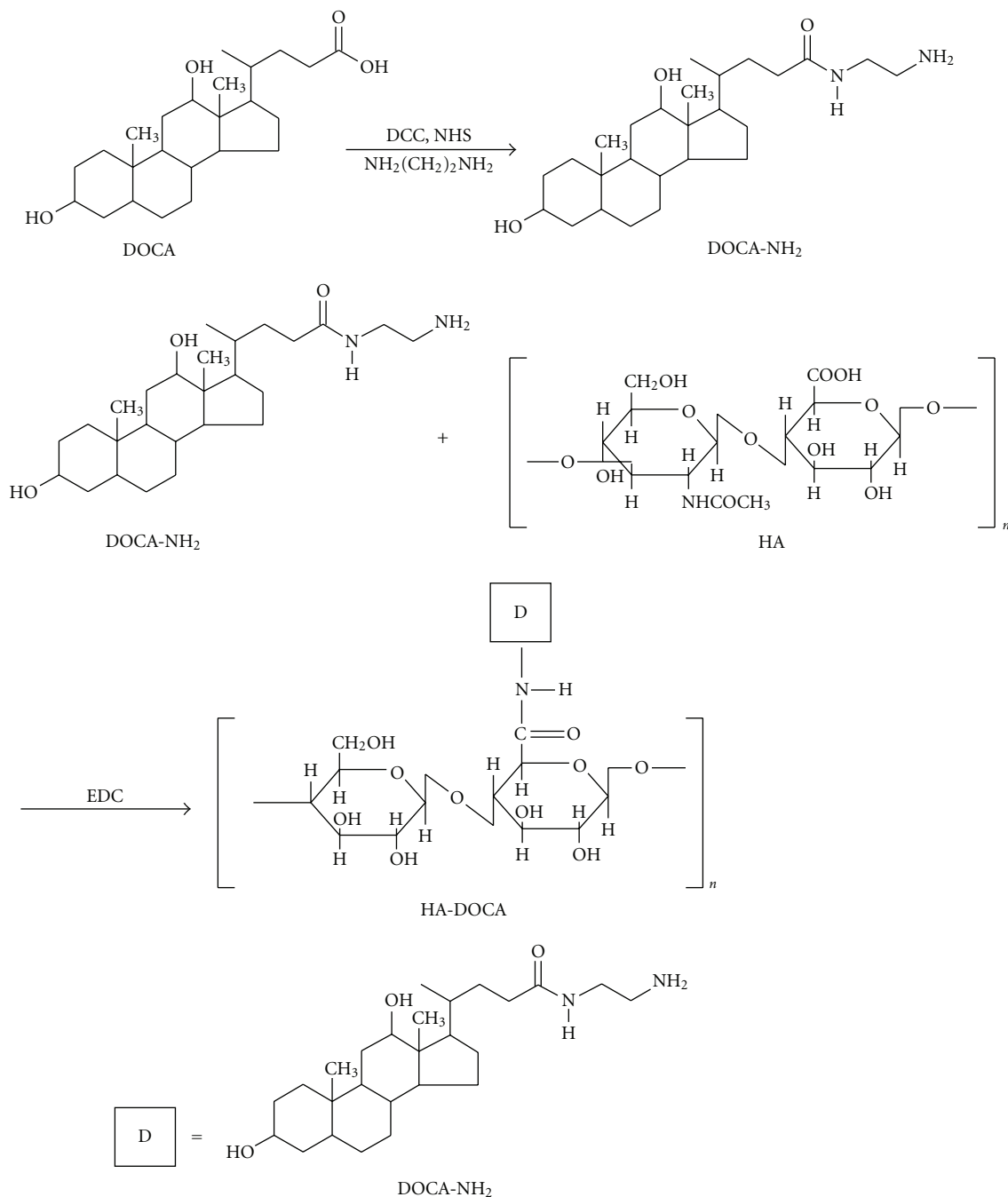


FIGURE 1: Synthesis scheme of HA-DOCA conjugates.

peaks of DOCA appearing at 0.85–2.3 ppm in the spectra (Figure 2(b)).

Various HD conjugates with different amounts of DOCA were prepared by changing the feed ratio of HA to DOCA. The results indicated that the degree of substitution (DS) of DOCA increases as the added feed ratio of DOCA and EDC increases. EDC could react with the carboxyl group of the HA to form an active ester intermediate which could chemically couple with DOCA-NH₂. The DS is in the range from 5.9 to 9.4 per one HA molecule in this experiment. The mean molecular weight and DS are summarized in Table 1.

3.2. Formation of Self-Aggregated Nanoparticles. The formation of self-assembled nanoparticles in an aqueous phase and the critical aggregation concentration (CAC) for HD self-aggregates were confirmed by the fluorescence technique with pyrene as a fluorescence probe. Pyrene was chosen as the fluorescence probe because its condensed aromatic structure is sensitive to polarity, and it produces distinctive excimer fluorescence under conditions of sufficiently high concentration and mobility [38]. When the self-aggregates are formed in an aqueous phase, pyrene molecules are preferentially located within or close to the hydrophobic

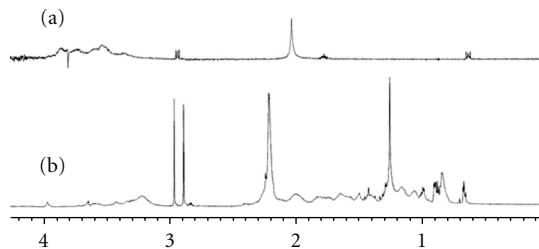


FIGURE 2: ^1H NMR spectra of HA in D_2O (a) and HD9 in CDCl_3 (b) at 25°C .

TABLE 1: General properties of hyaluronic acid-deoxycholic acid conjugates in distilled water.

Sample ^a	Feed ratio ^b	Mn ^c	DS	X ^d (%)
HD6	1 : 10	18925	5.9	12.3
HD7	1 : 20	19594	7.6	15.3
HD9	1 : 40	20304	9.4	18.2

^aHA-DOCA (HD) conjugates, where the number indicates the DS of DOCA. ^bMole ratio of HA:DOCA-NH₂. ^cNumber-average molecular weight, estimated from the titration results. ^dWeight fraction of DOCA in a HA molecule.

microdomain of the nanoparticles rather than to the aqueous phase. Consequently, there was a remarkable change in its fluorescence spectra, such as an increase in the quantum yield [38, 39]. Figure 3 shows the typical fluorescent emission spectra of pyrene in solutions of HD nanoparticles (sample HD9) with various concentrations. The fluorescent emission spectra of pyrene in solutions exhibit four predominant peaks, one for each concentration. The fluorescence intensities did remarkably increase with the increasing of self-aggregates concentrations especially for the first and third peaks suggesting that pyrene was shifted from polar water environment to less polar one because pyrene had a longer lifetime and a higher quantum yield in the non-polar environment. The intensities of fluorescence increase substantially, suggesting the formation of nanoparticles and the incorporation of pyrene in the hydrophobic core of self-aggregates.

The partition of pyrene from aqueous to hydrophobic phase of nanoparticles causes the ratios of peak III (I_3) with peak I (I_1) to increase with the increasing of HD conjugates concentration especially above the CAC. Critical aggregation concentration (CAC), which is the threshold concentration of self-aggregate formation by intra- and/or intermolecular association, can be determined from the change of intensity ratio (I_3/I_1) of pyrene in the presence of polymeric amphiphiles. The intensity ratio of I_3/I_1 is sensitive to the polarity of the microenvironment where the pyrene exists: the larger the I_3/I_1 ratio, the less polar microenvironment of pyrene. Figure 4 exhibits the changes of the I_3/I_1 value as a function of logarithm of concentration of HD self-aggregates for samples of HD6, HD7 and HD9. At low concentrations, the I_3/I_1 value remains nearly unchanged meaning that there is a lack of hydrophobic nonpolar environment with no occurrence of assemblage. However, the intensity ratios

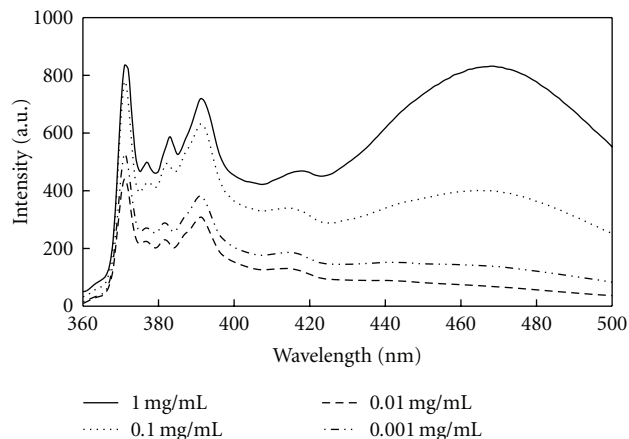


FIGURE 3: Fluorescence emission spectra of pyrene in the presence of HA-DOCA nanoparticles (HD9) at a fixed excitation wavelength of 343 nm. The concentrations of HA-DOCA conjugate were from 0.00001 to 1.0 mg/mL in distilled water with $1.0\ \mu\text{M}$ of pyrene.

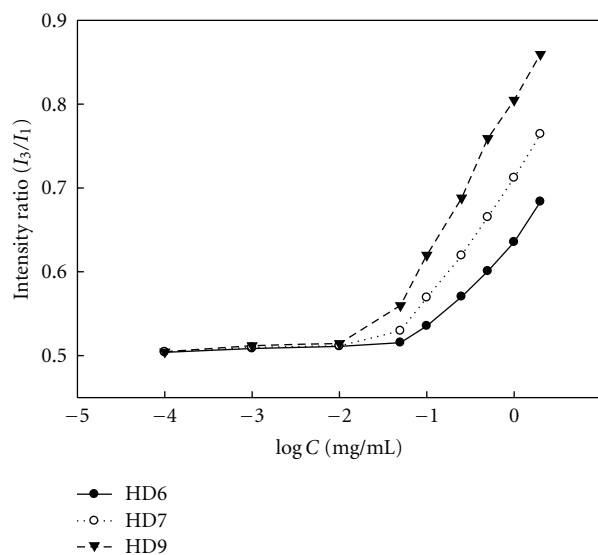


FIGURE 4: Intensity ratios (I_3/I_1) from pyrene emission spectra as a function of logarithm of HA-DOCA conjugate concentration in distilled water.

begin to increase with further increase in concentration, indicating the occurrence of self-aggregation of HD resulting from intermolecular hydrophobic interactions between the DOCA groups. The CAC was taken as the intersection of a flat region in the low concentration extreme and sigmoid region in the crossover region. The CAC values determined for HD conjugates HD6, HD7 and HD9 are 0.056, 0.037 and 0.025 mg/mL, respectively, which agree well with the conjugate compositions as the DOCA group in conjugates is increased in the same order as listed in Table 2. The CAC values of deoxycholic acid modified HA are similar to that of the deoxycholic acid modified chitosans self-aggregates (CAC are in the range of 0.01–0.07 mg/mL) [5, 40], but much lower than the critical micelle concentration

TABLE 2: Microscopic characteristics of HA-DOCA self-aggregates determined by the fluorescence probe method.

sample	CAC ^a (mg/mL)	K_v ^b ($\times 10^4$)	N_{DOCA} ^c	N_{chain} ^d
HD6	0.056	1.45	17.6	2.98
HD7	0.037	2.83	27.8	3.66
HD9	0.025	3.64	43	4.57

^aCritical aggregation concentration determined by pyrene emission spectra.

^bBinding equilibrium constant for pyrene in distilled water in the presence of HA-DOCA nanoparticles. ^cAggregation number of DOCA moieties per one hydrophobic domain. ^dNumber of HA-DOCA conjugate polymer chains per one hydrophobic domain.

(cmc) of low-molecular-weight surfactants (2.3 mg/mL for sodium dodecyl sulfate (SDS) in water and 1.0 mg/mL for deoxycholic acid in water) [41, 42]. The lower CAC values of the hydrophobic modified HA as compared with low-molecular-weight surfactants may be one of the important characteristics of polymeric amphiphiles, indicating the stability of HD self-aggregate in dilute condition.

3.3. Microscopic Structure of Self-Aggregates. Figure 4 shows that above the CAC, the intensity ratio increases due to the binding of pyrene is larger. This suggests that pyrene preferentially interacts with amphiphiles phase than to self aggregate and then distributes into the inner core of self-aggregates. The partition of pyrene between the aqueous and self-aggregates phase could reflect the hydrophobicity of the inner core of nanoparticles. The hydrophobicity is one important factor for its application as a drug carrier and it can be expressed as equilibrium constant K_v of pyrene, which is one of the critical parameters related to self-assembled nanoparticle stability. At the concentration range of HD conjugates from 0.0001 mg/mL to 1 mg/mL, the mean diameter and the size distribution factor of self-aggregates were not changed. Therefore, we assume a simple equilibrium, the equilibrium constant (K_v) for partitioning of pyrene between the water and micellar phases can be calculated according to the (1). Where the K_v values of pyrene can be determined using a plot of $(F - F_{\min})/(F_{\max} - F)$ versus the HD nanoparticle concentration as shown in Figure 5. Table 2 summarizes the K_v values for pyrene, and they are in the range of $1.45\text{--}3.64 \times 10^4$. As shown in Table 2, K_v values increase with increasing DS of DOCA in the conjugates, indicating the increase of hydrophobicity of inner core of the nanoparticles with the DS. On the basis of these K_v values, we determined that HD self-aggregates also formed less polar microdomains and that their hydrophobic cores were covered with hydrophilic HA shells. By comparing to the HD self-aggregates, other polymer amphiphiles based on poly (ethylene oxide) or poly (2-ethyl-2-oxazoline) as hydrophilic blocks have higher K_v values [33, 43]. Whereas the hydrophobicity of the interior core of HD self-aggregates is very similar to glycol chitosan nanoparticle bearing 5β -cholanic acid as a hydrophobic segment and heparin-DOCA nanoparticle, in addition it is higher than glycol chitosan-DOCA nanoparticle ($\sim 10^3$).

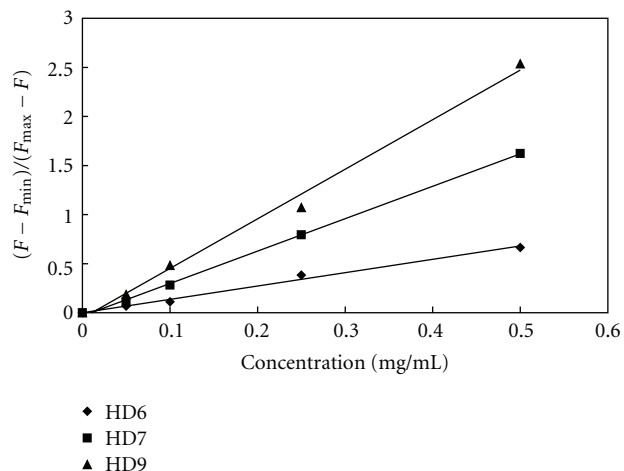


FIGURE 5: Plots of $(F - F_{\min})/(F_{\max} - F)$ versus concentration of HA-DOCA conjugate in distilled water.

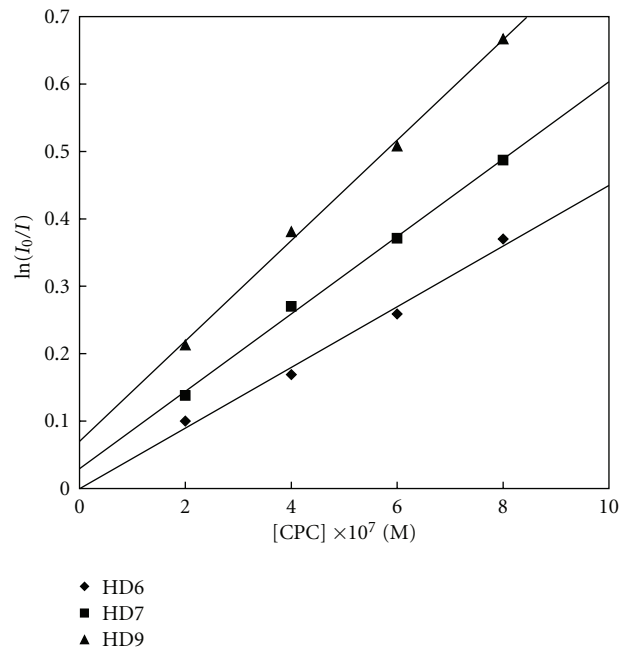


FIGURE 6: $\ln(I_0/I)$ of pyrene (1×10^{-6} M) fluorescence as a function of CPC concentration in the presence of HA-DOCA conjugates at the concentration of 0.5 mg/mL.

To investigate the associating number of hydrophobic moieties in one self-aggregate and to identify the microstructure of nanoparticles, a fluorescence quenching method was used which has been successfully applied to estimate the microstructure of polymeric amphiphiles [39, 44]. Figure 6 shows the intensity $[\ln(I_0/I)]$ of pyrene fluorescence as a function of CPC concentration in the presence of the HD conjugates at the concentration of 0.5 mg/mL in water. There is a good linear relationship with all the cases (correlation factor, $r = 0.9974$ (HD6), $r = 0.9974$ (HD7), $r = 0.9892$ (HD9)) and the data fit well to (2). Hence, the concentration of hydrophobic domains in self-aggregates could be obtained

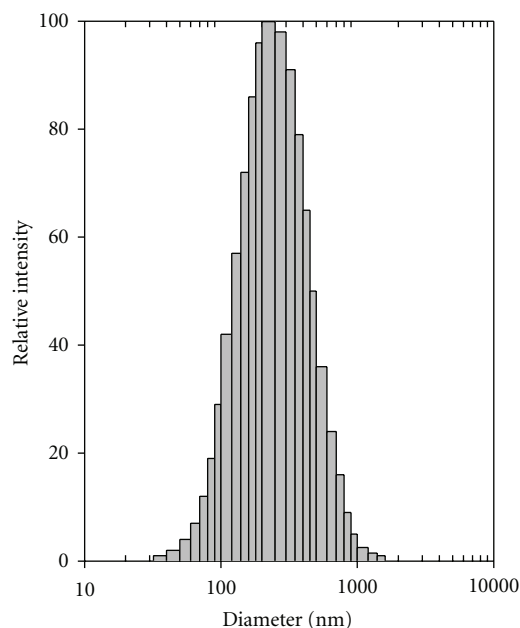


FIGURE 7: Size distribution of HA-DOCA nanoparticles (HD9, 1 mg/mL) prepared in distilled water.

from the slope of the straight line. The mean aggregation numbers of DOCA groups (N_{DOCA}) per single hydrophobic domain are calculated from (3) and the values are listed in Table 2. The aggregation number increase with increasing of the DS of DOCA which means that the conjugated DOCA groups may all interassociate to form hydrophobic microdomains. The N_{DOCA} values are much higher than the aggregation number of sodium deoxycholate in aqueous media (8 ± 2) [45]. The big aggregation number in self-aggregates is considered to result from the DOCA moieties didn't form dense hydrophobic interior core because of the limited mobility and steric hindrance of DOCA covalently attached to HA. The N_{chain} value is defined as the number of polymer chains per one hydrophobic domain. There are about 2.98–4.57 chains of HD conjugates forming one hydrophobic microdomain from the fluorescence quenching study. The N_{chain} values increased with the increase of DS of DOCA which means that compact hydrophobic domains may be formed with enhanced hydrophobicity. The increase of N_{DOCA} and N_{chain} values corresponds to the DS of DOCA which indicates the higher hydrophobicity resulting from the increasing DOCA moieties making the reinforced association between single polymer chains. From the microscopic characteristics of HD conjugate, it can be concluded that one HD nanoparticle could have multiple hydrophobic inter-cores. The results are very similar to the other hydrophobic modified polysaccharide biocopolymers with different fatty acids and bile acids [8, 9, 11, 44].

3.4. Characteristics of Self-Aggregated Nanoparticles. The self-aggregated nanoparticles of HD conjugates were produced by a simple sonication method in aqueous condition. Figure 7 shows the particle size and distribution of self-aggregates of



FIGURE 8: Transmission electron micrograph of self-aggregates based on HA-DOCA conjugate (HD9, 1 mg/mL).

HD conjugates in a distilled water solution determined by dynamic laser light scattering. A majority of nanoparticles size was in 100–600 nm with a mean hydrodynamic diameter of 293.5 nm as shown in Figure 7. The polydispersity factor of self-aggregates was 0.108 and it demonstrated a narrow particle size distribution. The mean diameter of each nanoparticle was reproducible with repeated experiments and it was not changed with respect to the sonication time that ranged from 3 to 20 min. The size of Nanoparticle was not significantly affected by changing concentration of HD conjugates. This implies that the interactions between self-aggregates are almost negligible.

TEM observation demonstrated the near spherical shape of self-aggregates with narrow size distribution, as shown in Figure 8. The mean diameter and size distribution of self-aggregates appeared to be a little different from the results obtained by dynamic light scattering measurement. For example, the size measured by the TEM methods was smaller than the laser light scattering method. This might be due to the different conditions for sample preparation. The TEM images depicted the size at the dried state of the sample, whereas the laser light scattering method involves the measurement of size in the hydrated state. In other words, the size determined by TEM is an actual diameter (dry state) of the nanoparticles, whereas the size measured by the dynamic laser scattering method is a hydrodynamic diameter (hydrated state) of the nanoparticles. Therefore, in the hydrated state, the nanoparticles will have a higher hydrodynamic volume due to solvent effect; hence, the size measured by the laser light scattering method was higher than the TEM method [32].

4. Conclusion

Novel polymeric amphiphiles, partially hydrophobic modified hyaluronic acid with deoxycholic acid as hydrophobic moieties in an aqueous solution, were studied. The diameters of self-aggregates were in the range of 100–600 nm with

a mean hydrodynamic diameter of 293.5 nm. The critical aggregation concentrations of HD conjugates depended on the DS of deoxycholic acid in a range of 0.025–0.056 mg/mL. The TEM images of self-aggregates showed a spherical shape. The K_V and N_{DOCA} values, confirmed by fluorescence probe studies, were substantially dependent on the DS of DOCA. Results demonstrate that a hydrophobic domain was composed of multiple HD polymer chains.

Acknowledgments

The authors thank the financial supports high-tech research and development plan (863 plan) of China (2007AA10Z349) and Dr. Mikael Gallstedt for reviewing the manuscript.

References

- [1] G. S. Kwon and T. Okano, "Polymeric micelles as new drug carriers," *Advanced Drug Delivery Reviews*, vol. 21, no. 2, pp. 107–116, 1996.
- [2] K. Akiyoshi, S. Kobayashi, S. Shichibe, et al., "Self-assembled hydrogel nanoparticle of cholesterol-bearing pullulan as a carrier of protein drugs: complexation and stabilization of insulin," *Journal of Controlled Release*, vol. 54, no. 3, pp. 313–320, 1998.
- [3] J. S. Park, T. H. Han, K. Y. Lee, et al., "N-acetyl histidine-conjugated glycol chitosan self-assembled nanoparticles for intracytoplasmic delivery of drugs: endocytosis, exocytosis and drug release," *Journal of Controlled Release*, vol. 115, no. 1, pp. 37–45, 2006.
- [4] K. Akiyoshi and J. Sunamoto, "Supramolecular assembly of hydrophobized polysaccharides," *Supramolecular Science*, vol. 3, no. 1–3, pp. 157–163, 1996.
- [5] K. Y. Lee, W. H. Jo, I. C. Kwon, Y. H. Kim, and S. Y. Jeong, "Physicochemical characteristics of self-aggregates of hydrophobically modified chitosans," *Langmuir*, vol. 14, no. 9, pp. 2329–2332, 1998.
- [6] J. Djordjevic, M. Barch, and K. E. Uhrich, "Polymeric micelles based on amphiphilic scorpion-like macromolecules: novel carriers for water-insoluble drugs," *Pharmaceutical Research*, vol. 22, no. 1, pp. 24–32, 2005.
- [7] K. Kuroda, K. Fujimoto, J. Sunamoto, and K. Akiyoshi, "Hierarchical self-assembly of hydrophobically modified pullulan in water: gelation by networks of nanoparticles," *Langmuir*, vol. 18, no. 10, pp. 3780–3786, 2002.
- [8] K. Kim, S. Kwon, J. H. Park, et al., "Physicochemical characterizations of self-assembled nanoparticles of glycol chitosan-deoxycholic acid conjugates," *Biomacromolecules*, vol. 6, no. 2, pp. 1154–1158, 2005.
- [9] M. Nichifor, A. Lopes, A. Carpvov, and E. Melo, "Aggregation in water of dextran hydrophobically modified with bile acids," *Macromolecules*, vol. 32, no. 21, pp. 7078–7085, 1999.
- [10] J. H. Kim, Y. S. Kim, S. Kim, et al., "Hydrophobically modified glycol chitosan nanoparticles as carriers for paclitaxel," *Journal of Controlled Release*, vol. 111, no. 1–2, pp. 228–234, 2006.
- [11] M. Hamidi, A. Azadi, and P. Rafiei, "Hydrogel nanoparticles in drug delivery," *Advanced Drug Delivery Reviews*, vol. 60, no. 15, pp. 1638–1649, 2008.
- [12] Z. Liu, Y. Jiao, Y. Wang, C. Zhou, and Z. Zhang, "Polysaccharides-based nanoparticles as drug delivery systems," *Advanced Drug Delivery Reviews*, vol. 60, no. 15, pp. 1650–1662, 2008.
- [13] J. E. Scott, "Extracellular matrix, supramolecular organisation and shape," *Journal of Anatomy*, vol. 187, no. 2, pp. 259–269, 1995.
- [14] C. Hardwick, K. Hoare, R. Owens, et al., "Molecular cloning of a novel hyaluronan receptor that mediates tumor cell motility," *Journal of Cell Biology*, vol. 117, no. 6, pp. 1343–1350, 1992.
- [15] L. Collis, C. Hall, L. Lange, M. Ziebell, R. Prestwich, and E. A. Turley, "Rapid hyaluronan uptake is associated with enhanced motility: implications for an intracellular mode of action," *FEBS Letters*, vol. 440, no. 3, pp. 444–449, 1998.
- [16] B. Gerdin and R. Hällgren, "Dynamic role of hyaluronan (HYA) in connective tissue activation and inflammation," *Journal of Internal Medicine*, vol. 242, no. 1, pp. 49–55, 1997.
- [17] D. Campoccia, P. Doherty, M. Radice, P. Brun, G. Abatangelo, and D. F. Williams, "Semisynthetic resorbable materials from hyaluronan esterification," *Biomaterials*, vol. 19, no. 23, pp. 2101–2127, 1998.
- [18] G. D. Prestwich, D. M. Marecak, J. F. Marecek, K. P. Vercruyse, and M. R. Ziebell, "Chemical modification of hyaluronic acid for drug delivery, biomaterials, and biochemical probes," in *The Chemistry, Biology, and Medical Applications of Hyaluronan and Its Derivatives*, T. C. Laurent, Ed., pp. 43–65, Protland Press, London, UK, 1998.
- [19] W. Knudson, "Tumor-associated hyaluronan: providing an extracellular matrix that facilitates invasion," *American Journal of Pathology*, vol. 148, no. 6, pp. 1721–1726, 1996.
- [20] W. Knudson, G. Chow, and C. B. Knudson, "CD44-mediated uptake and degradation of hyaluronan," *Matrix Biology*, vol. 21, no. 1, pp. 15–23, 2002.
- [21] J. W. Kuo, D. A. Swann, and G. D. Prestwich, "Chemical modification of hyaluronic acid by carbodiimides," *Bioconjugate Chemistry*, vol. 2, no. 4, pp. 232–241, 1991.
- [22] Y. Luo, K. R. Kirker, and G. D. Prestwich, "Cross-linked hyaluronic acid hydrogel films: new biomaterials for drug delivery," *Journal of Controlled Release*, vol. 69, no. 1, pp. 169–184, 2000.
- [23] T. Segura, P. H. Chung, and L. D. Shea, "DNA delivery from hyaluronic acid-collagen hydrogels via a substrate-mediated approach," *Biomaterials*, vol. 26, no. 13, pp. 1575–1584, 2005.
- [24] Y. Luo, N. J. Bernshaw, Z. R. Lu, J. Kopecek, and G. D. Prestwich, "Targeted delivery of doxorubicin by HPMA copolymer-hyaluronan bioconjugates," *Pharmaceutical Research*, vol. 19, no. 4, pp. 396–402, 2002.
- [25] E. Esposito, E. Menegatti, and R. Cortesi, "Hyaluronan-based microspheres as tools for drug delivery: a comparative study," *International Journal of Pharmaceutics*, vol. 288, no. 1, pp. 35–49, 2005.
- [26] K. Y. Choi, S. Lee, K. Park, et al., "Preparation and characterization of hyaluronic acid-based hydrogel nanoparticles," *Journal of Physics and Chemistry of Solids*, vol. 69, no. 5–6, pp. 1591–1595, 2008.
- [27] K. Y. Choi, K. H. Min, J. H. Na, et al., "Self-assembled hyaluronic acid nanoparticles as a potential drug carrier for cancer therapy: synthesis, characterization, and in vivo biodistribution," *Journal of Materials Chemistry*, vol. 19, no. 24, pp. 4102–4107, 2009.
- [28] K. Kataoka, T. Matsumoto, M. Yokoyama, et al., "Doxorubicin-loaded poly(ethylene glycol)-poly(β -benzyl-L-aspartate) copolymer micelles: their pharmaceutical characteristics and biological significance," *Journal of Controlled Release*, vol. 64, no. 1–3, pp. 143–153, 2000.

- [29] A. Lavasanifar, J. Samuel, and G. S. Kwon, "Poly(ethylene oxide)-*block*-poly(L-amino acid) micelles for drug delivery," *Advanced Drug Delivery Reviews*, vol. 54, no. 2, pp. 169–190, 2002.
- [30] K. S. Soppimath, T. M. Aminabhavi, A. R. Kulkarni, and W. E. Rudzinski, "Biodegradable polymeric nanoparticles as drug delivery devices," *Journal of Controlled Release*, vol. 70, no. 1-2, pp. 1–20, 2001.
- [31] A. Enhsen, W. Kramer, and G. Wess, "Bile acids in drug discovery," *Drug Discovery Today*, vol. 3, no. 9, pp. 409–418, 1998.
- [32] C. G. Liu, K. G. H. Desai, X. G. Chen, and H. J. Park, "Linolenic acid-modified chitosan for formation of self-assembled nanoparticles," *Journal of Agricultural and Food Chemistry*, vol. 53, no. 2, pp. 437–441, 2005.
- [33] M. Wilhelm, C. L. Zhao, Y. Wang, et al., "Poly(styrene-ethylene oxide) block copolymer micelle formation in water: a fluorescence probe study," *Macromolecules*, vol. 24, no. 5, pp. 1033–1040, 1991.
- [34] I. Astafieva, X. F. Zhong, and A. Eisenberg, "Critical micellization phenomena in block polyelectrolyte solutions," *Macromolecules*, vol. 26, no. 26, pp. 7339–7352, 1993.
- [35] E. Alami, M. Almgren, W. Brown, and J. François, "Aggregation of hydrophobically end-capped poly(ethylene oxide) in aqueous solutions. Fluorescence and light-scattering studies," *Macromolecules*, vol. 29, no. 6, pp. 2229–2243, 1996.
- [36] S. K. Kim, K. Kim, S. Lee, et al., "Evaluation of absorption of heparin-DOCA conjugates on the intestinal wall using a surface plasmon resonance," *Journal of Pharmaceutical and Biomedical Analysis*, vol. 39, no. 5, pp. 861–870, 2005.
- [37] V. Crescenzi, A. Francescangeli, A. Taglienti, D. Capitani, and L. Mannina, "Synthesis and partial characterization of hydrogels obtained via glutaraldehyde crosslinking of acetylated chitosan and of hyaluronan derivatives," *Biomacromolecules*, vol. 4, no. 4, pp. 1045–1054, 2003.
- [38] Y. Hu, X. Jiang, Y. Ding, et al., "Preparation and drug release behaviors of nimodipine-loaded poly(caprolactone)-poly(ethylene oxide)-polylactide amphiphilic copolymer nanoparticles," *Biomaterials*, vol. 24, no. 13, pp. 2395–2404, 2003.
- [39] K. Kalyanasundaram and J. K. Thomas, "Environmental effects on vibronic band intensities in pyrene monomer fluorescence and their application in studies of micellar systems," *Journal of the American Chemical Society*, vol. 99, no. 7, pp. 2039–2044, 1977.
- [40] K. Y. Lee, W. H. Jo, I. C. Kwon, Y. H. Kim, and S. Y. Jeong, "Structural determination and interior polarity of self-aggregates prepared from deoxycholic acid-modified chitosan in water," *Macromolecules*, vol. 31, no. 2, pp. 378–383, 1998.
- [41] Y. Nagasaki, T. Okada, C. Scholz, M. Iijima, M. Kato, and K. Kataoka, "The reactive polymeric micelle based on an aldehyde-ended poly(ethylene glycol)/poly(lactide) block copolymer," *Macromolecules*, vol. 31, no. 5, pp. 1473–1479, 1998.
- [42] G. Kwon, M. Naito, M. Yokoyama, T. Okano, Y. Sakurai, and K. Kataoka, "Micelles based on AB block copolymers of poly(ethylene oxide) and poly(β -benzyl L-aspartate)," *Langmuir*, vol. 9, no. 4, pp. 945–949, 1993.
- [43] C. Kim, S. C. Lee, S. W. Kang, I. C. Kwon, Y. H. Kim, and S. Y. Jeong, "Synthesis and the micellar characteristics of poly(ethylene oxide)-deoxycholic acid conjugates," *Langmuir*, vol. 16, no. 11, pp. 4792–4797, 2000.
- [44] K. Akiyoshi, S. Deguchi, H. Tajima, T. Nishikawa, and J. Sunamoto, "Microscopic structure and thermoresponsiveness of a hydrogel nanoparticle by self-assembly of a hydrophobized polysaccharide," *Macromolecules*, vol. 30, no. 4, pp. 857–861, 1997.
- [45] J. P. Kratochvil, W. P. Hsu, and D. I. Kwok, "How large are the micelles of di- α -hydroxy bile salts at the critical micellization concentrations in aqueous electrolyte solutions? Results for sodium taurodeoxycholate and sodium deoxycholate," *Langmuir*, vol. 2, no. 2, pp. 256–258, 1986.

Research Article

Preparation and Characterization of Water-Soluble Chitosan Nanoparticles as Protein Delivery System

Hong-liang Zhang,¹ Si-hui Wu,¹ Yi Tao,¹ Lin-quan Zang,¹ and Zheng-quan Su²

¹ College of Pharmacy, Guangdong Pharmaceutical University, Guangzhou 510006, China

² College of Public Health, Guangdong Pharmaceutical University, Guangzhou 510240, China

Correspondence should be addressed to Zheng-quan Su, suzhq@scnu.edu.cn

Received 6 July 2009; Revised 1 September 2009; Accepted 1 November 2009

Academic Editor: Gaurav Mago

Copyright © 2010 Hong-liang Zhang et al. This is an open access article distributed under the Creative Commons Attribution License, which permits unrestricted use, distribution, and reproduction in any medium, provided the original work is properly cited.

The objective of this study was to investigate the potential of water soluble chitosan as a carrier in the preparation of protein-loaded nanoparticles. Nanoparticles were prepared by ionotropic gelation of water-soluble chitosan (WSC) with sodium tripolyphosphate (TPP). Bovine serum albumin (BSA) was applied as a model drug. The size and morphology of the nanoparticles were investigated as a function of the preparation conditions. The particles were spherical in shape and had a smooth surface. The size range of the nanoparticles was between 100 and 400 nm. Result of the *in vitro* studies showed that the WSC nanoparticles enhance and prolong the intestinal absorption of BSA. These results also indicated that WSC nanoparticles were a potential protein delivery system.

1. Introduction

Peptides and proteins have become the drugs of choice for the treatment of numerous diseases as a result of their incredible selectivity and their ability to provide effective and potent action [1]. In general, they cause fewer side effects and have great potential to cure diseases, rather than merely treat their symptoms. The successful delivery of these protein drugs has been an ongoing topic in the pharmaceutical research for many years. Among various delivery methods, the oral delivery is the most convenient and desired way of drug delivery, especially when repeated or routine administration is concerned [2]. However, protein and peptide drugs are poorly absorbed after oral administration because of their susceptibility to enzymatic degradation and their low permeability across the intestinal epithelium. Various approaches have been proposed to overcome barriers and to attain better oral bioavailability, including the use of surfactants, permeation enhancers, protease inhibitors, enteric coatings, and carrier systems [3, 4]. Amongst these, the use of colloidal polymeric particulate delivery systems, particularly mucoadhesive nanoparticles, represents a promising concept [5, 6].

Nanoparticles have received much attention for the delivery of macromolecular drugs, such as peptides, proteins, and genes, due to their ability to protect protein and peptides from degradation in the gastrointestinal track by proteolytic enzymes [7–9]. Nanoparticles possess marked mucoadhesion properties that have been related to the combination of the particle size and the particle superficial charge. Furthermore nanoparticles have been referred to as capable of being absorbed into mucosal tissue.

Chitosan received attention as a material for nanoparticles for the decade [10]. Chitosan is a well-known natural cationic polyelectrolyte. It is a partially deacetylated form of chitin, which is a structural polysaccharide found in crustacea, insects, and some fungi, and it has attracted interest as a biocompatible, biodegradable, mucoadhesive, and nontoxic material for use in biomedical applications [11–14]. In addition, chitosan has a special feature of adhering to the mucosal surface and transiently opening the tight junction between epithelial cells [15]. Thus, chitosan nanoparticles are potential delivery system for hydrophilic drugs due to its outstanding physicochemical and biological properties.

Despite of its superiority as a biomaterial, chitosan is not fully soluble in water and then soluble in acidic solution. Aqueous solubility of chitosan only in acidic solution because of its rigid crystalline structure and the deacetylation which limits its application to bioactive agents such as gene delivery carriers, peptide carriers, and drug carriers. Water-soluble chitosan is easily soluble in neutral aqueous solution. Its advantage is ease of modification, useful as gene or peptide drug carriers. Therefore, water-soluble chitosan and functional property have been developing for pharmaceutical and new drug candidate.

Therefore, the major goal of the present study is to create a kind of new biodegradable nanoparticle as protein delivery system. The nanoparticles have been characterized in terms of size, polydispersity index, and association efficiency. Also *in vitro* release was investigated to determine the efficacy of this system and the effective factors on absorption via this system.

2. Materials and Methods

2.1. Material. WSC (degree of deacetylation 87%, molecular weight 21 kDa) was made from a shrimp shell and obtained from Shandong Aokang Biotech Ltd. (Shandong, China). BSA with Mw 68 kDa and Coomassie brilliant blue G250 were purchased from Sigma Chemical Co. (USA). All other reagents and solvents were of analytical grade.

2.2. Preparation of Chitosan Nanoparticles and BSA-Loaded Nanoparticles. WSC-BSA nanoparticles were prepared by methods adapted from that reported by Calvo et al. [16]. Briefly, WSC was dissolved in aqueous solution at different concentration. Then, tripolyphosphate (TPP) was dissolved in distilled water at 1.0 mg/mL. Nanoparticles were spontaneously obtained upon the addition of 1 mL (1 mg/mL, w/v) of a TPP aqueous basic solution to 5 mL of the chitosan aqueous solution (1 mg/mL, w/v) under magnetic stirring at room temperature. BSA-loaded nanoparticles were formed by the addition of 1 mL BSA solution to chitosan solution prior to the incorporation of TPP solution. The detailed formation conditions were shown in the corresponding figures. The factors tested included BSA initial concentration (0.1, 0.2, 0.5, 1.0 mg/mL) and chitosan concentration (0.5, 1.0, 1.5, 2.0, 3.0 mg/mL). When we evaluated one factor, we only altered its own parameters and kept the parameters of other factors constant. Without specific depiction, the parameters of chitosan were as follows: concentration 1.0 mg/mL, DD 96%, and Mw 210 kDa; initial concentration of BSA was 0.5 mg/mL; TPP concentration was 1.0 mg/mL. The nanoparticles are characterized immediately. All experiments were performed in triplicates.

2.3. Characterization of Nanoparticles. The particle size and size distributions of the nanoparticles were performed by particle sizer (Zetasizer 3000 HAS, Malvern Instruments Ltd., Worcs, UK). Chitosan nanoparticles separated from

suspension were dried by a freeze dryer; their FTIRs (Shimadzu, FT-IR 8700, Japan) were taken with KBr pellets on Perkin-Elmer Spectrum one FTIR.

2.4. Determination of BSA Encapsulation Efficiency of Nanoparticles. To determine the encapsulation efficiency and loading capacity, nanoparticles with the different formation were centrifuged at $15,000 \times r$ and 4°C for 30 minutes, and the amount of free BSA was determined in clear supernatant by UV spectrophotometry (Shimadzu UV-1601, Shimadzu Co. Ltd., Japan) at 595 nm using supernatant of nonloaded nanoparticles as basic correction. BSA encapsulation efficiency (AE) and loading capacity (LC) were calculated according to (1) indicated below:

$$\text{AE} = \frac{\text{Total amount BSA} - \text{Free amount BSA}}{\text{Total amount BSA}}, \quad (1)$$

$$\text{LC} = \frac{\text{Total amount BSA} - \text{Free amount BSA}}{\text{Nanoparticles weight}}.$$

2.5. In Vitro Release Study. BSA release from chitosan nanoparticles was determined as follows. A known amount of freeze-dried nanoparticles was transferred to a 25 mL tube and 10 mL of the respective dissolution buffer was added to the tube. The temperature and rotation were adjusted to 37°C and 90 rpm, respectively. At predetermined time of 0.5, 2, 4, 6, 8, 10, 12, and 24 hour 5 mL of sample was removed and ultracentrifuged at $15,000 \times r$ for 30 minutes, and 5 mL of the supernatant were replaced by fresh medium. The samples were further analyzed using UV.

3. Results and Discussion

3.1. Physicochemical Characterizations of Nanoparticles. The structure of BSA-loaded lyophilized nanoparticles was examined by TEM (Tokyo, Japan). They showed that the particles have a uniform spherical shape and smooth surface (Figure 1(b)), and they are about 150 nm in size (Figure 1(a)). FTIR spectra of WSC nanoparticles and WSC matrix are shown in Figure 2. A band at 3420/cm has been previously attributed to $-\text{NH}_2$ and $-\text{OH}$ group stretching vibration in WSC matrix [17]. In WSC nanoparticles a shift from 3420 to 3430/cm is shown, and the peak of 3430/cm becomes wider; this indicates that hydrogen bonding is enhanced. In nanoparticles a new sharp peak 1638/cm appears, and the 1630/cm peak of $-\text{NH}_2$ bending vibration shifts to 1645/cm. Knaul observed the similar result in the study of chitosan film treated with phosphate (NaH_2PO_4) and attributed it to the linkage between phosphoric and ammonium ion [18]. So we suppose that the tripolyphosphoric groups of TPP are linked with ammonium group of WSC; the inter- and intramolecular action are enhanced in chitosan nanoparticles.

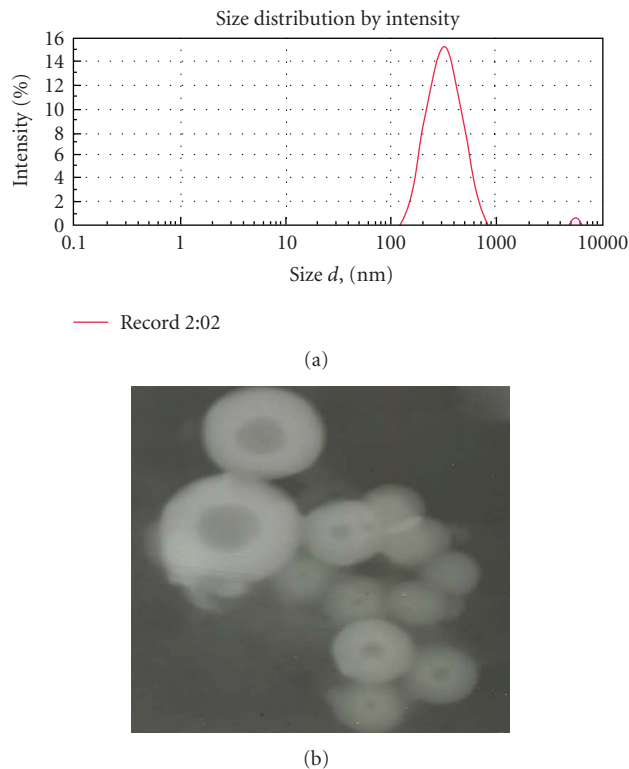


FIGURE 1: (a) Particle size distribution of WSC nanoparticles. (b) TEM image of WSC nanoparticles.

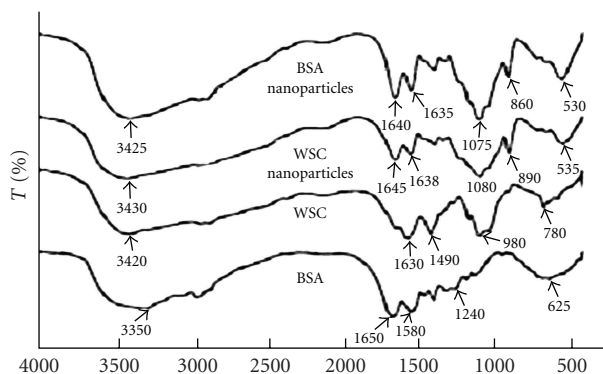


FIGURE 2: FTIR of BSA nanoparticles, WSC nanoparticles, WSC and BSA.

3.2. Encapsulation Efficiency

3.2.1. Effect of BSA Concentration. In most nanoparticle delivery systems, the drug carrying capacity is defined as an encapsulation efficiency. In the present study, BSA was carried on the nanoparticles via the ionic interaction. In water, the long hydrophilic chains extended to the water, and some BSA might be encapsulated among the positive hydrophilic chains, which indicated that the BSA was not only on the surface of the nanoparticles but also was distributed in the outer hydrophilic area. So, the BSA carrying capacity of the nanoparticles could be termed as encapsulation efficiency. In this study, BSA encapsulation efficiency from 40% to 95%

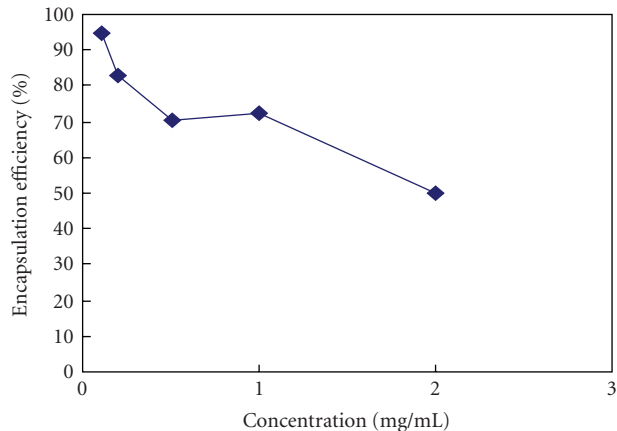


FIGURE 3: The influence of BSA initial concentration on encapsulation efficiency (WSC 1 mg/mL, TPP 1 mg/mL, $n = 5$).

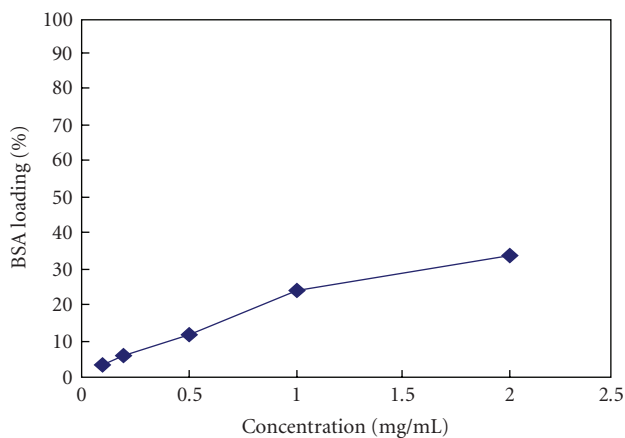


FIGURE 4: The influence of BSA initial concentration on loading capacity (WSC 1 mg/mL, TPP 1 mg/mL, $n = 5$).

was significantly affected by the initial BSA concentration in Figure 3; the lower the concentration, the higher the encapsulation efficiency. However, the protein loading was enhanced dramatically from 5% to 30% by increasing the initial BSA concentration from 0.1 to 2 mg/mL in Figure 4.

3.2.2. Effect of Chitosan Concentration. When TPP concentration was 1 mg/mL, decreasing chitosan concentration down to 0.5 mg/mL, aggregates with large diameter were formed; increasing chitosan concentration up to 4 mg/mL made encapsulation extremely difficult. Formation of nanoparticles is only possible for some specific concentration of chitosan and TPP. As for gelation between TPP solution of 1 mg/mL and chitosan solution of 1–3 mg/mL, we usually observed that some opalescent suspension was formed, which was examined as nanoparticles. Adding TPP solution of 1 mg/mL to chitosan solution of 4 mg/mL, firstly we observed some opalescent suspension and then disappeared immediately, and the nanoparticles formation was extremely difficult. Figure 5 shows that increasing the chitosan concentration decreased encapsulation efficiency of

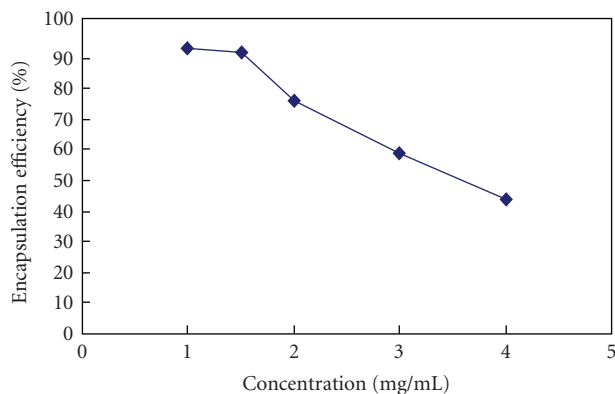


FIGURE 5: The influence of chitosan concentration on BSA encapsulation efficiency (BSA 0.5 mg/mL, TPP 1 mg/mL, $n = 5$).

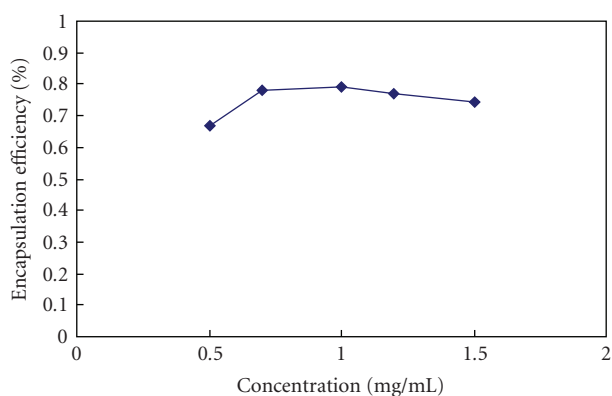


FIGURE 6: The influence of TPP concentration on BSA encapsulation efficiency (WSC 1 mg/mL, BSA 0.5 mg/mL, $n = 5$).

BSA. Vandenberg stated that the highly viscous nature of the gelation medium hinders encapsulation of BSA in the study of chitosan-alginate microspheres [19]. Relatively lower adhesiveness of chitosan with lower concentration promotes encapsulation of BSA and gelation between chitosan and TPP.

3.2.3. Effect of TPP Concentration. Many studies have reported that the quantity of TPP in a given formulation has a significant effect on the protein encapsulation and characteristic of NP [20, 21]. Therefore, the optimal amount of TPP in formulation was investigated in detail. As concluded in Figure 6 encapsulation efficiency of the nanoparticles was affected by the TPP solution, with increasing amount ratio of TPP to chitosan leading to a slight change of encapsulation efficiency. When WSC concentration was 1 mg/mL, BSA concentration was 0.5 mg/mL; decreasing TPP concentration down to 0.5 mg/mL, aggregates with large diameter were formed; increasing TPP concentration up to 2 mg/mL made encapsulation extremely difficult.

On the basis of above result, TPP did not affect the entrapment efficiency of BSA-chitosan nanoparticles when nanoparticles were formed at optimal chitosan/BSA mass of 1 : 0.5. Therefore, it is reasonable to assume

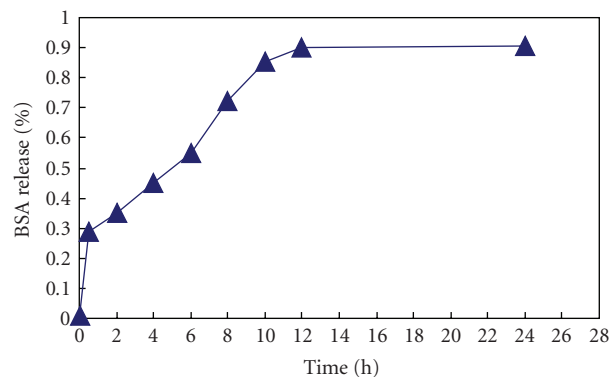


FIGURE 7: BSA release (WSC 1 mg/mL, BSA 0.5 mg/mL, TPP 1 mg/mL).

that polymer/BSA charge ratio plays an important role in nanoparticles formation.

3.3. In Vitro Release. The preliminary protein release test from BSA nanoparticles in vitro proves that they have a sustained release form as shown in Figure 7. Ionic strength in release medium may affect significantly the release properties of BSA nanoparticles based on ionic gelation; so we choose phosphate buffer (pH 7.4) as release medium which simulates body fluid according to literatures [22]. The in vitro protein release profiles obtained for each formulation showed three phases compositions [23]:

- (1) a first initial burst release of 30%, due to the drug desorbed from the particles surface,
- (2) a plateau for the following 8h, resulting from the only diffusion of the drug dispersed in the polymermatrix,
- (3) a constant sustained release of the drug, resulting from the diffusion of the protein through the polymer wall as well as its erosion.

4. Conclusion

In summary, novel ionic crosslinking nanoparticles composed of WSC and TPP loaded with BSA were successfully prepared. The size distribution was in the range of 200–400 nm. The nanoparticles were spherical shape and smooth surface. WSC nanoparticles showed higher protein encapsulation efficiency. In addition, the BSA release from the nanoparticles was sustained release. Therefore, WSCs have a potential carrier in a controlled drug delivery system for protein drugs.

References

- [1] S. Frokjaer and D. E. Otzen, "Protein drug stability: a formulation challenge," *Nature Reviews Drug Discovery*, vol. 4, no. 4, pp. 298–306, 2005.
- [2] B.-Y. Kim, J. H. Jeong, K. Park, and J.-D. Kim, "Bioadhesive interaction and hypoglycemic effect of insulin-loaded lectin-microparticle conjugates in oral insulin delivery system," *Journal of Controlled Release*, vol. 102, no. 3, pp. 525–538, 2005.

- [3] G. P. Carino, J. S. Jacob, and E. Mathiowitz, "Nanosphere based oral insulin delivery," *Journal of Controlled Release*, vol. 65, no. 1-2, pp. 261-269, 2000.
- [4] K. Nakashima, M. Miyagi, K. Goto, Y. Matsumoto, and R. Ueoka, "Enzymatic and hyperglycemia stability of chemically modified insulins with hydrophobic acyl groups," *Bioorganic and Medicinal Chemistry Letters*, vol. 14, no. 2, pp. 481-483, 2004.
- [5] G. Ponchel and J.-M. Irache, "Specific and non-specific bioadhesive particulate systems for oral delivery to the gastrointestinal tract," *Advanced Drug Delivery Reviews*, vol. 34, no. 2-3, pp. 191-219, 1998.
- [6] H. Takeuchi, H. Yamamoto, and Y. Kawashima, "Mucoadhesive nanoparticulate systems for peptide drug delivery," *Advanced Drug Delivery Reviews*, vol. 47, no. 1, pp. 39-54, 2001.
- [7] S. Sakuma, M. Hayashi, and M. Akashi, "Design of nanoparticles composed of graft copolymers for oral peptide delivery," *Advanced Drug Delivery Reviews*, vol. 47, no. 1, pp. 21-37, 2001.
- [8] B. Sarmento, D. C. Ferreira, L. Jorgensen, and M. van de Weert, "Probing insulin's secondary structure after entrapment into alginate/chitosan nanoparticles," *European Journal of Pharmaceutics and Biopharmaceutics*, vol. 65, no. 1, pp. 10-17, 2007.
- [9] F. Chen, Z.-R. Zhang, and Y. Huang, "Evaluation and modification of N-trimethyl chitosan chloride nanoparticles as protein carriers," *International Journal of Pharmaceutics*, vol. 336, no. 1, pp. 166-173, 2007.
- [10] K. A. Janes, P. Calvo, and M. J. Alonso, "Polysaccharide colloidal particles as delivery systems for macromolecules," *Advanced Drug Delivery Reviews*, vol. 47, no. 1, pp. 83-97, 2001.
- [11] W. Paul and C. P. Sharma, "Chitosan, a drug carrier for the 21st century: a review," *S.T.P. Pharma Sciences*, vol. 10, no. 1, pp. 5-22, 2000.
- [12] M. Thanou, J. C. Verhoef, and H. E. Junginger, "Oral drug absorption enhancement by chitosan and its derivatives," *Advanced Drug Delivery Reviews*, vol. 52, no. 2, pp. 117-126, 2001.
- [13] X. Z. Shu and K. J. Zhu, "Controlled drug release properties of ionically cross-linked chitosan beads: the influence of anion structure," *International Journal of Pharmaceutics*, vol. 233, no. 1-2, pp. 217-225, 2002.
- [14] E. Khor and L. Y. Lim, "Implantable applications of chitin and chitosan," *Biomaterials*, vol. 24, no. 13, pp. 2339-2349, 2003.
- [15] F. Qian, F. Cui, J. Ding, C. Tang, and C. Yin, "Chitosan graft copolymer nanoparticles for oral protein drug delivery: preparation and characterization," *Biomacromolecules*, vol. 7, no. 10, pp. 2722-2727, 2006.
- [16] P. Calvo, C. Remuñán-López, J. L. Vila-Jato, and M. J. Alonso, "Novel hydrophilic chitosan-polyethylene oxide nanoparticles as protein carriers," *Journal of Applied Polymer Science*, vol. 63, no. 1, pp. 125-132, 1997.
- [17] J.-H. Yu, Y.-M. Du, and H. Zheng, "Blend films of chitosan-gelatin," *Wuhan University Journal of Natural Sciences*, vol. 45, no. 4, pp. 440-444, 1999.
- [18] J. Z. Knaul, S. M. Hudson, and K. A. M. Creber, "Improved mechanical properties of chitosan fibers," *Journal of Applied Polymer Science*, vol. 72, no. 13, pp. 1721-1732, 1999.
- [19] R. J. Vandenberg and K. R. Aubrey, "Glycine transport inhibitors as potential antipsychotic drugs," *Expert Opinion on Therapeutic Targets*, vol. 5, no. 4, pp. 507-518, 2001.
- [20] K. A. Janes and M. J. Alonso, "Depolymerized chitosan nanoparticles for protein delivery: preparation and characterization," *Journal of Applied Polymer Science*, vol. 88, no. 12, pp. 2769-2776, 2003.
- [21] A. Grenha, B. Seijo, and C. Remuñán-López, "Microencapsulated chitosan nanoparticles for lung protein delivery," *European Journal of Pharmaceutical Sciences*, vol. 25, no. 4-5, pp. 427-437, 2005.
- [22] E. Leo, R. Cameroni, and F. Forni, "Dynamic dialysis for the drug release evaluation from doxorubicin-gelatin nanoparticle conjugates," *International Journal of Pharmaceutics*, vol. 180, no. 1, pp. 23-30, 1999.
- [23] A. Lamprecht, N. Ubrich, M. H. Pérez, C.-M. Lehr, M. Hoffman, and P. Maincent, "Influences of process parameters on nanoparticle preparation performed by a double emulsion pressure homogenization technique," *International Journal of Pharmaceutics*, vol. 196, no. 2, pp. 177-182, 2000.

Research Article

The Effects of Coupling Agents on the Properties of Polyimide/Nano- Al_2O_3 Three-Layer Hybrid Films

Lizhu Liu,^{1,2} Ling Weng,¹ Yuxia Song,¹ Lin Gao,¹ and Qingquan Lei²

¹College of Material Science and Engineering, Harbin University of Science and Technology, Harbin 150040, China

²Key Laboratory of Engineering Dielectric and Its Application, College of Electrical and Electronic Engineering, Harbin University of Science and Technology, Ministry of Education, Harbin 150040, China

Correspondence should be addressed to Lizhu Liu, mrliluzhu1964@yahoo.com.cn

Received 25 September 2009; Revised 10 January 2010; Accepted 14 May 2010

Academic Editor: Gaurav Mago

Copyright © 2010 Lizhu Liu et al. This is an open access article distributed under the Creative Commons Attribution License, which permits unrestricted use, distribution, and reproduction in any medium, provided the original work is properly cited.

PI/nano- Al_2O_3 hybrid films were prepared by ultrasonic-mechanical method. Before addition, nano- Al_2O_3 particles were firstly modified with different coupling agents. The micromorphology, thermal stability, mechanical properties, and electric breakdown strength of hybrid films were characterized and investigated. Results indicated that nano- Al_2O_3 particles were homogeneously dispersed in the PI matrix by the addition of coupling agents. The thermal stability and mechanical properties of PI/nano- Al_2O_3 composite films with KH550 were the best. The tensile strength and elongation at break of PI composite film were 119.1 MPa and 19.1%, which were 14.2% and 78.5% higher than unmodified PI composite film, respectively.

1. Introduction

As an engineering material, polyimide had been extensively applied in many areas such as microelectronics, electric industries, and aerospace and so forth [1]. During the past decade, increasing attention has been paid to the polyimide organic-inorganic hybrid materials, and it has been proved that the mechanical, thermal, and electrical properties of PI hybrid films can be improved by incorporation of fillers such as carbon nanotube [2], aluminum nitride [3], silica [4–7], and titania [8] into the pristine polyimide matrix.

Among these inorganic particles, nanoalumina (Al_2O_3) is often chosen as fillers to improve insulation properties of the polymer materials due to its extremely high insulating qualities and thermal conductivity [9–13]. These polyimide/ Al_2O_3 composites could widely be applied in electrical insulating fields. However, due to its huge surface areas and large surface free energy, nano- Al_2O_3 particles will aggregate with each other easily. So the combination of nano- Al_2O_3 particles with PI in nano scale is very difficult. One of the most important key points of PI/ Al_2O_3 hybrid films is to control the dispersion of alumina in the polymer matrix.

The coupling agents can make organic and inorganic materials connect together and improve the compatibility

between the two phases effectively. However, little information has been focused on the effects of different coupling agents on structure and properties of polyimide/ Al_2O_3 hybrid films.

In our present work, a series of PI/inorganic hybrid films with different kinds of coupling agents and different contents of each coupling agent was prepared. The microstructure and properties of these PI/nano- Al_2O_3 hybrid films were studied. Especially, the effects of different coupling agents on the microstructure and properties of hybrid films were investigated.

^a T_0 : the initial decomposition temperature.

^b T_{10} : the decomposition temperature at 10wt% weight loss.

^c T_{30} : the decomposition temperature at 30wt% weight loss.

2. Experiment

2.1. Materials. Pyromellitic diananocomposite(PMDA) and 4,4'-Oxydianiline(ODA) were chemic grade and purchased from Shandong Wanda Chemical Co. N,N-dimethylacetamide (DMAc) was analytical grade and purchased from Tianjin Basifu Chemical Co. α - Al_2O_3 (30 nm) was obtained

from Shanghai Wanjing New Materials Co. γ -aminopropyl triethoxysilane (KH550, $\text{NH}_2(\text{CH}_2)_3\text{Si}(\text{OCH}_2\text{CH}_3)_3$), γ -glycid-oxypropyl trimethoxysilane (KH560, $\text{C}_6\text{H}_{11}\text{O}_2\text{Si}(\text{OCH}_3)_3$) were purchased from Nanjing Shuguang Chemical Plant. 3-(N-Styrylmethyl-2-aminoethylamino)-propyltrimethoxysilane hydrochloride (AE3012, $\text{C}_{14}\text{H}_{21}\text{N}_2\text{HCISi}(\text{OCH}_3)_3$) was purchased from Dalian Aolikai Chemical Co. Ethanol absolute was analytical grade and purchased from Tianjin Shentai Chemical Reagent Co.

2.2. Preparation of PI/Al₂O₃ Hybrid Films. Nanometer alumina particles were firstly dissolved in ethanol absolute, then heated up in a water bath of 70–75 °C, and 4% content of coupling agent was added with the treatment of ultrasonic wave. The mixture was stirred mechanically again for 4 h, followed by heating at 100 °C for 16 h, and then abraded to use.

Poly(amic acid) (PAA) was synthesized by appropriate PMDA and ODA in DMAc. The solid content of PAA solution was 10 wt%. A typical synthesis of the precursors to alumina containing polymer is as follows ODA was added into a 250 mL three-necked bottle, and an appropriate amount of DMAc was added into it. After the ODA was completely dissolved, PMDA was added to this solution with a certain time sequence, and the mixture was stirred to get a yellow PAA solution. A calculated quantity of modified nano-Al₂O₃ particles with KH550 content 2 wt% was added to PAA solution with the aid of ultrasonic wave, and the mixture was stirred mechanically again for 10 h to form a homogeneous Al₂O₃/poly(amic acid) solution.

The Al₂O₃/PAA solution was casted on a clean glass substrate and followed by heating successively at 80 °C, 100 °C and 140 °C for 1 h, 220 °C for 2 h, and 300 °C for 3 h, respectively. The PI/Al₂O₃ hybrid films were obtained after the film peeled off the glass substrate.

2.3. Characterization. The fracture surfaces of film samples with aurum were examined on the FEI. Sirion Scanning Electron Micrographs (SEMs) at the voltage of 20.0 kV. FT-IR spectra of the nano-Al₂O₃ before and after treatment with the coupling agent were recorded on a BRUKER EQUINOX55 FT-IR spectrophotometer. The acquisition time was one minute at a resolution of four wave numbers. UV-Vis spectra were measured on a UV757CRT UV-Vis Spectrometer using the wavelength from 190 to 800 nm. Thermogravimetric analysis (TGA) was performed on a Pyris 6 series thermal analysis system at a heating rate of 20 °C/min under nitrogen atmosphere. TGA curves were recorded. The tensile-strength and elongation at break were measured on XLD-series Liquid Screen Electronic Tensile Apparatus 100×10 mm with specimens in accordance with GB/T13541-92 at a drawing rate of 50 mm/min. Averages of five individual determinations were used, the values took three significant digits, and the unit was MPa, the elongation ratio computation to the integer position, by percentage expression. The electric breakdown strength was tested on the regulating assembly at boosting manually in the polymethylphenyl siloxane fluid.

3. Results and Discussion

3.1. Microstructures of PI/Al₂O₃ Hybrid Films. Figure 1 shows the fractural surface microstructures of PI/Al₂O₃ hybrid films with or without coupling agents. It can be seen that all of the samples show the three-layer structure characteristics. However, there are also some obvious differences between these four samples. Sample of PI/unmodified-Al₂O₃ hybrid film (Figure 1(a)) shows an obvious stripping between three layers, indicating a bad structure integrity. While samples of PI/modified-Al₂O₃ hybrid films by KH560 and AE3012, respectively, as Figures 1(c) and 1(d) reflect a slight stripping phenomenon. A best combinational characteristics among these four samples can be found in Figure 1(b), which has a flattest fracture surface with smallest stripping among these four figures. This fairly good in microstructure of Figure 1(b) indicates a better combinational condition than others when KH560 addition.

3.2. FTIR Analysis of PI/Al₂O₃ Hybrid Films. Figure 2 illustrated the FT-IR spectra of the nano-Al₂O₃ particles before and after treatment with the coupling agent KH560, which was donated as a) and b), respectively. The characteristic peaks in these two FT-IR spectra present near at 3407.1 cm⁻¹, 1628.5 cm⁻¹ indicate the stretching vibration and bending vibration of hydroxyl group peaks on the Al₂O₃ particles' surface. Comparing a) and b) spectra, it can be clearly found that the strength of O-H peaks after treatment by coupling agent was greatly weaker than that of raw Al₂O₃ particles, indicating the decrease of absorbed water and the surface hydroxyl group after treatment by coupling agent. Moreover, the band at 2931 cm⁻¹ is the C-H band stretching vibration, it also indicated the effective linkage between KH560 and Al₂O₃ particles.

3.3. UV-Vis Transmittance of PI/Al₂O₃ Hybrid Films. UV-vis absorption spectra of PI hybrid films with unmodified and modified Al₂O₃ by coupling agents are shown in Figure 3. The cutoff wavelengths of the films are observed at about 440–460 nm. Comparing to the PI/unmodified-Al₂O₃ hybrid films, the transmittances of the PI/modified-Al₂O₃ hybrid films by coupling agents are slightly increase, which is attributed to the effective dispersion of Al₂O₃ inorganic phases. The addition of coupling agent can connect the Al₂O₃ inorganic particles and PAA organic phase through its reactive group then improve the interfacial compatibility between inorganic/organic phases. Further investigation indicates that the transmittances of the PI/modified-Al₂O₃ by coupling agent KH560 has a highest value among these four samples when the wavelength of UV is in the range of 500~600 nm. It can possibly attribute to the better interface combination of PI/Al₂O₃ hybrid films modified by coupling agent KH560 than the other three composites.

3.4. Thermal Stability of PI/Al₂O₃ Hybrid Films. The TGA analysis was examined to evaluate the thermal stability of the PI/Al₂O₃ hybrid films without and with coupling agents. Results are shown in Figure 4 and Table 2. It can be found

TABLE 1: Mechanical properties of PI composite films.

Samples	PI/unmodified Al ₂ O ₃	PI/unmodified with KH550	PI/unmodified with KH560	PI/unmodified with AE3012
Tensile strength (MPa)	104.3	119.1	108.5	107.5
Elongation (%)	10.7	19.1	10.9	11.6

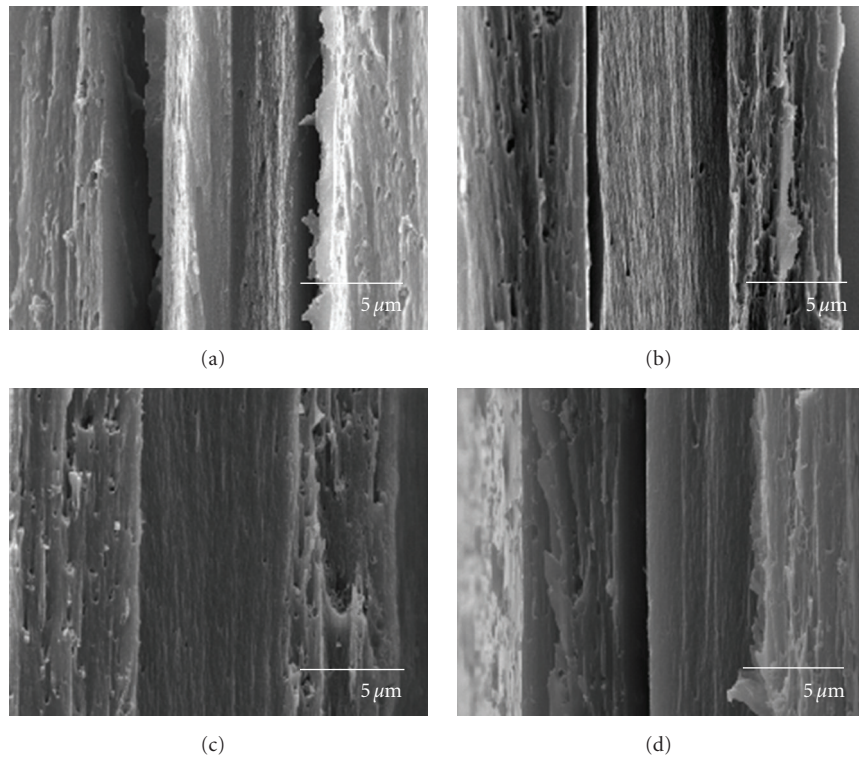


FIGURE 1: SEM images of the cross-section of PI/Al₂O₃ hybrid films: (a) PI/unmodified Al₂O₃ film; (b) PI/modified Al₂O₃ film with KH550; (c) PI/modified Al₂O₃ film with KH560; (d) PI/modified Al₂O₃ film with AE3012.

that the thermal stability of PI films with modified-Al₂O₃ addition is better than that of PI/unmodified-Al₂O₃ hybrid film. This superior in thermal stability of PI/modified-Al₂O₃ also indicates a rather good compatibility between the inorganic particles and the organic matrix by using the coupling agents to modify the inorganic particles, resulting in the occurrence of hydrogen bonds or other coordination bonds between PI and Al₂O₃ inorganic particles. These coordination bonds prevent the thermal motion of PI molecular and the breakdown of the polymer molecular chains, resulting in the increase of the breaking energy during the heating process and the improvement on thermal stability of the PI/Al₂O₃ hybrid films. Table 2 also indicates that the PI/Al₂O₃ composite film modified by KH550 has the highest value in decomposition temperature, about 624.7°C, among these four kinds of composites when 10wt.% mass loss is reached. This also can be attributed to the formation of some coordination bonds between the group of -NH₂ in the KH550 and the acid anhydride groups or the carboxyl group in PAA molecular chain, which cause the improvement in thermal decomposition temperature of the composite.

3.5. Mechanical Properties of PI/Al₂O₃ Hybrid Films. The mechanical properties of PI/Al₂O₃ hybrid films with different coupling agent (KH550, KH560, and AE3012) are examined and the results are listed in Table 1. It can be found that all of the tensile strength and the elongation at break of PI/modified-Al₂O₃ hybrid films are higher than that of the PI/unmodified-Al₂O₃ films. Table 1 also indicates that the tensile strength and the elongation at break of PI/Al₂O₃ hybrid films modified by KH550 are 119MPa and 19.1%, respectively, both of which are the best among these four samples. This can be attributed to the formation of some coordination bonds between the -NH₂ structure of coupling agent KH550 and the PAA or the nano-Al₂O₃ surface, such as Al-O-Si bonds and the hydrogen bond. The formation of these two linkages leads to form the strong single molecular interfacial layers between PI matrix and Al₂O₃ particles [14, 15]. The formation of these strong single molecular interfacial layers effectively improve the interactions between PI molecular and Al₂O₃ particles then increase the bonding strength between matrix and fillers, resulting in the increase in stiffness of PI composites.

TABLE 2: Thermal decomposition temperature of samples under nitrogen atmosphere.

Samples	T ₀ (°C)	T ₁₀ (°C)	T ₃₀ (°C)
PI/unmodified Al ₂ O ₃	597.8	617.4	679.9
PI/modified Al ₂ O ₃ with KH550	604.3	624.7	687.0
PI/modified Al ₂ O ₃ with KH560	601.6	622.3	698.9
PI/modified Al ₂ O ₃ with AE3012	599.3	623.5	682.2

^aT₀: the initial decomposition temperature. ^bT₁₀: the decomposition temperature at 10wt% weight loss. ^cT₃₀: the decomposition temperature at 30wt% weight loss.

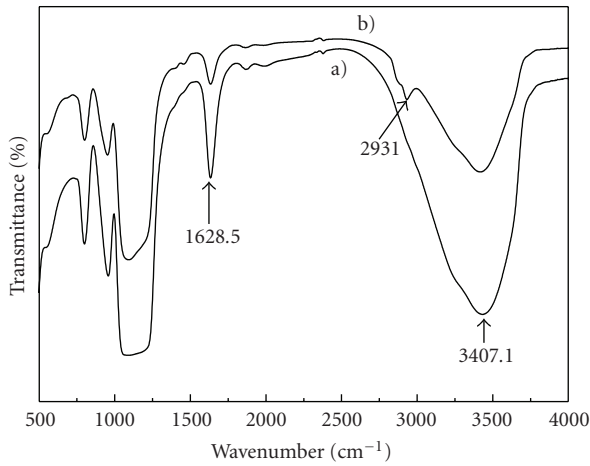


FIGURE 2: FT-IR spectra of nano-Al₂O₃ particles before and after treatment by coupling agent KH560.

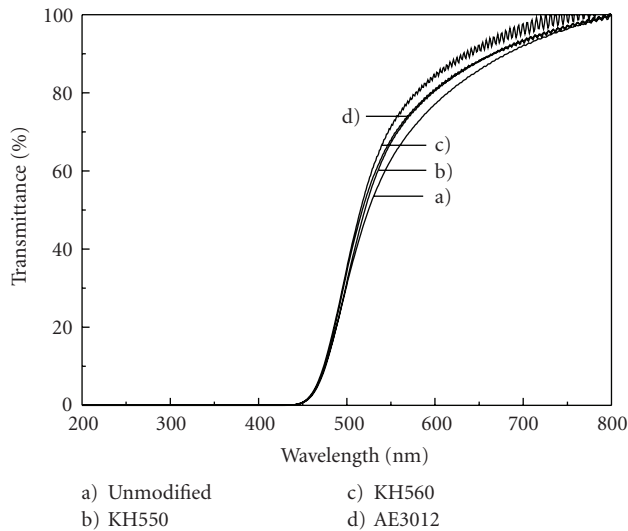


FIGURE 3: UV-Vis spectra of PI/Al₂O₃ hybrid films with different coupling agents.

3.6. Electric Breakdown Strength of PI/Al₂O₃ Hybrid Films.

Being a key parameter, the electrical breakdown strength is widely used to measure the insulating capability of the dielectrics, because breakdown would cause short circuit which could be a fatal malfunction for the power equipment

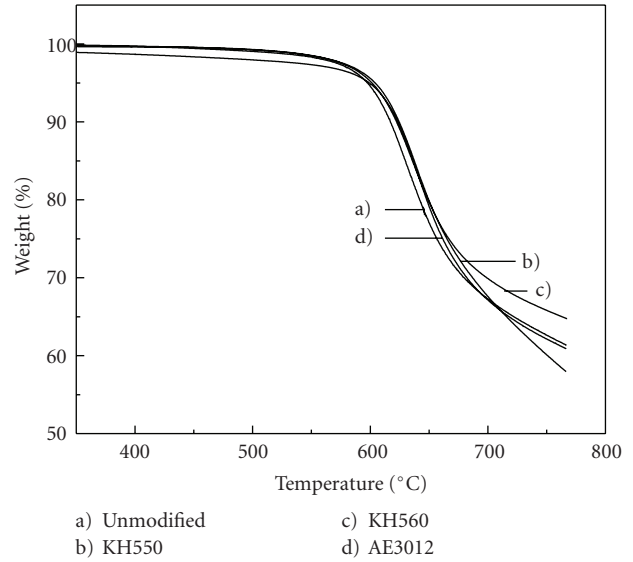


FIGURE 4: TGA curves of PI/Al₂O₃ hybrid films with different coupling agents.

[9, 16]. Figure 5 shows the average electric breakdown strength of the PI/Al₂O₃ hybrid films with different coupling agent varieties. It can be found that all of the average electric breakdown strengths of the PI/Al₂O₃ hybrid films are over 260 kV/mm. Moreover, Figure 5 also indicates that the average electric breakdown strengths of PI-modified Al₂O₃ hybrid films are higher than that of PI-modified Al₂O₃ hybrid film. Combining with the SEM microstructural analysis, we could attribute this better antielectric breakdown properties of PI/modified Al₂O₃ hybrid films to a better homogenous microstructures and a fewer structure defects than PI/unmodified Al₂O₃ film.

Further study indicates that among the PI hybrid films added with three kinds of Al₂O₃ particles modified by KH550, KH560, and AE3012, respectively, the average electric breakdown strength of PI/modified Al₂O₃ with AE3012 is the highest, which is as high as 290 kV/mm. This can be attributed to the homogeneously dispersion of nano-Al₂O₃ particles in the PI matrix.

4. Conclusions

In this work, a series of PI/Al₂O₃ hybrid films is prepared by ultrasonic-mechanical method. The nano-Al₂O₃

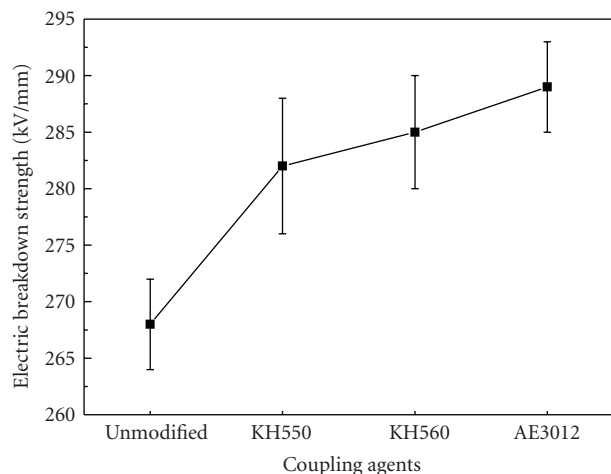


FIGURE 5: Average electric breakdown strength of the PI/Al₂O₃ hybrid films with different coupling agents.

particles are firstly modified by different coupling agents then dispersed homogenously in polyamic(acid) by some modes under the assistant of ultrasonic wave. Results of microstructure and performance analysis indicate that the coupling agents have a great effect on the microstructure of the PI/Al₂O₃ hybrid films. The usage of coupling agent can effectively improve the compatibility and the homogenous dispersion of nano-Al₂O₃ particles in PI matrix. Results also indicate that the PI/Al₂O₃ hybrid film modified by KH550 has the best of thermal stability and mechanical properties, while the PI/Al₂O₃ hybrid film modified by AE3012 has the highest of average electric breakdown strength.

Acknowledgments

This paper was supported by the Nation Science Foundation Grant (50137010) and the Heilong Jiang Science Foundation Grant (E200907).

References

- [1] L. Mascia and A. Kioul, "Influence of siloxane composition and morphology on properties of polyimide-silica hybrids," *Polymer*, vol. 36, no. 19, pp. 3649–3659, 1995.
- [2] X. Jiang, Y. Bin, and M. Matsuo, "Electrical and mechanical properties of polyimide-carbon nanotubes composites fabricated by in situ polymerization," *Polymer*, vol. 46, no. 18, pp. 7418–7424, 2005.
- [3] L. Rubia, F. S. Vasconcelos, and L. Wander, "Synthesis of titania-silica materials by sol-gel," *Materials Research*, vol. 5, pp. 1516–1439, 2002.
- [4] S. Al-Kandary, A. A. M. Ali, and Z. Ahmad, "Morphology and thermo-mechanical properties of compatibilized polyimide-silica nanocomposites," *Journal of Applied Polymer Science*, vol. 98, no. 6, pp. 2521–2531, 2005.
- [5] V. A. Bershtein, L. M. Egorova, and P. N. Yakushev, "The polyimide molecular," *Macromolecular Symposia*, vol. 46, p. 9, 1999.
- [6] J. Qin, H. Zhao, R. Zhu, X. Zhang, and Y. Gu, "Effect of chemical interaction on morphology and mechanical

properties of CPI-OH/SiO₂ hybrid films with coupling agent," *Journal of Applied Polymer Science*, vol. 104, no. 6, pp. 3530–3538, 2007.

- [7] P. Musto, M. Abbate, M. Lavorgna, G. Ragosta, and G. Scarinzi, "Microstructural features, diffusion and molecular relaxations in polyimide/silica hybrids," *Polymer*, vol. 47, no. 17, pp. 6172–6186, 2006.
- [8] Y. J. Tong, Y. S. Li, and M. X. Ding, "Characterization of polymer systems based on sulfonated poly(2,6-dimethyl-1,4-phenylene oxide)," *Polymer International*, vol. 49, no. 11, pp. 1534–1538, 2000.
- [9] H. Li, G. Liu, B. Liu, W. Chen, and S. Chen, "Dielectric properties of polyimide/Al₂O₃ hybrids synthesized by in-situ polymerization," *Materials Letters*, vol. 61, no. 7, pp. 1507–1511, 2007.
- [10] A. M. Lowman and N. A. Peppas, "Molecular analysis of interpolymer complexation in graft copolymer networks," *Polymer*, vol. 41, no. 1, pp. 73–80, 2000.
- [11] L. Lizhu, L. Bing, W. Wei, and L. Qingquani, "Preparation of polyimide/inorganic nanoparticle hybrid films by sol-gel method," *Journal of Composite Materials*, vol. 40, no. 23, pp. 2175–2183, 2006.
- [12] B. Zhao and B. L. N. Rao, "Preparation and properties of polyimide/inorganic phase hybrid films," *Chemistry of Materials*, vol. 34, p. 37, 2006.
- [13] H. Cai, F. Yan, Q. Xue, and W. Liu, "Investigation of tribological properties of Al₂O₃-polyimide nanocomposites," *Polymer Testing*, vol. 22, no. 8, pp. 875–882, 2003.
- [14] L. Gao, J. Sun, and Y. Q. Liu, *The Review of Coupling Agents*, Chemical Industry Press, China, 2003.
- [15] Y. Q. Li, Y. H. Zhang, M. Li, and S. Y. Fu, "The preparation and electric properties of polyimide composites," *Chinese Synthesis Research and Plastic*, vol. 21, p. 63, 2004.
- [16] R. Magaraphan, W. Lilayuthalert, A. Sirivat, and J. W. Schwank, "Preparation, structure, properties and thermal behavior of rigid-rod polyimide/montmorillonite nanocomposites," *Composites Science and Technology*, vol. 61, no. 9, pp. 1253–1264, 2001.

Research Article

Thermal and Mechanical Properties of Chitosan/SiO₂ Hybrid Composites

F. Al-Sagheer and S. Muslim

Department of Chemistry, Kuwait University, Faculty of Science, P.O. Box 5969, 13060 Safat, Kuwait

Correspondence should be addressed to F. Al-Sagheer, f.alsagheer@ku.edu.kw

Received 31 August 2009; Accepted 1 December 2009

Academic Editor: Gaurav Mago

Copyright © 2010 F. Al-Sagheer and S. Muslim. This is an open access article distributed under the Creative Commons Attribution License, which permits unrestricted use, distribution, and reproduction in any medium, provided the original work is properly cited.

Chitosan-silica (CSSi) hybrid films have been fabricated by sol-gel process using tetraethoxysilane (TEOS) as precursor. The structure of the resulting hybrid has been characterized by Fourier transform infrared spectroscopy (FTIR). Fracture surface has been revealed through a field emission-scanning electron microscopy/energy dispersive spectrometer (FE-SEM/EDS) to probe the dispersion degree and the size of SiO₂ particle. Study of morphology using a SEM micrograph and the High Resolution Transmission Electron Microscopy (HRTEM) images of the nanocomposite films suggests that the SiO₂ nanoparticles are within the range of 2–7 nm in diameter and are uniformly dispersed in the polymer matrix. Thermal properties of these composite materials have been studied as a function of silica, indicating that thermal stability of the chitosan film is enhanced. Dynamical mechanical thermal analysis (DMTA) has been carried out to measure the shift in the glass transition temperature (T_g) of the composites from the maxima of the α transition curves. The glass transition temperature and the storage modulus show an increase with increasing silica content. The maximum increase in the T_g value, that is, 159.37°C, is seen with 30 wt% silica. A gradual increase of 3.0 GPa in the modulus relative to the pure polymer is observed.

1. Introduction

Bio-nanohybrid materials are part of an interdisciplinary field between Life Sciences, Material Sciences, and Nanotechnology. They are gaining importance in areas such as biosensors, structural materials, catalysts, separation methods [1], and regenerative medicine [2].

Chitosan is a biopolymer derivative of chitin, a polysaccharide found abundantly in nature in crustacean exoskeletons of crab, shrimp, and lobster as well as in cuttlebone of cuttlefish. It is a linear chain of linked 2-acetoamido-2-deoxy- β -D-glycopyranose units. Chitosan possesses unique functional and biomedical properties. It is biodegradable, biocompatible, nontoxic, heat resistant showing adsorption properties and is easily accessible by recovering from marine waste [3]. It is especially attractive due to its film forming characteristic and finds multiple uses in applications of coatings, drug delivery, nutrients, controlled release of food ingredients, separation techniques, optical material, and so forth.

Organic/inorganic hybrids exhibit characteristics of both organic polymers and ceramics [4, 5]. These are easily produced through sol-gel chemistry [6–8] which is a very versatile method allowing incorporation of inorganic component like metal alkoxide namely, Si [9, 10], Ti [11, 12], Zr [13] or even bioactive materials to modify final chemical and physical properties of materials at low processing temperatures. The narrower distribution of particles and the reduced particle size due to in situ development of the metal oxide network leads to better strength and increased glass transition temperatures.

Chitosan which has hydroxyl and amine functional groups rapidly bonds to other groups. Thus the silicon precursor shows quick in situ development of the silica network in the presence of ethanol and water via the sol-gel route forming glassy, homogeneous and transparent films compatible over a wide composition range [14]. It is therefore expected that chitosan/silica hybrids should have increased interfacial interaction, greater ceramic nature, and

improved thermal, mechanical, optical and adsorbing properties. Chitosan is soluble in weak organic acid which renders it unsuitable for adsorbing in an acidic environment. Many studies have been conducted using chitosan or chitosan adsorbed onto conventional silica for metal ion removal and chelating agent. Lai et al. [15] prepared chitosan silica thick films with in situ silica from zero to hundred percent silica via the sol-gel process, to investigate the interfacial interaction of the two phases and its capability to chelate Cu(II) and Fe(III) to a large degree under wide environmental variation.

Attempts to arrive at an accurate glass transition temperature and effect of DDA on the T_g has been studied in the past, but information on the change in viscoelastic behavior of composites due to reinforcement has been wanting. In the present study, transparent chitosan-silica (CSSi) hybrid films with various silica contents have been prepared via in situ incorporation of silica by the sol-gel process at room temperature. These composites have been characterized for their viscoelastic nature, thermal stability, and optical sensitivity. Their modified morphology has been studied through X-ray mapping and SEM to show the nature of the nanophase silica particles and their homogeneous distribution.

2. Experimental

2.1. Materials. Practical grade chitosan (CS) was obtained from Aldrich. The Brookfield viscosity provided by the supplier was >200.00 cps. Tetraorthosilicate (TEOS) from Aldrich had purity of 98%. All other chemicals were of analytical grade and used as such.

2.2. Preparation of the Hybrid Films. Chitosan was dissolved in 2% acetic acid deionized aqueous solution to produce a 2 wt% chitosan solution. This solution was stirred for 48 hours at room temperature to form a homogeneous mixture. Required amount of this solution was taken in a 50 mL bottle, and measured amount of TEOS was added to it. This was stirred for 1 hour at room temperature. Stoichiometric amount of an equal mixture of ethanol and water was added to the solution and allowed to stir for 18 hours at room temperature. The water to TEOS ratio was 1 : 4. The solution was cast in Teflon petri dishes and dried at 50°C for 17 hours. The films were then dried under vacuum for another 48 hours at 50°C. Flexible chitosan-silica (CS-Si) hybrid films of 5, 10, 20, and 30 wt% silica were prepared.

2.3. Characterization of the Hybrid Films. Fourier Transform Infrared spectroscopy (FTIR) spectroscopic analysis was carried out on Perkin-Elmer FTIR-2000 spectrophotometer to monitor the physical bonding between the CS polymer matrix and silica network formation in the sol-gel process. The morphology of the hybrid films was studied using field emission scanning electron microscopy model *Leo Supra 50VP FESEM*. The films were fractured with liquid nitrogen, sputter coated with gold by means of Balzer's SCD 050 sputter coater, and mounted on aluminum mounts before analysis. Cross-sectional view of the hybrids was studied to

determine the modification in morphology. Samples prepared in the similar manner were then subjected to Elemental X-ray Microanalysis which was conducted using a JSM-6300 J scanning electron microscope which was attached to an Energy Dispersive X-ray Spectroscopy operated at 20 kV for analyzing material science specimens. Samples of 10% and 20% silica loading were degraded at 430°C for 9h to ensure that all the organic matter had decomposed, prior to imaging in HRTEM. The microscope used was JEOL's HRTEM-3010 equipped with a 300 kV electron gun. UV-vis spectroscopic analysis was carried out on Varian Cary 5. Absorption was measured in the 400–800 nm range. The dynamic mechanical thermal analysis (DMTA) on the hybrid films was carried out using DMA Q-800 (TA, USA). The measurements of storage modulus and $\tan \delta$ were made under tension mode in the temperature range 50–210°C at heating rate of 2°C/min using a frequency of 2 Hz under inert atmosphere. Thermogravimetry (TG) was performed on a 10 mg sample from ambient to 800°C at a heating rate of 10°C/min in a dynamic (30 mL/min) synthetic air atmosphere using TGA-50 Shimadzu automatic analyzer.

3. Results and Discussion

3.1. Structural Characterization. The interaction between chitosan and TEOS suggested the formation of hydrogen bonds between amide groups of chitosan and silanol groups, ionic bonds between chitosan amino groups and silanol groups, and covalent bonds due to esterification of chitosan hydroxyl groups on silanol groups of silica network [1]. Schematic suggestion of the CS-Si hybrid preparation is represented in Figure 1.

FTIR analysis was carried out to observe the interaction between the polymer matrix and the silica network formation. The spectra for the pristine CS and its hybrid composite with 20 wt% silica are shown in Figures 2 and 3. Characteristic absorbance for CS shows the Amide I (C=O) stretch at 1645 cm^{-1} , C-N stretch at 1616 cm^{-1} and at 1576 cm^{-1} ; the bending due to Amide II (N-H) is evident. The C-H bond interaction due to Amide II is clear with the band at 1402 cm^{-1} . C-O-C antisymmetric stretching is seen at 1152 cm^{-1} , and the C-O skeletal stretch characteristic of polysaccharides is observed at 1060 and 1084 cm^{-1} . The N-H control band for the amide vibration is seen as a single peak at 3249 in Figure 3. The incorporation of in situ silica shows an overall reduction in intensity including in the N-H regions, also shifting the peak to a slightly lower frequency and marking the increased interfacial interaction between the matrix and the inorganic phase. The appearance of the new absorption band at 969 cm^{-1} related to the Si-OH bonds is observed due to formation of H-bonds between silanol groups of silica network and amide- and oxy-groups of chitosan. The broad shoulder due to Si-OH also appears in the region of 3300–3370 cm^{-1} [16]. This region also overlaps the influence of phase interaction on the amine groups which show a clear band at 3334 cm^{-1} in pristine chitosan. A broad and strong band appears in the region between 3400 and 3200 cm^{-1} due to hydrogen bonding. This is evident in

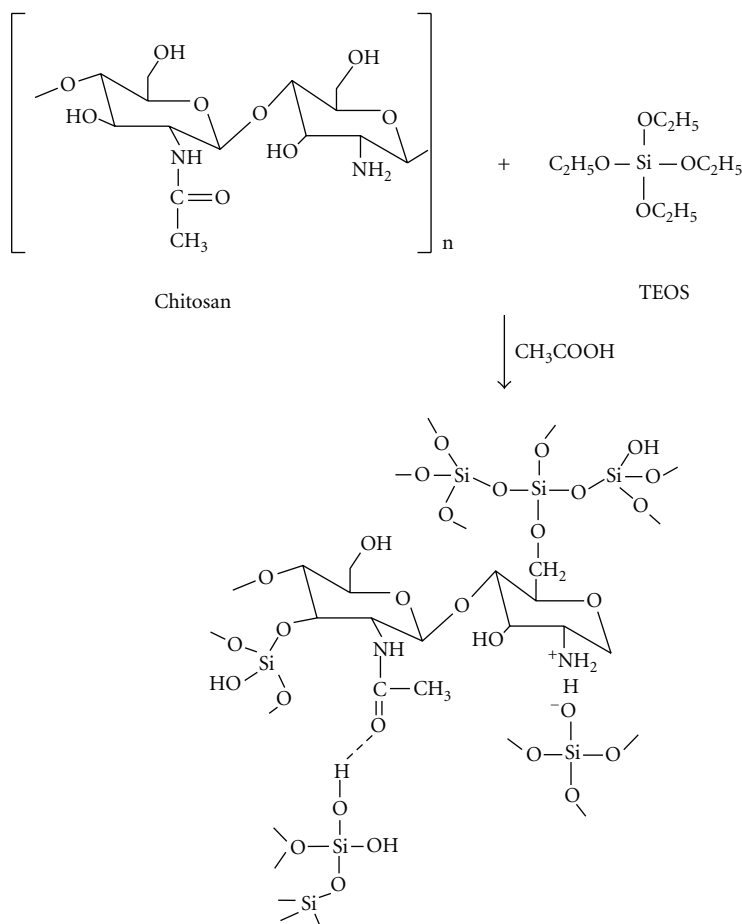


FIGURE 1: Schematic representation for preparation of chitosan siloxane (CS-Si) hybrids.

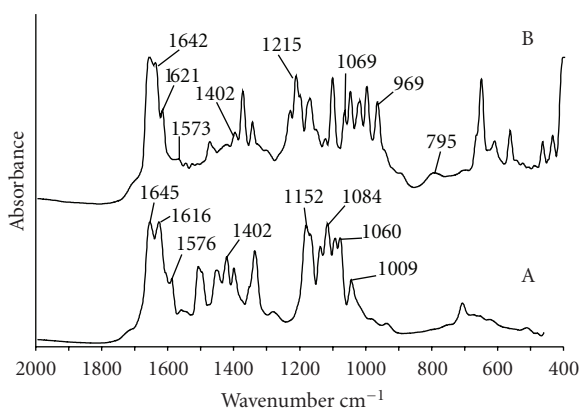


FIGURE 2: FTIR spectra for A: pristine chitosan, B: CS-Si 20%.

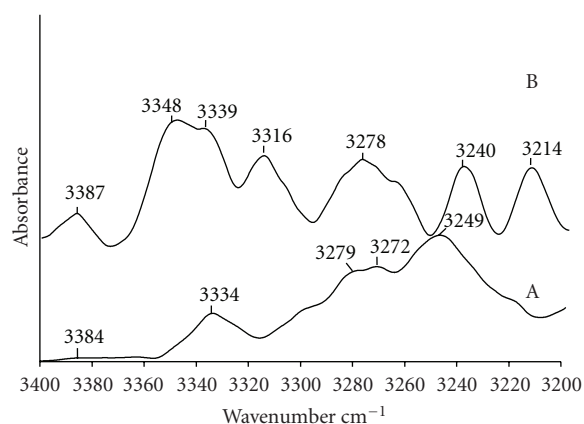


FIGURE 3: FTIR spectra for A: pristine chitosan, B: CS-Si 20%.

Figure 3 in the region of the broad and pronounced peak of 3278 cm^{-1} where interaction between the carbonyl group of chitosan and the silica network occurs. Specific bands in the region of $1000\text{--}1250\text{ cm}^{-1}$ [17] showing characteristic absorption for Si-O-Si are clearly seen in the modified system. The appearance of the Si-O-C bands at 1069 cm^{-1} and at 795 cm^{-1} is seen in the hybrid film spectra which

are not visible in the pure spectra indicating that there is a definite interaction between the phases.

3.2. Morphological Studies. The FE-SEM micrograph of fractured surfaces of hybrids with 10 and 20 wt% silica is shown in Figure 4. The silica particles are in the form of white round beads, and their dispersion within the matrix is clearly

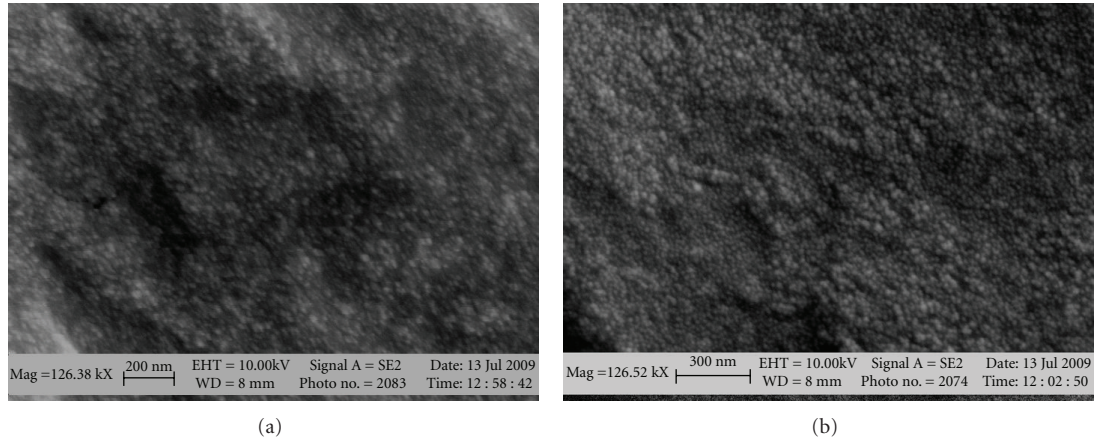


FIGURE 4: High magnification FE-SEM micrographs for CS-Si hybrid films with silica contents wt% (a) 10, (b) 20.

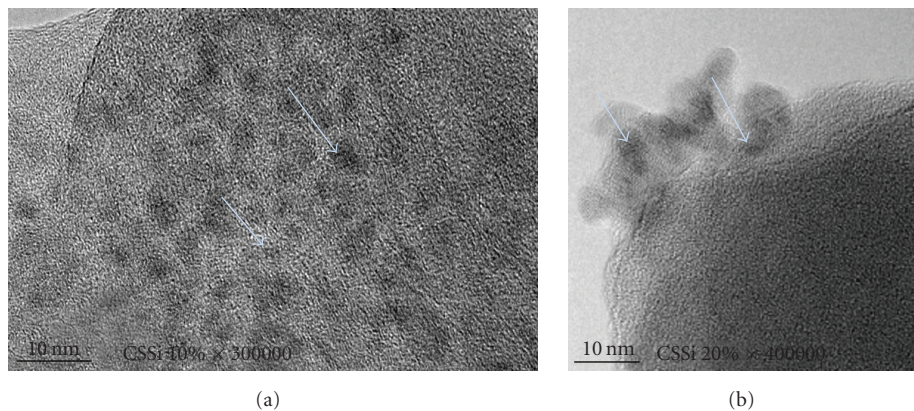
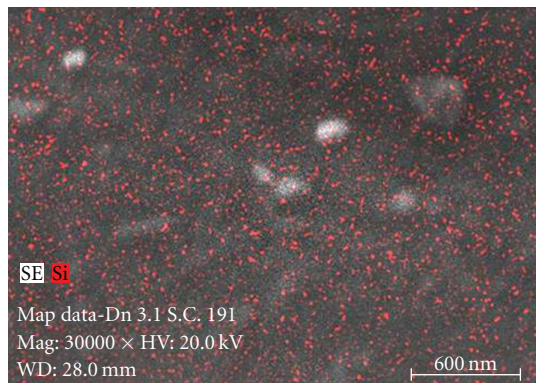


FIGURE 5: High Resolution Transmission Electron Microscopy images showing the individual particle size for CS-Si composites with (a) 10% and (b) 20% silica loading.

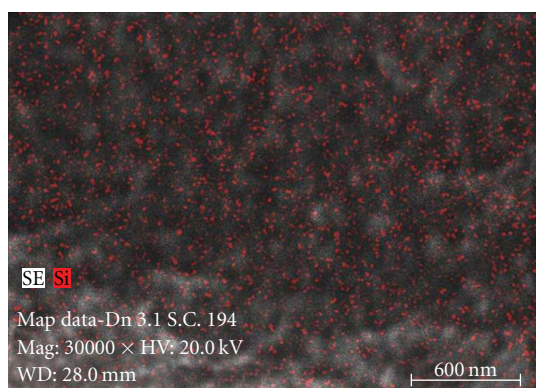
visible. The size of the individual silica particle within the hybrid films approximately ranges from 2 to 7 nm which is confirmed by the HRTEM results as depicted in Figure 5. As the concentrations of SiO_2 increase, the uniform and dense structure of silica in the polymer matrix is clearly observed in hybrids. This explains the interfacial interaction within the matrix and the clear, successful dispersion of the reinforcement material. Figure 6 presents the Si-mapping analysis of the hybrid membrane. The electron beam penetrates 2-3 microns below the surface of sample to reveal the embedded silica distribution. The bright spots representing the silicon element clearly reflect a homogeneous distribution of silica in CS polymer domains. The nanometer level dispersion of silica in chitosan also indicates that there should also be an influence on the mechanical and thermal properties of the polymer.

3.3. Optical Properties. Figure 7 shows the increasing nature of UV-vis light absorbance by the hybrid films in proportion to silica content. The absorbance values of the pure and hybrid CS-Si films tested for transparency via UV-Vis

spectroscopy in the 400–800 nm range are tabulated in Table 2. Transparency of films usually varies due to varying thicknesses. Films in the range of 0.85 ± 0.03 mm have been measured. The pure film is almost transparent with absorbance closest to zero at 0.067. It decreases further in the 800 nm range to show greater transparency at 0.049. Since the composite films have almost comparable thicknesses, the variation in absorbance is due to the spatial distribution and the size of the silica particles in the matrix. In the 5% CS-Si composite, the size of the ceramic particle is still smaller than the wavelength of light thus permitting light to transmit more easily. Also the distribution of the network is more uniform and homogeneous. With an increase in silica content the network becomes more extensive and bulky causing the smaller particles to agglomerate reducing the overall homogeneity of the system. As the size of the particles increases and the distribution is more overlapped, the absorbance increases as is evident in the 20% CS-Si hybrid result. Thus the pure film is more transparent when compared to the 20% hybrid film which is almost opaque. The films are off white in color.



(a)



(b)

FIGURE 6: Elemental X-ray mapping of CS–Si hybrids silica wt%; (a) CS–Si, 10%; (b) CS–Si, 20%.

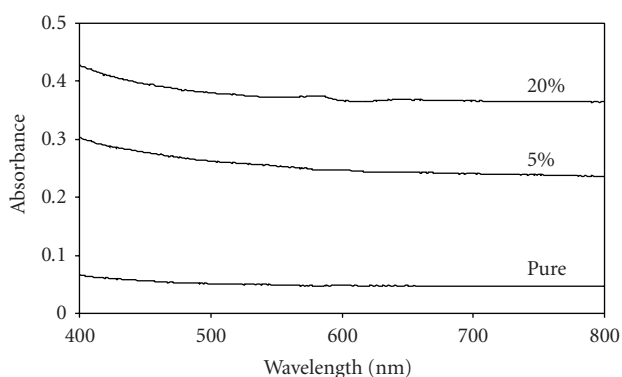


FIGURE 7: UV–visible spectra for the CS–Si hybrids.

3.4. Viscoelastic Properties. The variation in dynamical mechanical thermal properties of the CS–Si hybrids has been studied to determine the change in glass transition temperature and the viscoelastic stability of the polymer on incorporation of the silica enhancement. The storage modulus (E') of the polymer increases with the increase in

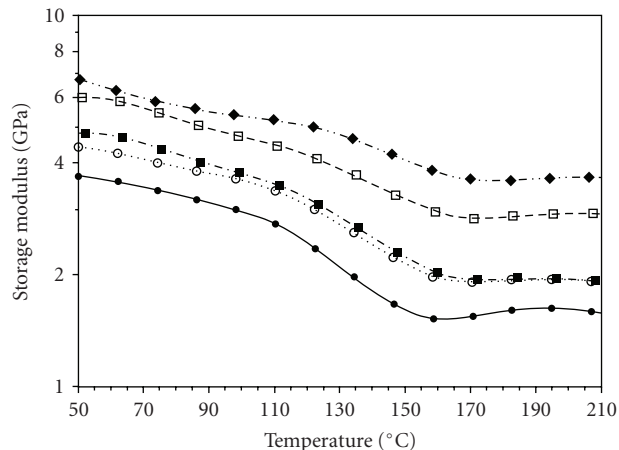


FIGURE 8: Temperature variation of storage modulus for CS–Si nanocomposites at 2 Hz. Silica wt% 0 (•), 5 (○), 10 (■), 20 (□), 30 (◆).

TABLE 1: Viscoelastic properties of chitosan-silica hybrids.

SiO ₂ (wt%)	CS–Si hybrids		
	Storage modulus (GPa) at 50°C	T_g (°C)	Tan delta (δ)
0	3.67	152	0.15
5	4.42	154	0.14
10	4.82	156	0.11
20	6.00	157	0.094
30	6.70	159	0.083

silica content, and its temperature variation is depicted in Figure 8. The storage modulus at 50°C is 3.67 GPa for the pure polymer and increases to 6.70 GPa for the 30% CS–Si hybrid film. Initially with the increase in temperature, the storage modulus drops linearly in the rubbery region from 110°C till 150°C for the pure polymer. The rate of decrease is considerably lower for hybrids with silica in this region. Increasing the temperature increases the segmental motion of the polymer and there is a sharp increase in $\tan \delta$ which corresponds to the α relaxation temperature associated with the glass transition temperature T_g (Figure 9). In the pure polymer this is seen at 152°C, and enhanced polymer silica interaction causes it to reach 159°C for the 30% CS–Si composite. The addition of silica restricts the mobility of the chains, and thus the glass transition temperature increases. But effectively the loss factor ($\tan \delta$) reduces, which is the ratio of the loss modulus to the storage modulus, showing enhanced ceramic nature of the polymer hybrids (Figure 10). The value of $\tan \delta$ progressively decreases from 0.15 for the pure polymer to 0.08 for the 30% CS–Si composite. The viscoelastic data is presented in Table 1.

3.5. Thermogravimetric Analysis of Nanocomposites. To study the effect of silica reinforcement on thermal stability of the CS nanocomposites, thermogravimetric analysis was carried out under synthetic air in the temperature range of 50–750°C

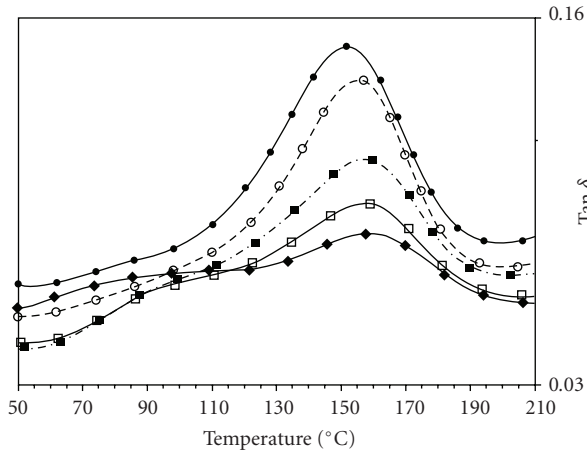


FIGURE 9: Temperature variation of $\text{Tan } \delta$ for the CS-Si nanocomposites at 2 Hz. Silica wt% 0 (\bullet), 5 (\circ), 10 (\blacksquare), 20 (\square), 30 (\blacklozenge).

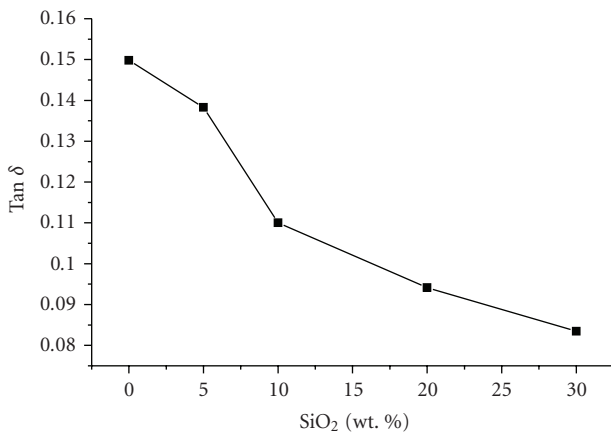


FIGURE 10: Variation of $\text{Tan } \delta$ with silica content for CS-Si hybrids.

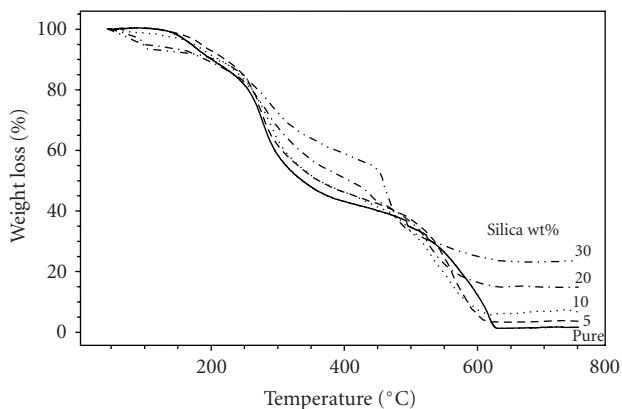


FIGURE 11: Thermogravimetric curves for the CS-Si nanocomposites showing various silica contents.

TABLE 2: UV-vis absorbance for the CS-Si hybrids.

CS-Si films	400 nm	600 nm	800 nm
Pure	0.067	0.049	0.049
5%	0.338	0.264	0.246
20%	0.358	0.284	0.266

(Figure 11). The initial weight loss observed between 100 and 160°C appears to be due to the loss of absorbed water on the surface of chitosan and side product of subsequent condensation of the Si-OH groups [18]. Chitosan shows slower weight loss in the region between 160°C and 270°C due to the decomposition of low molecular weight species. Thermal decomposition is more marked in the region between 170°C and 450°C relating to the complex dehydration of the saccharide rings, depolymerization, and decomposition of the acetylated and deacetylated units of the polymer [19]. Incorporation of silica network and its interaction with the polymer increases the thermal resistance of the hybrids and consequently the thermal decomposition temperature. The mass of residue retained at 750°C corresponds to the amount of silica content incorporated in the hybrids indicating that the sol-gel reaction was successful.

4. Conclusions

Chitosan-based silica hybrids have been prepared by the sol-gel process. Both organic and inorganic phases show increased interfacial interaction which is depicted in the FTIR spectra. The absorbance is proportional to the increase in silica content which is clear in the UV-vis range. Field emission scanning electron microscopy, high resolution transmission electron microscopy, and elemental X-ray mapping clearly depict the nanodimensional morphology of the particles in the matrix and a very homogeneous distribution throughout the matrix with a particle size in the range of 2–7 nm. The glass transition temperature and storage modulus (E') determined through DMTA indicate better cohesion between the phases, and the shift to higher temperature suggests increased interfacial interaction and an increase in the ceramic nature of the polymer due to a decrease of the area under the curve seen in the $\text{tan } \delta$ values. The thermal stability of the composites increases with the increase in silica concentration and the residue corresponds to the content used for reinforcement suggesting that the sol-gel reaction is complete.

Acknowledgments

The authors wish to acknowledge the Research Administration for financial support provided under Project SC 02/06 by Kuwait University. The technical support from E. M. unit and the general facilities projects GS01/0, GS01/03 under SAF program are also appreciated.

References

- [1] S. Sh. Rashidova, D. Sh. Shakarova, O. N. Ruzimuradov, et al., "Bionanocompositional chitosan-silica sorbent for liquid chromatography," *Journal of Chromatography B*, vol. 800, no. 1-2, pp. 49–53, 2004.
- [2] V. Thomas, D. R. Dean, and Y. K. Vohra, "Nanostructured biomaterials for regenerative medicine," *Current Nanoscience*, vol. 2, no. 3, pp. 155–177, 2006.
- [3] F. A. Al Sagheer, M. A. Al-Sughayer, S. Muslim, and M. Z. Elsabee, "Extraction and characterization of chitin and chitosan from marine sources in Arabian Gulf," *Carbohydrate Polymers*, vol. 77, no. 2, pp. 410–419, 2009.
- [4] H. K. Schmidt, "Organically modified silicates as inorganic-organic polymers," in *Proceedings of the NATO Advanced Research Workshop: Inorganic and Organometallic Polymers with Special Properties*, R. M. Laine, Ed., pp. 297–317, Kluwer Academic Publishers, Boston, Mass, USA, 1992.
- [5] G. Philipp and H. Schmidt, "New materials for contact lenses prepared from Si- and Ti-alkoxides by the sol-gel process," *Journal of Non-Crystalline Solids*, vol. 63, no. 1-2, pp. 283–292, 1984.
- [6] C. J. Brinker and G. W. Scherer, Eds., *Sol-Gel Science: The Physics and Chemistry of Sol-Gel Processing*, Academic Press, New York, NY, USA, 1990.
- [7] J. Wen and G. L. Wilkes, "Organic/inorganic hybrid network materials by the sol-gel approach," *Chemistry of Materials*, vol. 8, no. 8, pp. 1667–1681, 1996.
- [8] L. L. Hench and J. K. West, "The sol-gel process," *Chemical Reviews*, vol. 90, no. 1, pp. 33–72, 1990.
- [9] Z. Ahmad, M. I. Sarwar, and J. E. Mark, "Chemically bonded silica-polymer composites from linear and branched polyamides in a sol-gel process," *Journal of Materials Chemistry*, vol. 7, no. 2, pp. 259–263, 1997.
- [10] Z. Ahmad, M. I. Sarwar, and J. E. Mark, "Dynamic-mechanical thermal analysis of aramid-silica hybrid composites prepared in a sol-gel process," *Journal of Applied Polymer Science*, vol. 63, no. 10, pp. 1345–1352, 1997.
- [11] Z. Ahmad, M. I. Sarwar, and J. E. Mark, "Thermal and mechanical properties of aramid-based titania hybrid composites," *Journal of Applied Polymer Science*, vol. 70, no. 2, pp. 297–302, 1998.
- [12] Z. Ahmad, M. I. Sarwar, S. Wang, and J. E. Mark, "Preparation and properties of hybrid organic-inorganic composites prepared from poly(phenylene terephthalamide) and titania," *Polymer*, vol. 38, no. 17, pp. 4523–4529, 1997.
- [13] H. U. Rehman, M. I. Sarwar, Z. Ahmad, H. Krug, and H. Schmidt, "Synthesis and characterization of novel aramid-zirconium oxide micro-composites," *Journal of Non-Crystalline Solids*, vol. 211, no. 1-2, pp. 105–111, 1997.
- [14] J. Retuert, A. Nuñez, F. Martínez, and M. Yazdani-Pedram, "Synthesis of polymeric organic-inorganic hybrid materials. Partially deacetylated chitin-silica hybrid," *Macromolecular Rapid Communications*, vol. 18, no. 2, pp. 163–167, 1997.
- [15] S.-M. Lai, A. J.-M. Yang, W.-C. Chen, and J.-F. Hsiao, "The properties and preparation of chitosan/silica hybrids using sol-gel process," *Polymer-Plastics Technology and Engineering*, vol. 45, no. 9, pp. 997–1003, 2006.
- [16] Sh. Al-Kandary, A. A. M. Ali, and Z. Ahmad, "Morphology and thermo-mechanical properties of compatibilized polyimide-silica nanocomposites," *Journal of Applied Polymer Science*, vol. 98, no. 6, pp. 2521–2531, 2005.
- [17] Z. Ahmad, F. Al-Sagheer, A. A. M. Ali, and S. Muslim, "Inter-phase bonding in poly(hydroxyamide)-silica hybrids: effect of isocyanato-propyltriethoxysilane addition on the structure and properties," *Journal of Macromolecular Science A*, vol. 44, no. 1, pp. 79–90, 2007.
- [18] S. M. Jones, A. Amran, and S. E. Friberg, "Microemulsion-gel glass containing copper nitrate," *Journal of Dispersion Science and Technology*, vol. 15, no. 4, pp. 513–542, 1994.
- [19] C. Peniche-Covas, W. Argüelles-Monal, and J. S. Román, "A kinetic study of the thermal degradation of chitosan and a mercaptan derivative of chitosan," *Polymer Degradation and Stability*, vol. 39, no. 1, pp. 21–28, 1993.

Research Article

Multiscale Hybrid Micro-Nanocomposites Based on Carbon Nanotubes and Carbon Fibers

Fawad Inam,¹ Doris W. Y. Wong,² Manabu Kuwata,² and Ton Peijs^{1,2,3}

¹ Nanoforce Technology Limited, Joseph Priestley Building, Mile End Road, London E1 4NS, UK

² Centre for Materials Research, School of Engineering and Materials Science, Queen Mary University of London, Mile End Road, London E1 4NS, UK

³ Eindhoven Polymer Laboratories, Eindhoven University of Technology, P.O. Box 40, 5600 MB Eindhoven, The Netherlands

Correspondence should be addressed to Ton Peijs, t.peijs@qmul.ac.uk

Received 30 November 2009; Accepted 16 March 2010

Academic Editor: Frank T. Fisher

Copyright © 2010 Fawad Inam et al. This is an open access article distributed under the Creative Commons Attribution License, which permits unrestricted use, distribution, and reproduction in any medium, provided the original work is properly cited.

Amino-modified double wall carbon nanotube (DWCNT-NH₂)/carbon fiber (CF)/epoxy hybrid micro-nanocomposite laminates were prepared by a resin infusion technique. DWCNT-NH₂/epoxy nanocomposites and carbon fiber/epoxy microcomposites were made for comparison. Morphological analysis of the hybrid composites was performed using field emission scanning electron microscope. A good dispersion at low loadings of carbon nanotubes (CNTs) in epoxy matrix was achieved by a bath ultrasonication method. Mechanical characterization of the hybrid micro-nanocomposites manufactured by a resin infusion process included three-point bending, mode I interlaminar toughness, dynamic mechanical analysis, and drop-weight impact testing. The addition of small amounts of CNTs (0.025, 0.05, and 0.1 wt%) to epoxy resins for the fabrication of multiscale carbon fiber composites resulted in a maximum enhancement in flexural modulus by 35%, a 5% improvement in flexural strength, a 6% improvement in absorbed impact energy, and 23% decrease in the mode I interlaminar toughness. Hybridization of carbon fiber-reinforced epoxy using CNTs resulted in a reduction in T_g and dampening characteristics, presumably as a result of the presence of micron-sized agglomerates.

1. Introduction

From virtually the moment carbon nanotubes (CNTs) were discovered, it was expected that they would display superior mechanical properties as compared to carbon fibers. It has been shown that CNTs can significantly strengthen polymer matrices if the nanotubes are well dispersed, bonded, and aligned [1, 2]. A number of reports have however also shown positive effects of the incorporation of randomly dispersed nanotubes on the crack resistance of polymer resins [3–8]. Gojny et al. [3], for example, reported a 43% increase in the fracture toughness of a standard epoxy resin with the addition of 0.5 wt% amine-functionalized double wall carbon nanotubes. Besides the (often modest) mechanical property improvements, CNTs have been especially successful in improving the electrical properties of polymers. Their combination of good intrinsic conductivity and high aspect-ratio makes them very interesting filler for the creation of

conductive nanocomposites with low percolation thresholds [9–14]. The introduction of such CNT modified resins into already matured carbon fiber-reinforced plastics (CFRP) opens the possibility for the creation of new multifunctional multiscale materials with optimized mechanical, thermal, as well as electrical properties.

Recent interest in multiscale composite materials has often been inspired by nature which is full of interesting biocomposites with multiple hierarchical levels of reinforcement. Bone, for example, is a fascinating multiscale hierarchical composite consisting of macro-, meso-, micro- as well as nanofeatures, all of which are responsible for imparting unique mechanical characteristics such as high stiffness and high toughness. Man-made multiscale micro-nanocomposites offer a route by which multifunctionality, such as enhanced thermal stability, lower coefficient of thermal expansion, and high thermal and electrical conductivity, can be imparted to the fiber-reinforced composite through

an addition level of hierarchy. While fiber-dominated properties of such multiscale hybrid micro-nanocomposites may benefit to some extent from the incorporation of nanoparticles, it is expected that especially resin-dominated properties will benefit the most.

The purpose of hybridization in composites is to extend the concept of tailoring properties to suit requirements and to offset the disadvantages of one component by the addition of another [15–17]. Recent research efforts in this field have focused on properties of hybrid micro-nanocomposites in which dispersed second phase nanoparticles are added to the epoxy matrix [18–32]. Mahrolz et al. [20] reported a significant enhancement in mechanical performance including improvements in stiffness and tensile strength, delamination resistance, and safety factors of their epoxy-based multiscale composites. Mode II fracture behavior of the laminates was examined by Karapappas et al. [18] and an increase was reported in fracture energy of the CFRP doped with 0.5% and 1% CNTs (about 45% and 75%, resp.). Chen et al. [22, 23] prepared an epoxy-silicate nanocomposite using an aerospace grade epoxy resin and carbon fibers and showed higher storage modulus as compared to neat resin properties. Gojny et al. [24] made glass fiber/CNT/epoxy composites and reported an increase in interlaminar shear strength by 20%. Tsantzalidis et al. [25, 26] doped carbon fiber reinforced epoxy laminates with carbon nanofibers (CNFs) and titanate piezoelectric (PZT) particles and reported a 100% increase in fracture energy of laminates with the addition of 1 wt% CNFs. Wichmann et al. [27] developed fumed silica/glass fiber/epoxy, carbon black/glass fiber/epoxy, and CNT/glass fiber/epoxy micro-nanocomposites by resin transfer moulding technique (RTM) and reported a 16% increase in interlaminar shear strength and superior electrical properties as a result of a small addition (0.3 wt%) of CNTs. Chowdhury et al. [28] investigated the effects of nanoclay on the mechanical and thermal properties of woven carbon fiber-reinforced epoxy and reported an 18% and 9% improvement in flexural strength and modulus, respectively, with the addition of 3 wt% nanoclay. Dean et al. reported on the synthesis and fabrication of glass fiber-reinforced composites based on vinyl ester and epoxy nanocomposites, respectively [29, 30]. Qiu et al. [32] improved electrical conductivity and mechanical properties of CFRPs by effective infiltration of CNTs using vacuum-assisted resin transfer molding technique.

Thostenson et al. [33] and Kepple et al. [34] grew CNTs on carbon fibers and embedded these fibers into an epoxy matrix and reported superior interfacial bond strength between the polymer and the CNT-modified carbon fiber. Gou et al. [35] worked on the fabrication of carbon nanofiber-modified glass fiber-reinforced polyester matrix. Vlasveld et al. [36, 37] showed a more than 40% increase in flexural and compressive strength at elevated temperatures with the incorporation of 10 wt% nanoclay in continuous fiber-reinforced thermoplastics. Additional interesting properties of nanocomposite resins for advanced composites reported in literature are a reduced creep rate [37] and coefficient of thermal expansion [38], improved

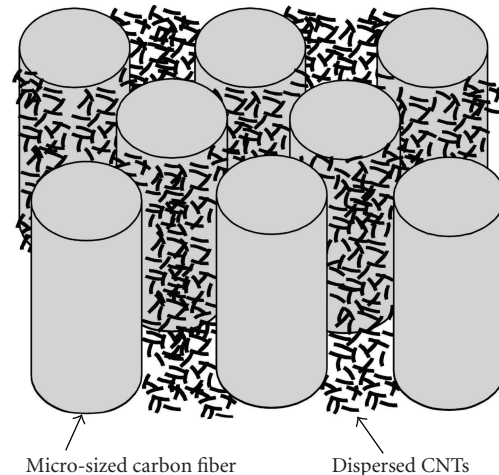


FIGURE 1: Multiscale hybrid micro-nanocomposite based on CNTs and carbon fiber. (adapted from [36]).

barrier properties for gasses and vapors [39, 40], and reduced flammability [37, 41, 42]. Micron-sized carbon fibers coated with aligned CNTs and their derivatives provide an effective means to connect nanoscale entities to the macroscopic world and were shown to possess interesting electrochemical properties attractive for a wide range of potential applications, including methanol direct fuel cells and highly sensitive chemical and biological sensors [43]. Frankland et al. [44] modeled multiscale hybrid micro-nanocomposites based on CNT/carbon fiber/epoxy and indicated that the presence of nanotubes near the surface of carbon fibers can have a small, but positive, effect on the properties of the lamina.

The use of the nanotube-modified epoxies as a matrix system for carbon fiber-reinforced composites has not been fully studied, which is the aim of this study. It is not the aim of this study to replace any continuous carbon fiber with CNTs. However, dispersing them in small amounts in the polymer resin can potentially enhance matrix-dominated properties of these carbon fiber composites (Figure 1). In this work, we prepared multiscale hybrid micro-nanocomposites, based on amino-functionalized double wall carbon nanotubes (DWCNT-NH₂), carbon fiber fabrics, and epoxy matrix.

2. Experimental Details

2.1. Materials. The epoxy matrix used in this study consists of a CYCOM 823 RTM liquid epoxy resin with an aromatic anhydride hardener, supplied by Cytec Engineering Materials Ltd., UK. This epoxy system is a standard resin for the aerospace industry and infusion processes [45]. Plain weave carbon fiber fabric (P1726, 0/90°), with an areal density of 0.445 kg/m², was also obtained from Cytec. Cadek et al. [46] showed that DWCNTs-polymer composites, as compared to other CNTs, give potentially the best balance of properties in terms of dispersibility and mechanical properties for use as reinforcement of polymers. Amino-functionalized CNTs

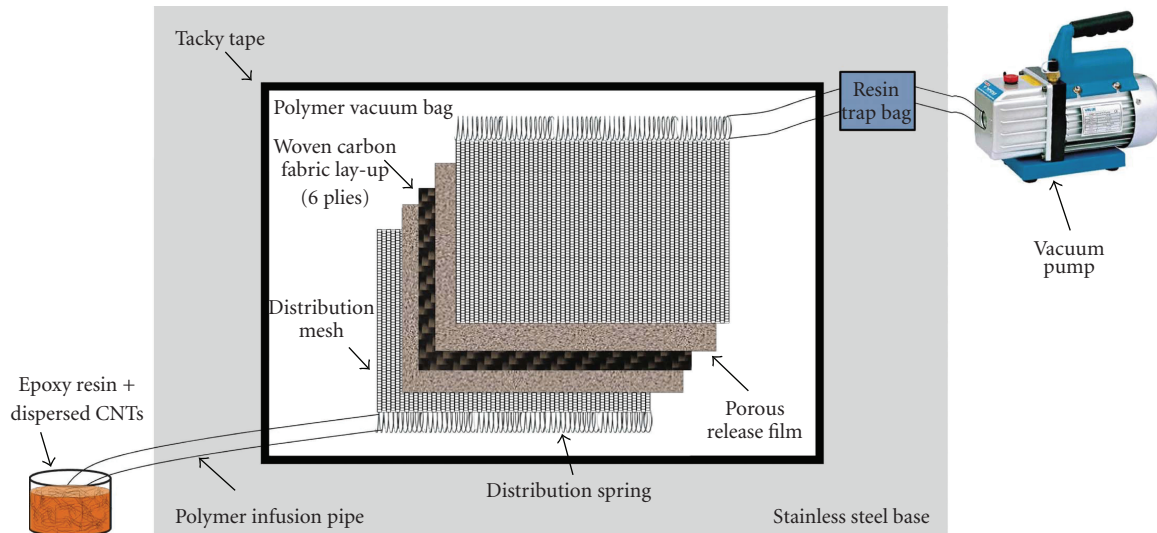


FIGURE 2: Vacuum infusion lay-up sequence.

lead to a more homogeneous distribution in the matrix and a reduced risk for agglomerates, as compared to pristine CNTs [4, 5]. DWCNT-NH₂ (Nanocycl 2152) was supplied by Nanocyl S.A., Belgium. As per supplier, these CNTs were synthesized by CVD method, having diameters of around 4.7 nm, lengths up to several microns, a carbon purity of more than 90%, and a functionalization of less than 0.5%.

2.2. Dispersion Procedure. Three compositions (0.025, 0.05, and 0.1 wt%) of DWCNT-NH₂ were dispersed in the epoxy matrix using a high-power bath ultrasonication (Decon Ultrasonics Ltd, FS Minor, 75 Watts) for five hours. As per authors' previous work [47], this method is highly effective for lower concentrations of CNTs and results in a good level of dispersion. Anhydride hardener (20 wt%) was added after dispersing CNTs in epoxy. The mixtures were extensively hand-mixed for 5 minutes. After degassing (at 50°C/30 mmHg) the suspension for 30 minutes in a vacuum oven, one batch of materials was used to make DWCNT-NH₂/epoxy nanocomposites by an open mould casting method, while a second batch was used for the manufacturing of the hybrid micro-nanocomposites by vacuum infusion technique.

2.3. Open Mould Casting. The homogenized suspensions were slowly poured between two mirror-polished stainless steel plates at an angle (~30°) in a vertical position to prevent entrapment of air bubbles during casting. Demoulding spray (Frekote 44, Hysol, The Dexter Corp.) was applied to the plates before casting for easy separation. The resin was cured at 125°C (heating rate = 1°C/min) for an hour and cooled slowly in an oven to avoid thermally induced matrix cracking. The thickness of the epoxy nanocomposite plates was 3 ± 0.25 mm. No voids and shrinkage marks were observed by the naked eye. The same procedure was employed to make neat epoxy plates.

2.4. Vacuum Infusion. The dispersed mixtures were slowly infused into a vacuum bag containing six plies of woven carbon fabric with a (0/90°) lay-up under a negative pressure (Figure 2). The authors would like to emphasize that even the small amounts of DWCNT-NH₂ employed in this study drastically increased the viscosity of the matrix. To reduce the viscosity and promote fluidity, the colloidal suspension and vacuum infusion stainless steel base was heated to 50°C. The infused lay-up was cured at 125°C (heating rate = 1°C/min) for an hour and slowly cooled in a closed oven to avoid matrix cracking. The thickness of the laminates was 3 ± 0.30 mm. By matrix digestion test [48], the fiber volume fraction and void content was estimated to be 55% and 0.5%, respectively. More details of this process are described elsewhere [28]. The same procedure was followed for making neat carbon fiber-reinforced epoxy laminates without CNTs. A list of specimens prepared is given in Table 1. For the mode I interlaminar fracture toughness testing, the same lay-up and resin infusion procedures were carried out. However, an insert film, made of 12 μm thick PTFE film, was placed in the mid-plane of the lay-up to create a crack opening.

2.5. Mechanical Characterization. Flexural strength was measured in a three-point bending test using an Instron 6025 screw-driven universal tensile testing machine at a cross-head speed of 5 mm/min at room temperature. At least five specimens were tested for each composition. Double cantilever beam (DCB) specimens were prepared for mode I fracture toughness tests according to ASTM D5528-01. The composite specimens were cut to size (120 mm × 20 mm) and a composite material made of glass fiber and epoxy (commonly used for end-tabs) was cut (120 mm × 20 mm) and bonded to both sides of the specimens to increase the flexural rigidity. Piano hinges were bonded to the ends of the specimens, and the distance between the loading points to the end of the insert film (beginning of the crack) was 50 mm. The sides of the specimens were spray painted with

TABLE 1: Samples prepared for this study.

Sample description	Method of preparation	Sample ID	Fiber volume fraction (%)	Void Content (%)
Neat epoxy	Open mould casting	A	—	Negligible
0.025 wt% DWCNT-NH ₂ + epoxy	Open mould casting	B	—	Negligible
0.05 wt% DWCNT-NH ₂ + epoxy	Open mould casting	C	—	Negligible
0.1 wt% DWCNT-NH ₂ + epoxy	Open mould casting	D	—	Negligible
CF + epoxy	Vacuum infusion	E	56.5	0.50
0.025 wt% DWCNT-NH ₂ + CF + epoxy	Vacuum infusion	F	55	0.67
0.05 wt% DWCNT-NH ₂ + CF + epoxy	Vacuum infusion	G	57	0.80

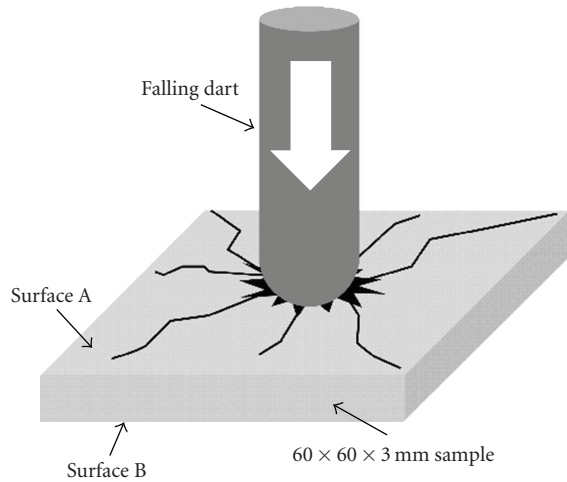


FIGURE 3: Schematics of falling dart impact testing.

a white paint primer, and marking was drawn on the primer for every mm. The sample was loaded in tensile mode in a Hounsfield universal testing machine, at 1 mm/min. Crack growth was observed using a digital microscope and the measurements of load and displacement at corresponding crack length were recorded. The G_{IC} values in this study were calculated using the modified beam theory (MBT) using (1):

$$G_{IC} = \frac{3P\delta}{2b(a + |\Delta|)}, \quad (1)$$

where P is the load, δ is the load point displacement, b is specimen width, a is the delamination length, and Δ is determined experimentally by generating a least square plot of the cube root of compliance, $C^{1/3}$, as a function of delamination length.

Dynamic modulus and viscoelastic response was studied in a DMA Q800 (TA Instruments Ltd., UK) in bending mode at a frequency of 1 Hz. Heating occurred at a rate of 5°C/min and in a temperature range between 30 and 200°C. Flexural properties were measured according to ASTM D 790-03 (sample size = 68 × 12.7 × 3 mm, span-to-depth ratio = 16). Similar size samples were used in DMA.

Energy absorption during impact was measured on flat plates (sample size = 60 × 60 × 3 mm) using a Ceast instrumented dart impact tester (Dart Vis, diameter = 18 mm) fitted with a data acquisition system (Figure 3). The

laminates were clamped between two plates. At least five samples were tested for each composition and were impacted at a fixed initial impact energy level of 6 joules. Ultrasonic C-scan was performed using a jet probe inspection system (Midas-NDT) to measure the damaged area in laminates.

2.6. Field Emission Scanning Electron Microscopy. Small samples were cut from fractured specimens. All samples were gold coated and then transferred to an FE-SEM (FEI, Inspect F, 10 kV) for examination. Gold coating was done to visualize agglomerates rather than individual CNT.

3. Results and Discussion

3.1. SEM Characterization. Using SEM analysis, the interply resin (between 3rd and 4th ply) of the cured laminate was studied to evaluate the level of impregnation of the nanotube modified resin within the carbon fiber plies as well as in between the plies. Figure 4 shows the interply region in the centre of the woven fabric laminate (between 3rd and 4th plies). No clear filtering effect of the carbon fabric on the DWCNT-NH₂ for samples F and G was observed, as was reported in earlier studies [27]. However, for sample H, which contains 0.1 wt% DWCNT-NH₂, there was a clear difference in the clearness of the resin coming out of the suction line, indicating lower nanotube content due to filtering of larger agglomerates present in this resin system by the carbon fabric. It should be noted that due to the large difference in scale, it is not possible to directly observe both DWCNTs-NH₂ and carbon fibers in the same image (see Figures 4(a) and 4(b)). Agglomerates of DWCNT-NH₂ are visible in Figures 4(b) and 4(c) for sample F. The lower viscosity may lead to better wetting of the carbon fibers and dispersion of the DWCNT-NH₂ but a nonuniform distribution of CNT aggregates is observed in Figure 4b. The nonuniform dispersion of DWCNT-NH₂ (Figures 4(a), 4(b), and 4(c)) in between carbon fiber layers should be due to the aggregate nature of CNTs because of their high specific surface area and strong interaction forces between them. Key failure mechanisms in continuous fiber reinforced composites like fiber fracture, fiber pull-out, fiber/matrix debonding, crack bridging (Figure 4(d)), and matrix cracking have also been observed in CNT-modified polymer composites as demonstrated by Thostenson and

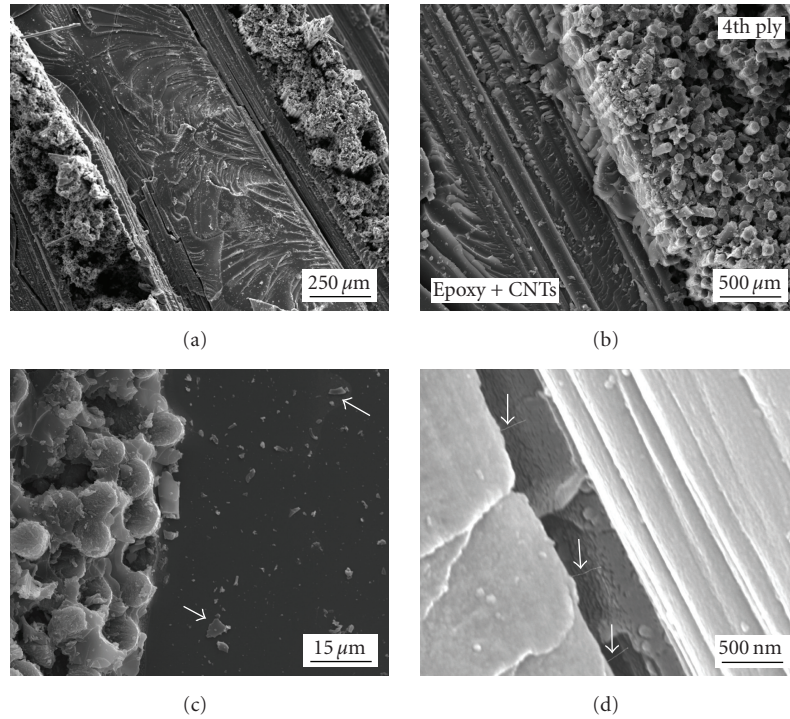


FIGURE 4: FE-SEM images of hybrid (0.025 wt% DWCNT-NH₂) micro-nanocomposites: (a), (b) middle of cured laminate (between 3rd and 4th plies), (c) agglomerates of DWCNT-NH₂ (pointed), and (d) individual DWCNT-NH₂ bridging epoxy matrix (pointed).

Chou [49, 50] and the same is expected for these hybrid micro-nanocomposites.

3.2. Flexural Testing. So far nanotube-filled polymers have not had many industrial successes in which they showed a mechanical property advantage over traditional carbon fibers [51], even though the potential reinforcing properties, notably strength, of CNTs are superior to those of carbon fibers [52]. The low loadings of CNTs often employed in epoxy resins imply less inhomogenities but also less positive perturbations of mechanical properties [53]. Previous attempts to combine nanocomposites with micron-size fibers often resulted in a strong decrease in strength, presumably caused by poor adhesion [37]. In our case, adding CNTs to CFRP imparted a small increase in flexural strength (Figure 5(a)) of around 5% for sample F, indicating a good bonding between the CNT-modified epoxy resin and the carbon fibers. Nanotube modification of the pure epoxy resin showed an increase in flexural strength of nearly 50% for sample C, but this is still significantly below the theoretically predicted values [54]. Flexural strength of the CNT/epoxy nanocomposites increased up to a loading of 0.05 wt% of DWCNT-NH₂ (sample C) and then decreased, presumably due to agglomeration at higher nanotube concentrations. For hybrid micro-nanocomposites flexural strength only increased up to 0.025 wt% of DWCNT-NH₂ (sample F). As compared to sample A, a very small improvement in flexural stiffness (Figure 5(b)) for samples B (10%), C (11%), and D (8%) was observed. However, the introduction of DWCNT-NH₂ in CFRP resulted in a near 35% improvement in flexural

modulus for sample G. Flexural modulus increased up to 0.05 wt% of DWCNT-NH₂ (sample G) and then decreased.

3.3. Impact Testing. Falling-weight impact testing has potential for evaluating the damage tolerance of laminated composite materials. This type of testing gives significant information about failure mechanisms and behavior of materials under low velocity impact [17, 55]. Postprocessing of the measured impact parameters, force, time, and impact velocity results in the complete energy history and the energy absorbed during impact by the composite laminate. Upon impact the total impact energy can be divided into two parts. The first is the elastically stored energy in the composite plate, which is released after maximum deflection by rebounding of the laminate. This rebounding energy is successfully transferred back to the impactor. The second is, the energy absorbed in the composite laminate available for damage that consequently controls the extent of damage and residual strength [16, 17, 55].

To study the impact damage tolerance of the micro-nanocomposites, here, the authors only report the “absorbed energy” of the composite laminates. It should be noted that the neat resin-based samples A, B, C, and D cannot be compared with the CFRP-based samples E, F, G, and H. The first four samples were too brittle and shattered upon (full-penetrating) impact, whereas the latter four containing carbon fiber did not penetrate. The energy absorbed, calculated by the area under the force-displacement curve, is presented in Figure 5(c). CNTs improved the impact strength

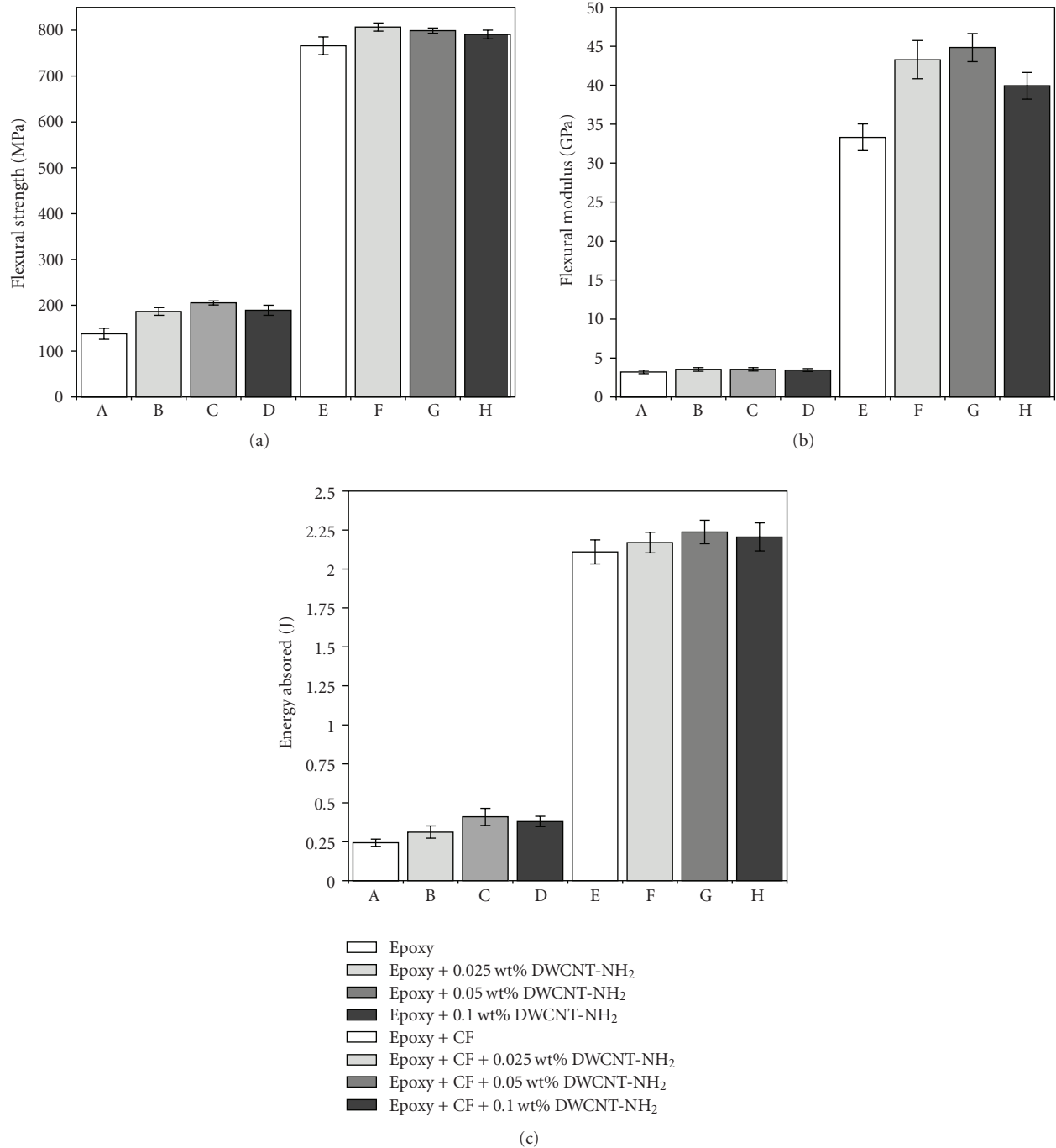


FIGURE 5: Mechanical characterizations (three-point bending test and drop-weight impact test): (a) flexural strength, (b) flexural modulus, and (c) energy absorbed (area under the curve of force versus displacement).

by up to 30% (sample C) for the nanotube-modified epoxy resin. In the case of hybrid micro-nanocomposites, carbon fibers were expected to absorb most of the energy during impact because of their large volume. After hybridization, slightly more energy was absorbed by the hybrid micro-nanocomposites. However, no significant effect on damage area was observed in the ultrasonic C-scans (Figure 6). Hybridized (0.1 wt% CNTs) and nonhybridized CFRP

laminates both showed similar damage areas ($\sim 254 \text{ mm}^2$) on the impacted surface (Figure 6). At the initial impact energies of 6 Joules, no damage was detected at the nonimpacted surfaces (surface B, Figure 3) of the laminates. Results in Figure 5(c) show a negligible enhancement in the energy absorbed by samples F (3% improvement) and G (6% improvement) as a result of the presence of DWCNT-NH₂. This small increase was not very exciting given the large

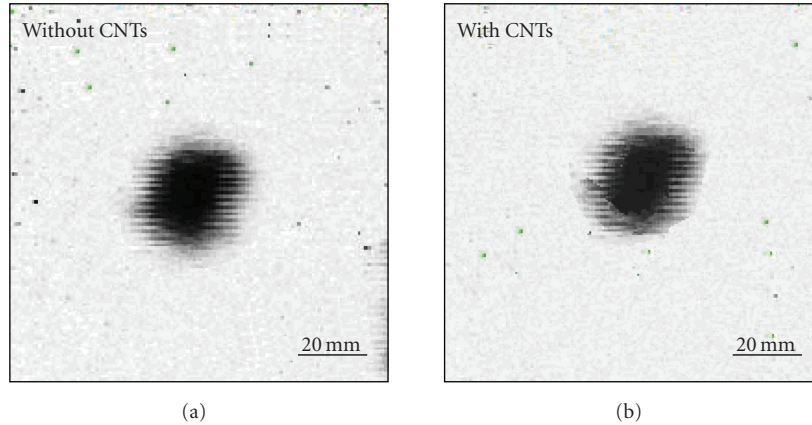


FIGURE 6: C-scan images of nonhybridized CFRP and hybridized (0.1 wt% CNTs) micro-nanocomposite.

increase in surface area offered by the CNTs. Regarding the enormous surface area of nanofillers, only small volume fractions of CNTs are needed to modify a large volume of the matrix, resulting in a high interphase fraction [27]. Energy absorbed by the hybrid micro-nanocomposites increased only up to loadings of 0.05 wt% DWCNT-NH₂ (sample G) and then decreased for sample H. A similar trend was also observed for epoxy nanocomposites in which the maximum energy was absorbed by sample C (0.33 J, 30% enhancement as compared to neat epoxy). However, compared to standard rubber or thermoplastic toughened epoxy systems these enhancements in impact toughness of CFRP through the introduction of CNTs are not all that significant. Significantly higher improvements in toughness can be achieved using more traditional methods such as polymer blends [56] or hybridization with other more ductile fibers [16, 17, 57, 58].

3.4. Mode I Fracture Toughness Analysis. The load-displacement curve (Figure 7) of the CFRP laminate without CNTs shows a stick-slip failure mode which is common for epoxy laminates. Stick-slip fracture follows a crack propagation and crack arrest behavior which indicates unstable crack growth. In neat CFRP composites the crack propagated gradually and only a small drop in load was recorded (Figure 7). The laminate with 0.1 wt% CNTs also shows a stick-slip fracture mode. However, as there are less drop steps in the load-displacement curve for the hybrid micro-nanocomposite, fracture was fast and more catastrophic, as compared to cracking in the neat CFRP composite. Consequently, load decreases significantly during propagation of the crack for hybrid micro-nanocomposites. Average G_{IC} values for nonhybridized CFRP micro-composites and hybridized micro-nanocomposites are 0.38 kJ/m² and 0.31 kJ/m², respectively. Hence, the mode I interlaminar fracture toughness decreased (~23%) with the introduction of the CNT. FE-SEM images of fractured surfaces are shown in Figure 8. Both fracture surfaces show hackle formation as the predominant failure mode for both matrices.

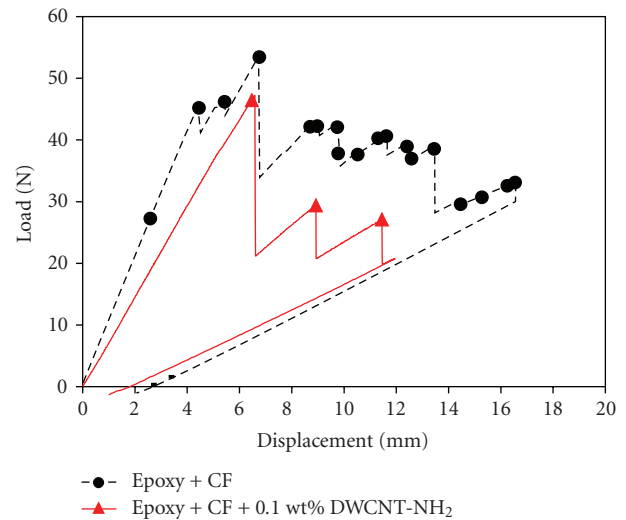


FIGURE 7: Mode I interlaminar fracture toughness analysis of nonhybridized CFRP and hybridized (0.1 wt% DWCNT-NH₂) micro-nanocomposite. Data points represent stick-slip fracture mode.

3.5. Dynamic Mechanical Analysis. Dynamic mechanical analysis (DMA) is a powerful technique for studying the viscoelastic behavior of polymer-based materials. It is also the preferred method of measuring the glass-transition temperature (T_g) of polymeric materials. Experiments involve the application of an oscillatory stress to the sample while monitoring the resulting strain which consists of both in-phase and out-of-phase components. The strain can then be used to calculate the in-phase response, or storage modulus (G'), and the out-of-phase response, or loss modulus (G''). The ratio of G'/G'' is known as the $\tan \delta$, which is a parameter for the damping characteristics of materials. The T_g is determined by the corresponding peak of the loss modulus curve [51] or $\tan \delta$.

As expected from the three-point bending results, CNTs improved the storage modulus of the nanocomposites and the hybrid micro-nanocomposites, as evidenced from

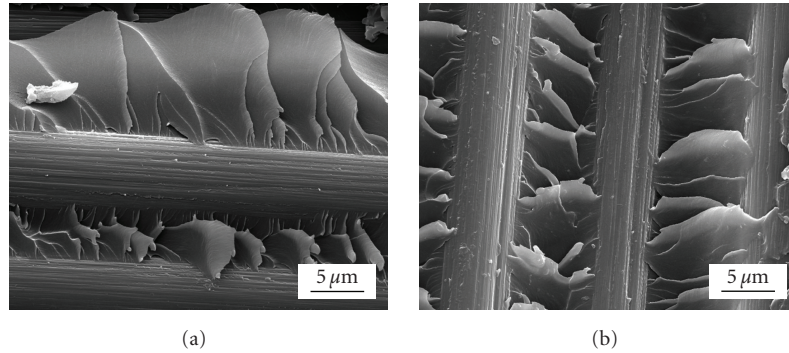


FIGURE 8: FE-SEM images of mode I fractured surface: (a) nonhybridized CFRP, and (b) hybrid micro-nanocomposite (0.1 wt% DWCNT-NH₂).

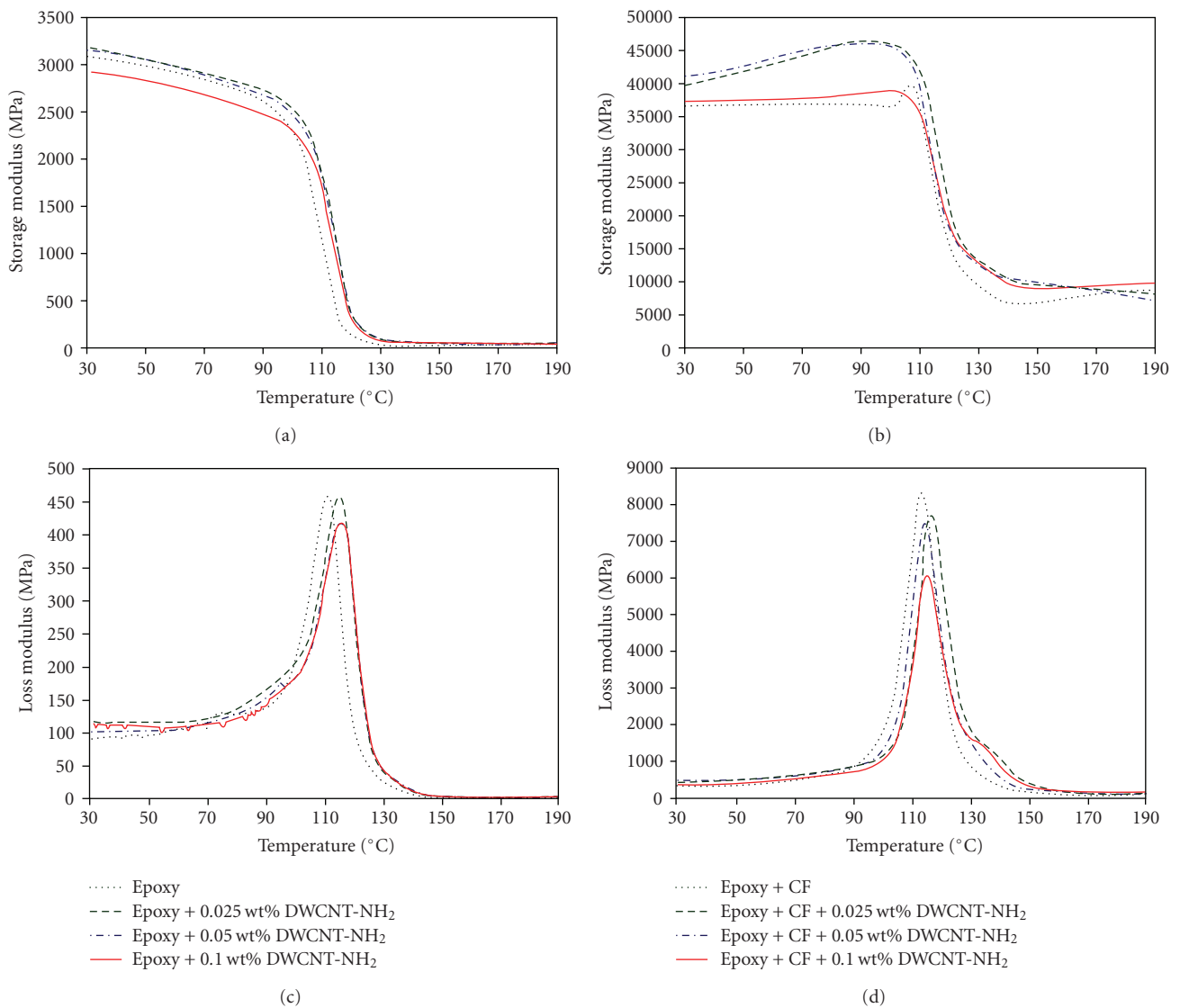


FIGURE 9: Dynamic mechanical analysis: (a) storage modulus for neat epoxy and nanocomposites, (b) storage modulus for CFRP and hybrid micro-nanocomposites, (c) loss modulus for neat epoxy and nanocomposites, and (d) loss modulus for CFRP and hybrid micro-nanocomposites.

TABLE 2: Effect of CNTs on glass transition temperature and tan-delta for nanocomposites and hybrid micro/nanocomposites.

Sample description	Sample ID	Glass transition temperature (°C)	Tan-delta*
Neat epoxy	A	116 ± 3	34 ± 2
0.025 wt% DWCNT-NH ₂ + epoxy	B	122 ± 4	27 ± 3
0.05 wt% DWCNT-NH ₂ + epoxy	C	122 ± 5	31 ± 4
0.1 wt% DWCNT-NH ₂ + epoxy	D	122 ± 3	26 ± 4
CF + epoxy	E	118 ± 5	108 ± 4
0.025 wt% DWCNT-NH ₂ + CF + epoxy	F	118 ± 3	89 ± 3
0.05 wt% DWCNT-NH ₂ + CF + epoxy	G	118 ± 6	84 ± 4
0.1 wt% DWCNT-NH ₂ + CF + epoxy	H	118 ± 4	100 ± 3

*at room temperature.

Figures 9(a) and 9(b). It can be seen in Figure 9(a) that sample D (0.1 wt% CNT/epoxy) possessed a lower storage modulus as compared to neat epoxy and other nanocomposites (having lower concentrations) over the temperature range (30–130°C). This is an indication that agglomerates in sample D may act as flaws, lowering the storage modulus. Above 130°C neat epoxy and all the epoxy nanocomposites possessed the same storage modulus, indicating that the presence of nano-reinforcement was not significant above T_g . A similar trend was observed for the micro-nanocomposites as shown in Figure 9(b). Sample H (0.1 wt% CNT/CF/epoxy) possessed an inferior storage modulus as compared to other lower compositions of hybrid micro-nanocomposites over the temperature range 30 to 115°C. At high temperatures, the loss modulus of the nanocomposites and the hybrid micro-nanocomposites decreased with increasing CNT content, shifting the T_g peak downward (Figures 9(c) and 9(d)). Higher concentrations possessed lower-energy dissipation ability as well. This effect is very clear at higher temperature (above 90°C). Hence, it can be concluded that dampening characteristics (tan δ) of nanocomposites and hybrid micro-nanocomposites start to improve above 90–100°C, because of increased energy dissipation ability of the matrix.

Based on the tan δ peak, the T_g for all samples are given in Table 2. At least five samples were tested for each condition. According to Table 2, CNTs slightly enhanced the T_g of epoxy nanocomposites up to 6°C (sample C, $T_g = 122^\circ\text{C}$). Instead of having a positive effect on T_g , hybridization resulted in a reduction in T_g , possibly due to a more non-uniform distribution of CNT's in the CFRP laminates as a result of filtering effects by the carbon fabrics [59]. These results are consistent with the work performed by Lee et al. [59]. It is interesting to note that micro-nanocomposites and epoxy nanocomposites showed inferior dampening properties (at room temperature) as compared to CFRP and neat epoxy, respectively. Here it can be concluded that hybridization with CNTs results in a significant reduction (22% in case of sample G) in dampening properties of these composites at room temperature. More work needs to be done to explain this reduction in properties and the nonuniform behavior in Table 2. On the other hand, lower values for loss modulus at higher temperatures (near

T_g , 110–130°C) in Figures 9(c) and 9(d) suggest higher dampening characteristics of hybrid micro-nanocomposites and nanocomposites containing higher CNT concentrations.

Most of the mechanical features of hybrid micro-nanocomposite started to decrease above 0.05 wt% CNT, mainly because of three reasons: (i) filtering of CNTs by the carbon fabric, leading to reduced dispersion and inhomogeneous CNT dispersions throughout the laminate; (ii) higher CNT contents in epoxy reducing the wetting and bonding between carbon fibers and the nanotube modified resin [60]; and (iii) agglomeration, which has a significant effect on the strength, stiffness, and especially toughness of the CNT-modified epoxy [59, 61]. The presence of large agglomerates decreases the effective surface area of CNTs or, in other words, reduces the efficiency of the nano-reinforcement. For pure nanocomposites (samples B, C, and D) the latter reason is more appropriate, explaining the drop in mechanical properties with the addition of 0.05 wt% CNTs. CNTs need to be separated from the bundles and dispersed uniformly in a polymer matrix to maximize their interaction with the matrix [50]. In a CNT/polymer composite, aggregation of CNTs may become a defect that causes the mechanical properties of the resin and hence the composite to deteriorate. Therefore, the primary problem in fabricating a nanocomposite is to ensure a homogeneous dispersion of CNTs in the polymer matrix. So far, only ultrasonic, three-roll milling and high-speed mechanical stirring have been verified to be effective methods for the dispersion of CNT in epoxy resin [62]. But from this study, it appeared that bath ultrasonication is a good way to disperse lower concentrations of CNT in epoxy. Better homogenizing techniques should be employed for dispersing higher contents of CNTs in epoxy. The results of Allaoui et al. [63] suggest that it would not be helpful to use high CNTs concentrations to improve the mechanical properties of composites if they are in random distribution. The upper limit, for the addition of CNTs, is governed by the distribution and topology (aspect ratio) of the CNTs. Similar to short fiber composites, the orientation of the nanofibers plays an important role, and the higher the degree of alignment of CNTs, the higher their reinforcing efficiency [64].

4. Conclusion

Multiscale hybrid micro-nanocomposites offer a route by which multifunctionality can be introduced in fiber-reinforced composites. DWCNT-NH₂/carbon fiber/epoxy micro-nanocomposites were prepared and their mechanical properties were compared with their respective pure micro- and nanocomposites. Apart from flexural modulus, fracture toughness, T_g , and $\tan \delta$, CNTs imparted a rather minor enhancement in mechanical properties of woven fabric-based CFRP. The addition of small amounts of CNTs (0.025, 0.05, and 0.1 wt%) to epoxy resins for the fabrication of multiscale carbon fiber composites resulted in a maximum enhancement in flexural modulus by 35%, a 5% improvement in flexural strength, a 6% improvement in absorbed impact energy, and a 23% decrease in the mode I interlaminar toughness. Hybridization of carbon fiber-reinforced epoxy using CNTs also resulted in a reduction in T_g and dampening characteristics, owing to the presence of micron-sized agglomerates. However, even without these aggregates, it was concluded that DWCNT-NH₂ achieved only a limiting toughening effects in the CFRP. Especially compared to standard rubber or thermoplastic toughened epoxy the enhancements were not all that significant. These results are especially disappointing considering the large surface-to-volume ratio of CNTs compared to other fillers, including carbon fibers, and the effect this—in theory—can have on energy absorption mechanisms such as nanotube debonding or pull-out [64]. Therefore, a careful future optimization of processing parameters such as nanotube dispersion at higher concentrations, nanotube alignment and localization, should lead to further improvements in mechanical properties of these multiscale composites.

References

- [1] P. Ciselli, Z. Wang, and T. Peijs, "Reinforcing potential of carbon nanotubes in oriented polymer fibres," *Materials Technology*, vol. 22, no. 1, pp. 10–21, 2007.
- [2] Z. Wang, P. Ciselli, and T. Peijs, "The extraordinary reinforcing efficiency of single-walled carbon nanotubes in oriented poly(vinyl alcohol) tapes," *Nanotechnology*, vol. 18, no. 45, Article ID 455709, 2007.
- [3] F. H. Gojny, M. H. G. Wichmann, B. Fiedler, and K. Schulte, "Influence of different carbon nanotubes on the mechanical properties of epoxy matrix composites—a comparative study," *Composites Science and Technology*, vol. 65, no. 15–16, pp. 2300–2313, 2005.
- [4] F. H. Gojny, M. H. G. Wichmann, U. Kopke, B. Fiedler, and K. Schulte, "Carbon nanotube-reinforced epoxy-composites: enhanced stiffness and fracture toughness at low nanotube content," *Composites Science and Technology*, vol. 64, no. 15, pp. 2363–2371, 2004.
- [5] B. Fiedler, F. H. Gojny, M. H. G. Wichmann, M. C. M. Nolte, and K. Schulte, "Fundamental aspects of nano-reinforced composites," *Composites Science and Technology*, vol. 66, no. 16, pp. 3115–3125, 2006.
- [6] B. Wetzell, P. Rosso, F. Hauptert, and K. Friedrich, "Epoxy nanocomposites—fracture and toughening mechanisms," *Engineering Fracture Mechanics*, vol. 73, no. 16, pp. 2375–2398, 2006.
- [7] J. H. Du, J. Bai, and H. M. Cheng, "The present status and key problems of carbon nanotube based polymer composites," *Express Polymer Letters*, vol. 1, no. 5, pp. 253–273, 2007.
- [8] Y. X. Zhou, P. X. Wu, Z.-Y. Cheng, J. Ingram, and S. Jeelani, "Improvement in electrical, thermal and mechanical properties of epoxy by filling carbon nanotube," *Express Polymer Letters*, vol. 2, no. 1, pp. 40–48, 2008.
- [9] J. Sandler, M. S. P. Shaffer, T. Prasse, W. Bauhofer, K. Schulte, and A. H. Windle, "Development of a dispersion process for carbon nanotubes in an epoxy matrix and the resulting electrical properties," *Polymer*, vol. 40, no. 21, pp. 5967–5971, 1999.
- [10] J. K. W. Sandler, J. E. Kirk, I. A. Kinloch, M. S. P. Shaffer, and A. H. Windle, "Ultra-low electrical percolation threshold in carbon-nanotube-epoxy composites," *Polymer*, vol. 44, no. 19, pp. 5893–5899, 2003.
- [11] R. Zhang, A. Dowden, H. Deng, M. Baxendale, and T. Peijs, "Conductive network formation in the melt of carbon nanotube/thermoplastic polyurethane composite," *Composites Science and Technology*, vol. 69, no. 10, pp. 1499–1504, 2009.
- [12] R. Zhang, M. Baxendale, and T. Peijs, "Universal resistivity-strain dependence of carbon nanotube/polymer composites," *Physical Review B*, vol. 76, no. 19, Article ID 195433, 2007.
- [13] F. Inam and T. Peijs, "Re-aggregation of carbon nanotubes in two-component epoxy system," *Journal of Nanostructured Polymers and Nanocomposites*, vol. 2, no. 3, pp. 87–95, 2006.
- [14] F. Inam, H. Yan, D. D. Jayaseelan, T. Peijs, and M. J. Reece, "Electrically conductive alumina—carbon nanocomposites prepared by Spark Plasma Sintering," *Journal of the European Ceramic Society*, vol. 30, no. 2, pp. 153–157, 2010.
- [15] A. A. J. M. Peijs, R. W. Venderbosch, and P. J. Lemstra, "Hybrid composites based on polyethylene and carbon fibres—part 3. Impact resistant structural composites through damage management," *Composites*, vol. 21, no. 6, pp. 522–530, 1990.
- [16] A. A. J. M. Peijs and R. W. Venderbosch, "Hybrid composites based on polyethylene and carbon fibres Part IV Influence of hybrid design on impact strength," *Journal of Materials Science Letters*, vol. 10, no. 19, pp. 1122–1124, 1991.
- [17] B. Schrauwen, P. Bertens, and T. Peijs, "Influence of hybridisation and test geometry on the impact response of glass-fibre-reinforced laminated composites," *Polymers and Polymer Composites*, vol. 10, no. 4, pp. 259–272, 2002.
- [18] P. Karapappas, A. Vavouliotis, P. Tsotra, V. Kostopoulos, and A. Paipetis, "Enhanced fracture properties of carbon reinforced composites by the addition of multi-wall carbon nanotubes," *Journal of Composite Materials*, vol. 43, no. 9, pp. 977–985, 2009.
- [19] J. Njuguna, K. Pielichowski, and J. R. Alcock, "Epoxy-based fiber reinforced nanocomposites," *Advanced Engineering Materials*, vol. 9, no. 10, pp. 835–847, 2007.
- [20] T. Mahrholz, J. Mosch, D. Rostermundt, U. Riedel, L. Herbeck, and M. Sinapius, "Fiber-reinforced nanocomposites for spacecraft structures: manufacturing, characterization and application," in *Proceedings of the European Conference on Spacecraft Structures, Materials and Mechanical Testing*, pp. 1445–1454, 2005.
- [21] G. Romhany and G. Szebenyi, "Interlaminar crack propagation in MWCNT/fiber reinforced hybrid composites," *Express Polymer Letters*, vol. 3, no. 3, pp. 145–151, 2009.
- [22] C. Chen and D. Curliss, "Resin matrix composites: organoclay-aerospace epoxy nanocomposites—part 2," *SAMPE Journal*, vol. 37, no. 5, pp. 11–18, 2001.

- [23] B. P. Rice, C. Chen, L. Cloos, and D. Curliss, "Carbon fiber composites: organoclay-aerospace epoxy nanocomposites—part 1," *SAMPE Journal*, vol. 37, no. 5, pp. 7–9, 2001.
- [24] F. H. Gojny, M. H. G. Wichmann, B. Fiedler, W. Bauhofer, and K. Schulte, "Influence of nano-modification on the mechanical and electrical properties of conventional fibre-reinforced composites," *Composites Part A*, vol. 36, no. 11, pp. 1525–1535, 2005.
- [25] S. Tsantzalidis, P. Karapappas, A. Vavouliotis, et al., "Enhancement of the mechanical performance of an epoxy resin and fiber reinforced epoxy resin composites by the introduction of CNF and PZT particles at the microscale," *Composites Part A*, vol. 38, no. 4, pp. 1076–1081, 2007.
- [26] S. Tsantzalidis, P. Karapappas, A. Vavouliotis, et al., "On the improvement of toughness of CFRPs with resin doped with CNF and PZT particles," *Composites Part A*, vol. 38, no. 4, pp. 1159–1162, 2007.
- [27] M. H. G. Wichmann, J. Sumfleth, F. H. Gojny, M. Quaresimin, B. Fiedler, and K. Schulte, "Glass-fibre-reinforced composites with enhanced mechanical and electrical properties—benefits and limitations of a nanoparticle modified matrix," *Engineering Fracture Mechanics*, vol. 73, no. 16, pp. 2346–2359, 2006.
- [28] F. H. Chowdhury, M. V. Hosur, and S. Jeelani, "Studies on the flexural and thermomechanical properties of woven carbon/nanoclay-epoxy laminates," *Materials Science and Engineering A*, vol. 421, no. 1–2, pp. 298–306, 2006.
- [29] F. Hussain, D. Dean, A. Haque, and A. M. Shamsuzzoha, "S2 glass/vinylester polymer nanocomposites: manufacturing, structures, thermal and mechanical properties," *Journal of Advanced Materials*, vol. 37, no. 1, pp. 16–27, 2005.
- [30] A. Haque, M. Shamsuzzoha, F. Hussain, and D. Dean, "S2-glass/epoxy polymer nanocomposites: manufacturing, structures, thermal and mechanical properties," *Journal of Composite Materials*, vol. 37, no. 20, pp. 1821–1838, 2003.
- [31] T. Yokozeki, Y. Iwahori, and S. Ishiwata, "Matrix cracking behaviors in carbon fiber/epoxy laminates filled with cup-stacked carbon nanotubes (CSCNTs)," *Composites Part A*, vol. 38, no. 3, pp. 917–924, 2007.
- [32] J. Qiu, C. Zhang, B. Wang, and R. Liang, "Carbon nanotube integrated multifunctional multiscale composites," *Nanotechnology*, vol. 18, no. 27, Article ID 275708, 2007.
- [33] E. T. Thostenson, W. Z. Li, D. Z. Wang, Z. F. Ren, and T. W. Chou, "Carbon nanotube/carbon fiber hybrid multiscale composites," *Journal of Applied Physics*, vol. 91, no. 9, pp. 6034–6037, 2002.
- [34] K. L. Kepple, G. P. Sanborn, P. A. Lacasse, K. M. Gruenberg, and W. J. Ready, "Improved fracture toughness of carbon fiber composite functionalized with multi walled carbon nanotubes," *Carbon*, vol. 46, no. 15, pp. 2026–2033, 2008.
- [35] J. Gou, W. Hollinghead, A. Whitaker, B. Sheffer, J. Foster, and D. Hui, "Processing of fiber reinforced composites with carbon nanofiber-modified matrix using resin transfer molding," in *Proceedings of 11th International Conference on Composites/Nano Engineering (ICCE '04)*, SC, USA, August 2004.
- [36] D. P. N. Vlasveld, W. Daud, H. E. N. Bersee, and S. J. Picken, "Continuous fibre composites with a nanocomposite matrix: improvement of flexural and compressive strength at elevated temperatures," *Composites Part A*, vol. 38, no. 3, pp. 730–738, 2007.
- [37] D. P. N. Vlasveld, H. E. N. Bersee, and S. J. Picken, "Creep and physical aging behaviour of PA6 nanocomposites," *Polymer*, vol. 46, no. 26, pp. 12539–12545, 2005.
- [38] M. A. V. Es, *Polymer clay nanocomposites. The importance of particle dimensions*, Ph.D. thesis, Delft University of Technology, The Netherlands, 2001.
- [39] E. P. Giannelis, "Polymer layered silicate nanocomposites," *Advanced Materials*, vol. 8, no. 1, pp. 29–35, 1996.
- [40] Y. Kojima, A. Usuki, M. Kawasumi, A. Okada, T. Kurauchi, and O. Kamigaito, "Sorption of water in nylon 6-clay hybrid," *Journal of Applied Polymer Science*, vol. 49, no. 7, pp. 1259–1264, 1993.
- [41] H. L. Qin, Q. S. Su, S. M. Zhang, B. Zhao, and M. S. Yang, "Thermal stability and flammability of polyamide 66/montmorillonite nanocomposites," *Polymer*, vol. 44, no. 24, pp. 7533–7538, 2003.
- [42] T. Kashiwagi, R. H. Harris Jr., X. Zhang, et al., "Flame retardant mechanism of polyamide 6-clay nanocomposites," *Polymer*, vol. 45, no. 3, pp. 881–891, 2004.
- [43] L. Qu, Y. Zhao, and L. Dai, "Carbon microfibers sheathed with aligned carbon nanotubes: towards multidimensional, multicomponent, and multifunctional nanomaterials," *Small*, vol. 2, no. 8–9, pp. 1052–1059, 2006.
- [44] S. J. V. Frankland, J. C. Riddick, and T. S. Gates, "Multi-scale rule-of-mixtures model of carbon nanotube/carbon fiber/epoxy lamina," in *Proceedings of the Materials Research Society Symposium*, vol. 887, pp. 61–70, 2006.
- [45] CYTEC Engineered Materials, CYCOM 823 Technical Data sheet, 2004.
- [46] M. Cadek, J. N. Coleman, K. P. Ryan, et al., "Reinforcement of polymers with carbon nanotubes: the role of nanotube surface area," *Nano Letters*, vol. 4, no. 2, pp. 353–356, 2004.
- [47] F. Inam and T. Peijs, "Transmission light microscopy of carbon nanotubes-epoxy nanocomposites involving different dispersion methods," *Advanced Composites Letters*, vol. 15, no. 1, pp. 7–13, 2006.
- [48] ASTM, "Standard test methods for constituent content of composite materials," *Annual Book of ASTM Standards*, D 3171-99, 2004.
- [49] E. T. Thostenson and T.-W. Chou, "Aligned multi-walled carbon nanotube-reinforced composites: processing and mechanical characterization," *Journal of Physics D*, vol. 35, no. 16, pp. L77–L80, 2002.
- [50] E. T. Thostenson, C. Li, and T. W. Chou, "Nanocomposites in context," *Composites Science and Technology*, vol. 65, no. 3–4, pp. 491–516, 2005.
- [51] D. Dean, A. M. Obore, S. Richmond, and E. Nyairo, "Multi-scale fiber-reinforced nanocomposites: synthesis, processing and properties," *Composites Science and Technology*, vol. 66, no. 13, pp. 2135–2142, 2006.
- [52] I. A. Guz and Ya. Ya. Rushchitskii, "Comparison of mechanical properties and effects in micro- and nanocomposites with carbon fillers (carbon microfibers, graphite microwhiskers, and carbon nanotubes)," *Mechanics of Composite Materials*, vol. 40, no. 3, pp. 179–190, 2004.
- [53] M. B. Bryning, M. F. Islam, J. M. Kikkawa, and A. G. Yodh, "Very low conductivity threshold in bulk isotropic single-walled carbon nanotube-epoxy composites," *Advanced Materials*, vol. 17, no. 9, pp. 1186–1191, 2005.
- [54] A. A. Mamedov, N. A. Kotov, M. Prato, D. M. Guldi, J. P. Wicksted, and A. Hirsch, "Molecular design of strong single-wall carbon nanotube/polyelectrolyte multilayer composites," *Nature Materials*, vol. 1, no. 3, pp. 190–194, 2002.
- [55] B. Schrauwen and T. Peijs, "Influence of matrix ductility and fibre architecture on the repeated impact response of glass-fibre-reinforced laminated composites," *Applied Composite Materials*, vol. 9, no. 6, pp. 331–352, 2002.

- [56] R. W. Venderbosch, T. Peijs, H. E. H. Meijer, and P. L. Lemstra, "Fibre-reinforced composites with tailored interphases using PPE/epoxy blends as a matrix system," *Composites Part A*, vol. 27, no. 9, pp. 895–905, 1996.
- [57] H. Kishi, K. Uesawa, S. Matsuda, and A. Murakami, "Adhesive strength and mechanisms of epoxy resins toughened with preformed thermoplastic polymer particles," *Journal of Adhesion Science and Technology*, vol. 19, no. 15, pp. 1277–1290, 2005.
- [58] Y. Liu, W. Zhang, and H. Zhou, "Mechanical properties of epoxy resin/hydroxyl-terminated polyester blends: effect of two-phase structure," *Polymer International*, vol. 54, no. 10, pp. 1408–1415, 2005.
- [59] K.-C. Lee, H. H. Yu, S.-J. Hwang, Y.-S. Li, M.-H. Cheng, and C.-C. Lin, "Preparation and characterization of the modified carbon nanotubes enhanced epoxy resin composites," *Materials Science Forum*, vol. 505–507, pp. 1075–1080, 2006.
- [60] S.-M. Yuen, M. Chen-Chi, H.-H. Wu, et al., "Preparation and thermal, electrical, and morphological properties of multiwalled carbon nanotube and epoxy composites," *Journal of Applied Polymer Science*, vol. 103, no. 2, pp. 1272–1278, 2007.
- [61] L. R. Xu, V. Bhamidipati, W.-H. Zhong, et al., "Mechanical property characterization of a polymeric nanocomposite reinforced by graphitic nanofibers with reactive linkers," *Journal of Composite Materials*, vol. 38, no. 18, pp. 1563–1582, 2004.
- [62] G. S. Zhuang, G. X. Sui, Z. S. Sun, and R. Yang, "Pseudo reinforcement effect of multiwalled carbon nanotubes in epoxy matrix composites," *Journal of Applied Polymer Science*, vol. 102, no. 4, pp. 3665–3672, 2006.
- [63] A. Allaoui, S. Bai, H. M. Cheng, and J. B. Bai, "Mechanical and electrical properties of a MWNT/epoxy composite," *Composites Science and Technology*, vol. 62, no. 15, pp. 1993–1998, 2002.
- [64] M. H. G. Wichmann, K. Schulte, and H. D. Wagner, "On nanocomposite toughness," *Composites Science and Technology*, vol. 68, no. 1, pp. 329–331, 2008.

Research Article

Foaming Behaviour, Structure, and Properties of Polypropylene Nanocomposites Foams

M. Antunes, V. Realinho, and J. I. Velasco

Departament de Ciència del Materials i Enginyeria Metal·lúrgica, Centre Català del Plàstic, Universitat Politècnica de Catalunya, C/ Colom 114, 08222 Terrassa, Barcelona, Spain

Correspondence should be addressed to J. I. Velasco, jose.ignacio.velasco@upc.edu

Received 30 November 2009; Revised 25 February 2010; Accepted 2 April 2010

Academic Editor: Frank T. Fisher

Copyright © 2010 M. Antunes et al. This is an open access article distributed under the Creative Commons Attribution License, which permits unrestricted use, distribution, and reproduction in any medium, provided the original work is properly cited.

This work presents the preparation and characterization of compression-moulded montmorillonite and carbon nanofibre-polypropylene foams. The influence of these nanofillers on the foaming behaviour was analyzed in terms of the foaming parameters and final cellular structure and morphology of the foams. Both nanofillers induced the formation of a more isometric-like cellular structure in the foams, mainly observed for the MMT-filled nanocomposite foams. Alongside their crystalline characteristics, the nanocomposite foams were also characterized and compared with the unfilled ones regarding their dynamic-mechanical thermal behaviour. The nanocomposite foams showed higher specific storage moduli due to the reinforcement effect of the nanofillers and higher cell density isometric cellular structure. Particularly, the carbon nanofibre foams showed an increasingly higher electrical conductivity with increasing the amount of nanofibres, thus showing promising results as to produce electrically improved lightweight materials for applications such as electrostatic painting.

1. Introduction

Although the increasing interest in the preparation and study of polyolefin foams, there is still lack of information regarding the characterization of rigid polypropylene foams thought for structural applications with typical relative densities, that is, the density of the foam divided by that of the respective solid, higher than 0.1. Hence the interest in preparing and studying new polypropylene-based foams by carefully controlling the expansion and final cellular structure [1].

Nowadays, the use of low-density PP foams is rather limited when compared to PE to situations where higher service temperatures or thermal stabilities are required. PE is cheaper and displays a wider range of molecular architectures, making it easier to reach the high melt strengths and extensibilities required for foaming. Also, the rubbery plateau of the polymer melt can be easily increased via cross-linking, that way it widens the optimum temperature window for stable foam production [1]. Contrarily, PP's linear structure makes it harder to foam due to its intrinsically low melt strength [2]. In order to achieve the high expansions required

for applications such as packaging, PP is often blended with other polyolefins, mainly low melting point ethylene copolymers such as EVA or ethylene-octene copolymers [3] or used as random copolymer with low ethylene content [4].

Some of the advantages of PP, such as its higher stiffness, strength, and better impact strength, only start to be relevant at higher foam densities ($\rho > 100 \text{ kg/m}^3$). That is why medium density PP foams have been considered in this work. Nevertheless, even at these relatively high densities, the use of PP requires the improvement of its melt resistance. This was possible with the development of long-chain branching modified grades, conventionally known as high melt strength polypropylenes (HMS-PP). The use of these polypropylenes has been shown to improve the volume expandability and cell uniformity, retard cell coalescence, and increase the expansion ratio, globally broadening the optimum foaming processing window [5, 6].

Four basic foaming processes are commonly used to produce PP foams: (1) direct extrusion, where a foam is directly obtained by sudden decompression at the exit of an extrusion die [7, 8]; (2) injection, where expansion is adjusted inside a closed injection mould; (3) compression

moulding, where the material is foamed by simultaneously applying heat and pressure and later expanding the material by sudden decompression, conventionally using exothermic chemical blowing agents such as azodicarbonamide (ADC) [9]; (4) batch foaming, where the material is foamed by initially dissolving N_2 or CO_2 in the solid polymer inside high pressure reactors and afterwards expanding the material by heating at low pressure above the glass transition temperature of the polymer-gas mixture or by sudden pressure drop [10–12].

Due to its versatility, compression moulding was used in this work for the preparation of the medium-density polypropylene foams. It is a process that allows to control the expansion by varying the amount of ADC and processing parameters. Therefore, it enables the analysis of incorporating nanometric-sized reinforcements on the foaming behaviour, cellular structure, and final properties of the material and the effect of the foaming process on the particles' distribution and dispersion [6, 13]. With the disadvantage of presenting solid residues inherent to the thermal decomposition of ADC or an anisotropic cellular distribution with cells smaller close to the surface, foams produced using this technique may reach thicknesses as high as 10 cm with cell sizes in the micrometer range [8]. Comparatively, gas dissolution is a very time-consuming process due to the high times required for dissolving the gas, and the Mucell injection foaming process is rather limited to high density foams ($>300 \text{ kg/m}^3$) [14]. Albeit the small moulds used in this work, these can be easily scaled-up to produce very complex foamed elements and components by replacing the mould, while in the case of injection, mould replacement would be very costly.

During the last couple of years, polymer nanocomposite foams have received increasing attention in both scientific and industrial communities [15]. It has been proven that small amounts of finely-dispersed nanoparticles may act as sites for bubble nucleation during the foaming process. Particularly, the cell density has been found to increase linearly with the clay concentration for low clay values [16, 17]. Besides, the highest cell density was obtained when the clay platelets were exfoliated, attained to a higher effective particle concentration and thus higher nucleation efficiency [16, 18]. In accordance with the higher cell densities, smaller cell sizes were obtained in the presence of the nanoparticles. Thus, the presence of exfoliated nanoparticles may result in finer cellular structures due to a combined bubble nucleation and melt strain hardening effects [19]. The nanometric size of the particles also increases the interaction with the polymer matrix, offering a high potential for local reinforcement, resulting in macroscopic mechanical enhancements. If one considers the micrometer or submicrometer thickness of the cell walls in foams, the extremely small size of the nanoparticles could locally act reinforcing them. In the case of layered-like nanoparticles such as montmorillonite, good barrier properties can also be expected by the nanosized-platelets limiting gas diffusion during the expansion and stabilization of the foam [15].

Several works have compared the mechanical properties of PVC and PS nanocomposite foams with that of the

respective unfilled ones under tensile and compressive conditions [18, 20]. In all cases, using layered silicates such as montmorillonite or carbon nanofibres resulted in higher moduli and tensile strengths; in some cases the nanocomposite foams even display higher specific moduli than the solid unfilled material [21].

Therefore, the specific properties of the foams could be extended with the incorporation of low amounts of functional inorganic phases with high specific surface areas. With that in mind, two types of nanometric-sized reinforcements, montmorillonite, MMT [6, 22] and different amounts of carbon nanofibres, CNF [23, 24], were added to a PP-based foaming formulation, the nanocomposite materials later chemically foamed by compression moulding. The particular case of incorporating conductive nanofillers such as carbon nanofibres could result in the improvement of properties such as the electrical conductivity [25], thus contributing to the development of new lightweight electrically conductive materials.

2. Materials and Compounding

2.1. Nanocomposite Preparation. A PP material specifically formulated for foaming applications, referred to as PP, was prepared by meltcompounding using a corotating twin-screw extruder (Collin Knetter 25X36D, L/D = 36), 50 phr of a PP-HMS, and 50 phr of an extrusion grade-type with stearic acid (0.2 phr), talc (1.0 phr), and two different amounts of a chemical blowing agent, azodicarbonamide (1.5 and 3.5 phr). These two concentrations of ADC were used to reach the desired expansion ratios. A constant temperature of 165°C and screw speed of 160 rpm were used for all the materials.

The PP-HMS used was an especially modified long-chain branched PP with a density of $0.902 \text{ g}\cdot\text{cm}^{-3}$ and melt flow index (MFI) of 2.1 g/10 min at 230°C and 2.16 kg. The linear extrusion-grade type of PP had a density of $0.905 \text{ g}\cdot\text{cm}^{-3}$, and MFI of 5.8 g/10 min (230°C and 2.16 kg). The azodicarbonamide (Porofor ADC/M-C1), with an ADC content of 99.1%, a density of $1.65 \text{ g}\cdot\text{cm}^{-3}$ and an average particle size of $3.9 \pm 0.6 \mu\text{m}$, was added to the polymer blend in the extruder.

In the case of the montmorillonite nanocomposite, a commercial masterbatch of 75 wt.% of PP with 25 wt.% of an octadecyl amine modified montmorillonite (Nanomer C32P) was melt-compounded with the PP material in the extruder so as to obtain a final nanocomposite with 5.0 phr of the modified montmorillonite (PP-MMT).

Three different carbon nanofibre-polypropylene nanocomposites (PP-CNF) were prepared by melt mixing in the twin screw extruder 5, 10, and 20 wt.% of carbon nanofibres with the previously mentioned PP matrix. The carbon nanofibres used in this work were highly graphitized submicron vapour grown carbon nanofibres, with a typical diameter of 20–80 nm, fibre length $>30 \mu\text{m}$, density of $1.97 \text{ g}\cdot\text{cm}^{-3}$, specific surface area BET (N_2) of $150\text{--}200 \text{ m}^2\cdot\text{g}^{-1}$, and electrical resistivity of $10^{-3} \Omega\cdot\text{m}$. The reason behind the preparation of these three nanocomposites

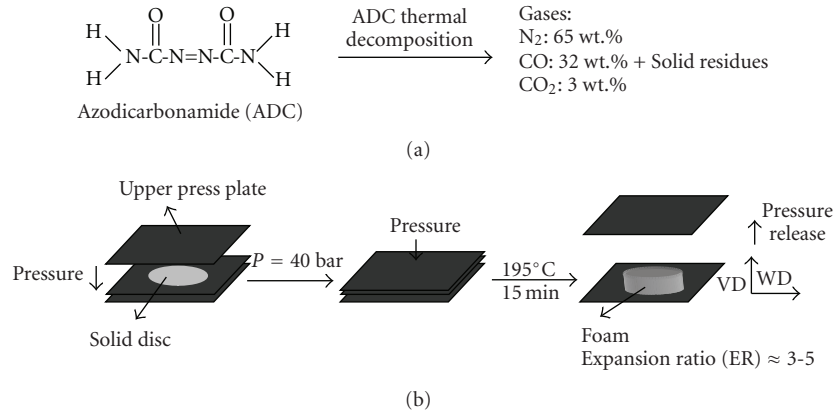


FIGURE 1: (a) Thermal decomposition of the ADC and (b) one-step compression moulding foaming process schematic. VD: Vertical direction of foaming; WD: Width direction.

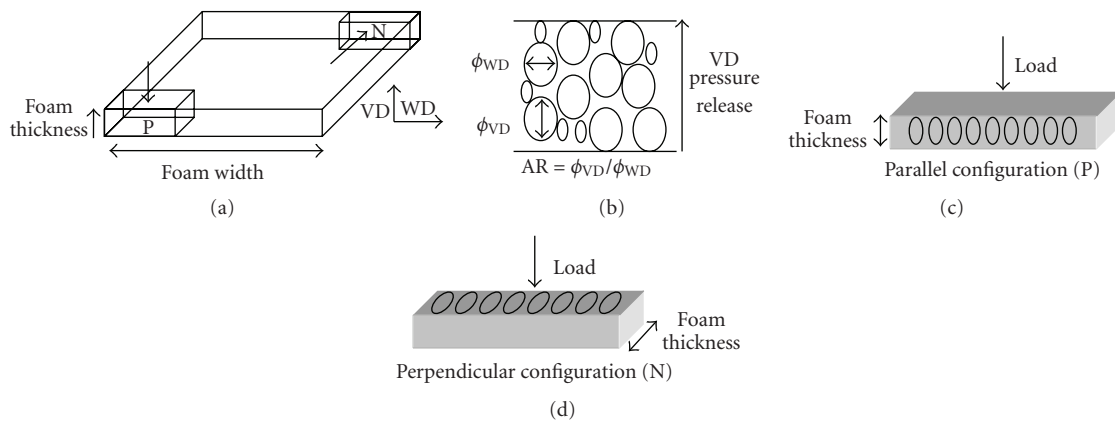


FIGURE 2: (a) Schematic showing specimen configurations; (b) characteristic cellular structure parameters; (c) parallel (P); (d) perpendicular (N) specimen configurations.

lies on the interest in studying the electrical conductivity as a function of the amount of nanofibres.

The rather low processing temperatures (165°C) and high screw speeds (160 rpm) prevented the azodicarbonamide from thermally decomposing inside the extruder.

2.2. Foaming Process. Prior to foaming by thermal decomposition of the ADC (Figure 1(a)), solid discs of the different materials with a thickness of 3.5 mm and diameter of 74 mm were prepared by compression moulding the extruded pellets in a hot-plate press IQAP-LAP PL-15.

A one-step compression moulding process was used to foam the solid discs by placing them inside a circular mould ($\Phi = 74$ mm) and heating at 195°C applying a pressure of 40 bar for 15 min using the hot-plate press (see Figure 1(b)).

2.3. Testing Procedure. Density of the several solids and foams was measured according to standard procedures (ISO 845).

The cellular structure of the foams was analyzed by scanning electron microscopy, SEM (JEOL JSM-5610). Samples were fractured at low temperature and made conductive by

depositing a thin layer of gold. The average cell size (ϕ) and cell density were obtained using the intercept counting method [26]. Two different cell sizes were determined using the procedure presented in [13]: ϕ_{VD} (VD: Vertical Direction), that is, the average cell size in the direction of pressure release and ϕ_{WD} (Width Direction). The aspect ratio, AR ($\text{AR} = \phi_{\text{VD}}/\phi_{\text{WD}}$), was determined using a representative cell population. Schematics showing specimen configurations and most characteristic cellular structure parameters are presented in Figure 2.

The morphology of the foamed nanocomposites was assessed from high-magnification SEM micrographs and using transmission electron microscopy, TEM (HITACHI H-800). For TEM, sheets with a typical thickness of 60 nm were cut using an ultramicrotome Ultracut E from Reichert-Jung.

Differential scanning calorimetry (DSC) was used to study the thermal characteristics of the matrix. A Perkin Elmer, Pyris 1 model with a glycol-based Perkin Elmer Intracooler IIP calorimeter was employed with samples weighting around 8.0 mg. The following program was used: heating from 30 to 200°C at $10^\circ\text{C}/\text{min}$ and holding for 1 min to erase the thermal history, followed by cooling at $10^\circ\text{C}/\text{min}$ from 200°C to 30°C and a second heating from 30

TABLE 1: Cellular characterization results of the unfilled (PP), montmorillonite (PP-MMT), and carbon nanofibre (PP-CNF) polypropylene foams.

Code	Foam density ($\text{kg}\cdot\text{m}^{-3}$)	V_{gas}	V_{PP}	V_{p}	$\phi_{\text{VD}} (\mu\text{m})$	$\phi_{\text{WD}} (\mu\text{m})$	AR	Cell density ($\text{cells}\cdot\text{cm}^{-3}$)
PP	346 ± 9	0.62	0.38	—	194 ± 7	175 ± 1	1.1	4.71×10^4
	311 ± 9	0.66	0.34	—	177 ± 2	196 ± 1	0.9	4.63×10^4
	268 ± 6	0.71	0.29	—	241 ± 9	266 ± 12	0.9	3.52×10^4
	261 ± 13	0.72	0.29	—	243 ± 14	239 ± 2	1.0	3.42×10^4
	236 ± 7	0.75	0.25	—	456 ± 5	479 ± 10	1.0	1.30×10^4
	189 ± 8	0.80	0.20	—	564 ± 6	523 ± 11	1.1	9.13×10^3
PP-MMT	256 ± 8	0.72	0.28	0.003	146 ± 3	160 ± 7	0.9	9.01×10^4
	245 ± 5	0.73	0.27	0.003	169 ± 13	156 ± 12	1.1	8.78×10^4
	240 ± 10	0.74	0.26	0.003	190 ± 12	164 ± 15	1.2	6.56×10^4
	238 ± 12	0.74	0.25	0.003	296 ± 7	211 ± 4	1.4	3.57×10^4
	220 ± 7	0.76	0.24	0.003	218 ± 6	204 ± 8	1.1	4.19×10^4
	208 ± 4	0.78	0.22	0.003	289 ± 12	206 ± 6	1.4	3.98×10^4
PP-CNF	176 ± 3	0.81	0.19	0.002	410 ± 12	293 ± 12	1.4	1.97×10^4
	265 ± 10	0.70	0.29	0.01	569 ± 25	508 ± 19	1.1	8.13×10^3
	270 ± 10	0.69	0.29	0.02	462 ± 28	394 ± 22	1.2	1.35×10^4
	290 ± 8	0.68	0.29	0.03	239 ± 10	258 ± 12	0.9	3.05×10^4

to 200°C (10°C/min). The crystallinity percentage (X_c) was determined according to

$$X_c(\%) = \frac{\Delta H_m}{\Delta H_m^0 w_p} \times 100, \quad (1)$$

where w_p is the weight fraction of PP, ΔH_m is the melting enthalpy of the sample and ΔH_m^0 the theoretical, 100% crystalline polypropylene enthalpy (207.1 J/g [27]).

Polypropylene's crystalline characteristics were analyzed by wide angle X-ray scattering (WAXS). A Bruker D8 diffractometer with $\text{CuK}\alpha$ radiation ($\lambda = 0.154$ nm) operating at 45 kV and 40 mA was used. Scans were taken from 1 to 60° with a rotation step of 0.033° and a step time of 0.06 s.

Dynamic mechanical analysis (DMA) was used to measure the dynamic-mechanical properties and study the viscoelastic behaviour of the several foamed nanocomposites. A TA Instruments Q800 Dynamic Mechanical Analyzer was used and calibrated according to the standard procedure. The glass transition temperature (T_g), storage modulus (E'), and loss factor ($\tan \delta$) were obtained in a three-point bending configuration using a span length of 50.00 mm. Two configurations, parallel (P) and perpendicular (N), respectively shown in Figures 2(c) and 2(d), were considered. Experiments were performed from -20 to 150°C at $2^\circ\text{C}/\text{min}$ and 1 Hz. A static strain of 2% and dynamic of 0.02% with a preload force of 0.01 N and force track of 120% were chosen. Test specimens were prepared in a prismatic shape (see Figures 2(c) and 2(d)) with a nominal length of 55.00 ± 0.10 mm, width of 13.00 ± 0.10 mm, and thickness of 3.00 ± 0.05 mm (solids) and 3.50 ± 0.10 mm (foams). Three experiments were performed for each material. The values reported in the text (T_g , E' , and $\tan \delta$) are the average of these three experiments, and in all cases the standard deviation was lower than 5%.

The electrical conductivity of the several solid and foamed PP-CNF nanocomposites was measured as a function of frequency between 10^{-2} and 10^6 Hz using a Novo-control impedance analyzer (HP 4192 A LF). A typical thickness of 130 μm and 1.5 mm was, respectively, used for the solid and foams. All the measurements were made by previously gold-coating the surfaces of the samples, as it has previously been shown to directly affect the measurement of the electrical conductivity [23]. Five experiments were performed for each material, in all cases the standard deviation being lower than 3%.

3. Results and Discussion

3.1. Foaming Behaviour and Cellular Structure. The material's code, density and respective gas (V_{gas}), polypropylene (V_{PP}) and filler (V_{p}) volume fractions are presented in Table 1 alongside the most characteristic cellular structure results for all the foams.

As expected, the average cell size in VD and WD directions increased with foaming ($> V_{\text{gas}}$). Results show that the cell size of the unfilled PP foams increased a lot faster than the PP-MMT ones for V_{gas} between 0.70 and 0.80 (between 250–550 μm for the first and ≈ 150 –300 μm for the second, determined as the average of the cell sizes on both directions). The MMT particles reduced the cell sizes (compare Figure 3(a) with Figure 3(c)) and narrowed the cell size distribution (AR closer to 1). The nanoparticles acted as bubble nucleators in the early stages of foaming, locally increasing the melt strength and extensibility of the polymer, thus explaining the increasingly higher cell size differences between both foams.

A good intercalation/exfoliation of the nanoparticles was mainly obtained after foaming the material (see arrows

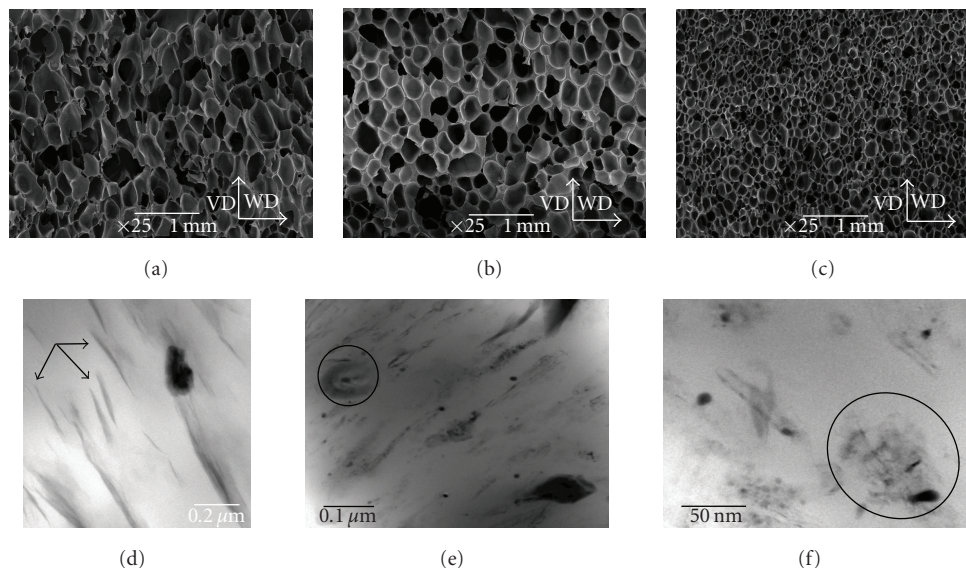


FIGURE 3: Typical SEM micrographs ($\times 25$) of the (a) unfilled PP, (b) PP-CNF, and (c) PP-MMT nanocomposite foams; (d) typical TEM picture showing partial exfoliation of the MMT platelets; (e) and (f) TEM pictures showing CNF dispersion. VD: Vertical direction of foaming; WD: Width direction.

showing partially exfoliated MMT platelets in Figure 3(d) and the WAXS results shown later), thus supporting earlier results stating that foaming could come as a useful tool to exfoliate platelet-like structures such as montmorillonite [6, 16].

In the case of the carbon nanofibre-reinforced foams (PP-CNF), the cell size decreased for similar volume gas fractions with adding increasingly higher amounts of carbon nanofibres (see Table 1). Besides, the carbon nanofibres contributed to the formation of an isotropic cellular structure, that is, foams with aspect ratios close to 1. For similar expansion ratios ($V_{\text{gas}} \approx 0.70$), a considerable cell size reduction was observed with increasing the amount of nanofibres from 550 to 250 μm , respectively, for the 10 and 20 wt.% CNF foams. A typical SEM micrograph displaying the cellular structure of the PP-CNF foams is presented in Figure 3(b).

Also presented in Figure 3 are two TEM pictures obtained at different magnifications showing the dispersion of the carbon nanofibres in the PP matrix (Figures 3(e) and 3(f)). Although some aggregates were observed (see black circles), these were a lot scarcer than in similar thermoplastic carbon nanotube-reinforced composites [28], thus supporting the combined efficiency of the melt-mixing and foaming processes.

3.2. Effects on the Crystalline Characteristics. The X-ray scattering analysis allowed studying eventual effects induced by the foaming process and incorporation of both types of nanofillers on polypropylene's crystallinity. Typical WAXS spectra of the solid and foamed nanocomposites are shown in Figure 4.

A considerable intensity shift from polypropylene's (040) diffraction peak towards the (110) was found with foaming

for all the materials. The intensity ratio between peaks, $I(040)/I(110)$, decreased for the unfilled PP from around 4 for the solid to 1.5 for the foam. A remarkable further decrease was found with foaming the nanocomposites: 1.4 to 0.9 and 1.5 to 0.9, respectively, for the MMT and CNF nanocomposite foams. This ratio is directly related to the arrangement of the b lattice parameter of the α -monoclinic polypropylene crystal, a higher value being indicative of a preferential orientation parallel to the sample's surface [29]. Despite the crystal anisotropy induced during the preparation of the solid discs, especially noticeable for the unfilled material ($I(040)/I(110) \approx 4$), foaming reduced this preferential crystal orientation. Especially relevant is the fact that foaming totally erased all possible crystal orientation in the case of the nanocomposites ($I(040)/I(110) \approx 1$).

Concerning polypropylene's crystallinity, the differences observed between the unfilled materials and the nanocomposites show that there is a less α -crystal perfection in the pure PP foams than that in the solid (lower values of the full width at half maximum, FWHM). Contrarily, the nanoparticles promoted a higher crystalline perfection (lower FWHM values for the foams).

WAXS spectra were also used to ascertain the efficiency of the melt-mixing and foaming processes in guaranteeing an intercalated/exfoliated MMT nanocomposite morphology. Analyzing the (001) MMT peak, a lower diffraction angle was obtained for the foamed nanocomposite compared to its solid counterpart, indicating an increase in the interlayer distance (d_{001}) from 2.99 nm to 4.01 nm. Nevertheless, the foaming process was not enough to promote a total exfoliation of the montmorillonite particles. Despite the decrease in intensity, the (001) peak still appeared for the foamed nanocomposite, as seen in Figure 4(b). In good agreement, TEM analysis showed that the typical morphology of the

foamed MMT nanocomposites consisted of mixed dispersed individual montmorillonite and stacks of montmorillonite platelets (see Figure 3(d)).

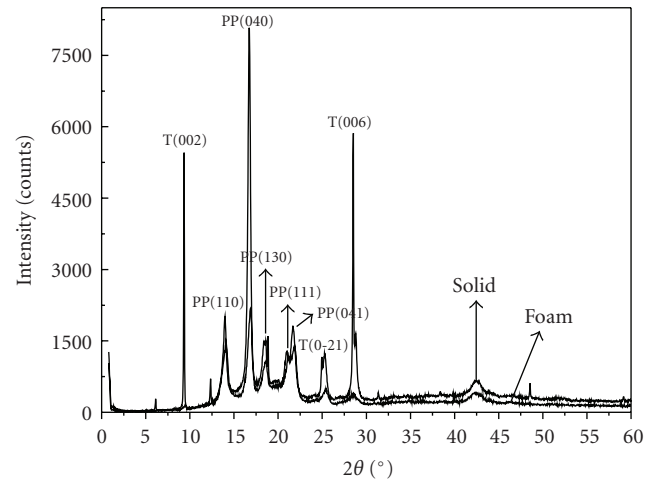
The PP-MMT nanocomposites showed a higher crystallization temperature and crystallinity than the unfilled polymer measured by DSC, indicating that the well-dispersed nanoparticles acted nucleating crystals. The same type of nucleating effect was observed with incorporating the carbon nanofibres, mainly noticeable for the higher amounts. Higher crystallization temperatures were observed with adding the montmorillonite nanoparticles as well as the carbon nanofibres: from 130.2 and 126.7°C corresponding, respectively, to the beginning and maximum of the crystallization peak of the unfilled PP to 135.3 and 132.9°C for the PP-MMT nanocomposite and 135.6 and 131.8°C for the 20 wt.% CNF material. In the case of the PP-CNF nanocomposites, the crystallization temperature measured at the maximum steadily increased around 2°C with adding the nanofibres: from the 126.7°C of PP, to 128.8°C (5 wt.% CNF), 129.6°C (10 wt.% CNF), and 131.8°C (20 wt.% CNF). The crystallinity increased from the 46.2% of the material without nanofiller to 49.0% for the PP-MMT nanocomposite and 46.5, 48.9, and 49.6%, respectively, for the 5, 10, and 20 wt.% CNF materials. See Figure 5 for comparison between the unfilled and 20 wt.% CNF foams.

3.3. Dynamic-Mechanical Thermal Analysis. Typical DMA curves of the several foamed nanocomposites are presented in the two considered directions, that is, parallel (P) and perpendicular (N) to the foam's surface, in Figure 6.

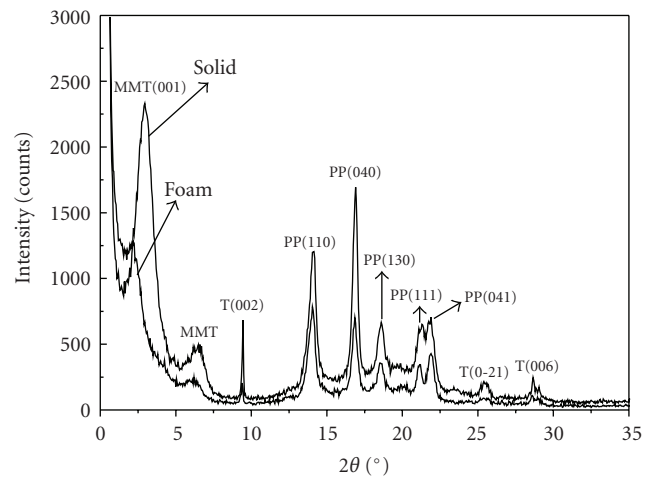
At low strain values, the main mechanisms governing the materials response are bending and stretching of the cell walls, thus enabling the study of the viscoelastic relaxations of the polymer matrix. Such is the case of the glass transition temperature (T_g), that accounts for the glass-rubber relaxation of the amorphous portions of the material. Considering that all the foams analyzed here displayed similar expansion ratios, it was possible to analyze the effects of the MMT nanoparticles and carbon nanofibres on the viscoelastic behaviour of the foams.

In the case of the CNF-reinforced nanocomposites, as seen in Table 2, the glass transition temperature (T_g) raised with increasing the amount of nanofibres, from the 5.2°C of the 5 wt.% CNF solid to the 7.3 and 7.5°C, respectively, of the 10 and 20 wt.% CNF solid nanocomposites. This is the direct result of a higher crystallinity (lower amorphous fraction) and less matrix mobility due to the presence of the nanofibres. Nevertheless, its value decreased with foaming for all the materials.

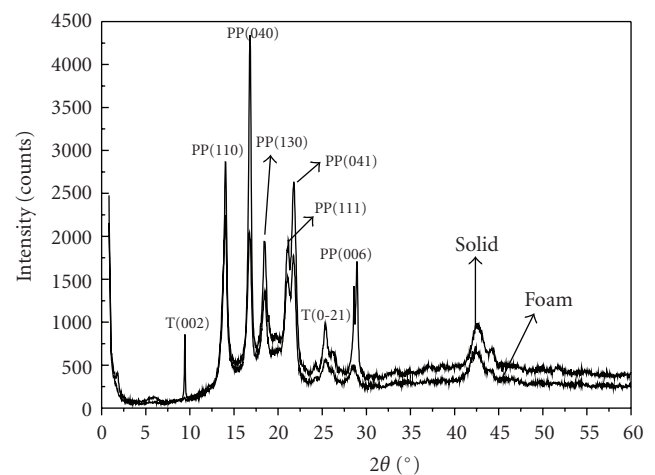
As expected, the storage modulus (E') increased with increasing the amount of carbon nanofibres. In the particular case of the foams, the storage modulus only slightly increased with CNF's content for similar relative densities. Nonetheless, the specific storage modulus, that is, the storage modulus relative to the foam's density, increased considerably with adding a higher amount of nanofibres (from the around 800 MPa·cm³/g of the 5 wt.% CNF foams to the



(a)



(b)



(c)

FIGURE 4: Typical WAXS spectra of the solid and foamed (a) unfilled PP, (b) PP-MMT and (c) PP-CNF nanocomposites.

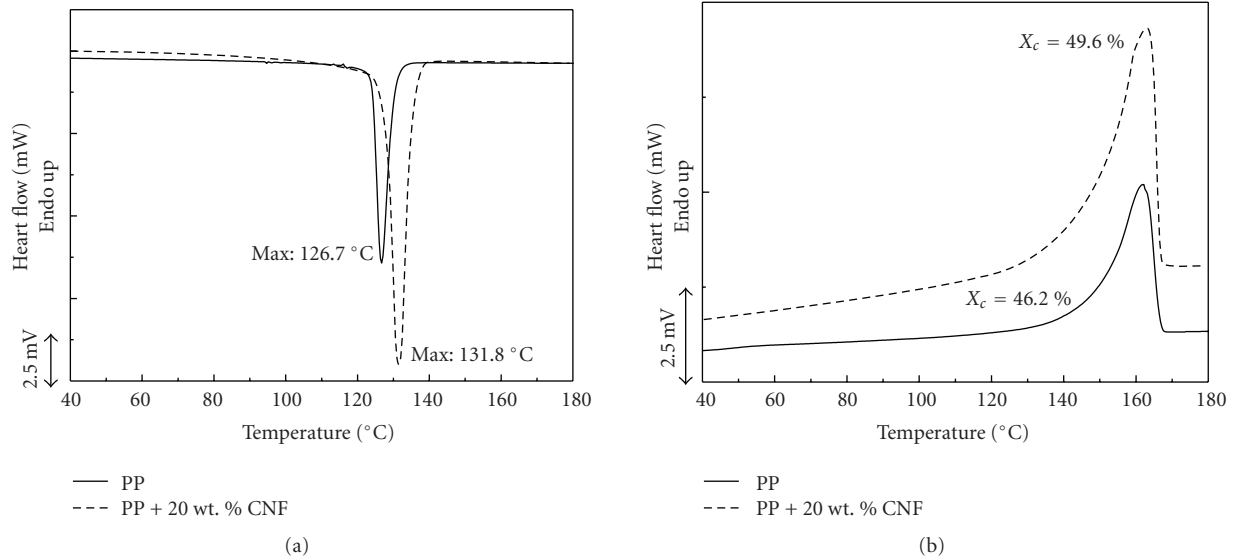


FIGURE 5: Comparative differential scanning calorimetry between the unfilled and 20 wt.% CNF PP foams showing (a) the peak's maximum crystallization temperatures and (b) crystallinity determination.

1200 MPa·cm³/g of the 20 wt.% CNF ones), indicating the carbon nanofibres efficiency as mechanical reinforcements.

Although displaying almost the same storage modulus than similar relative density unfilled PP foams, comparing the specific value, it is noticeable the reinforcement effect of the montmorillonite particles, with a more than 30% increase.

A parameter S , defined as the specific storage modulus in the parallel direction divided by that in the perpendicular direction was determined as to ascertain the isotropic mechanical properties of the foamed composites. As can be seen by the values presented in the last column of Table 2, the MMT- and CNF-reinforced foams presented a more isotropic mechanical behaviour, especially the PP-MMT nanocomposite foams, displaying an S value of 1, result of their finer isotropic-like cellular structure.

Generally speaking, the MMT nanocomposite foams displayed loss factor values ($\tan \delta$) slightly higher than the unfilled ones. Taking into account the high densities of the nanocomposite foams and these less importance of the gas enclosed inside the cells, these slight differences may be attained to the different microstructures of the polymer present in the cell walls, as has been previously shown in the partially exfoliated MMT nanoparticles to induce a higher crystallinity and less crystal anisotropy in the PP.

3.4. Electrical Conductivity Measurements. The carbon nanofibres were initially added with the main objective of developing new conductive lightweight materials. With that in mind, measurements of the electrical conductivity of the several solid and foamed PP-CNF nanocomposites were performed over a wide range of frequencies.

Figure 7 presents the broadband electrical conductivity values of the several solid and foamed nanocomposites as a function of frequency.

In the case of a 5 wt.% CNF content the electrical conductivity of the solids and foams followed a linear behaviour with frequency characteristic of insulating materials such as PP ($\sigma_{PP} \approx 10^{-16} \text{ S} \cdot \text{cm}^{-1}$). This indicates that the electrical properties of the composite are being controlled by the matrix, as the nanofibres are clearly too far apart to allow electrical conduction. Nonetheless, for a 10 wt.% CNF concentration the materials started to show a characteristic electrical conduction behaviour, displaying a critical frequency (ν_c) below which conductivity gets frequency independent (known as the direct current conductivity, σ_{dc}). For comparative purposes, the dc conductivity (σ_{dc}) was always taken at the same frequency (10^{-1} Hz).

Comparatively, foams reached a dc conductivity value earlier than the solid materials. For instance, the 10 wt.% CNF foam displayed a value of $1.06 \times 10^{-7} \text{ S/cm}$, considerably higher than the $1.22 \times 10^{-11} \text{ S/cm}$ of the respective solid. Nevertheless, this conductivity value is still low based on the theoretical value and amount of nanofibres as well as compared to other polymer systems [25]. In these cases, there is a critical concentration of filler, known as the percolation threshold, ϕ_c , where the formation of a 3D conductive network results in an abrupt increase in the electrical conductivity [30]. It has been shown that the electrical efficiency of these conductive fillers depends on the presence of polymer chains between contacts, and particularly on local crystal formation. Electrical conduction considerably decreases in the crystalline regions compared to the amorphous ones, where ion conductivity is the dominating conduction mechanism [31–33]. These particularities act to the formation of electrical resistances between the nanofibres, limiting an effective electrical conduction by percolation. Under these conditions, a model based on tunnelling conduction fits better to the analyzed system, with the dc conductivity being depicted by $\sigma_{dc} \propto \exp(-Ad)$ [34, 35], where A is a tunnel parameter and d is the

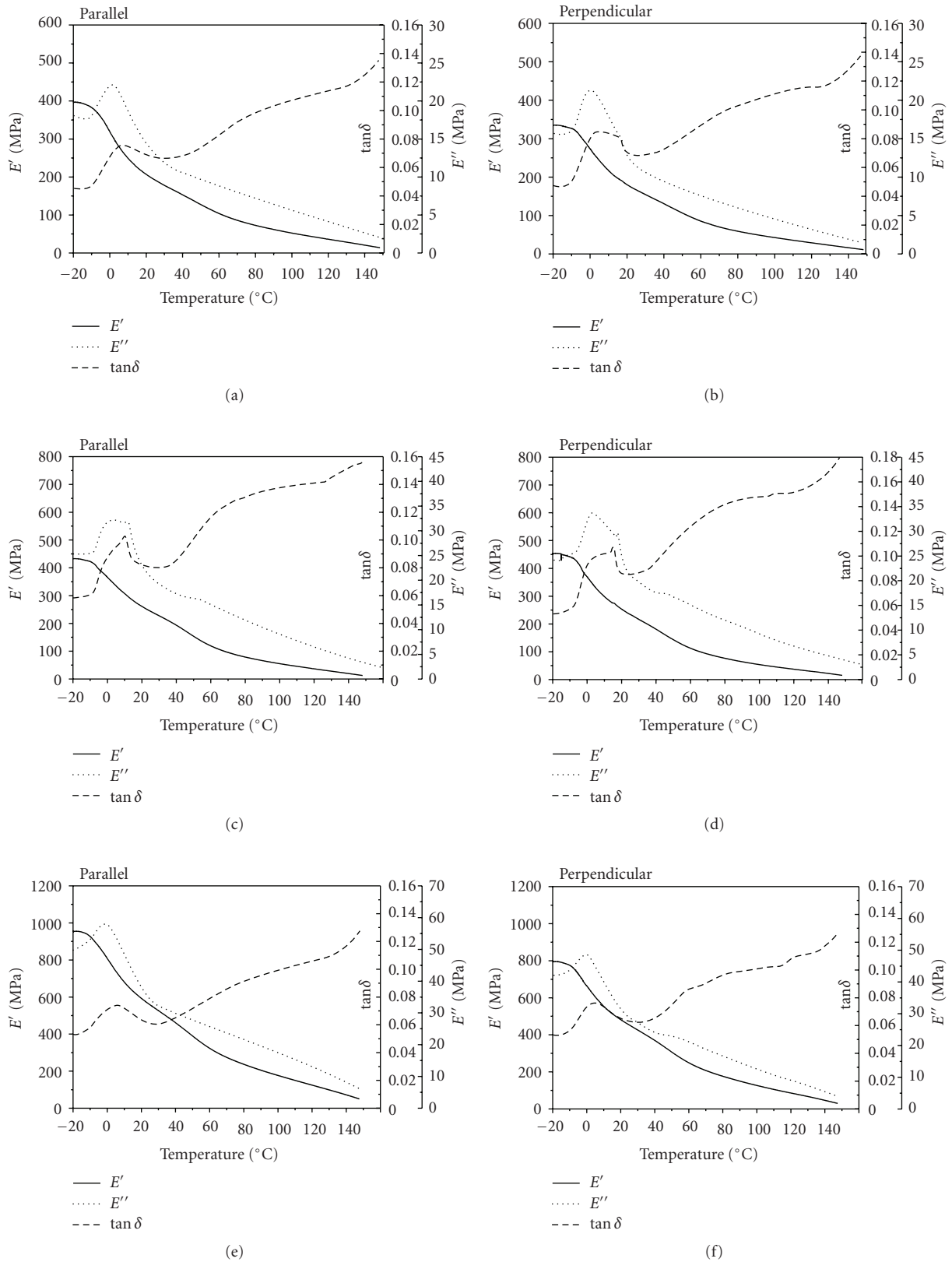


FIGURE 6: Typical DMA curves of the unfilled PP foams, (a) and (b); PP-MMT foams, (c) and (d); PP-20% CNF foams, (e) and (f).

TABLE 2: DMA results of the solid and foamed unfilled, MMT, and CNF-reinforced PP foams.

Material	Direction	T_g^* ($^{\circ}\text{C}$)	E' at 20 $^{\circ}\text{C}$ (MPa)	Specific modulus ($\text{MPa}\cdot\text{cm}^3\cdot\text{g}^{-1}$)	S
PP	Solid	5.4	1961.3	2114.4	—
	P	6.6	206.5	676.3	1.1
	N	4.7	179.9	589.2	
PP-MMT	Solid	6.0	2010.0	2152.0	—
	P	5.6	261.5	839.9	1.0
	N	5.9	252.7	823.1	
PP-5% CNF	Solid	5.2	1827.5	2006.0	—
	P	4.5	235.4	801.5	1.1
	N	2.5	209.6	713.6	
PP-10% CNF	Solid	7.3	2300.3	2532.6	—
	P	6.9	231.4	806.6	0.7
	N	5.2	328.6	1100.9	
PP-20% CNF	Solid	7.5	2732.7	2832.1	—
	P	4.5	543.5	1230.0	1.0
	N	4.3	473.6	1185.5	

* T_g —Glass transition temperature measured in $\tan \delta$.

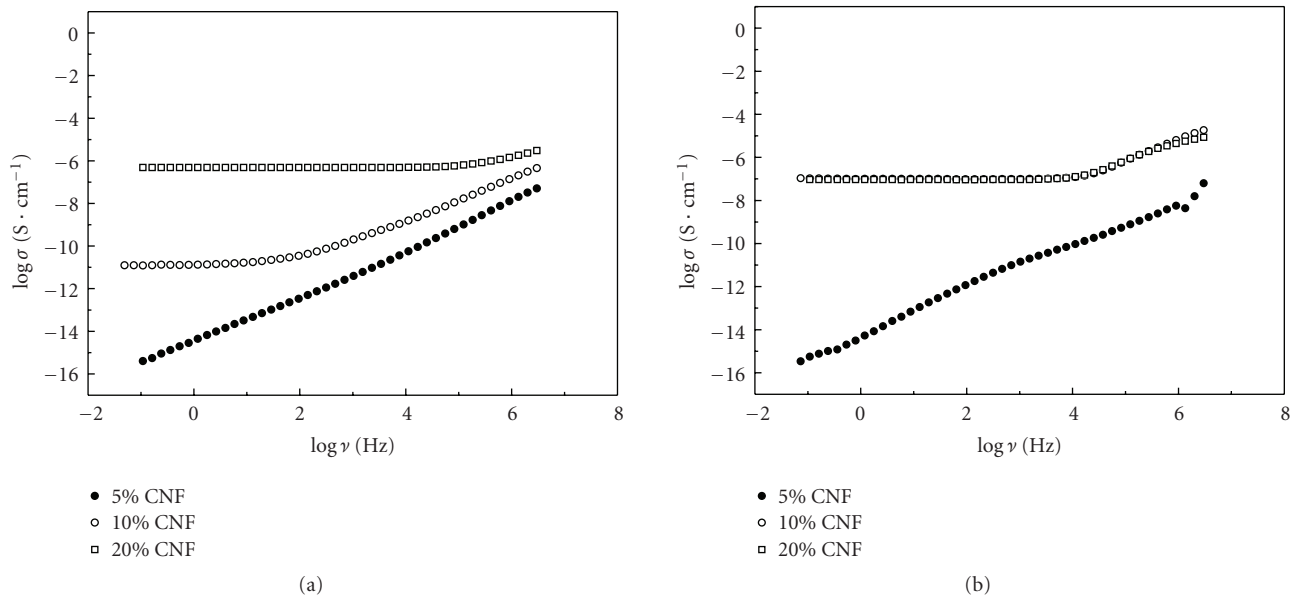


FIGURE 7: Broad-band electrical conductivity (σ) as a function of frequency (ν) for the (a) solid, and (b) foamed PP-CNF nanocomposites.

so-called tunnel distance. This predominant tunnelling conduction behaviour has been previously shown in other research works to be typical of carbon nanofibre polyolefin nanocomposites, due to fibre breaking during processing the dispersed short carbon nanofibres making it a lot harder to reach a direct contact between the fibres at low contents [36]. Using the tunnelling conduction approach, the theoretical critical concentration of nanofibres for electrical conduction for the nanocomposite foams was found to be 10 wt.% lower than the 12 wt.% determined for the solids, indicating that the foaming process is adding to a higher nanofibre functionality due to improved dispersion (see Figure 3(f)).

4. Conclusions

This work presents the preparation and preliminary characterization of montmorillonite and carbon nanofibre-reinforced rigid polypropylene foams, with the objective of developing new multifunctional lightweight materials for structural applications.

Regarding the foaming behaviour and cellular structure of the foams, the incorporation of MMT and CNF resulted in finer isometric-like cellular structures, especially noticeable for the MMT nanocomposite foams. This was attained to a cell nucleation effect, supported by the higher crystallization temperatures and crystallinities. In the case of the PP-CNF

foams, increasingly smaller cell sizes were observed for similar expansion ratios with increasing the amount of nanofibres.

The nanofillers, adding to the foaming process, totally erased the preferential crystal orientation of the α -PP's crystal observed in the unfilled solid and in a lesser extent in the unfilled PP foams (b lattice parallel to the sample's surface). Although the FWHM values of the unfilled PP increased with foaming, the incorporation of the nanofillers promoted the opposite effect, related to a higher crystalline perfection.

The dynamic-mechanical behaviour of the unfilled and nanocomposite polypropylene foams showed that the nanofillers acted as mechanical reinforcements, increasing the specific storage moduli of the foams. They also promoted a more isotropic-like mechanical behaviour, especially the MMT nanoparticles, related to a finer isotropic cellular structure of the nanocomposite foams.

As a previous step to the study of incorporating conductive nanofillers on the electrical conduction behaviour of PP foams, electrical conductivity measurements were performed on the different solid and foamed PP-CNF nanocomposites. Interesting results were found with foaming the nanocomposites, the foams displaying a higher electrical conductivity than their solid counterparts, indicating that foaming may come as a useful tool in creating an electrically-conductive network.

Acknowledgments

The financial assistance from the Spanish Ministry of Science and Education for the project MAT2007-62956 is gratefully acknowledged. The authors would like to thank Professor Miguel Mudarra for all the help with the electrical conductivity measurements.

References

- [1] M. A. Rodríguez-Pérez, "Crosslinked polyolefin foams: production, structure, properties, and applications," *Advances in Polymer Science*, vol. 184, pp. 97–126, 2005.
- [2] C. B. Park and L. K. Cheung, "A study of cell nucleation in the extrusion of polypropylene foams," *Polymer Engineering and Science*, vol. 37, no. 1, pp. 1–10, 1997.
- [3] Sekisui Alveo, *Product Guide*, Sekisui Alveo, Roermond, The Netherlands, 2003.
- [4] S. Tokuda and T. Kemmotsu, "Electron beam irradiation conditions and foam seat properties in polypropylene-polyethylene blends," *Radiation Physics and Chemistry*, vol. 46, no. 4–6, pp. 905–908, 1995.
- [5] P. Spital, C. W. Macosko, and A. Sahnoune, "Extensional rheology of polypropylene and its effect on foaming of thermoplastic elastomers," in *Proceedings of the Annual Technical Conference (ANTEC '02)*, pp. 1792–1796, Society of Plastics Engineers, San Francisco, Calif, USA, 2002.
- [6] M. Antunes, J. I. Velasco, V. Realinho, and E. Solórzano, "Study of the cellular structure heterogeneity and anisotropy of polypropylene and polypropylene nanocomposite foams," *Polymer Engineering and Science*, vol. 49, no. 12, pp. 2400–2413, 2009.
- [7] N. Mills, *Polymer Foams Handbook. Engineering and Biomechanics Applications and Design Guide*, Elsevier, Oxford, UK, 1st edition, 2007.
- [8] D. Klemperer and V. Sendjarevic, *Polymeric Foams and Foam Technology*, Hanser, Munich, Germany, 2nd edition, 2004.
- [9] R. R. Puri and K. T. Collington, "The production of cellular crosslinked polyolefins. 2. The injection-molding and press molding techniques," *Cellular Polymer*, vol. 7, pp. 219–231, 1988.
- [10] UK Zotefoams. High Performance Polymers, October 1999.
- [11] D. Eaves, *Handbook of Polymer Foams*, Rapra Technology, Shawbury, UK, 2004.
- [12] M. Antunes, V. Realinho, and J. I. Velasco, "Study of the influence of the pressure drop rate on the foaming behaviour and dynamic-mechanical properties of CO₂ dissolution microcellular polypropylene foams," *Journal of Cellular Plastics*. In press.
- [13] J. I. Velasco, M. Antunes, O. Ayyad, et al., "Foaming behaviour and cellular structure of LDPE/hectorite nanocomposites," *Polymer*, vol. 48, no. 7, pp. 2098–2108, 2007.
- [14] J. E. Martini, N. P. Suh, and F. A. Waldman, US patent 4,473,665, 1984.
- [15] L. J. Lee, C. Zeng, X. Cao, X. Han, J. Shen, and G. Xu, "Polymer nanocomposite foams," *Composites Science and Technology*, vol. 65, pp. 2344–2363, 2005.
- [16] C. Zeng, X. Han, L. J. Lee, K. W. Koelling, and D. L. Tomasko, "Polymer-clay nanocomposite foams prepared using carbon dioxide," *Advanced Materials*, vol. 15, no. 20, pp. 1743–1747, 2003.
- [17] Y. Di, S. Iannace, E. Di Maio, and L. Nicolais, "Poly(lactic acid)/organoclay nanocomposites: thermal, rheological properties and foam processing," *Journal of Polymer Science—Part B*, vol. 43, no. 6, pp. 689–698, 2005.
- [18] X. Han, C. Zeng, L. J. Lee, K. W. Koelling, and D. L. Tomasko, "Extrusion of polystyrene nanocomposite foams with supercritical CO₂," *Polymer Engineering and Science*, vol. 43, no. 6, pp. 1261–1275, 2003.
- [19] M. Okamoto, P. H. Nam, P. Maiti, et al., "Biaxial flow-induced alignment of silicate layers in polypropylene/clay nanocomposite foam," *Nano Letters*, vol. 1, no. 9, pp. 503–505, 2001.
- [20] M. Lee, B.-K. Lee, and K.-D. Choi, "Foam compositions of polyvinyl chloride nanocomposites," WO/2004/074357, International Application No.: PCT/KR2004/000328. 2004.
- [21] J. Shen, X. Han, and L. J. Lee, "Nucleation and reinforcement of carbon nanofibers on polystyrene nanocomposite foam," in *Proceedings of the 63rd Annual Technical Conference (ANTEC '05)*, vol. 7, pp. 117–121, November 2005.
- [22] M. Antunes, V. Realinho, A. B. Martínez, E. Solórzano, M. A. Rodríguez-Pérez, and J. I. Velasco, "Heat transfer of mineral-filled polypropylene foams," *Defect and Diffusion Forum*, vol. 297–301, pp. 990–995, 2010.
- [23] M. Antunes, J. I. Velasco, V. Realinho, and D. Arencón, "Characterization of carbon nanofibre-reinforced polypropylene foams," *Journal of Nanoscience and Nanotechnology*, vol. 10, pp. 1241–1250, 2010.
- [24] M. Antunes, V. Realinho, E. Solórzano, M. A. Rodríguez-Pérez, J. A. de Saja, and J. I. Velasco, "Thermal conductivity of carbon nanofibre-polypropylene composite foams," *Defect and Diffusion Forum*, vol. 297–301, pp. 996–1001, 2010.
- [25] M. Shaffer and J. Sandler, "Carbon nanotube/nanofibre polymer composites," in *Processing and Properties of Nanocomposites*, S. Advani, Ed., pp. 1–59, World Scientific, River Edge, NJ, USA, 2006.

- [26] G. L. A. Sims and C. Khunniteekool, "Cell size measurement of polymeric foams," *Cellular Polymers*, vol. 13, no. 2, pp. 137–146, 1994.
- [27] B. Wunderlich, *Thermal Analysis*, Academic Press, New York, NY, USA, 1990.
- [28] J. Sandler, G. Broza, M. Nolte, K. Schulte, Y.-M. Lam, and M. S. P. Shaffer, "Crystallization of carbon nanotube and nanofiber polypropylene composites," *Journal of Macromolecular Science*, vol. 42, no. 3-4, pp. 479–488, 2003.
- [29] J. I. Velasco, C. Morhain, A. B. Martínez, M. A. Rodríguez-Pérez, and J. A. de Saja, "The effect of filler type, morphology and coating on the anisotropy and microstructure heterogeneity of injection-moulded discs of polypropylene filled with aluminium and magnesium hydroxides. Part 1. A wide-angle X-ray diffraction study," *Polymer*, vol. 43, no. 25, pp. 6805–6811, 2002.
- [30] D. Stauffer and A. Aharony, *Introduction to Percolation Theory*, Taylor & Francis, London, UK, 2nd edition, 2003.
- [31] P. Pötschke, M. Abdel-Goad, I. Alig, S. Dudkin, and D. Lellinger, "Rheological and dielectrical characterization of melt mixed polycarbonate-multiwalled carbon nanotube composites," *Polymer*, vol. 45, no. 26, pp. 8863–8870, 2004.
- [32] I. Alig, S. M. Dudkin, W. Jenninger, and M. Marzantowicz, "Ac conductivity and dielectric permittivity of poly(ethylene glycol) during crystallization: percolation picture," *Polymer*, vol. 47, p. 1722, 2006.
- [33] I. Alig, D. Lellinger, S. M. Dudkin, and P. Pötschke, "Conductivity spectroscopy on melt processed polypropylene-multiwalled carbon nanotube composites: recovery after shear and crystallization," *Polymer*, vol. 48, no. 4, pp. 1020–1029, 2007.
- [34] E. K. Sichel, J. I. Gittleman, and P. Sheng, "Tunneling conduction in carbon-polymer composites," in *Carbon Black Polymer Composites: The Physics of Electrically Conducting Composites*, E. K. Sichel, Ed., Marcel Dekker, New York, NY, USA, 1982.
- [35] N. Ryvkina, I. Tchmutin, J. Vilčáková, M. Pelíšková, and P. Sába, "The deformation behavior of conductivity in composites where charge carrier transport is by tunneling: theoretical modeling and experimental results," *Synthetic Metals*, vol. 148, no. 2, pp. 141–146, 2005.
- [36] A. Linares, J. C. Canalda, M. E. Cagiao, et al., "Broadband electrical conductivity of high density polyethylene nanocomposites with carbon nanoadditives: multiwall carbon nanotubes and carbon nanofibers," *Macromolecules*, vol. 41, no. 19, pp. 7090–7097, 2008.

Research Article

Enhancing Fatigue Performance of Sandwich Composites with Nanophased Core

S. Zainuddin,¹ H. Mahfuz,² and S. Jeelani¹

¹ Center for Advanced Materials (T-CAM), Tuskegee University, Tuskegee, AL 36088, USA

² Department of Ocean and Mechanical Engineering, Florida Atlantic University, Boca Raton, FL 33431, USA

Correspondence should be addressed to H. Mahfuz, hmahfuz@fau.edu

Received 27 October 2009; Accepted 31 March 2010

Academic Editor: Gaurav Mago

Copyright © 2010 S. Zainuddin et al. This is an open access article distributed under the Creative Commons Attribution License, which permits unrestricted use, distribution, and reproduction in any medium, provided the original work is properly cited.

We report fatigue performance of sandwich composites with nanophased core under shear load. Nanophased core was made from polyurethane foam dispersed with carbon nanofiber (CNF). CNFs were dispersed into part-A of liquid polyurethane through a sonication process and the loading of nanoparticles was 1.0 wt%. After dispersion, part-A was mixed with part-B, cast into a mold, and allowed to cure. Nanophased foam was then used to fabricate sandwich composites. Static shear tests revealed that strength and modulus of nanophased foams were 33% and 19% higher than those of unreinforced (neat) foams. Next, shear fatigue tests were conducted at a frequency of 3 Hz and stress ratio (R) of 0.1. S-N curves were generated and fatigue performances were compared. Number of cycles to failure for nanophased sandwich was significantly higher than that of the neat ones. For example, at 57% of ultimate shear strength, nanophased sandwich would survive 400,000 cycles more than its neat counterpart. SEM micrographs indicated stronger cell structures with nanophased foams. These stronger cells strengthened the sub-interface zones underneath the actual core-skin interface. High toughness of the sub-interface layer delayed initiation of fatigue cracks and thereby increased the fatigue life of nanophased sandwich composites.

1. Introduction

In most of the applications, sandwich beams are subjected to repetitive transverse loading. Because of this, sandwich beams constituents are subjected to a variety of loading situations. The face sheets exhibit membrane tension/compression behavior, and the core undergoes the most critical stress, that is, pure shear [1]. The most common failure of sandwich construction is the core shear failure that occurs when the shear stress reaches its critical value [2]. Many researchers have studied sandwich structures emphasizing face sheets, and it is generally agreed that behavior of face sheets is well known. On the other hand, comparatively less has been done to study the core behavior of sandwich structures. It has been demonstrated over time [3, 4] that during flexural or shear loading, core basically controls the failure and is first to fail. Studies [5, 6] on the flexural behavior of foam core sandwiches showed that numerous cracks are initiated in the core sub-interface area. These cracks grow together and propagated on the

compression side of the beam, immediately below the sub-interface. Cracks propagate parallel to the beam up to a short length, then kink into core, and proceed as core shear until it reaches the sub-interface zone on the tension side of the specimen. Shipsha et al. [7] performed tests on H100 foams and found that crack continuously propagated along the interface in the core material below the resin rich cells with diagonal secondary fracture cracks. In all these cases, core shear stresses produced global deformation. Therefore it will be highly beneficial to enhance the core material properties which can offer high resistance to failure.

Recent advances in nanocomposites showed significant improvement in mechanical and thermal properties [8–11]. One additional advantage in nanocomposites is that in order to achieve these enhancements, it requires only a small wt%, typically 1–3 wt%, loading of nanoparticles [12, 13]. Experimental results of nanophased composites have shown significant increase in strength and modulus [5, 14, 15] and decrease in permeability, flammability, and shrinkage [16–18]. One of the present authors also showed

that by infusing a small percentage of nanoparticles in the foam, the static properties of sandwich structures can also be enhanced under flexural loading [19]. Similar trend has been demonstrated when nanophased sandwich structures were tested under compression and high strain rate loadings [20].

As far as particles are concerned, vapor-grown carbon nanofibers (CNFs) are drawing significant attention due to their high strength, modulus, and relatively low cost [21, 22]. These particles are synthesized from pyrolysis of hydrocarbon or carbon monoxide in the gaseous state, in presence of a catalyst [23, 24]. As opposed to carbon nanotubes (CNTs), CNFs do not have tubular structure—rather they have carbon fiber-like structure with diameter in the nanometer range and a good aspect ratio. Carbon nanofibers have been used in this investigation as reinforcement. One of the main reasons to use CNF as reinforcement was of course the cost but more than that was the acicular aspect of CNF. Carbon nanofibers having large aspect ratio would allow more entanglement with polymer chains at the mesophase stage of the foaming process. This entanglement of CNFs with the polymer would introduce interfacial tension when stresses are applied and allow large deformation—a property that would be desirable under shear and fatigue loading.

Uniform dispersion of nanoparticles poses another problem in the preparation of nanocomposites. Due to high surface energy, nanoparticles tend to agglomerate and produce unwanted stress concentration which may act as a precursor for failure. High-intensity ultrasonic waves have been used successfully to get uniform dispersion of nanoparticles [25, 26]. Ultrasound waves generate nonlinear effects in the liquid, namely transient cavitation and acoustic streaming [27–30]. Acoustic cavitation involves formation, growth, pulsating, and collapsing of minute bubbles, producing transient (in the order of microseconds) microhot spots that can reach temperatures of about 5000°C, pressure of about 1000 atm, and heating and cooling rates above 1010 K/s [31]. Strong acoustic impact coupled with local high temperature effects accelerates intrinsic mixing of polymer and nanoparticles and can break the agglomerated particles by damaging the Coulomb and Van der Waals forces resulting in a homogenous dispersion.

Mechanical behavior of foam cores for simple stress states such as uniaxial tension or compression has been studied extensively [32–35]. Only a limited number of investigations have dealt with multiaxial behavior [36, 37]. In this study, polyurethane foam properties have been modified by dispersing nanoparticles through sonic cavitation. Sandwich panels were then fabricated using the nanophased foam as core materials through the CIRT process. In parallel, control sandwich panels were also made using neat polyurethane foam. Response of these sandwich structures under static and cyclic shear loading are described in the paper.

2. Materials and Manufacturing of Sandwich Composites

Materials used for making two categories of sandwich composites are shown in Table 1. The manufacturing of panels

was carried out in three steps; the first was the dispersion of nanoparticles into liquid polyurethane, the second was casting of the foam (core materials), and the final was fabrication of sandwich panels using CIRT process. In addition, a number of sandwich panels were also made with neat polyurethane foam without having any nanoparticle infusion.

2.1. Dispersion of Nanoparticles into Liquid Polyurethane.

The steps used for dispersion of nanoparticles in liquid foam are shown in Figure 1. The liquid foam has two parts: part A (Diphenylmethane Diisocyanate) and part B (Fluorocarbon blown Polyol). Part A was selected for infusion of nanoparticles since it is less reactive than part B. Carbon nanofibers (CNFs) were first measured to have 1% by weight of part-A plus part-B (step 1). It was observed that beyond 1.0 wt% loading, agglomeration increased significantly and the cell structures were collapsing. In our earlier investigations [5, 11, 20] nanoparticle loading also remained within 1–3 wt%. The mixing was carried out in a Sonic Vibra Cell ultrasonic liquid processor (Ti-horn, 20 kHz, 100 W/cm²) for about 30 minutes at 5°C temperature (step 2). At this time it was visually observed that nanoparticles were uniformly dispersed in Part-A. We varied the sonication parameters time, frequency, and intensity many times to come up with 30 minutes, 20 kHz, and 100 W/cm², respectively as optimum parameters for the system. After each trial, foam was made and looked under SEM to check the cell structures—if they were broken or collapsed, parameters were changed until we came up with the best possible cell structure. In order to avoid temperature rise during sonication, external cooling was applied for the entire period of irradiation. External cooling was applied through an NESLAB RTE Series refrigerated bath. After infusion of nanoparticles, the modified Part-A was mixed with Part-B at a ratio of 48 : 52 by weight using a mechanical stirrer at 2500 rpm for about 30 s (step 3). The mixture was then cast into a mildly preheated steel rectangular mold. After about 8–9 hours, the cast foam (step 4) was demolded and postcured for about 20 minutes at 80°F. The density of the foam in both categories was measured to be around 0.08 g/cc.

2.2. Sandwich Fabrication.

CIRT process was employed to fabricate the sandwich panels. Both the top and bottom face sheets were infused simultaneously during the CIRT process. A schematic of the co-injection process is shown in Figure 2. Dry fabric preforms with required orientations were first laid out on the top of a flat aluminum tool. The fabric used in this investigation was plane weave S2-Glass fibers. Three layers of fabrics were used for each face sheet. The core was then placed on the top of the bottom face sheet fabrics, and upon which the preforms for the top face sheets were stacked. Two types of core materials were used during the fabrication; one was neat polyurethane, and the other was dispersed with CNF. After stacking, infusion lines were installed and the assembly was vacuum bagged. Before infusion the system was debulked for several hours. SC-15 epoxy resin (Part-A: epoxy, Part-B: Hardener, Alkyl Polyamine) manufactured by Applied Poceramic, Inc. was used in this study due to its low viscosity (300 cps) and longer

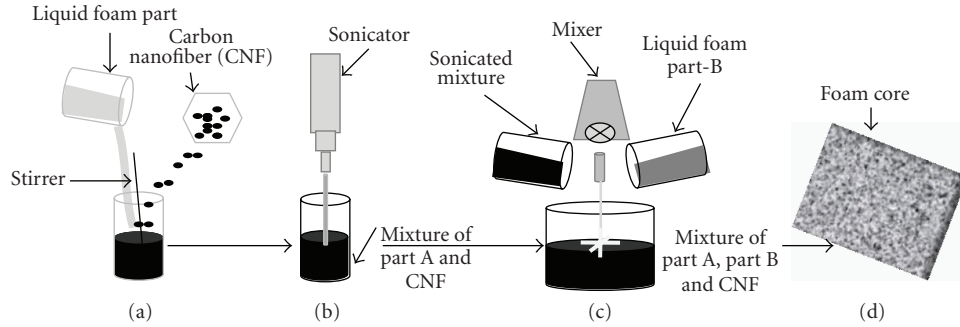


FIGURE 1: Schematic of manufacturing of nanophased PU foam: (a) step 1; (b) step 2; (c) step 3; (d) step 4.

TABLE 1: Materials used for sandwich construction.

	Face sheet (skin)		Foam	Core materials
	Fiber	Resin		Nanoparticles(CNF)
No. of layer 3	S-2 Glass 240 F	Epoxy SC-15	Polyisocyanurate density 80 Kg/m ³	Purity: 95%, density: 1.95 g/cm ³ , diameter: 70–200 nm, length: 50–100 μm

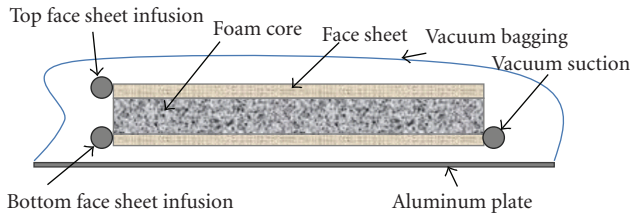


FIGURE 2: Schematic of co-injection resin transfer molding (CIRTM) process.

pot life (6 hours). After the resin infusion, the vacuum was kept on until the complete cure took place. No additional adhesives were used for the skin-core bonding, since it developed during the cure process. It is to be noted here that the surfaces of the nanophased foams had to be sanded prior to setting them up in the CIRTM mold. This allowed better adhesion between the core and the skin. Several panels were fabricated in this manner and were machined for shear characterization.

3. Experimental Procedure

3.1. Quasistatic Shear Tests. Several test coupons of neat and nanophased polyurethane foam sandwich specimens of dimension 40 mm × 160 mm were cut from 12.5 mm thick panels, using a diamond-coated steel blade, as per ASTM C273-61 standard test method. The specimen was bonded between the two parallel loading steel plates as shown in the test set-up in Figure 3(a) which shows the schematic of the shear fatigue test fixture. The arrows indicate the

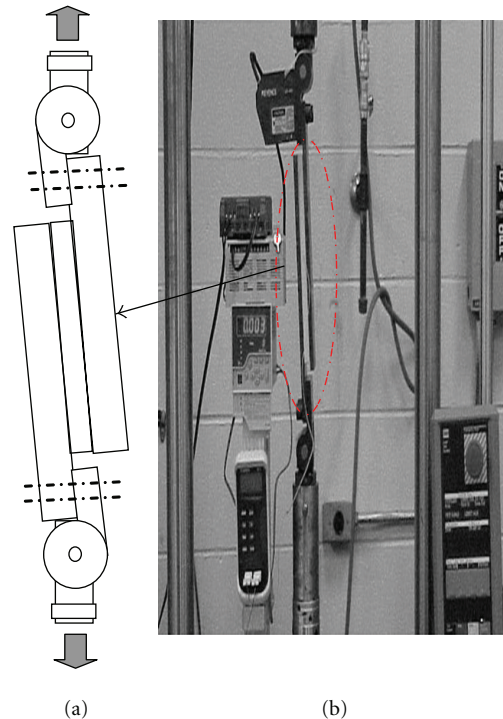


FIGURE 3: (a) Schematic of shear text fixture. (b) Photograph showing experimental setup.

direction of loading. The steel plates were truly parallel since a small deviation in parallelism of the loading plates can cause considerable errors in the calculation of the shear strength and shear modulus. A two-part epoxy, Hysol EA 9309.3NA was used as the adhesive to bond the sandwich

TABLE 2: Quasi-static shear test results.

Property	Neat Polyurethane Foam Sandwich	1% CNF Polyurethane Foam sandwich	% Improvement
Shear Strength (MPa)	0.55	0.83	+33
	0.64	0.81	
	0.66	0.78	
	Ave.: 0.61 ± 0.014	Ave. : 0.81 ± 0.02	
Shear Modulus (Mpa)	11.7	13.7	+19
	11.9	14.9	
	12.4	14.4	
	Ave. : 12.0 ± 0.35	Ave. : 14.3 ± 0.32	

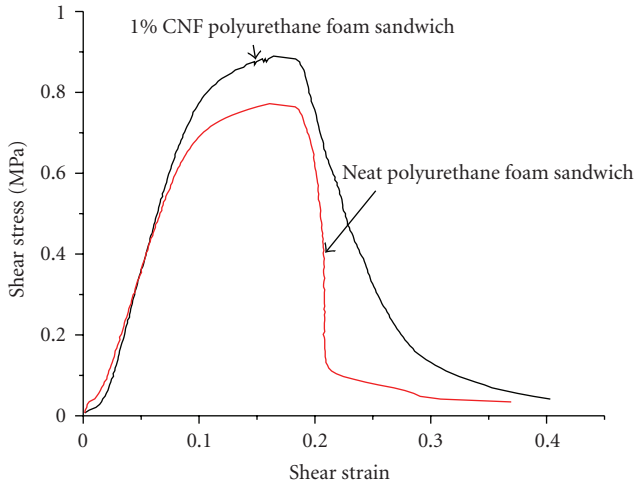


FIGURE 4: Stress-Strain curves for pure and nanophased foam sandwich.

samples to the steel plates. The epoxy was allowed to cure at room temperature for a minimum of 48 hours prior to testing. The fixture was installed in a servo hydraulic testing machine (MTS) fitted with a 100 kN load cell as shown in Figure 3(b). The tests were conducted at room temperature in displacement control mode at a cross-head speed of 1.27 mm/min. A Keyence laser displacement unit coupled to an RD-50R controller was installed (Figure (3b)) to measure the sliding movement of the loading plates relative to each other in the direction parallel to the loading plates.

The shear stress, τ , is given by

$$\tau = \frac{P}{Lb}, \quad (1)$$

where P is the load on the specimen, L is the length of the specimen, and b is its width. The shear strain, γ , is

$$\gamma = \frac{r}{c}, \quad (2)$$

where r is the displacement of one loading plate with respect to the other and, c , denotes the thickness of the core.

3.2. Shear Fatigue Tests. Shear fatigue tests were performed in accordance to ASTM 394-62 at room temperature under load control on the sandwich specimens at a load ratio of $R = |P_{\min}|/|P_{\max}| = 0.1$, using an MTS machine at a frequency of 3 Hz. The runout cycle number was set at 10^6 cycles. Fatigue data for a minimum of three specimens in each category of sandwich composites were generated at stress levels of 90%, 80%, 70%, 60%, and 50% of the ultimate static shear strength.

3.3. Microscopic Analysis. Virgin surfaces were examined in a JEOL JSM 5800 scanning electron microscope. The specimens were glued to an aluminum base and coated with gold to prevent charge build-up by the electrons absorbed by the specimen. Microstructural analysis was performed on both neat and nanophased polyurethane foams.

4. Results and Discussion

4.1. Quasi-Static Shear Tests. Quasi-static shear tests were conducted primarily to obtain strength values for the fatigue tests. Load was applied to the neat and nanophased sandwich specimens via the steel plates as shown in Figure 3(b). The laser displacement unit recorded displacement of the moving steel plate relative to the fixed plate. This displacement was used to calculate the shearing strain, γ . Figure 4 shows representative stress-strain (τ - γ) curves for neat and nanophased sandwiches. Shear strength of nanophased foam as seen in Figure 4 was higher than that of neat. At the initial stage of loading small cracks were noticed in the core near the edge of the specimen. As the loading continued, the specimen elongated, small cracks coalesced into a dominant crack, and kinked into the core. Crack formation and propagation were identical with both categories of foams, but elongation with nanophased foam was higher. In the next sequence, rapid shearing of the core occurred and the specimen failed at the sub-interface section and also diagonally across the thickness of the core. Nanophased foam core sandwich demonstrated more ductile behavior than neat sandwich. This ductility is evident by the longer shear deformation region for nanophased sandwich seen in Figure 4. The large difference in the shear elongation clearly demonstrates that nanophased foam core has higher resistance to shear failure.

High shear deformation with the nanophased foam is due to dissipation of energy at multiple sites created by CNF/PU interfaces. Polymer chemistry and kinetics are different at these interfaces and can be viewed as nanoscale defects in the polymer. Energy at crack tips can be easily dissipated into these defects attributing an effective energy absorption feature to the nanocomposites.

Shear strength and modulus data for quasi-static tests are shown in Table 2. Improvement in strength and modulus were approximately 33% and 19% higher than those of the neat foam sandwiches. An approximation of the area under the curves in Figure 4 suggests that the energy absorption capability of nanophased foam sandwich is almost 30% more than that of the neat foam sandwich.

The crack propagation in the core during quasi-static loading was very similar to what was observed earlier with PVC foams [4]. A schematic of the core shear process is shown in Figure 5. First, crack initiated at the free edge in the uppermost section of the specimen adjacent to the core-skin interface. The crack then propagated parallel to the plate for a short distance, after which it kinked into the core moving diagonally towards the opposite end. This diagonal shearing event was the final failure mode in both categories of sandwich specimens. In few specimens, free-edge effects occurred, that is, the core tore apart from the skin at the free ends in the upper corners.

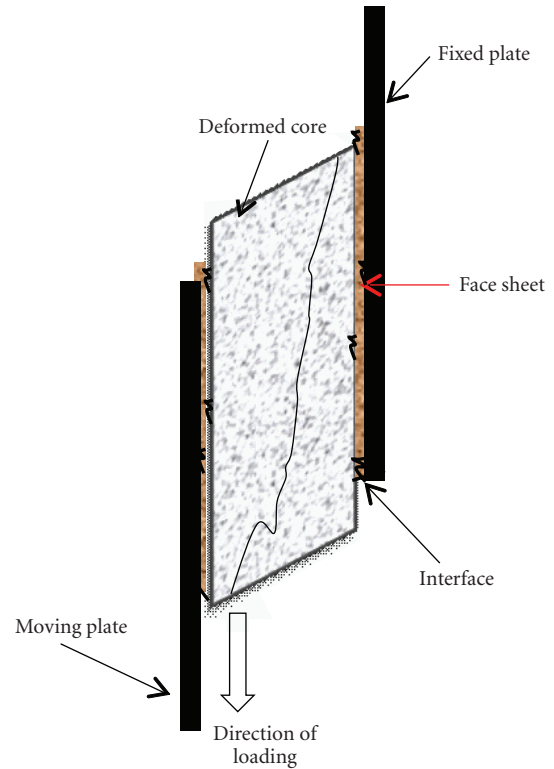


FIGURE 5: Schematic of crack propagation during static loading.

4.2. Fatigue Tests. Shear fatigue data for both neat and nanophased sandwich composites are shown in Table 3. S-N (stress versus number of cycles) diagram for the fatigue tests is shown in Figure 6. The stress axis is normalized with ultimate shear strength. Data shown in the S-N diagram are the average values from Table 3. Under constant amplitude loading many engineering materials exhibit a plateau in the stress life plot typically beyond 10^6 cycles, which is also true in this case. The fatigue limit is seen to be about 55% of the ultimate strength for the nanophased specimen while it is 50% for neat specimen. It is seen in Figure 6 and in Table 3 that at each stress level, the number of cycles to failure for nanophased foam was significantly higher than that of neat specimen. The failure process in both the nanophased and neat sandwiches was similar to that of PVC foam sandwich composites studied by one of the authors [4]. Fatigue failure modes are shown in Figure 7. Small cracks first appeared near the core-skin interface that coalesced into several larger cracks and progressed along the interface. After propagating for a relatively short distance, these larger cracks as seen in Figure 7 kinked into the core and traversed through the thickness of the core. This suggests that during fatigue as well as in static loading, the weakest region in a sandwich composite is the core-skin interface region which is prone to failure at the initial stage of the loading. These minute cracks coalesce into one or many major cracks depending on the type of loading. If it is quasi-static, usually there is only one major crack. However in case of fatigue loading the number of major cracks is several. During quasi-static loading, the major crack kinks into the core at a sharp angle and diagonally crosses the entire thickness of the core.

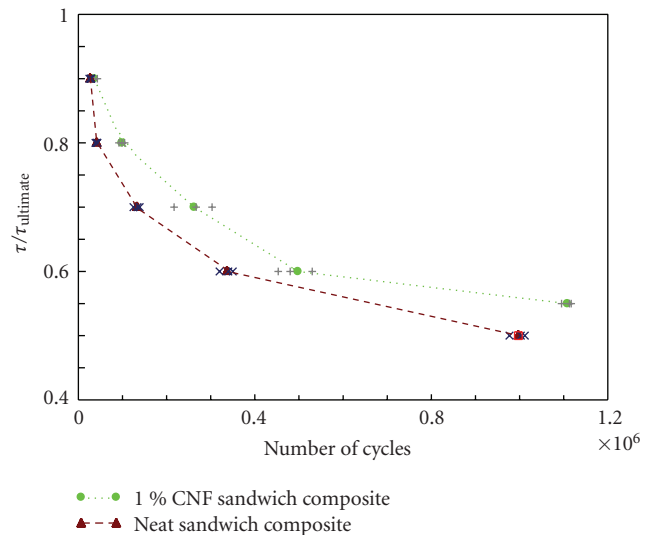


FIGURE 6: S-N curves for neat and nanophased specimens. Stress ratio $R = 0.1$ and frequency = 3 Hz.

During fatigue the scenario is somewhat different—large cracks kink into the core at multiple places and propagate at about $20\text{--}40^\circ$ angle. Cracks kinking into the core in fact signals the final failure event as the core shear process is very quick. As seen in Figure 7, some of the shear cracks reach the interface on the opposite side depending on the energy available at the crack tip and resistance offered by the embedded nanoparticles.

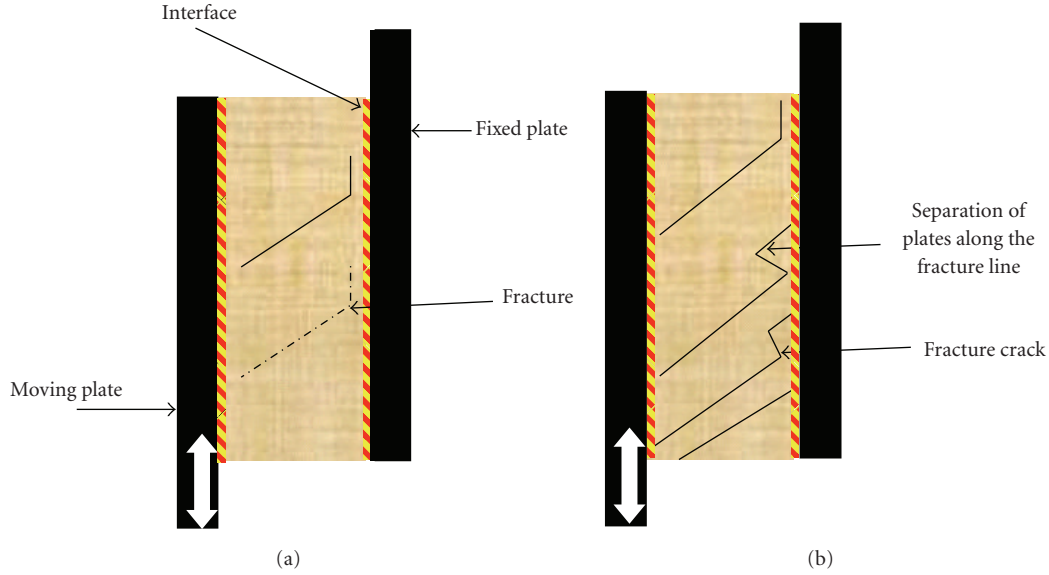


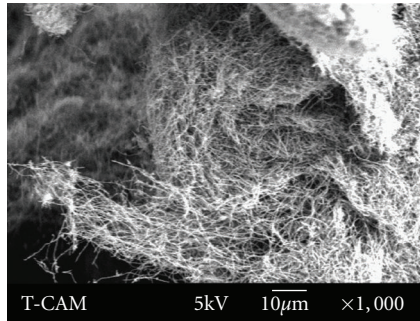
FIGURE 7: (a) Schematic of crack formation in the core and (b) schematic showing the line along which final shearing occurs.

TABLE 3: Fatigue test data for neat and 1% CNF sandwich composites.

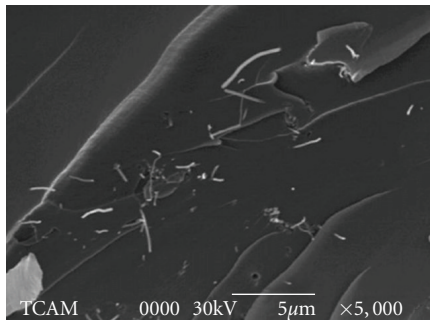
Material	Number of Cycles $\times 10^6$				
	90% $\tau_{ultimate}$	80% $\tau_{ultimate}$	70% $\tau_{ultimate}$	60% $\tau_{ultimate}$	50% $\tau_{ultimate}$
Neat PUF Sandwich Composite	0.025	0.043	0.125	0.32	0.977
	0.028	0.039	0.134	0.34	1.003
	0.03	0.04	0.14	0.35	1.01
	Avg. : 0.027 ± 0.002	Avg. : 0.041 ± 0.002	Avg. : 0.13 ± 0.01	Avg. : 0.37 ± 0.02	Avg. : 1.0 ± 0.02
1% CNF PUF Sandwich Composite	0.029	0.092	0.217	0.453	1.095
	0.036	0.099	0.267	0.48	1.117
	0.043	0.105	0.303	0.53	1.113
	Ave. : 0.04 ± 0.01	Avg. : 0.10 ± 0.01	Avg. : 0.26 ± 0.04	Avg. : 0.49 ± 0.04	Avg. : 1.11 ± 0.01

4.3. SEM Analysis. To investigate the dispersion of nanoparticles and their effect on the foam microstructures, SEM analyses were carried out on both neat and nanophased foam as shown in Figures 8(a)-8(d). It was observed that as-received CNFs were agglomerated due to high surface energy as shown in Figure 8(a). Since the length of CNF is in the order of micron, it is possible to observe individual CNF-dimensional parameters. The diameter of CNF was measured to be about 200 nm, which agrees with the data sheet [38]. Embedded CNFs in the cell edges are shown in Figure 8(b). Figure 8(b) also indicates that the CNFs were well separated and dispersed. The micrographs (c) and (d) show that both neat and nanophased foams have a fairly uniform distribution of regular cells. As seen in these figures, cell edges and walls are distinctly visible with almost uniform cell structures throughout. It is observed in the micrographs that CNF nanoparticle has somewhat different effect on the microstructure of the cell as it was observed in earlier studies [5, 11, 20]. In the present case the size of the cell does not change whereas the shape of the cell has changed significantly—from spherical to pentagon or hexagonal shape. It is well known that closed cell foam

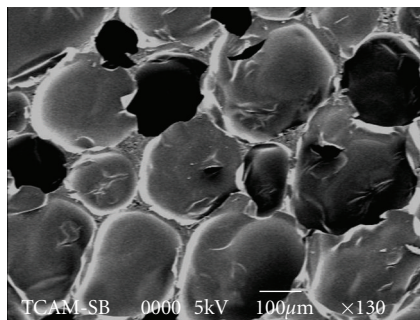
derives its strength from its edges, walls, faces, and the entrapped gas. Nanophased core will provide more resistance to crack propagation due to its hexagonal shape, relatively thicker edges, and walls as seen in Figure 8(d). It is quite possible that as the resin gets filled into the partially opened cells, it soaks the cell walls and edges up to a certain depth. When the resin is cured, these soaked cells become stronger than the regular dry cells just underneath. A sub-interface is therefore created between these so-called soaked and dry cells, which are apparently weaker than the actual core-skin interface mentioned earlier. It is indicated in earlier studies [11, 20] that nanoparticle acts as a catalyst during the foaming process and controls the rate of CO_2 generation, which in turn affects the cell wall and edge thicknesses. It is believed that more resins are absorbed in thicker edges and walls during the fabrication of sandwich composites. This will make the soaked region relatively stronger and consequently delay the initiation of cracks in the nanophased foams during fatigue. In particular, two phenomena will dominate the failure of the core during shear fatigue: (i) cell stretching in the loading direction which gives rise to initial interface cracks and (ii) kinking of the interface



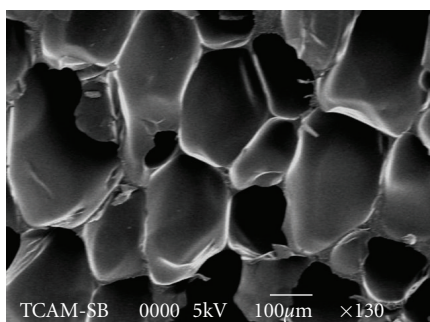
(a)



(b)



(c)



(d)

FIGURE 8: Micrographs of (a) as-received CNFs (b) embedded CNFs in PUF (c) cell structure of neat PUF (d) cell structure of PUF with 1.0 wt% CNFs

cracks into the core. Both of these phenomena are delayed by the nanophased foam as they possess higher strength and modulus. As a result nanophased sandwich composites demonstrate higher fatigue performance.

5. Summary

- (1) It is shown that shear strength and modulus of nanophased sandwich composites can be increased by about 30% by reinforcing the polyurethane core material with 1 wt% loading of carbon nanofibers (CNFs)
- (2) Significant improvements have also been observed during fatigue loading under shear. In an average sense fatigue limit (i.e., stress level to survive more than 1 million cycles) of nanophased sandwich composites was found to be around 55% of the ultimate shear strength as opposed to 50% in case of neat foam. On a specific note, for example, at 57% of $\tau_{ultimate}$, nanophased sandwich would survive 400,000 cycles more than its neat counterpart.
- (3) It is observed that quasi-static shear failure is mostly governed by a single shear crack diagonally traversing through the core. On the other hand in case of shear fatigue, failure is due to multiple cracks across the thickness of the core. In both cases, cracks initially appear at the coreskin interface, propagate for a short distance along the interface, and then kink into the core signaling the final failure event.
- (4) Embedded nanoparticles seem to modify the cell structures, offer resistance to crack propagation, and delay the kinking of interface cracks into the core.

Acknowledgment

The authors would like to thank the Office of Naval Research (ONR) (Grant no. N00014-06-1-0696) and the National Science Foundation, (NSF) (Grant no. HRD-976871) for supporting this research.

References

- [1] D. Zenkert, *An Introduction to Sandwich Construction*, EMAS, Solihull, UK, 1995.
- [2] E. E. Gdoutos, I. M. Daniel, and K. A. Wang, "Failure of cellular foams under multiaxial loading," *Composites Part A*, vol. 33, no. 2, pp. 163–176, 2002.
- [3] N. Kulkarni, H. Mahfuz, S. Jeelani, and L. A. Carlsson, "Fatigue crack growth and life prediction of foam core sandwich composites under flexural loading," *Composite Structures*, vol. 59, no. 4, pp. 499–505, 2003.
- [4] T. Thomas, H. Mahfuz, K. Kanny, and S. Jeelani, "Dynamic compression of sandwich composites at sub-ambient temperatures," *Journal of Composite Materials*, vol. 38, no. 8, pp. 641–653, 2004.
- [5] H. Mahfuz, V. K. Rangari, M. S. Islam, and S. Jeelani, "Fabrication, synthesis and mechanical characterization of nanoparticles infused polyurethane foams," *Composites Part A*, vol. 35, no. 4, pp. 453–460, 2004.

- [6] K. Kanny, H. Mahfuz, L. A. Carlsson, T. Thomas, and S. Jeelani, "Dynamic mechanical analyses and flexural fatigue of PVC foams," *Composite Structures*, vol. 58, no. 2, pp. 175–183, 2002.
- [7] A. Shipsha, M. Burman, and D. Zenkert, "Interfacial fatigue crack growth in foam core sandwich structures," *Fatigue and Fracture of Engineering Materials and Structures*, vol. 22, no. 2, pp. 123–131, 1999.
- [8] E. Reynaud, C. Gauthier, and J. Perez, "Nanophases in polymers," *Revue de Metallurgie*, vol. 96, no. 2, pp. 169–176, 1999.
- [9] C. L. Wu, M. Q. Zhang, M. Z. Rong, and K. Friedrich, "Tensile performance improvement of low nanoparticles filled-polypropylene composites," *Composites Science and Technology*, vol. 62, no. 10–11, pp. 1327–1340, 2002.
- [10] H. Mahfuz, N. Chisholm, and S. Jeelani, "Quasi-static and high strain rate response of nano-featured carbon/epoxy composites," in *Proceedings of the ASME Winter Annual Meeting*, New Orleans, La, USA, November 2002.
- [11] H. Mahfuz, V. K. Rangari, M. S. Islam, and S. Jeelani, "Fabrication, synthesis and mechanical characterization of nanoparticles infused polyurethane foams," *Composites Part A*, vol. 35, no. 4, pp. 453–460, 2004.
- [12] T. J. Pinnavaia and F. W. Beall, *Polymer-Clay Nanocomposites*, Wiley Series in Polymer Science, John Wiley & Sons, Chichester, UK, 2000.
- [13] M. Alexandre and Ph. Dubois, "Polymer-layered silicate nanocomposites: Preparation, properties and uses of a new class of materials," *Materials Science and Engineering R*, vol. 28, no. 1, pp. 1–63, 2000.
- [14] C. Zilg, R. Thomann, R. Mülhaupt, and J. Finter, "Polyurethane nanocomposites containing laminated anisotropic nanoparticles derived from organophilic layered silicates," *Advanced Materials*, vol. 11, no. 1, pp. 49–52, 1999.
- [15] Y. Kojima, A. Usuki, M. Kawasumi, et al., "Mechanical properties of nylon 6-clay hybrid," *Journal of Materials Research*, vol. 8, no. 5, pp. 1185–1189, 1993.
- [16] P. B. Messersmith and E. P. Giannelis, "Synthesis and barrier properties of poly(ϵ -caprolactone)-layered silicate nanocomposites," *Journal of Polymer Science Part A*, vol. 33, no. 7, pp. 1047–1057, 1995.
- [17] Y. Kojima, K. Fukumori, A. Usuki, A. Okada, and T. Kurauchi, "Gas permeabilities in rubber-clay hybrid," *Journal of Materials Science Letters*, vol. 12, no. 12, pp. 889–890, 1993.
- [18] P. Kelly, A. Akelah, S. Qutubuddin, and A. Moet, "Reduction of residual stress in montmorillonite/epoxy compounds," *Journal of Materials Science*, vol. 29, no. 9, pp. 2274–2280, 1994.
- [19] E. Andrews, W. Sanders, and L. J. Gibson, "Compressive and tensile behavior of aluminum foams," *Journal of Materials Science and Engineering*, vol. 270, pp. 113–124, 1998.
- [20] H. Mahfuz, M. F. Uddin, V. K. Rangari, M. C. Saha, S. Zainuddin, and S. Jeelani, "High strain rate response of sandwich composites with nanophased cores," *Applied Composite Materials*, vol. 12, no. 3–4, pp. 193–211, 2005.
- [21] F. Pervin, Y. Zhou, V. K. Rangari, and S. Jeelani, "Testing and evaluation on the thermal and mechanical properties of carbon nano fiber reinforced SC-15 epoxy," *Materials Science and Engineering A*, vol. 405, no. 1–2, pp. 246–253, 2005.
- [22] M. E. Kabir, M. C. Saha, and S. Jeelani, "Effect of ultrasound sonication in carbon nanofibers/polyurethane foam composite," *Materials Science and Engineering A*, vol. 459, no. 1–2, pp. 111–116, 2007.
- [23] M. L. Lake and J. M. Ting, "Vapor grown carbon fiber composites," in *Carbon Materials for Advanced Technologies*, T. D. Burchell, Ed., pp. 139–167, Pergamon Press, Oxford, UK, 1999.
- [24] K. P. De Jong and J. W. Geus, "Carbon nanofibers: catalytic synthesis and applications," *Catalysis Reviews—Science and Engineering*, vol. 42, no. 4, pp. 481–510, 2000.
- [25] Y. Zheng, Y. Zheng, and R. Ning, "Effects of nanoparticles SiO₂ on the performance of nanocomposites," *Materials Letters*, vol. 57, no. 19, pp. 2940–2944, 2003.
- [26] B. Wetzel, F. Hauptert, and M. Q. Zhang, "Epoxy nanocomposites with high mechanical and tribological performance," *Composites Science and Technology*, vol. 63, no. 14, pp. 2055–2067, 2003.
- [27] W. L. M. Nyborg, "Acoustic streaming," in *Physical Acoustics, IIB*, W. P. Mason, Ed., vol. 355, Academic Press, Boston, Mass, USA, 1965.
- [28] B. E. Noltingk and E. A. Neppiras, "Cavitation produced by ultrasonics," *Proceedings of the Physical Society. Section B*, vol. 63, no. 9, pp. 674–685, 1950.
- [29] K. S. Suslick, Ed., *Ultrasound: It's Chemical, Physical, and Biological Effects*, Wiley-VCH, Vancouver, Canada, 1988.
- [30] O. Abramov, *Ultrasound in Liquid and Solid Metals*, vol. 289, CRC Press, Boca Raton, Fla, USA, 1994.
- [31] K. S. Suslick, Y. Didenko, M. M. Fang, et al., "Acoustic cavitation and its chemical consequences," *Philosophical Transactions of the Royal Society A*, vol. 357, no. 1751, pp. 335–353, 1999.
- [32] S. Torquato, L. V. Gibiansky, M. J. Silva, and L. J. Gibson, "Effective mechanical and transport properties of cellular solids," *International Journal of Mechanical Sciences*, vol. 40, no. 1, pp. 71–82, 1998.
- [33] M. C. Shaw and T. Sata, "The plastic behaviour of cellular materials," *International Journal of Mechanical Sciences*, vol. 8, pp. 469–478, 1966.
- [34] C. M. Ford and L. J. Gibson, "Uniaxial strength asymmetry in cellular materials: an analytical model," *International Journal of Mechanical Sciences*, vol. 40, no. 6, pp. 521–531, 1998.
- [35] R. M. Christensen, "Mechanics of cellular and other low-density materials," *International Journal of Solids and Structures*, vol. 37, no. 1–2, pp. 93–104, 2000.
- [36] M. R. Patel and I. Finnie, "Structural features and mechanical properties of rigid cellular plastics," *Journal of Materials Chemistry*, vol. 5, no. 4, pp. 909–932, 1970.
- [37] M. Zawlawsky, "Multiaxial stress studies ion rigid polyurethane foam," *Experimental Mechanics*, vol. 13, pp. 70–76, 1973.
- [38] "Material data sheet: PUR240," Utah Foam, 3609 South 700 West, Salt Lake City, UT 84119, USA.

Research Article

Mechanical and Fracture Behaviors of Elastomer-Rich Thermoplastic Polyolefin/SiC_p Nanocomposites

Cheng Zhu Liao and Sie Chin Tjong

Department of Physics and Materials Science, City University of Hong Kong, Tat Chee Avenue, Kowloon, Hong Kong

Correspondence should be addressed to Sie Chin Tjong, aptjong@cityu.edu.hk

Received 3 November 2009; Accepted 10 April 2010

Academic Editor: Gaurav Mago

Copyright © 2010 C. Z. Liao and S. C. Tjong. This is an open access article distributed under the Creative Commons Attribution License, which permits unrestricted use, distribution, and reproduction in any medium, provided the original work is properly cited.

Elastomer-rich thermoplastic polyolefin (ETPO) resin containing 70 wt% maleated styrene-ethylene-butadiene-styrene (SEBS-g-MA) and 30 wt% polypropylene and its nanocomposites filled with 1–5 wt% SiC nanoparticles (SiC_p) were fabricated using extrusion and injection molding techniques. The mechanical and thermal behaviors of ETPO and its nanocomposites were investigated. Tensile measurements showed that the SiC_p additions lead to reductions in both tensile stiffness and strength of ETPO. However, Izod impact and EWF measurements indicated that the impact strength and fracture toughness of ETPO improve substantially with increasing SiC_p content. This demonstrated that SiC nanoparticles toughen the ETPO blend effectively. Furthermore, SiC_p additions were found to improve the thermal resistance of ETPO blend considerably.

1. Introduction

Thermoplastic polyolefin (TPO) blends consisting of polypropylene (PP) and elastomer components find extensive industrial applications in the automotive and construction sectors because of their low cost, low density, good weather resistance, and recycling characteristics. They can be easily processed like thermoplastics but maintain the resilience and elasticity behaviors of elastomers. The elastomers commonly used to toughen PP including styrene-ethylene-butadiene-styrene (SEBS), ethylene-propylene rubber (EPR), ethylene-propylene-diene monomer (EPDM), and polyethylene octane elastomer (POE). Due to the addition of elastomer, the stiffness and mechanical strength of TPO are lower than those of pure PP. Therefore, conventional microfillers such as talc and short glass fibers have been used to restore the mechanical strength of TPO blends. However, the incorporation of large concentration of microfillers (ca 20–30 wt%) generally leads to poor processability of TPO-based composites [1]. In the past decade, nanomaterials with high mechanical strength and stiffness are used as nanofillers to enhance the mechanical strength of polymers. In the case of TPO

blends, nanoclay [2–7] and nanosilica particles [8, 9] of low loading levels have been incorporated into TPO blends to form ternary PP/elastomer/filler nanocomposites. TPO-clay nanocomposites have found applications as materials for the “step-assist” of automobiles. The fracture toughness is a property which describes the ability of a material containing a crack to resist fracture. It is one of material properties commonly used for engineering design purposes. Therefore, it is of particular importance to study the fracture toughness of nanoparticle modified TPO. Based on the ratio of PP and elastomer contents, TPO-clay nanocomposites with rubber-poor ($\leq 30\%$ elastomer) and rubber-rich ($\geq 70\%$ elastomer) domains have been fabricated [2–9]. For rubber-poor TPO blends and composites, the rubber phase disperses as spherical domains in PP matrix and contributes to improved toughness of these materials. In the case of rubber-rich TPO blends and composites, rubber is the main or continuous phase of the materials. Thus the rubber-rich TPO blends behave like ideal elastomers with distinctly low elastic modulus. It is of particular interest to investigate the structure-property of rubber-rich TPO blends reinforced with rigid nanofillers. The effect of nanoclay additions on the structure and property of rubber-rich TPO blends has

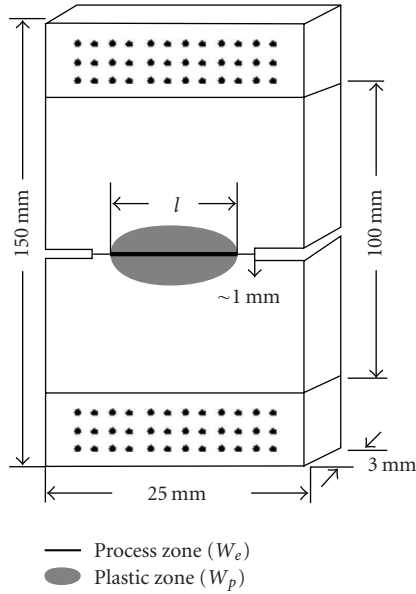


FIGURE 1: Geometry of DENT specimen showing formation of a sharp notch.

been investigated by Mishra et al. [5] and Tjong and Ruan [4] more recently. Mishra et al. [5] prepared the TPO/clay nanocomposites where the TPO contains PP and EPDM with the ratio of 25 : 100 by weight. They reported that the nanocomposites exhibit remarkable improvement of tensile and storage moduli over their pristine TPO blend. Tjong and Ruan [4] reported that TPO-based nanocomposites reinforced with 0.1–1.5 wt% organically modified clay exhibits enhanced stiffness and tensile strength. Moreover, the fracture toughness of TPO/clay nanocomposites increases with the increasing clay content.

Silicon carbide generally exhibits outstanding mechanical and physical properties such as very high hardness and modulus, good abrasive wear resistance as well as very high thermal conductivity. Silicon carbide microparticles are commonly used the reinforcement materials to enhance the mechanical performance of metals/alloys [10, 11]. Very recently, one-dimensional silicon carbide nanowires have been used as nanofillers to improve the wear resistance of epoxy [12]. Till to now, there is no work available in the literature reporting the mechanical behavior of elastomer-rich TPO (ETPO) filled with silicon carbide nanoparticles (SiC_p). In this paper, we aim to investigate the effect of SiC_p addition on the mechanical and thermal properties of ETPO/ SiC_p nanocomposites. Particular attention is paid to the fracture toughness of such nanocomposites determined with the essential work of fracture (EWF) approach under tensile mode. The ETPO matrix consists of SEBS-g-MA and PP with a composition ratio of 70 : 30 by weight.

2. Experimental

2.1. Material. PP (Basell Moplen HP500N) with a melt flow index of 12 g/10 minutes [13] was obtained commercially

from Saudi Arabia. Poly (styrene-ethylene-butylene-styrene) elastomer grafted with 1.84 wt% of maleic anhydride (SEBS-g-MA, Kraton, FG 1901X) was purchased from Bayer Company (Hong Kong). SiC_p (45–55 nm) powders were provided by Nanostructured & Amorphous Materials Inc (Los Alamos, USA). All the polymeric materials and SiC nanoparticles were dried in 70°C for 24 hours prior to melt processing.

2.2. Nanocomposites Preparation. SiC_p -filled rubber-rich thermoplastic polyolefin nanocomposites (ETPO) were prepared by a two-step compounding method. This involved an initial melt mixing of SiC_p with PP followed by melt compounding of the PP/ SiC_p mixtures with SEBS-g-MA in a twin-screw Brabender extruder at 40 rpm. The blending temperature profile was set at 205–210–210–210–190–180°C from hopper to die, respectively. The ratio of SEBS-g-MA and PP was fixed at 70 : 30 by weight. The SiC_p loadings varied from 1 to 5 wt%. For the purpose of comparison, pure PP was prepared under the same processing conditions. The extrudates were then pelletized and dried again before injection molding. Subsequently, the nanocomposite pellets were directly injection-molded into a 3.2 mm thickness plaque. The molding temperature was maintained at 40°C, whereas the barrel zone temperatures were set at 210, 205 and 200°C.

2.3. Morphology. The impact cryofractured surfaces were etched with tetrahydrofuran (THF) for 5 minutes to remove SEBS-g-MA phase from the nanocomposites. Then the impact cryofractured specimens prior to and after etching were coated with a thin gold film prior to observation in a field-emission scanning electron microscope (JEOL JSM-7100F).

2.4. Differential Scanning Calorimetry (DSC). The crystallization and melting behaviors of pure PP, ETPO blend and ETPO/ SiC_p nanocomposites were measured using DSC (TA model 2910) under a nitrogen atmosphere. In this test, the specimen was initially heated to 220°C at a fast rate. It was held for 3 minutes at this temperature to remove the thermal histories before cooling at a specific cooling rate. The cooling rates employed were 10°C/min and the cooling traces were recorded. Then it was reheated to 220°C at a rate of 10°C/min and the melting curves were recorded.

2.5. Heat Deflection Temperature. The heat deflection temperature (HDT) of ETPO nanocomposites was determined using a dynamic mechanical analyzer (mode 2980) under the three-point bending mode according to ASTM D648-07 from 25–65°C with a heating rate of 2°C/min. In the measurement, a force (F) was preloaded on the specimen according to the following equation: $F = (2B^2W/3L)\sigma$, where σ is the maximum tensile stress (0.455 MPa), B is the thickness and W the width of specimen, L is the span length (50 mm here).

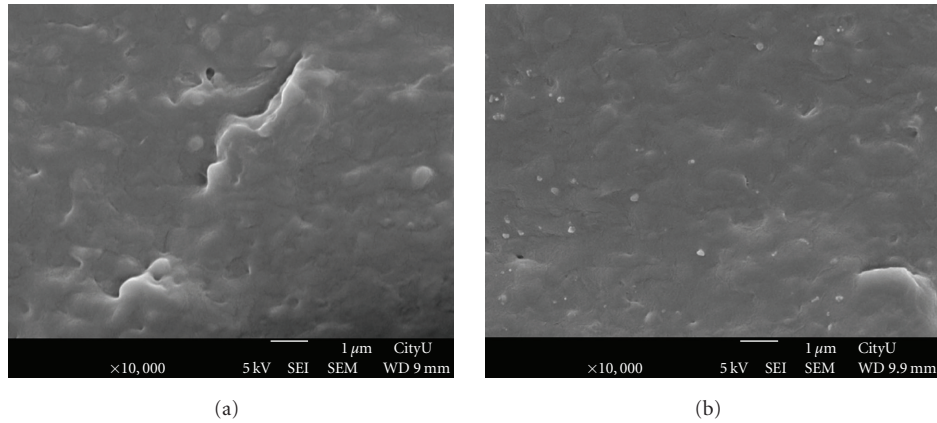


FIGURE 2: SEM cryofractographs of (a) ETPO (b) ETPO-3 wt%SiC_p prior to chemical etching.

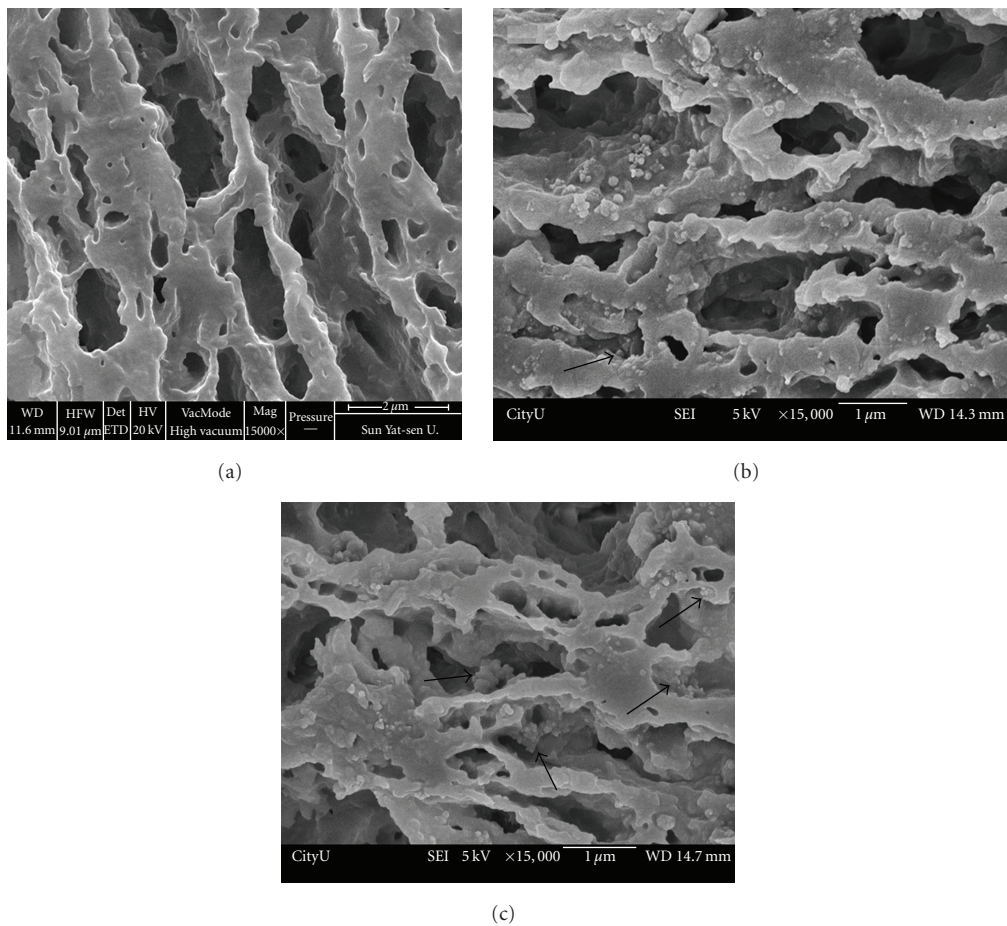


FIGURE 3: SEM cryofractographs of (a) ETPO (b) ETPO-3 wt% SiC_p and (c) ETPO-5 wt% SiC_p specimens after etching with THF. White arrows show remnant SiC nanoparticles dispersed in SEBS phase.

2.6. Mechanical Tests. The injection-molded plates were cut into dumbbell tensile bars along the melt flowing direction according to ASTM D638. Tensile tests were carried out with an Instron tester (model 5567) at crosshead speeds of 10 and 300 mm/min. The Young's modulus was determined with an extensometer at 10 mm/min. TPO-based specimens

are very ductile and elastic, so higher crosshead speeds are recommended. Impact specimens with a dimension of $63.5 \times 12.7 \times 3.2$ mm were also cut from the plates according to ASTM D256. The impact tests were performed with an Izod impact tester (Ceast model 6545). Before testing, the specimens were immersed in liquid nitrogen for 20 minutes.

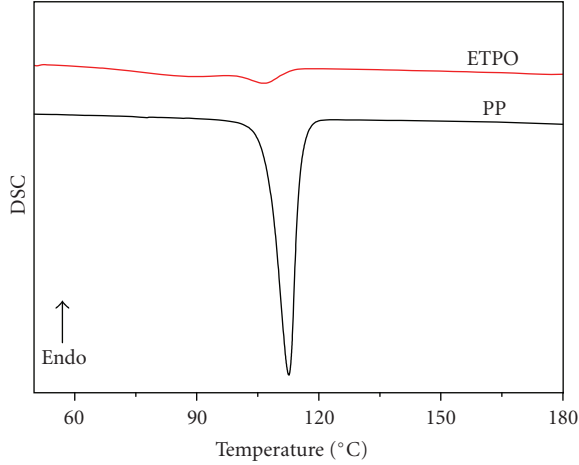


FIGURE 4: DSC cooling traces of PP and ETPO.

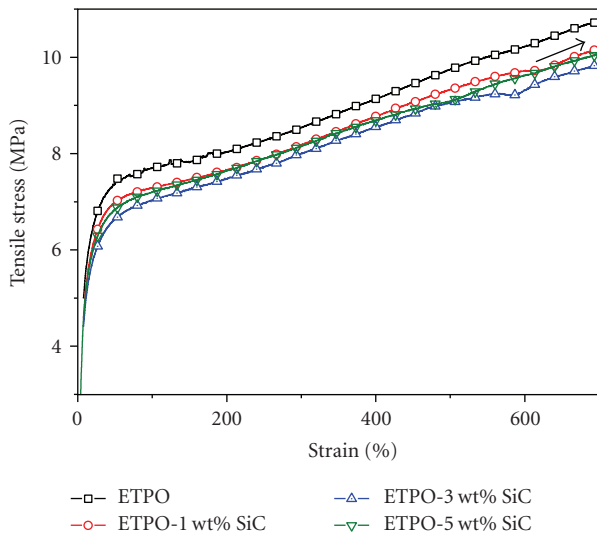


FIGURE 5: Tensile stress-strain curves for ETPO blend and ETPO/SiC_p nanocomposites at a crosshead speed of 10 mm/min.

Five specimens of each composition were used for tensile and impact tests, and the average values reported.

2.7. Fracture Toughness Characterization. Double-edge notched tension (DENT) specimens with a dimension of $150 \times 25 \times 3.2$ mm were used (Figure 1). They were cut from injection molded plaques in which the longitudinal direction of the specimens was parallel to the melt flow direction. Ligament lengths were varied by saw-cutting the specimens into notches of different lengths. The notches were further sharpened with a fresh razor blade to a length of ~ 1 mm. Thus a sharp notch was formed accordingly. The exact ligament length (l) was measured with a traveling microscope (Tropcon profile projector). The gauge length of the sample was 100 mm. The DENT samples were loaded in an Instron tensile tester (model 5567) with a crosshead speed of 1 mm/min. The load versus displacement plots for

TABLE 1: Crystallization and thermal parameters for PP, ETPO blend and their composites.

Sample	T_c ($^{\circ}\text{C}$)	T_m ($^{\circ}\text{C}$)	ΔH_c (J/g)	X_c (%)
PP	112.6	161.9	88.5	42.3
PP/1 wt% SiC _p	116.8	162.0	87.6	42.3
PP/3 wt% SiC _p	116.8	162.6	86.2	42.5
PP/5 wt% SiC _p	118.4	162.5	85.6	43.1
ETPO	107.1	164.7	4.2	6.7
ETPO-1 wt% SiC _p	107.6	164.5	2.0	3.2
ETPO-3 wt% SiC _p	108.5	164.4	0.5	0.8
ETPO-5 wt% SiC _p	108.5	164.8	0.5	0.8

the specimens were recorded. The fracture surfaces of some specimens were also observed in SEM.

3. Results and Discussion

3.1. Morphology (SEM). The cryogenic fracture surface SEM morphology of the ETPO blend and its composites prior to and after etching by tetrahydrofuran (THF) are shown in Figures 2(a) and 2(b) and Figures 3(a)–3(c), respectively. Without THF etching, it is rather difficult to differentiate elastomeric SEBS-g-MA and PP phases (Figures 2(a) and 2(b)). THF selectively dissolves the main SEBS-g-MA phase thereby forming various cavities in these specimens. The SiC nanoparticles are found to disperse in the PP phase, but most SiC_p dispersed in SEBS-g-MA phase are removed by THF during etching (Figures 3(b) and 3(c)). Only few remnant SiC_p nanoparticles (indicated by the arrows) dispersed in the etched elastomer phase are seen in Figures 3(b) and 3(c). Furthermore, SiC_p nanoparticles are not well homogeneously distributed, particularly for the nanocomposite with 5 wt% SiC_p. As recognized, inorganic nanoparticles of high volume content tend to agglomerate into clusters in the polymer matrix of nanocomposites. Such clustering behavior is commonly seen in polymer nanocomposites.

3.2. Thermal Properties. Figure 4 shows the DSC curves of pure PP, ETPO and its nanocomposites at a cooling rate of $10^{\circ}\text{C}/\text{min}$. The crystallization temperature (T_c) of pure PP is located at 112.6°C . This agrees reasonably with the value provided by the supplier [13]. The incorporation of a large amount of SEBS-g-MA elastomer (70 wt%) into PP leads to a sharp decrease of its T_c from 112.6°C to 107.1°C . Thus the SEBS-g-MA elastomer retards the crystallization process of PP phase. The DSC results for pure PP, ETPO and its nanocomposites are summarized in Table 1. This table reveals that the T_c of PP in the ETPO blend remains nearly unchanged (i.e., 107.6°C) by adding 1 wt% SiC_p. The T_c of PP in the ETPO blend increases very slightly to 108.5°C by adding 3 and 5 wt% SiC_p. Accordingly, SiC nanoparticles do not provide nucleation sites for PP crystallization.

For the purpose of comparison, the crystallization temperature of PP/SiC_p binary nanocomposites having the same SiC_p content is also listed in Table 1. Apparently, additions of 1 and 3 wt% SiC_p to PP increase its T_c

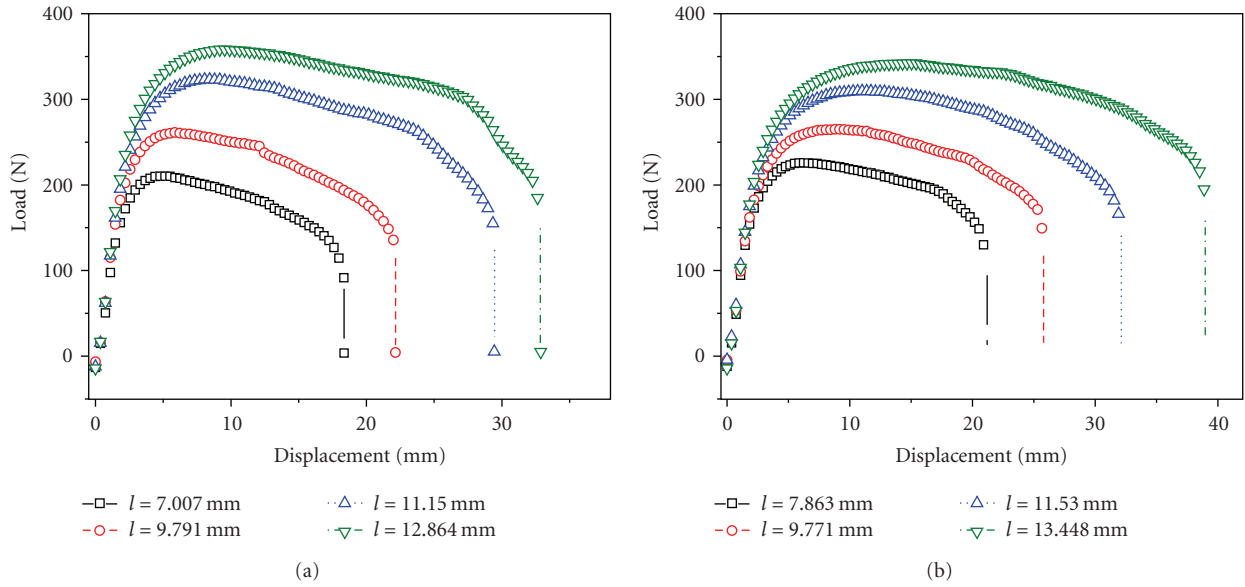


FIGURE 6: Load-displacement curves for (a) ETPO and (b) ETPO-5 wt% SiC_p specimens of various ligament lengths (l).

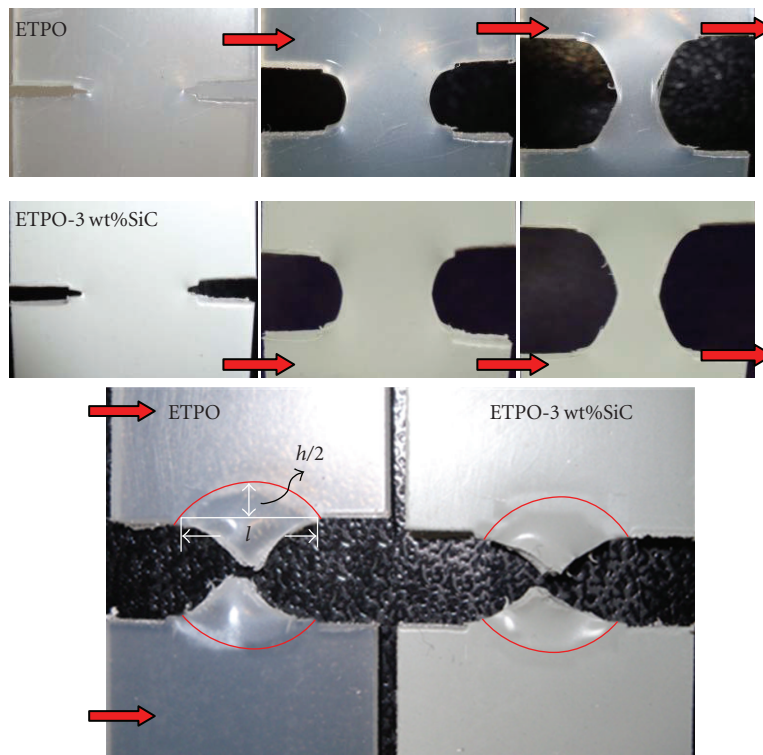


FIGURE 7: Photographs showing development of deformation zone in ETPO and ETPO-3 wt% SiC_p specimens during tensile EWF test.

from 112.6°C to 116.8°C. The T_c of PP further increases to 118.4°C by adding 5 wt% SiC_p. These results demonstrate that the SiC nanoparticles act as effective nucleation sites for PP in the binary PP/SiC nanocomposites during crystallization.

The degree of crystallinity (X_c) of nanocomposites can be determined according to the following equation:

$$X_c(\%) = \frac{\Delta H_c}{(1 - \phi)\Delta H_m^0} \times 100, \quad (1)$$

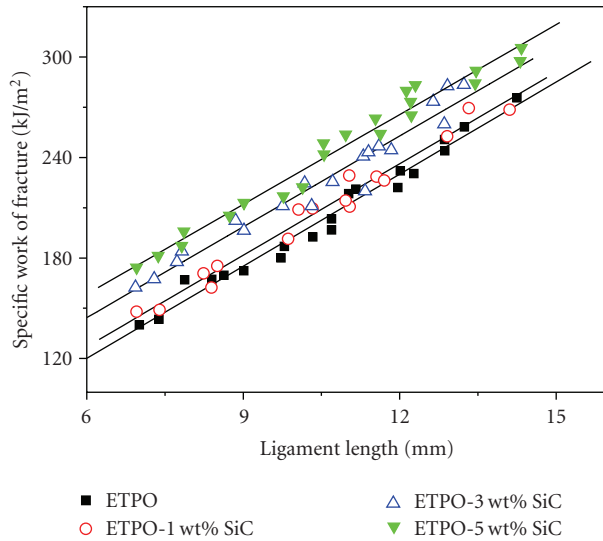


FIGURE 8: Specific work of fracture w_f versus l plots for ETPO blend and ETPO/SiC_p nanocomposites.

where ΔH_c is the apparent enthalpy of crystallization, ΔH_m^0 is the extrapolated value of the enthalpy corresponding to the melting of 100% crystalline PP, and ϕ is the weight fraction of the filler in the hybrids. The ΔH_m^0 value is estimated to be 209 J/g [14, 15].

From Table 1, it can be seen that the incorporation of 70 wt% SEBS-g-MA to PP leads to a sharp decrease in the degree of crystallinity. The large amount of SEBS-g-MA molecules hampers the movement of PP segments to the nucleating sites, resulting in a less crystalline matrix. The SiC nanoparticle additions further result in a decrease of the degree of crystallinity due to their predominant dispersion in the elastomer phase as shown in Figures 3(b) and 3(c). Thus SiC nanoparticles are ineffective nucleating agents for PP macromolecular chains in ternary PP/SEBS-g-MA/SiC nanocomposites.

Heat deflection temperature (HDT) is recognized to be an important indicator for the heat resistance of polymer blends and its composites under an applied load. The effect of SiC_p addition on the heat resistance of ETPO blend and its nanocomposites is given in Table 2. It is apparent that the SiC_p addition improves the thermal properties of ETPO blend. The HDT value of ETPO blend increases from 53.64°C to 56.57°C by adding 5 wt% SiC_p. This result is of technological importance for TPO blends that are widely used in outdoor roof and industrial applications.

3.3. Mechanical Properties. Representative tensile stress-strain curves for the ETPO blend and its nanocomposites are shown in Figure 5. The stress-strain curve of rubber-rich ETPO blend displays a typical tensile behavior of an elastomer, that is, extensive range of ductility. The tensile strength values of ETPO-SiC_p nanocomposites at 50% and 300% strain are lower than those of the ETPO blend. This is related to the predominant dispersion of SiC_p in the elastomer phase. Recently, Mai and coworkers studied the

effect of clay platelet dispersion on the tensile properties of SEBS-g-MA toughened PA6,6 composites [16]. They indicated that the best microstructure for toughness and other mechanical properties is to have the maximum percentage of clay platelet dispersed in the PA6,6 matrix rather than to have it distributed in the SEBS-g-MA phase. Another reason for inferior tensile strength of ETPO-SiC_p nanocomposites is due to weak interfacial bonding between the ETPO matrix and SiC nanoparticles. As recognized, strong interfacial bonding enables effective transfer of applied load from the polymer matrix to reinforcing particles during tensile test, leading to enhanced tensile strength of resulting composites.

ETPO and its nanocomposites with excellent ductility did not break into two pieces during Izod impact test at room temperature. To obtain the impact strength, the specimens were dipped into liquid nitrogen for 20 minutes, then removed them from liquid nitrogen and subjected to the fast strike of a pendulum. It is interesting to note that the SiC_p additions are beneficial to enhance the impact strength of the ETPO blend. The impact strength of the blend (2.84 kJ/m²) generally increases with increasing filler content. A maximum value of 3.11 kJ/m² can be achieved by adding 5 wt% SiC_p. The enhanced impact strength is due to the debonding of SiC nanoparticles during impact test, leading to cavitation and extensive shear banding of the matrix. Kontopoulou and coworkers studied the physical properties of thermoplastic polyolefin containing nanosilica [8, 9]. The tensile modulus, impact, and flexural properties of TPO/nanosilica composites show improvements at low loadings of nanosilica. They also found that silane-modified nanosilica gives rise to more significant enhancement in impact strength due to the efficiently dispersion in the polymer matrix phase [8]. Similarly, nanoclay additions are beneficial to enhance the tensile strength and impact strength of TPO blend [4, 5]. In contrast, SiC_p only improves the impact strength but deteriorates the tensile strength of TPO blend.

3.4. Fracture Toughness. In general, conventional Izod impact tests are used to determine the impact fracture behavior of polymers and their composites. The test measures the energy needed to break a notched specimen of specific notch geometry. The results simply denote the energy absorption in the notched specimens. Impact strength is not an appropriate parameter for materials design.

In this regard, essential work of fracture method has been increasingly employed to characterize the fracture toughness of ductile polymers and tough composite materials under tensile loading. The essential work of fracture concept was originally suggested by Broberg [17–19] then developed by Mai and coworkers [20–23]. In a quasistatic tensile test, the total fracture work (W_f) can be divided into two components: one corresponding to the essential work required to fracture the polymer in its process zone (W_e) and another corresponding to the nonessential plastic work (W_p) corresponding to the energy consumed by various deformation mechanisms in the plastic zone. W_f can be

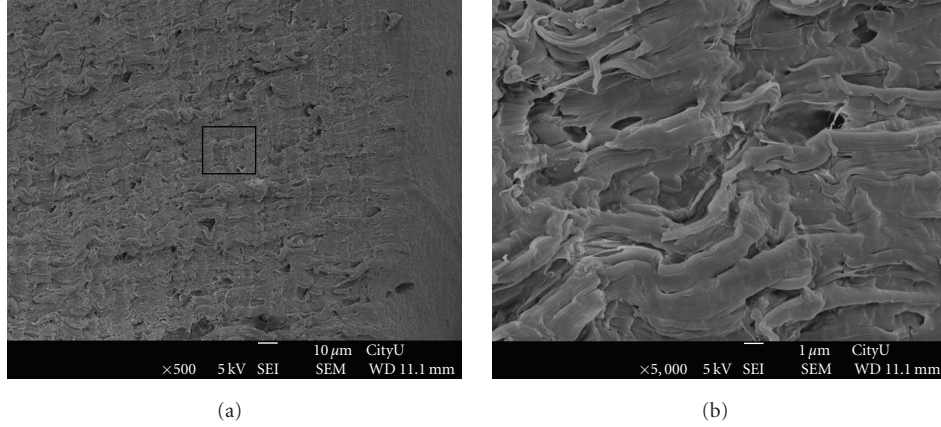


FIGURE 9: SEM fractographs of ETPO after tensile EWF test. (a) Low and (b) high magnification micrographs.

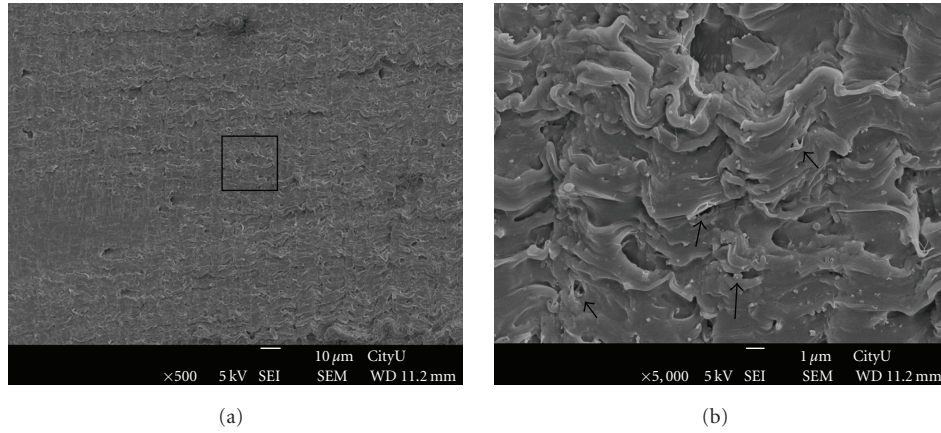


FIGURE 10: SEM fractographs of ETPO-3 wt% SiC nanocomposite after tensile EWF test. (a) Low and (b) high magnification micrographs.

expressed as follows:

$$\begin{aligned}
 W_f &= W_e + W_p, \\
 W_f &= w_e l t + \beta w_p l^2 t, \\
 w_f &= \frac{W_f}{l t} = w_e + \beta w_p l,
 \end{aligned} \tag{2}$$

where w_f is the specific total fracture work; w_e and w_p are the specific essential fracture work and specific plastic work, respectively; l is the ligament length; t is the sample thickness; and β is a shape factor of the plastic zone. Apparently, the EWF approach is a simple method by testing the specimens with different l values, integrating the area under the load displacement curve (W_f), plotting the w_f versus l diagram, and obtaining the best fit regression line. The slope of the w_f versus l plot yields w_p , and the intercept produces w_e . It is worth noting that the specimen must be fully yielded prior to the crack initiation for the validity of the EWF approach. Moreover, self-similarity in load-displacement curves is also a necessary criterion for the suitability of the EWF method for fracture characterization [22].

Figures 6(a) and 6(b) show the representative load-displacement curves with different ligament lengths (l) for

ETPO and ETPO-5 wt% SiC_p specimens at room temperature, respectively. It is obvious that the self-similarity in load-displacement curves at various ligament lengths is maintained for these specimens. Self-similarity of the curves demonstrates that all tested specimens with different ligament lengths have a common geometry of fracture. Furthermore, the specimens experience full yielding prior to the crack propagation.

The shapes of plastic zone developed in the ETPO and ETPO-3 wt% SiC nanocomposites during tensile EWF test are shown in Figure 7. The shapes of plastic zone of ETPO and ETPO-3 wt% SiC nanocomposites are nearly elliptical. Since β is a shape factor of the plastic zone, its value as listed in Table 3 can be determined from the following equation [24, 25]:

$$\beta = \frac{\pi h}{4l}, \tag{3}$$

where h is minor axis of ellipse as shown in Figure 7, and l the ligament length. The plots of w_f versus l for ETPO and its nanocomposites are depicted in Figure 8. Excellent linear regression with high correlation coefficient between the w_f and l is obtained for these samples. The results of tensile

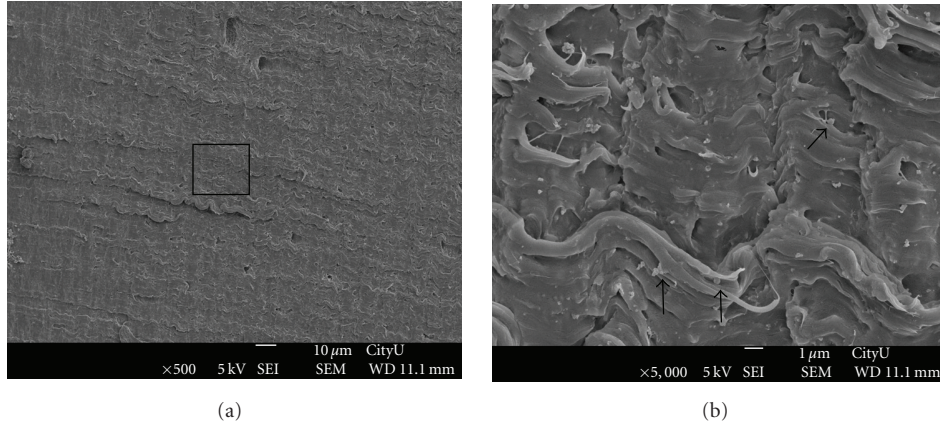


FIGURE 11: SEM fractographs of ETPO-5 wt% SiC nanocomposite after tensile EWF test. (a) Low and (b) high magnification micrographs.

TABLE 2: Mechanical properties of ETPO blend and its nanocomposites.

Sample	HDT (°C)	Young's Modulus (MPa)	Tensile strength (MPa)				Impact strength (kJ/m ²)
			10 mm/min		300 mm/min		
			10 mm/min	50%	300%	50%	
ETPO	53.64	269 ± 5	6.92 ± 0.02	8.00 ± 0.11	8.57 ± 0.10	9.30 ± 0.05	2.84 ± 0.02
ETPO-1 wt% SiC _p	54.32	255 ± 7	6.61 ± 0.22	7.80 ± 0.02	8.30 ± 0.12	9.18 ± 0.14	2.90 ± 0.02
ETPO-3 wt% SiC _p	55.28	236 ± 10	6.21 ± 0.13	7.54 ± 0.16	7.81 ± 0.09	8.96 ± 0.13	2.92 ± 0.02
ETPO-5 wt% SiC _p	56.57	238 ± 12	6.22 ± 0.08	7.86 ± 0.09	7.92 ± 0.21	9.10 ± 0.07	3.11 ± 0.25

TABLE 3: Tensile specific essential work of fracture (w_e) and specific plastic work (βw_p) for the samples studied.

Sample	w_e (kJ/m ²)	βw_p (MJ/m ³)	β	R (coefficient)
ETPO	10.15	18.32	0.648	0.988
ETPO-1 wt% SiC _p	17.78	18.20	0.625	0.987
ETPO-3 wt% SiC _p	35.98	18.07	0.615	0.977
ETPO-5 wt% SiC _p	51.13	17.87	0.620	0.986

EWF measurements for all samples investigated are listed in Table 3. The results clearly demonstrate that a significant improvement in w_e with increasing SiC_p loading. The βw_p values for ETPO remains unchanged by adding SiC_p up to 3 wt%. These imply that the SiC nanoparticles toughen the ETPO matrix effectively. In other words, SiC_p additions do not deteriorate the fracture toughness of the ETPO blend owing they can cause cavitation and plastic deformation (shear banding) of the matrix, thereby leading to enhanced fracture toughness. In this study, the size of SiC_p employed is about 45–55 nm. It is considered that the size of reinforcing particles can influence the energy absorption and toughness of polyolefin materials. Further work is needed to elucidate the effect of the sizes of SiC particles (in submicrometer and nanometer) on the fracture toughness of rubber-rich TPO blends.

The enhancement in fracture toughness of ETPO due to the SiC_p additions can also be verified from their SEM fractographs. Figures 9(a), 9(b), 10(a), 10(b), 11(a), and 11(b) show field-emission SEM micrographs of ETPO,

ETPO-3 wt% SiC_p, and ETPO-5 wt% SiC_p specimens after tensile EWF measurements, respectively. Wavy shear banding of the matrix can be readily seen in the fractographs. Thus considerable energy is absorbed in these specimens during tensile EWF measurements. Moreover, debonding and cavitation of SiC nanoparticles as indicated by arrows can be seen in some areas of the nanocomposites, thereby facilitating fibrillation and shear banding of polymer matrix. From tensile and EWF tests, it can be concluded that the tensile strength decreases but the fracture toughness of ETPO increases by adding SiC nanoparticles up to 5 wt%. Severe agglomeration of SiC nanoparticles is expected by further increasing the filler content on the basis of microscopic examination as described above. Thus the optimum SiC_p content is 5 wt% for enhancement of fracture toughness of ETPO.

4. Conclusions

Elastomer-rich TPO blend and its nanocomposites filled with 1–5 wt% SiC_p were prepared by melt mixing followed by injection molding. The resulting nanocomposites were subjected to mechanical and thermal characterizations. Tensile measurements showed that the additions of SiC nanoparticles to ETPO lead to decrements in both tensile stiffness and strength. Young's modulus of ETPO blend decreases from 269 to 236 MPa by adding 3 to 5 wt% SiC_p. The tensile strength of ETPO blend decreases from 6.92 MPa (at 50% strain) to 6.21 MPa by adding 3–5 wt% SiC_p. In contrast, Izod impact and EWF measurements revealed that

the impact strength and fracture toughness of ETPO improve with increasing SiC_p content. The fracture toughness of ETPO-5 wt% SiC_p nanocomposite is fivefold higher than that of ETPO blend. This implied that SiC nanoparticles toughen the ETPO blend markedly. Finally, SiC_p additions improved the thermal resistance of ETPO blend on the basis of the heat deflection temperature measurement.

References

- [1] Z. Ling, W. Zhenghua, H. Rui, L. Liangbin, and Z. Xinyuan, "PP/elastomer/calcium carbonate composites: effect of elastomer and calcium carbonate contents on the deformation and impact behavior," *Journal of Materials Science*, vol. 37, no. 13, pp. 2615–2621, 2002.
- [2] S. C. Tjong, S. P. Bao, and G. D. Liang, "Polypropylene/montmorillonite nanocomposites toughened with SEBS-g-MA: structure-property relationship," *Journal of Polymer Science B*, vol. 43, no. 21, pp. 3112–3126, 2005.
- [3] S. P. Bao and S. C. Tjong, "Impact essential work of fracture of polypropylene/montmorillonite nanocomposites toughened with SEBS-g-MA elastomer," *Composites A*, vol. 38, no. 2, pp. 378–387, 2007.
- [4] S. C. Tjong and Y. H. Ruan, "Fracture behavior of thermoplastic polyolefin/clay nanocomposites," *Journal of Applied Polymer Science*, vol. 110, no. 2, pp. 864–871, 2008.
- [5] J. K. Mishra, K.-J. Hwang, and C.-S. Ha, "Preparation, mechanical and rheological properties of a thermoplastic polyolefin (TPO)/organoclay nanocomposite with reference to the effect of maleic anhydride modified polypropylene as a compatibilizer," *Polymer*, vol. 46, no. 6, pp. 1995–2002, 2005.
- [6] H.-S. Lee, P. D. Fasulo, W. R. Rodgers, and D. R. Paul, "TPO based nanocomposites. Part 1. Morphology and mechanical properties," *Polymer*, vol. 46, no. 25, pp. 11673–11689, 2005.
- [7] D. H. Kim, P. D. Fasulo, W. R. Rodgers, and D. R. Paul, "Effect of the ratio of maleated polypropylene to organoclay on the structure and properties of TPO-based nanocomposites—part I: morphology and mechanical properties," *Polymer*, vol. 48, no. 20, pp. 5960–5978, 2007.
- [8] Y. Liu and M. Kontopoulou, "The structure and physical properties of polypropylene and thermoplastic olefin nanocomposites containing nanosilica," *Polymer*, vol. 47, no. 22, pp. 7731–7739, 2006.
- [9] M. Bailly and M. Kontopoulou, "Preparation and characterization of thermoplastic olefin/nanosilica composites using a silane-grafted polypropylene matrix," *Polymer*, vol. 50, no. 11, pp. 2472–2480, 2009.
- [10] S. C. Tjong and K. C. Lau, "Tribological behaviour of SiC particle-reinforced copper matrix composites," *Materials Letters*, vol. 43, no. 5, pp. 274–280, 2000.
- [11] S. C. Tjong, S. Q. Wu, and H. C. Liao, "Wear behaviour of an Al-12% Si alloy reinforced with a low volume fraction of SiC particles," *Composites Science and Technology*, vol. 57, no. 12, pp. 1551–1558, 1998.
- [12] W. Nhuapeng, W. Thamjaree, S. Kumfu, P. Singjai, and T. Tunkasiri, "Fabrication and mechanical properties of silicon carbide nanowires/epoxy resin composites," *Current Applied Physics*, vol. 8, no. 3-4, pp. 295–299, 2008.
- [13] <http://www.basell.com/>.
- [14] J. E. Mark, *Physical Properties of Polymer Handbook*, AIP Press, New York, NY, USA, 1996.
- [15] Z. Stojanović, Z. Kačarević-Popović, S. Galović, D. Miličević, and E. Suljovrujić, "Crystallinity changes and melting behavior of the uniaxially oriented iPP exposed to high doses of gamma radiation," *Polymer Degradation and Stability*, vol. 87, no. 2, pp. 279–286, 2005.
- [16] A. Dasari, Z.-Z. Yu, and Y.-W. Mai, "Effect of blending sequence on microstructure of ternary nanocomposites," *Polymer*, vol. 46, no. 16, pp. 5986–5991, 2005.
- [17] K. B. Broberg, "Critical review of some theories in fracture mechanics," *International Journal of Fracture Mechanics*, vol. 4, no. 1, pp. 11–19, 1968.
- [18] K. B. Broberg, "Crack-growth criteria and non-linear fracture mechanics," *Journal of the Mechanics and Physics of Solids*, vol. 19, no. 6, pp. 407–418, 1971.
- [19] K. B. Broberg, "On stable crack growth," *Journal of the Mechanics and Physics of Solids*, vol. 23, no. 3, pp. 215–237, 1975.
- [20] Y.-W. Mai and B. Cotterell, "On the essential work of ductile fracture in polymers," *International Journal of Fracture*, vol. 32, no. 2, pp. 105–125, 1986.
- [21] Y. W. Mai, B. Cotterell, R. Horlyck, and G. Vigna, "The essential work of plane stress ductile fracture of linear polyethylenes," *Polymer Engineering and Science*, vol. 27, no. 11, pp. 804–809, 1987.
- [22] Y. Mai and P. Powell, "Essential work of fracture and J-integral measurements for ductile polymers," *Journal of Polymer Science B*, vol. 29, no. 7, pp. 785–793, 1991.
- [23] S.-C. Wong and Y.-W. Mai, "Essential fracture work of short fiber reinforced polymer blends," *Polymer Engineering and Science*, vol. 39, no. 2, pp. 356–364, 1999.
- [24] E. Clutton, "Essential work of fracture," in *Fracture Mechanics Testing Methods for Polymers, Adhesives and Composites*, D. R. Moore, A. Pavan, and J. G. Williams, Eds.,ESIS Publications 28, pp. 177–195, Elsevier Science, Amsterdam, The Netherlands, 2001.
- [25] A. B. Martinez, J. Gamez-Perez, M. Sanchez-Soto, J. I. Velasco, O. O. Santana, and M. Ll Maspocho, "The essential work of fracture (EWF) method—analyzing the post-yielding fracture mechanics of polymers," *Engineering Failure Analysis*, vol. 16, no. 8, pp. 2604–2617, 2009.

Research Article

Thermomechanical Assessment of Plastic Deformation in Model Amorphous Polyamide/Clay Nanocomposites

Kunal Tulsyan,¹ Saurabh Toshniwal,¹ Gowri Dorairaju,¹ Daniel F. Schmidt,¹
and Emmanuelle Reynaud²

¹ Department of Plastics Engineering, University of Massachusetts Lowell, One University Avenue, Lowell, MA 01854, USA

² Department of Mechanical Engineering, University of Massachusetts Lowell, One University Avenue, Lowell, MA 01854, USA

Correspondence should be addressed to Emmanuelle Reynaud, emmanuelle.reynaud@uml.edu

Received 11 January 2010; Accepted 22 March 2010

Academic Editor: Frank T. Fisher

Copyright © 2010 Kunal Tulsyan et al. This is an open access article distributed under the Creative Commons Attribution License, which permits unrestricted use, distribution, and reproduction in any medium, provided the original work is properly cited.

In an effort to isolate the role of nanofiller independent of changes in polymer microstructure, we report the processing and characterization of model amorphous polyamide/clay nanocomposites. Analyses confirm fully amorphous character, no change in T_g or thermal stability, and a partially exfoliated structure. The tensile modulus, yield stress, and failure stress increase with the clay content, both in dried and conditioned samples. In contrast, failure strain decreases with increasing clay content in conditioned samples but is independent of clay content in dried samples. Concurrently, the conversion of mechanical work to heat during plastic deformation was studied using infrared thermography, with the heat of deformation estimated based on these results and compared to the work of deformation. These results allow us to quantify changes in deformation mechanism and to conclude that the presence of clay enhances the conversion of mechanical energy to heat in these materials.

1. Introduction

Polymer nanocomposites have generated significant interest among both academic and industrial researchers thanks to the various properties enhancements that may be realized in such systems versus the neat resins alone. Achieving such enhancements means realizing thermodynamic compatibility between the nanoparticle and the polymer matrix. Likewise, most polymers with the needed polarity to achieve such compatibility with commonly used nanoparticles based on silica, silicates, and other polar metal oxide derivatives are semicrystalline in nature. While various literature models attempt to account for the mechanical properties enhancements observed in polymer nanocomposites, in general they neglect nanoparticle-induced variations in polymer microstructure. That said, a large body of the publications dealing with polyamide/clay nanocomposites demonstrates that the clays induce a change in the crystalline form. Likewise, conflicting literature reports indicate increased, decreased, or unchanged overall crystallinity in these systems [1, 2]. Furthermore, it is likely that such changes affect the mechanical properties of these materials [1, 3].

Building on this observation, the goal of the present study is to isolate the effect of the nanofiller alone on the mechanical properties of a model nanocomposite while ensuring high levels of nanoscale dispersion. In particular, we report the production by conventional melt-processing techniques (twin-screw extrusion and injection molding) and the characterization of a polymer nanocomposite based on a fully amorphous yet polar matrix. By eliminating the presence of crystallinity while retaining high polarity, the effect of reinforcement by dispersed clay layers may be studied independent of changes in polymer microstructure.

2. Experimental

2.1. Materials and Processing. Grilamid TR-90 (EMS Grivory), a fully amorphous copolyamide, was selected as the basis for this work; its structure is illustrated in Figure 1. This polymer has processing characteristics similar to those of polyamide 6 (PA 6) and polarity similar to that of polyamide 12 (PA 12), allowing for comparisons with literature reports involving semi-crystalline polyamides.

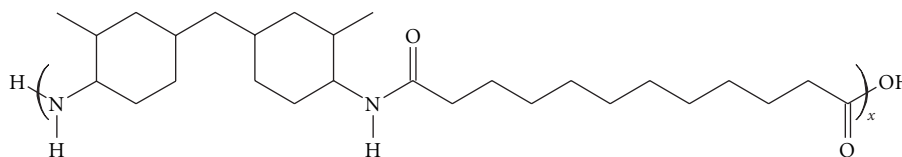


FIGURE 1: Chemical structure of Grilamid TR-90 [4].

Cloisite 30B (Southern Clay Products), a bis(2-hydroxyethyl)methyl tallow ammonium-modified montmorillonite clay, was chosen as the nanofiller for this effort, given its proven compatibility with a range of polyamides [5–15].

Amorphous copolyamide pellets and clay powder were dry blended to produce mixtures with inorganic contents of 0.125, 0.25, 0.5, and 1% by volume. This concentration range was chosen so that all nanocomposites compared here fall below the percolation threshold for platelets with aspect ratios of 100 (~1.2 vol.%) [16], ensuring that the dispersion states realized are comparable and independent of clay content. The nanocomposite naming convention used here is TR90-Cl30B-X, where X is the volume percent of clay platelets (considering inorganic content only), the relevant concentration as far as all mechanical models are concerned.

All samples (including clay-free polymer) were fed via a volumetric feeder into an intermeshing 27 mm corotating twin-screw extruder (Leistritz ZSE 27HP-40D) with an L/D ratio of 40:1. Based on the screw programming recommended by Nanocor to produce semicrystalline polyamide nanocomposites [17], a high-shear twin-screw extrusion profile with three sections of kneading blocks was used. As minimizing moisture content is critical in this process, a vent zone was present midway down the extruder barrel. A vacuum-assisted vent zone at the end of the barrel was used for the same purpose. A room-temperature water bath was used for cooling the strand exiting the die, which was then pelletized using a pelletizer (Reduction Engineering model 604).

Following extrusion, each formulation was first dried under vacuum at 80°C for twelve hours before molding. Injection molding of ASTM D638 Type I tensile test specimens was then performed using a Milacron FANUC 55 ton Roboshot (Model S200i 55B) unit.

2.2. Characterization

2.2.1. X-Ray Diffraction (XRD). Wide-angle X-ray scattering (WAXS) measurements were carried out using a Bruker Instruments D8 DISCOVER/GADDS system (40 kV, 40 mA, Cu K α radiation, $\lambda = 0.15418$ nm). Specimens cut from the center of tensile bars were used for this purpose, and FIT2D v12.077 was used to generate 2-theta versus intensity plots from the 2D WAXS patterns.

Small-angle X-ray scattering (SAXS) data was recorded using a Statton camera/image plate X-ray diffraction system based on a Rigaku ultraX generator (50 kV, 200 mA, Cu K α radiation, $\lambda = 0.15418$ nm).

2.2.2. Transmission Electron Microscopy (TEM). Transmission electron microscopy was performed using a Philips EM 400T transmission electron microscope (100 kV). The sample was first microtomed into thin sections ($t \sim 100$ nm) using a Leica EM UC6 ultramicrotome equipped with a diamond knife and operated at room temperature.

2.2.3. Thermogravimetric Analysis (TGA). TGA was performed using a TA instruments Q50 TGA. Specimens were heated to 850°C at a rate of 20°C/min in a platinum pan in flowing ultra zero air (60 mL/min). In addition, in order to evaluate the rate of degradation, the first derivative of the standard TGA curves was taken with respect to temperature; these curves are referred to as dTGA curves.

2.2.4. Differential Scanning Calorimetry (DSC). DSC was conducted using a TA instruments Q200 DSC in an ultra high-purity helium environment using heating and cooling rates of 10°C/min in the temperature range of -50°C to 320°C.

2.2.5. Tensile Testing. Tensile testing was performed using an Instron 6025 universal testing machine as per ASTM D638, using the Type I tensile bars previously described. At least ten specimens of each formulation were tested at a strain rate of 50 mm/min and with a gauge length of 100 mm. The test specimens were conditioned before testing for 48 hours at 50% relative humidity and 23°C as per ASTM D618. A second set of samples were dried at 80°C in a vacuum oven for twelve hours and otherwise tested as per ASTM D638 to identify the effect of moisture on the mechanical properties. Materials availability also allowed a smaller number of specimens to have their maximum surface temperature recorded using a FLIR Systems Thermovision A20M infrared camera during tensile testing.

3. Results and Discussion

3.1. Nanocomposite Composition. Prior to all other analyses, the actual concentration of clay in the nanocomposites was determined via TGA. These calculations accounted for both residue from nonclay sources (based on TGA data for unfilled polymer with the same process history) and high-temperature dehydroxylation of the clay layers (as determined via TGA of the clay alone). The results of these analyses are shown in Table 1, with variations reported being the standard deviations based on three independent analyses of each formulation. Note that “clay” in this context refers to the alkylammonium-modified clay, while “inorganic”

TABLE 1: Nanocomposite compositions (actual values measured via three independent TGA measurements).

Nanocomposite	Desired composition		Actual composition	
	Inorganic (vol. %)	Clay (wt%)	Inorganic (vol. %)	Clay (wt%)
TR90-Cl30B-0.125	0.125	0.51	0.11 ± 0.02	0.42 ± 0.07
TR90-Cl30B-0.25	0.25	1.01	0.23 ± 0.01	0.89 ± 0.04
TR90-Cl30B-0.5	0.5	2.02	0.50 ± 0.02	1.93 ± 0.08
TR90-Cl30B-1	1	4	0.91 ± 0.02	3.47 ± 0.07

refers only to the silicate layers themselves, excluding the alkylammonium modifier.

3.2. Nanocomposite Structure. Clay dispersion levels were assessed via SAXS and WAXS on a central cross-section of injection-molded tensile bars of each composition, with additional confirmation via TEM. The reported d -spacing of Cloisite 30B is 18.5 Å [18]. Figure 2 shows an overlay plot of X-ray intensity versus 2θ obtained from WAXS for all nanocomposites studied. A small peak can be observed at 6° , corresponding to a d -spacing of 14.7 Å or 29.4 Å, corresponding to either the first- or the second-order diffraction peak. A value of 14.7 Å is unlikely, as it would imply that the platelets have collapsed on one another, inconsistent with our TEM observations. We therefore interpret this as a second-order diffraction peak, indicative of the presence of intercalated clay layers, with the first-order diffraction peak obscured by the intensity of the incident beam. The peaks observed at $\sim 9^\circ$ and $\sim 18^\circ$ correspond to the amorphous halo (i.e., scattering from the amorphous domains of the polymer) [19], and are effectively independent of clay content in terms of both position and intensity, supporting the lack of microstructural changes in the polymer phase.

2D SAXS and WAXS patterns for the center section of a TR90-Cl30B-1 tensile specimen are shown in Figure 3. These false color images reveal the orientation of the clay layers in the flow direction and parallel to the long axis of the tensile bar cross-section. The dark line observed in the lower-left quadrant of the SAXS pattern comes from the beam-stop, while the unbroken rings observed on the WAXS pattern correspond to the unoriented amorphous halo of the polymer.

The state of dispersion was further studied by TEM (representative image shown in Figure 4), which indicated the presence of both individual clay layers and thin stacks and confirmed some level of parallel orientation. When coupled with the WAXS and SAXS data, we conclude that these systems are partially exfoliated and oriented in the direction of the flow of the polymer melt in the tensile bar.

3.3. Thermal Behavior. A heat-cool-heat DSC analysis was used to confirm the fully amorphous nature of the copolyamide matrix and to assess whether any changes in thermal properties had occurred as a result of the presence of the clay. The values for the glass transition temperature from the first and second heating cycles (T_{gI} and T_{gII} , resp.) are reported in Table 2. In all cases, a transition very close

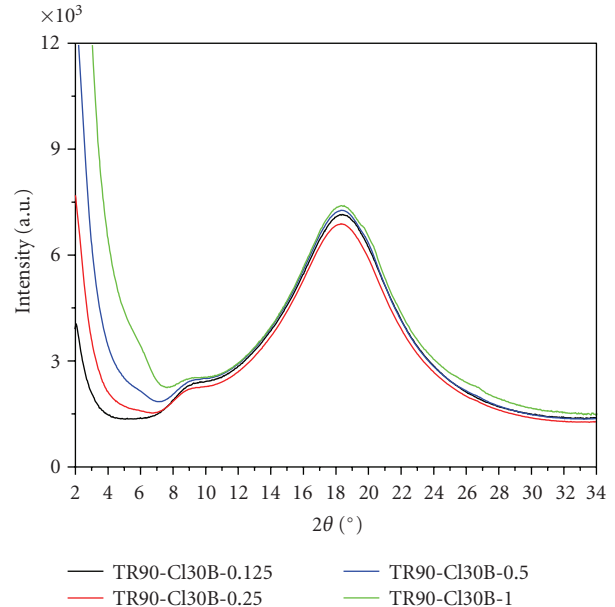


FIGURE 2: 1D WAXS data for the TR90-Cl30B nanocomposite system.

TABLE 2: T_g values for the TR90-Cl30B nanocomposite system (each value derived from a single DSC heating cycle).

Material	T_{gI} (°C)	T_{gII} (°C)
TR90	141	153
TR90-Cl30B-0.125	137	152
TR90-Cl30B-0.25	145	151
TR90-Cl30B-0.5	138	149
TR90-Cl30B-1	146	149

to the documented T_g of 157°C is observed [20], with this difference easily explained by differences in analytical parameters. There is no indication of melting during heating or crystallization during cooling in the pure polymer or any of the nanocomposites, confirming their amorphous nature. Finally, there is no particular trend in the evolution of the T_g or the size or shape of the transition versus clay content.

In addition to its utility in confirming the actual clay content, TGA was also used to assess the thermal stability of the nanocomposites studied here. In general it was observed that the peak in the dTGA curve increased in intensity and decreased in width with increasing clay content, consistent

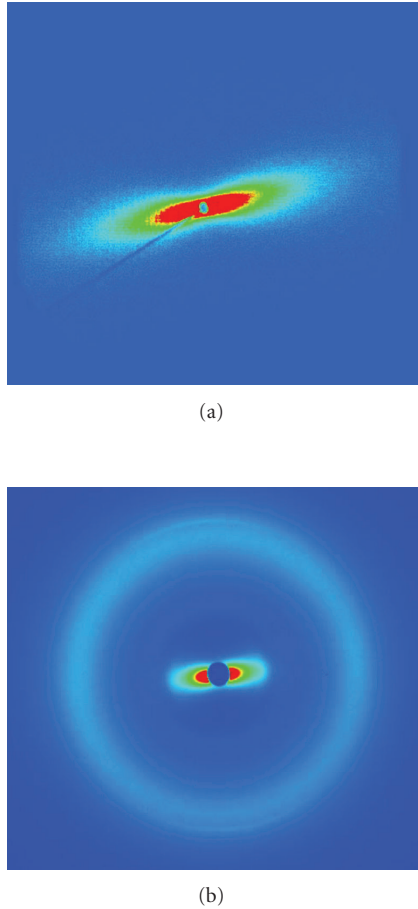


FIGURE 3: 2D SAXS (a) and 2D WAXS (b) data for TR90-Cl30B-1.

TABLE 3: T_{onset} and T_{max} values for TR90-Cl30B nanocomposite system and its components (each value derived from the average of three independent TGA measurements).

Material	T_{onset} ($^{\circ}$ C)	T_{max} ($^{\circ}$ C)
Cloisite 30B	255	260
TR90	411 ± 2	454 ± 4
TR90-Cl30B-0.125	412 ± 1	465 ± 3
TR90-Cl30B-0.25	413 ± 1	460 ± 2
TR90-Cl30B-0.5	414 ± 2	465 ± 4
TR90-Cl30B-1	416 ± 3	460 ± 6

with a clay-induced increase in the maximum degradation rate over a narrower range of temperatures. Table 3 presents a more complete picture of the dTGA results with respect to the temperature at 5% weight loss (T_{onset}) and the temperature at which the maximum degradation rate is observed (T_{max}). As this data clearly shows, the clay has little or no effect on the thermal stability of the polymer matrix as measured via TGA.

3.4. Mechanical Properties. As noted previously, mechanical properties were measured for both conditioned (23 $^{\circ}$ C, 50%

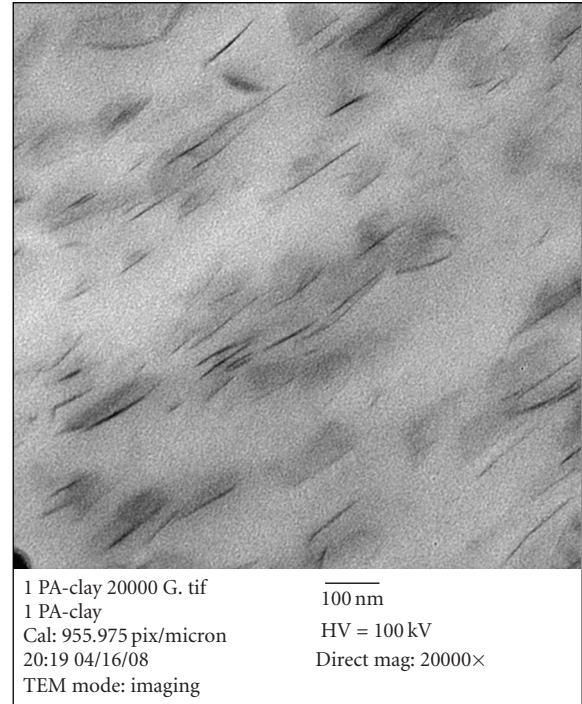


FIGURE 4: Representative TEM image for TR90-Cl30B-1.

relative humidity, 48 hours) and dried (80 $^{\circ}$ C under vacuum for 12 hours) materials to assess the effects of moisture on the underlying properties. The results of these efforts are summarized in Tables 4 and 5, with the number of samples tested indicated parenthetically adjacent to the material designation.

We begin the discussion of these properties with a consideration of the evolution of the tensile modulus, as illustrated in Figure 5.

While more variation is observed in the data from the dried samples, the TR90-Cl30B nanocomposite system generally shows an increase in tensile modulus with increasing clay content. These results are consistent with literature results obtained in analogous semi-crystalline polyamide/clay nanocomposites [21], where an increase of 30–40% in tensile modulus is observed at clay concentrations similar to the highest investigated here.

We now turn our attention to the yield stress trends, as illustrated in Figure 6. The yield stress was observed to follow a very similar (though less pronounced) trend, with an increase of \sim 12% at the highest clay concentration investigated here. Drying increases the yield stress by 5–10% but the relative trend remains the same. As above, a literature report by Fornes et al. [22] indicates a \sim 10–15% increase in yield stress in an analogous polyamide 6/clay system. In terms of yield strain (data presented in Tables 4 and 5), the presence of the clay results in an earlier transition from elastic to plastic deformation, with both the conditioned and dried TR90-Cl30B nanocomposites showing a gradual decrease in yield strain values with increasing clay content. Drying slightly increases yield strain, perhaps due to the lack of moisture-induced plasticization.

TABLE 4: Mechanical properties data for conditioned samples (23°C, 50% RH, 48 hours).

Material	Tensile modulus (GPa)	Yield strain (%)	Yield stress (MPa)	Failure strain (%)	Failure stress (MPa)
TR90 ($n = 10$)	1.14 ± 0.02	10.5 ± 0.3	58.7 ± 0.7	99 ± 24	43.8 ± 2.2
TR90-Cl30B-0.125 ($n = 10$)	1.18 ± 0.02	10.3 ± 0.2	58.8 ± 0.7	70 ± 15	41.6 ± 2.1
TR90-Cl30B-0.25 ($n = 9$)	1.22 ± 0.02	10.1 ± 0.2	60.0 ± 1.0	85 ± 25	43.8 ± 2.2
TR90-Cl30B-0.5 ($n = 10$)	1.29 ± 0.03	9.7 ± 0.2	62.3 ± 0.9	45 ± 17	45.3 ± 2.1
TR90-Cl30B-1 ($n = 10$)	1.44 ± 0.05	9.0 ± 0.3	64.7 ± 0.6	38 ± 10	47.8 ± 2.3

TABLE 5: Mechanical properties data for dried samples (80°C under vacuum, 12 hours).

Material	Tensile modulus (GPa)	Yield strain (%)	Yield stress (MPa)	Failure strain (%)	Failure stress (MPa)
TR90 ($n = 10$)	0.98 ± 0.13	11.1 ± 0.5	62.7 ± 0.7	60 ± 31	44.1 ± 0.4
TR90-Cl30B-0.125 ($n = 10$)	1.08 ± 0.06	10.8 ± 0.5	64.9 ± 0.9	37 ± 15	42.9 ± 1.7
TR90-Cl30B-0.5 ($n = 10$)	1.13 ± 0.04	10.3 ± 0.3	65.6 ± 1.3	61 ± 46	47.1 ± 3.3

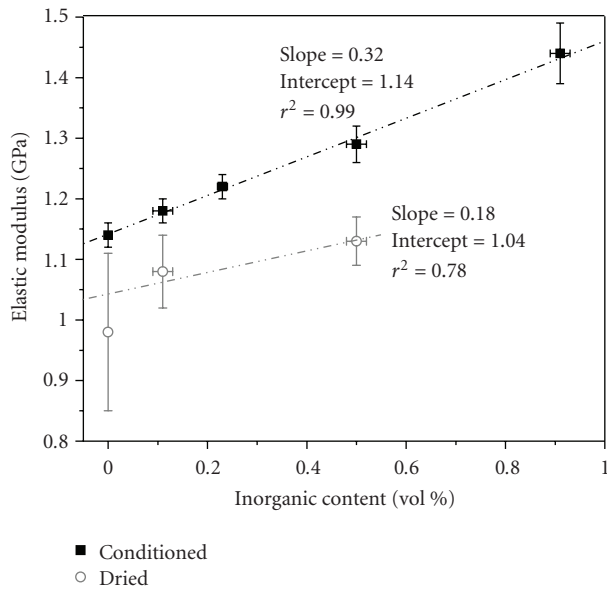


FIGURE 5: Evolution of the tensile modulus with the filler content for both conditioned and dried samples (lines are error-weighted linear fits of the experimental data).

Finally, observations may be made regarding the failure stress as well. The TR90-Cl30B nanocomposite system shows some variability in stress at failure in both the dried and the conditioned systems but with an overall increasing trend versus clay content and with no significant moisture effects, as shown in Figure 7.

Strain at failure data is shown graphically in Figure 8. While the variations in strain at failure are significant, there appears to be a decreasing trend in strain at failure versus clay content in the conditioned state. This is consistent with the observation of embrittlement in a range of analogous polyamide nanocomposites tested following identical conditioning procedures [23]. In contrast, no significant trend is observed in the dry state. When dried, polyamides are known to show reductions in failure strain, as we observe in the pure polyamide system. That said, a shift from a

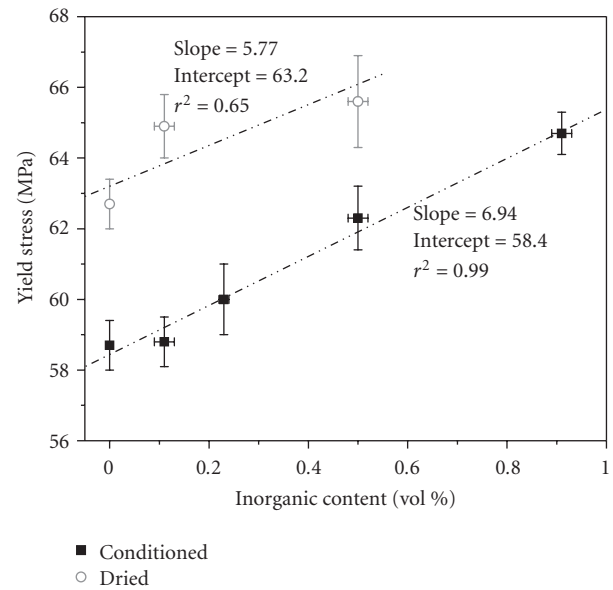


FIGURE 6: Evolution of the yield point with filler content for both conditioned and dried samples (lines are error weighted linear fits of the experimental data).

decreasing trend in the presence of moisture to no trend in its absence is difficult to completely explain by lack of water-induced plasticization alone, and would seem to imply a change in polymer/clay interactions. While further study is required to positively identify the nature of these changes, one clue from the literature that may support this conclusion is the report of Xie et al. [24], which shows ATR-FTIR evidence of obvious changes in hydrogen-bonding patterns in analogous polyamide-6 nanocomposites following 6 hours at 80°C under vacuum. While some of this may be ascribed to changes in polymer microstructure, a reduction in water content during this process cannot be ruled out as a contributing factor.

Having covered conventional mechanical properties testing, we will now address the use of an IR camera to observe changes in the specimen temperature during the

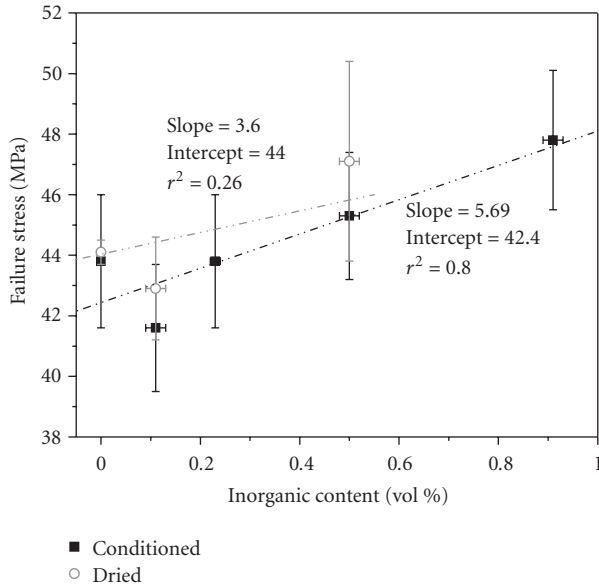


FIGURE 7: Evolution of the tensile strength with the filler content for both conditioned and dried samples (lines are error-weighted linear fits of the experimental data).

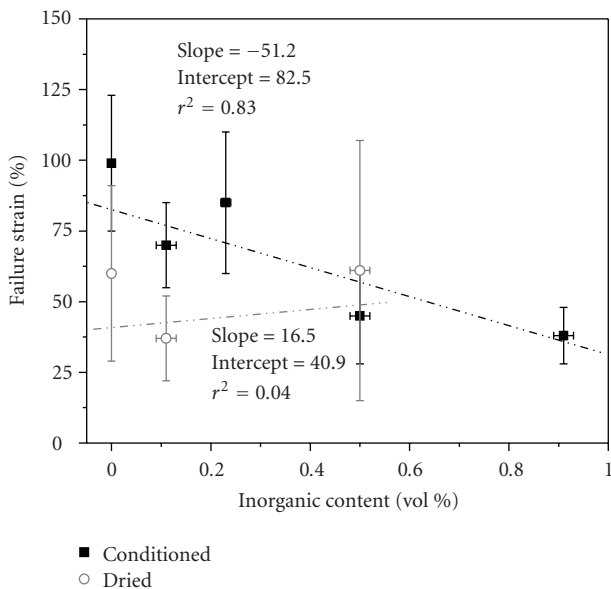


FIGURE 8: Strain at failure versus filler content for both conditioned and dried samples (lines are error-weighted linear fits of the experimental data).

tensile testing of selected specimens. No significant increase in the temperature was observed until the yield point, at which point the temperature increased, then stabilized on further elongation to produce what we term the yield plateau in the stress-temperature data. Most samples also displayed a sudden rise in temperature at the point of failure. Representative IR images in the prenecking, necking, and postfracture regimes are shown in Figure 9. The data obtained for maximum temperature versus time was then

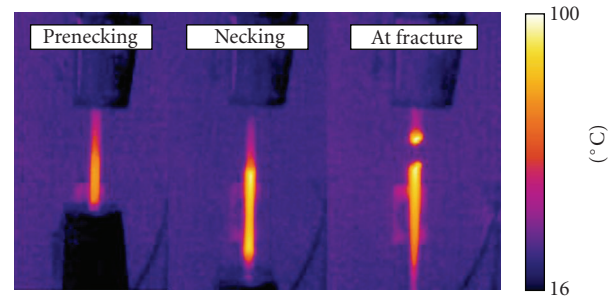


FIGURE 9: Representative IR pictures of a sample at different stages during tensile deformation.

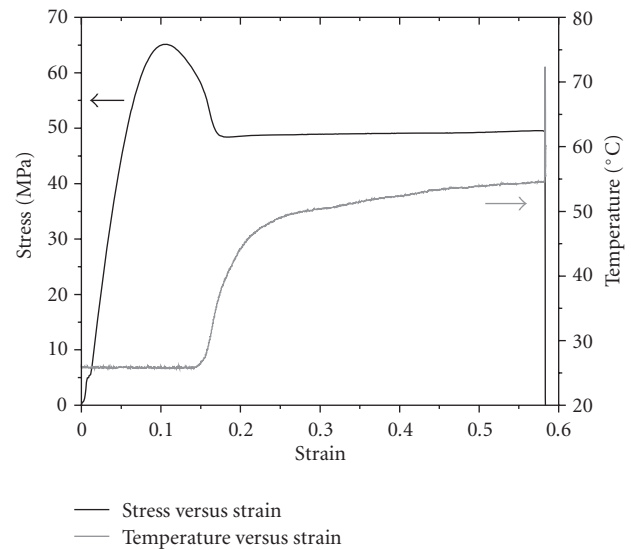


FIGURE 10: A representative stress-strain-temperature curve for a TR90-Cl30B-0.5 sample.

correlated with the tensile data to generate a stress-strain-temperature curve of the type shown in Figure 10.

The data collected by the IR camera was then used to evaluate the amount of thermal energy liberated by the sample during plastic deformation. In particular, following baseline subtraction based on the initial temperature reading prior to yield, the area under the temperature curve was calculated for each specimen, correcting for the clay content (as only the polymer plastically deforms). This corrected area was then multiplied by the heat capacity ($C_p = 2000 \text{ J/kg}\cdot\text{K}$ [25]) and density ($\rho = 1010 \text{ kg/m}^3$ [26]) of the polymer to estimate the heat of deformation in units of energy per unit volume of polymer.

Figure 11 illustrates the linear relationship observed between thermal energy output (the aforementioned estimated heat of deformation) and the mechanical energy input (area under the post-yield portion of the stress-strain curve) during the plastic deformation. Here we observe that, regardless of sample conditioning or any tendency to fail earlier versus later in the tensile test, the thermal energy liberated is directly proportional to the mechanical energy input. An additional practical benefit of this approach is

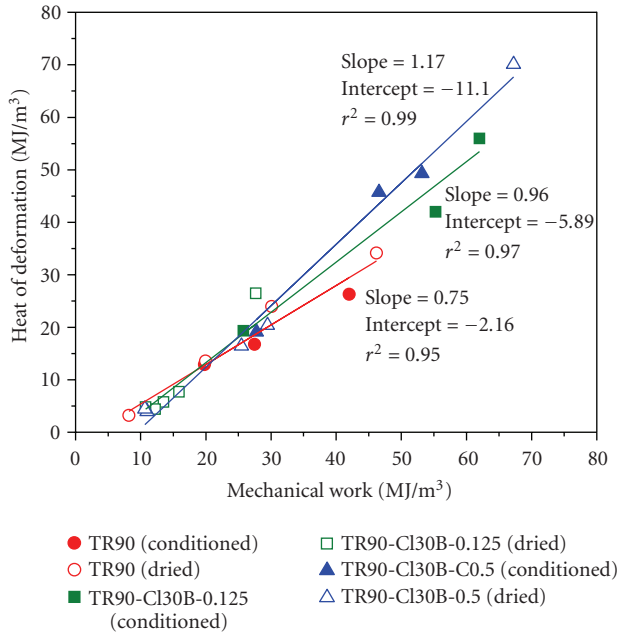


FIGURE 11: Thermal energy versus mechanical energy input of the TR90 composites, both conditioned (solid symbols) and dried (open symbols).

that it is able to produce such clear trends using engineering stress and strain, which tend to underestimate the work of deformation. Furthermore, the slopes of these lines show evenly spaced, statistically significant increases with increasing clay content, indicating that the presence of the clay nanoparticles enhances the ability of the polymer to convert work to heat. As reported by McNally et al. [27] for a polyamide-12 nanocomposite system, the clay particles are thought to enable other heat mechanisms to contribute to the generation of additional heat above and beyond the adiabatic heating observed in the virgin polymer. In particular, loading-induced friction at the polymer/clay interface as well as debonding and cavitation in and around clay particles could all contribute to increases in temperature.

We believe that this combined thermal/mechanical testing method is a very convenient means of assessing the influence of the nanofiller on the macroscopic behavior of a polymer. In particular, this approach enables us to shed new light on the ability of polymer nanocomposites to convert work to heat during plastic deformation. The insensitivity of these results to moisture content and early versus late failure represents a significant benefit, as compared to the high degree of variability typically observed in conventional mechanical testing of moisture-sensitive polymers due to changes in moisture content, the presence of flaws, and so forth. Likewise, thanks to the amorphous character of the matrix, its compatibility with the clay, and the use of concentrations below the percolation threshold, we may conclude that the effects observed arise as a direct result of variations in concentration of the dispersed clay layers, independent of dispersion state and polymer microstructure (both comparable for all samples).

The generation of heat during the necking of semi-crystalline polymers was noted at least as far back as 1960 [28], while Haward et al. [29–31] and Roseen [32] first applied infrared thermography to the deformation of semi-crystalline polymers in the mid 1970s. With that said, the use of this technique to study the plastic deformation of amorphous polymers has received much less attention, and we believe this to be the first attempt to quantify the thermomechanical behavior of filled polymers and of nanocomposites in particular. These results will be confirmed and extended via ongoing studies of comparable amorphous and semi-crystalline nanocomposite systems to evaluate the role of polymer microstructure as well as clay content.

4. Conclusions

Nanocomposites based on a completely amorphous nylon (Grilamid TR90) in combination with organically modified montmorillonite clay (Cloisite 30B) were successfully prepared. These nanocomposites were characterized as partially exfoliated based on SAXS, WAXS, and TEM data and consistent with literature reports for polyamide nanocomposites in general. Thermal analysis (TGA, DSC) confirmed the composition and amorphous character of the materials studied and showed no major changes in either the glass transition temperature or the thermal stability as a function of clay content.

Conventional tensile testing indicated that the tensile modulus was significantly improved with increasing clay content in conditioned samples, and to a lesser extent in dried samples, a trend reflected in other measures of reinforcement as well. Elongation at break for the conditioned TR90-Cl30B materials was highly scattered but observed to decrease with increased clay content, whereas no apparent effect of clay content was observed in the dried samples.

In addition, a new approach to the mechanical testing of nanocomposites was applied for the first time, involving simultaneous IR imaging and tensile testing, and a means of extracting an estimate of the heat of (plastic) deformation was reported. A linear relationship was observed between mechanical energy input and thermal energy output during plastic deformation for each composition studied, regardless of moisture content or failure point. A trend was seen with respect to clay content, however, with the addition of clay enhancing the conversion of mechanical energy to heat.

This work represents an initial step in a series of comparisons on the influence of the presence or absence of crystallinity on the thermomechanical behavior of polymer nanocomposites. It is hoped that this work will lead to an improved understanding of post-yield properties in this important class of materials, and confirm the utility of our approach as a means of quantifying changes in deformation behavior.

Acknowledgments

This work was supported by the National Science Foundation as a Nanoscale Science and Engineering Centers Program

(Award no. NSF-0425826). The authors would like to thank Professor Stephen Orroth and the UML Department of Plastics Engineering for access to the Processing equipment and general support; the UML Advanced Composite Materials and Textile Research Laboratory for use of the infrared camera; Dr. Earl Ada and Mr. Chris Santeufemio from the UML Materials Characterization Lab for the SEM-EDS, TEM sectioning, and imaging; Mr. Erik Dunkerley and the UML Center for High-Rate Nanomanufacturing for assistance with thermal analysis (TGA, DSC); Dr. Hilmar Koerner, Dr. Rich Vaia et al. of the United States Air Force Research Labs for the X-ray diffraction data; and Mr. Louis Freitas of EMS-Grivory America for the donation of the Grilamid TR 90.

References

- [1] E. Picard, A. Vermogen, J.-F. Gérard, and E. Espuche, "Barrier properties of nylon 6-montmorillonite nanocomposite membranes prepared by melt blending: influence of the clay content and dispersion state: consequences on modelling," *Journal of Membrane Science*, vol. 292, no. 1-2, pp. 133–144, 2007.
- [2] A. N. Wilkinson, Z. Man, J. L. Stanford, et al., "Structure and dynamic mechanical properties of melt intercalated polyamide 6—montmorillonite nanocomposites," *Macromolecular Materials and Engineering*, vol. 291, no. 8, pp. 917–928, 2006.
- [3] Y. Zhang, J. H. Yang, T. S. Ellis, and J. Shi, "Crystal structures and their effects on the properties of polyamide 12/clay and polyamide 6-polyamide 66/clay nanocomposites," *Journal of Applied Polymer Science*, vol. 100, no. 6, pp. 4782–4794, 2006.
- [4] H. J. Kim and H. G. Jeon, US patent US2006166762, 2006.
- [5] M. Mehrabzadeh and M. R. Kamal, "Melt processing of PA-66/clay, HDPE/clay and HDPE/PA-66/clay nanocomposites," *Polymer Engineering and Science*, vol. 44, no. 6, pp. 1152–1161, 2004.
- [6] D. Homminga, B. Goderis, S. Hoffman, H. Reynaers, and G. Groeninckx, "Influence of shear flow on the preparation of polymer layered silicate nanocomposites," *Polymer*, vol. 46, no. 23, pp. 9941–9954, 2005.
- [7] F.-C. Chiu, S.-M. Lai, Y.-L. Chen, and T.-H. Lee, "Investigation on the polyamide 6/organoclay nanocomposites with or without a maleated polyolefin elastomer as a toughener," *Polymer*, vol. 46, no. 25, pp. 11600–11609, 2005.
- [8] A. Dasari, Z.-Z. Yu, M. Yang, Q.-X. Zhang, X.-L. Xie, and Y.-W. Mai, "Micro- and nano-scale deformation behavior of nylon 66-based binary and ternary nanocomposites," *Composites Science and Technology*, vol. 66, no. 16, pp. 3097–3114, 2006.
- [9] P. M. Gyoo, S. Venkataramani, and S. C. Kim, "Morphology, thermal, and mechanical properties of polyamide 66/clay nanocomposites with epoxy-modified organoclay," *Journal of Applied Polymer Science*, vol. 101, no. 3, pp. 1711–1722, 2006.
- [10] P. Médéric, T. Razafinimaro, and T. Aubry, "Influence of melt-blending conditions on structural, rheological, and interfacial properties of polyamide-12 layered silicate nanocomposites," *Polymer Engineering and Science*, vol. 46, no. 8, pp. 986–994, 2006.
- [11] N. K. Borse and M. R. Kamal, "Melt processing effects on the structure and mechanical properties of PA-6/clay nanocomposites," *Polymer Engineering and Science*, vol. 46, no. 8, pp. 1094–1103, 2006.
- [12] S. Mohanty and S. K. Nayak, "Effect of clay exfoliation and organic modification on morphological, dynamic mechanical, and thermal behavior of melt-compounded polyamide-6 nanocomposites," *Polymer Composites*, vol. 28, no. 2, pp. 153–162, 2007.
- [13] N. A. Hocine, P. Médéric, and T. Aubry, "Mechanical properties of polyamide-12 layered silicate nanocomposites and their relations with structure," *Polymer Testing*, vol. 27, no. 3, pp. 330–339, 2008.
- [14] Y. Yoo and D. R. Paul, "Effect of organoclay structure on morphology and properties of nanocomposites based on an amorphous polyamide," *Polymer*, vol. 49, no. 17, pp. 3795–3804, 2008.
- [15] B. Alexandre, D. Langevin, P. Médéric, et al., "Water barrier properties of polyamide 12/montmorillonite nanocomposite membranes: structure and volume fraction effects," *Journal of Membrane Science*, vol. 328, no. 1-2, pp. 186–204, 2009.
- [16] E. J. Garboczi, K. A. Snyder, J. F. Douglas, and M. F. Thorpe, "Geometrical percolation threshold of overlapping ellipsoids," *Physical Review E*, vol. 52, no. 1, pp. 819–828, 1995.
- [17] http://www.nanocor.com/tech_sheets/N662.pdf, September 2008.
- [18] http://www.scpod.com/product_bulletins/PB%20Cloisite%2030B.pdf, September 2008.
- [19] D. Adame and G. W. Beall, "Direct measurement of the constrained polymer region in polyamide/clay nanocomposites and the implications for gas diffusion," *Applied Clay Science*, vol. 42, no. 3-4, pp. 545–552, 2009.
- [20] http://www.emsgrivory.com/mytools/datenblaetter/datenblaetter/grilamid_tr/TR_90_E.pdf, September 2008.
- [21] I. Y. Phang, T. Liu, A. Mohamed, et al., "Morphology, thermal and mechanical properties of nylon 12/organoclay nanocomposites prepared by melt compounding," *Polymer International*, vol. 54, no. 2, pp. 456–464, 2005.
- [22] T. D. Fornes, P. J. Yoon, H. Keskkula, and D. R. Paul, "Nylon 6 nanocomposites: the effect of matrix molecular weight," *Polymer*, vol. 42, no. 25, pp. 9929–9940, 2001.
- [23] T. D. Fornes and D. R. Paul, "Structure and properties of nanocomposites based on nylon-11 and -12 compared with those based on nylon-6," *Macromolecules*, vol. 37, no. 20, pp. 7698–7709, 2004.
- [24] S. Xie, S. Zhang, F. Wang, H. Liu, and M. Yang, "Influence of annealing treatment on the heat distortion temperature of nylon-6/montmorillonite nanocomposites," *Polymer Engineering and Science*, vol. 45, no. 9, pp. 1247–1253, 2005.
- [25] J. E. Mark, Ed., *Polymer Data Handbook*, Oxford University Press, Oxford, UK, 1999.
- [26] http://www.emsgrivory.com/mytools/datenblaetter/datenblaetter/grilamid_tr/TR_90_E.pdf, October 2007.
- [27] T. McNally, W. R. Murphy, C. Y. Lew, R. J. Turner, and G. P. Brennan, "Polyamide-12 layered silicate nanocomposites by melt blending," *Polymer*, vol. 44, no. 9, pp. 2761–2772, 2003.
- [28] P. I. Vincent, "The necking and cold-drawing of rigid plastics," *Polymer*, vol. 1, pp. 7–19, 1960.
- [29] A. Cross and R. N. Hayward, "Thermal fracture of plastics," *Journal of Polymer Science: Polymer Physics Edition*, vol. 11, no. 12, pp. 2423–2439, 1973.
- [30] A. Cross, M. Hall, and R. N. Haward, "Thermal effects in the necking of thermoplastics," *Nature*, vol. 253, no. 5490, pp. 340–341, 1975.
- [31] J. W. Maher, R. N. Haward, and J. N. Hay, "Study of the thermal effects in the necking of polymers with the use of an infrared camera," *Journal of Polymer Science: Polymer Physics Edition*, vol. 18, no. 11, pp. 2169–2179, 1980.
- [32] R. Roseen, "Temperature effect at self-oscillating necking during extension of polyethylene terephthalate (PETP)," *Journal of Materials Science*, vol. 9, no. 6, pp. 929–933, 1974.